NEUTRINO

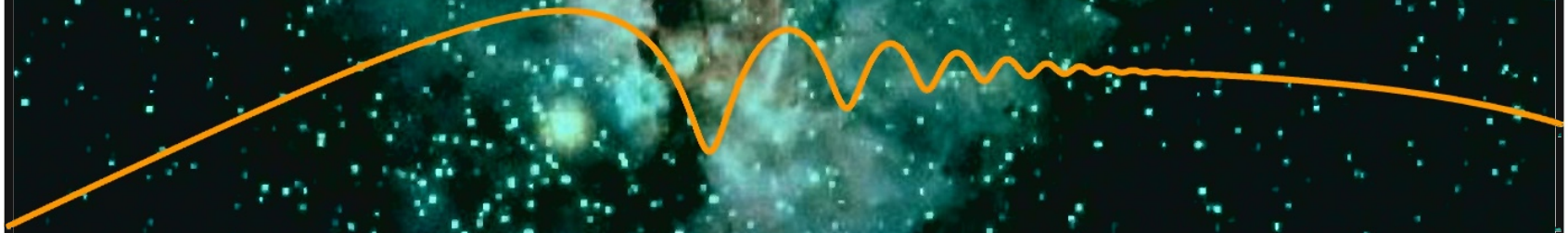

V.Naumov

Lipnya School, June 30, 2006

Contents

PREFACE

1 Neutrinos on Earth

Neutrino fluxes on Earth (tentative)

Energy range or average energy (eV)	Source	Local flux ($1/\mathrm{cm}^2\,\mathrm{s}$)
1.7×10^{4}	Big Bang (relic)	10^{13}
$10^{3}-10^{7}$	Sun	5×10^{10}
$10^{3}-10^{7}$	Terrestrial radioactivity	7.5×10^{6}
$10^{3}-10^{7}$	Man-made nuclear reactors	7.5×10^{6}
$10^{9}-10^{12}$	Man-made accelerators	$<10^{6}$
$>10^{8}$	Cosmic rays (atmospheric)	$<10^{6}$
$>10^{12}$	Astrophysical objects (e.g. AGN)	$<10^{6}$
$>10^{15}$	UHECR+ γ_{rel} (cosmogenic)	10^{-12}

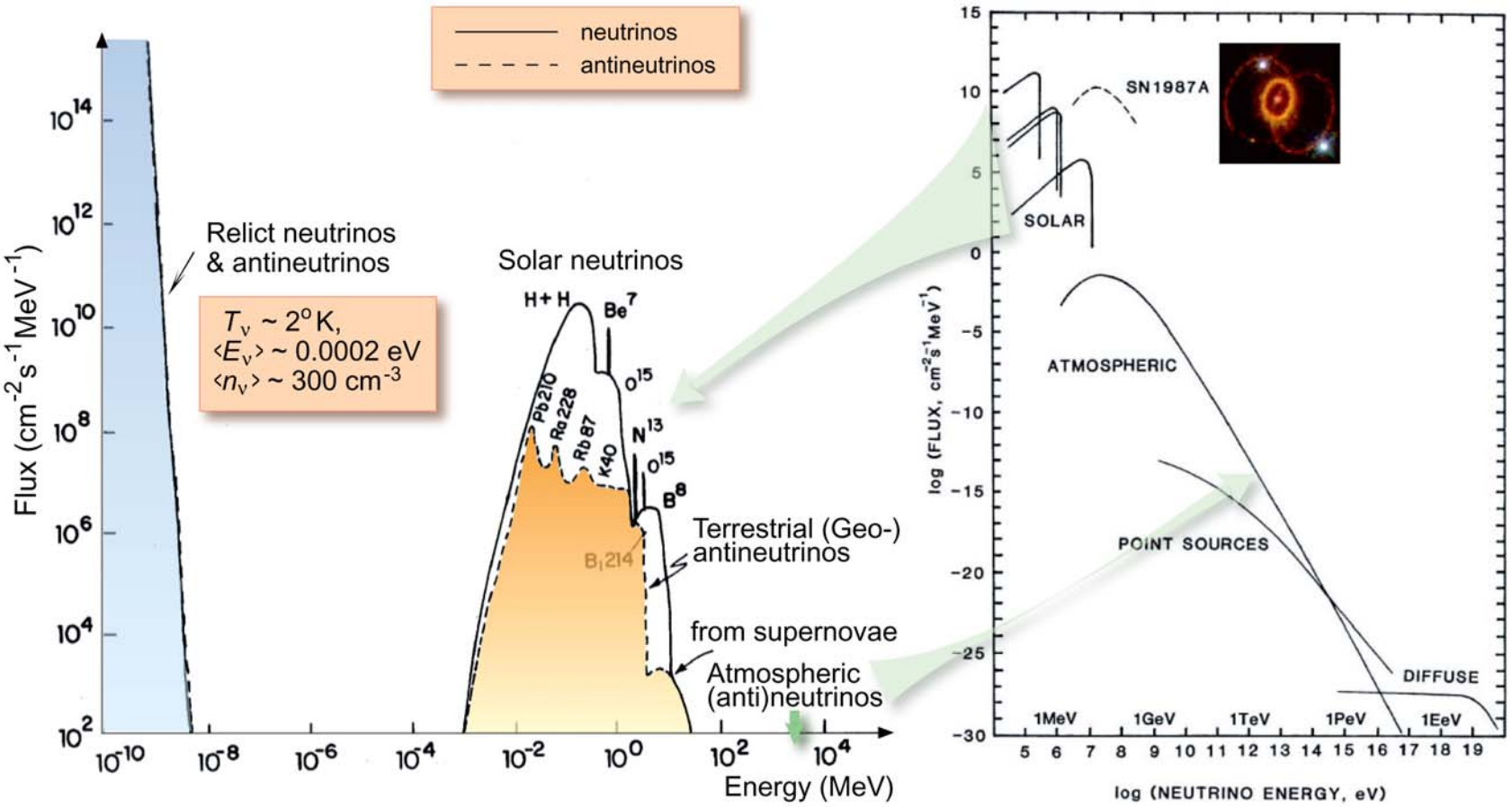

Figure 1: Tentative representation of neutrino and antineutrino fluxes on Earth.

[From L. M. Krauss, S. L. Glashow, and D. N. Schramm, "Antineutrino astronomy and geophysics," Nature **310** (1984) 191–198 (left) and A. M. Bakich, "Aspects of neutrino astronomy," Space Sci. Rev. **49** (1989) 259–310 (right).]

Examples of astrophysical sources of high-energy neutrinos

Candidate point sources

- ⋆ **Young supernova remnants**
  [due to CR acceleration by shock waves from SN explosions]
- ⋆ **Accreting neutron stars and black holes**
- ⋆ **Binary (multiple) systems**
  [pulsar + giant, pulsar + star filling its Roche lobe, white dwarf + (super)giant, etc.]
- ⋆ **The Galactic center**
  [within the model of a supermassive accreting black hole]
- ⋆ **Active Galactic Nuclei (AGNs)**
  [Seyfert galaxies, N galaxies, quasars, Lacertae (BLLac objects), blazars (radio-loud AGNs); particle acceleration in extragalactic jets from radio-quiet and radio-loud AGNs]
- ⋆ **Gamma-Ray Bursts (GRBs)**
  [example: γ's and ν's arise from decay of pions produced in shock front collisions]
- ⋆ **Hidden or latent sources**
  [young SN shell, cocooned massive black hole (MBH) in AGN, Thorne–Żytkow star (the binary with a neutron star submerged into a red supergiant core), AGN with standing shock in the vicinity of a MBH, etc.]

Diffuse neutrino backgrounds

- ⋆ **Galactic neutrinos**
  [including ν's from CR interactions with the spherical halo of baryonic dark matter]
- ⋆ **Quasi-diffuse background from AGN's**
- ⋆ **Neutrinos from intergalactic space**
  [the most important are UHE ν's from the CR spectrum tail (GZK cutoff)]
- ⋆ **Pregalactic neutrinos and neutrinos from the bright phase of galaxy evolution**

Speculative sources of the highest-energy neutrinos and science fiction

- ⋆ **Topological defects**
  [ultra-heavy particle emission and acceleration by saturated superconducting cosmic strings, cusp radiation from ordinary cosmic strings, vortons, textures, global monopoles, etc.]
- ⋆ **Mini-black-hole evaporation**
- ⋆ **Decay of super-heavy exotic particles** [such as long-lived Big Bang relics or the Planck mass objects (planckeons $\sim$ fridmons $\sim$ maximons $\sim$ cosmions)]
- ⋆
- ⋆

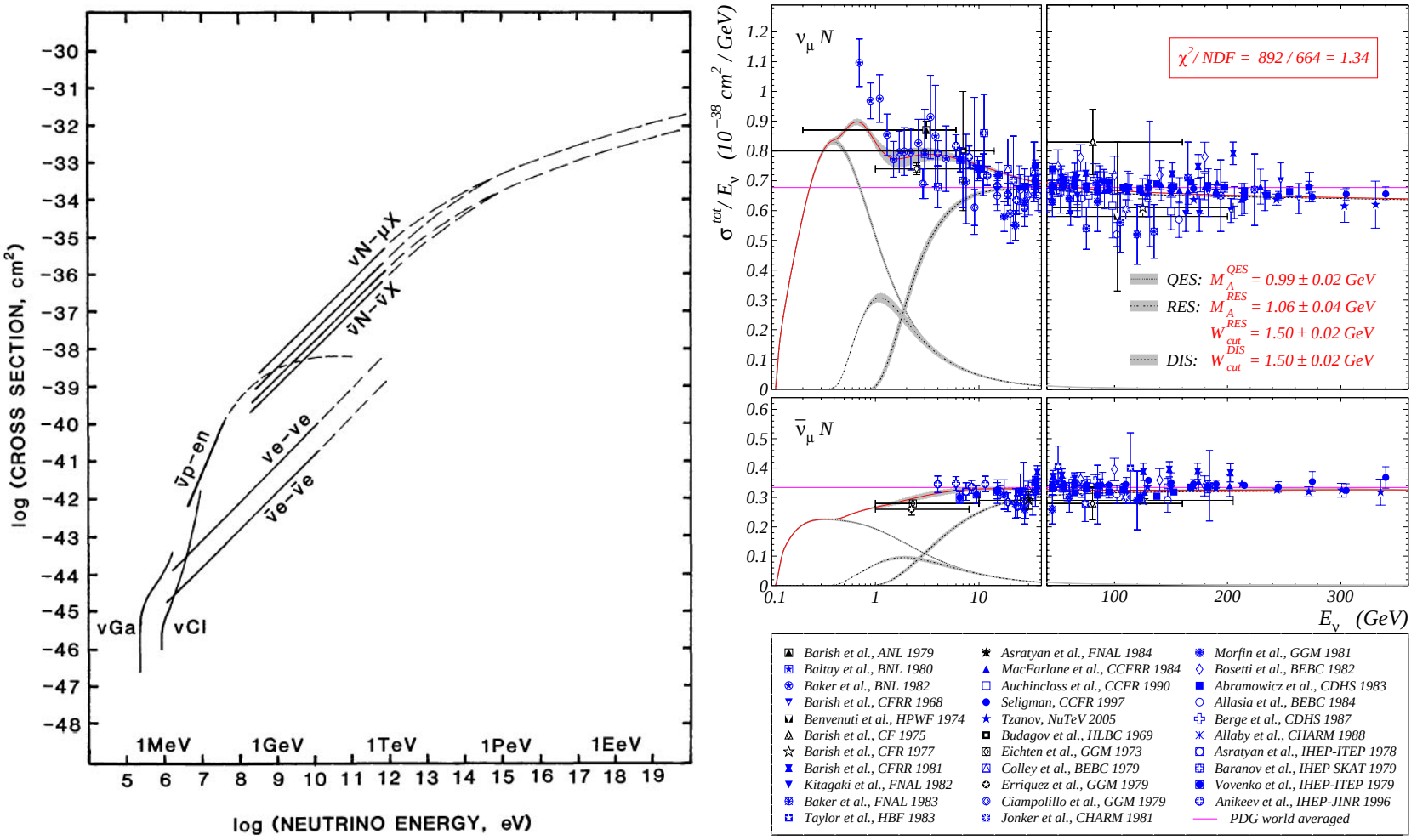

Figure 2: **Left**: Tentative representation of the cross sections for neutrino interactions with nuclei, nucleons and electrons. **Right**: Measured slopes of the muon neutrino and antineutrino total cross sections; three main contributions and their sums are shown.

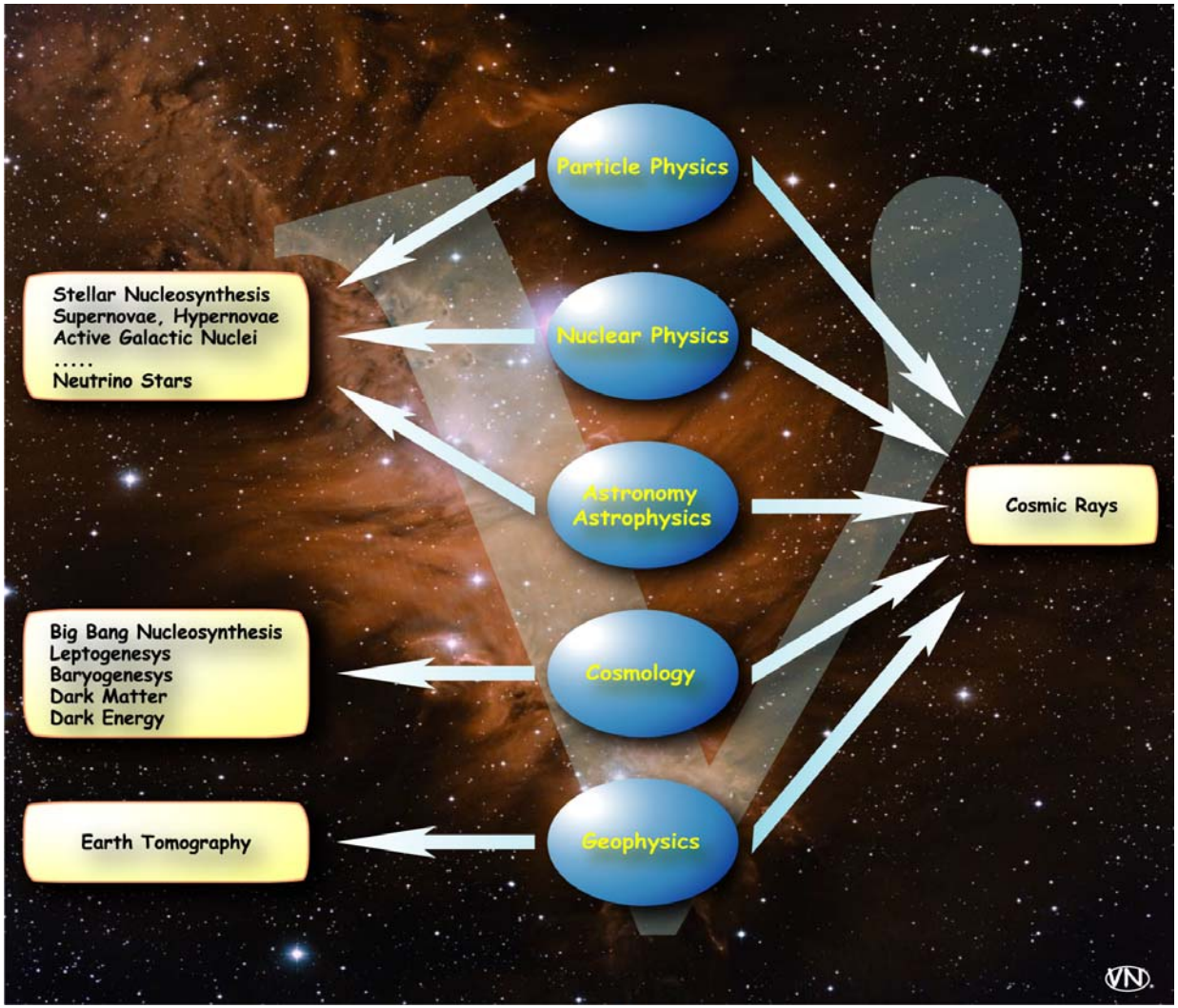

Figure 3: Neutrino is a keystone of modern physics and astrophysics.

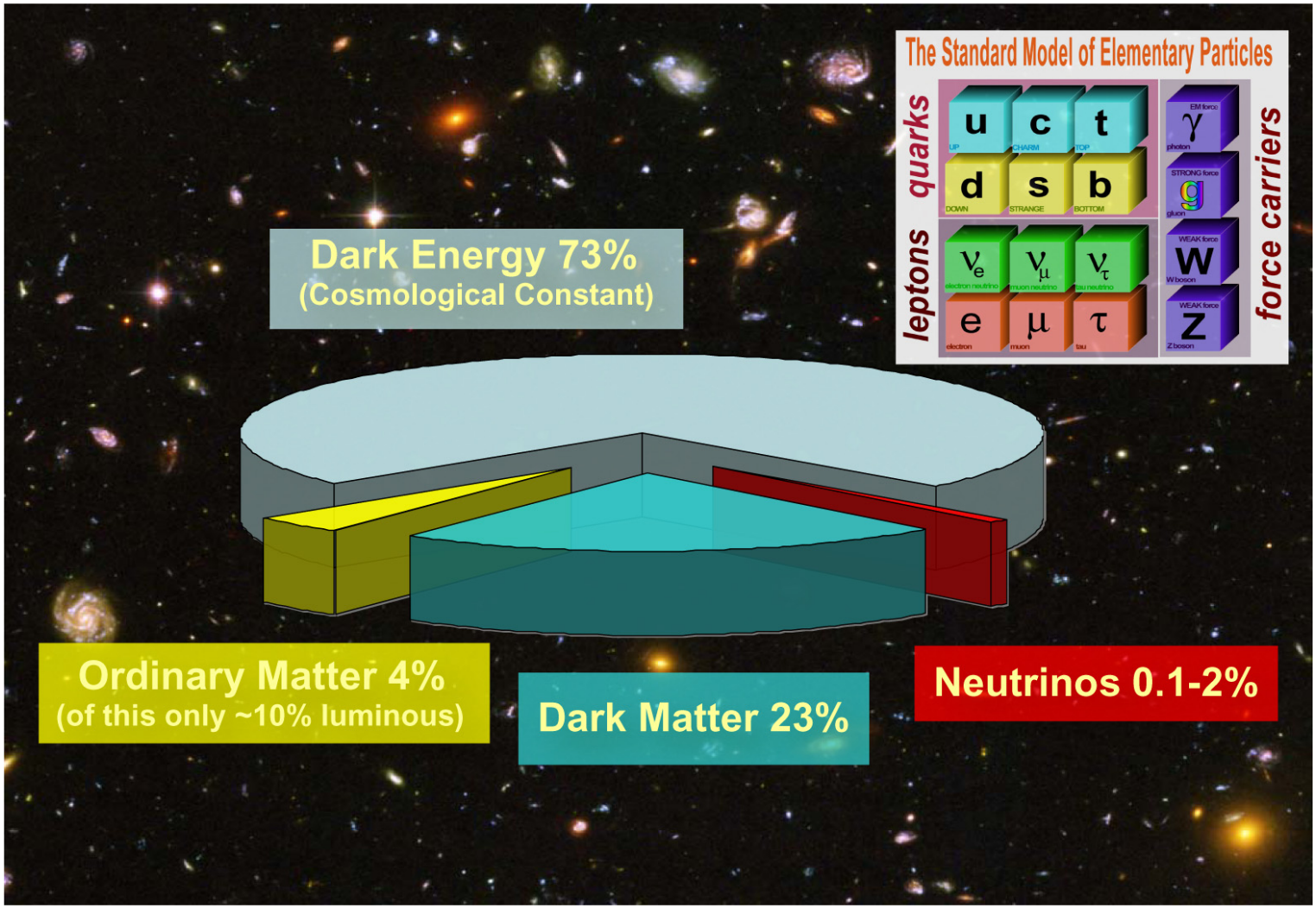

Figure 4: Neutrinos compose a part of invisible (nonluminous) matter in the universe.

2 Bruno Pontecorvo

Bruno M. Pontecorvo (*Pisa, August 22, 1913 – Dubna, September 24, 1993*) was a great physicist who had enormous impact on the development of neutrino physics. In particular he was the pioneer of neutrino oscillations. He came to this idea in 1957, soon after the two-component neutrino theory was proposed by Landau, Lee and Yang and Salam and confirmed by Goldhaber *et al.*

It was very nontrivial to propose neutrino oscillations in 1957, at the time when only one type of neutrino was known. Oscillations which B. Pontecorvo considered were $\nu_L \rightleftarrows \overline{\nu}_L$ i.e. oscillations between active and sterile neutrinos.[a]

[a] B. Pontecorvo proposed the existence of sterile neutrinos as well as the term "sterile neutrino" itself (1967) so popular nowadays.

[From the JINR's official site about Bruno Pontecorvo, URL: <http://pontecorvo.jinr.ru/>.]

Chlorine-Argon idea (Canada).

Swinging neutrinos.

Both cartoons were drawn by Mikhail Bilenky for the celebration of Bruno Pontecorvo's 75th Anniversary held at Dubna (August 1988).

[Borrowed from S. M. Bilenky, "Bruno Pontecorvo: Mister Neutrino," a report at the 3rd International Workshop "Neutrino Oscillations in Venice," Venice, February 7-10, 2006 (physics/0603039).]

Part I

INTRODUCTION TO NEUTRINO OSCILLATIONS

3 Neutrino masses and mixing in the Standard Model

3.1 Interaction Lagrangians and currents

The Standard Model (SM) Lagrangians for charged and neutral current neutrino interactions are assumed to be

$$\mathcal{L}_I^{\mathsf{CC}}(x) = -\frac{g}{2\sqrt{2}} j_\alpha^{\mathsf{CC}}(x) W^\alpha(x) + \mathsf{H.c.} \quad \text{and} \quad \mathcal{L}_I^{\mathsf{NC}}(x) = -\frac{g}{2\cos\theta_{\mathsf{W}}} j_\alpha^{\mathsf{NC}}(x) Z^\alpha(x).$$

Here g is the $SU(2)$ (electro-weak) gauge coupling constant

$$g^2 = 4\sqrt{2} M_W^2 G_F, \quad g \sin\theta_{\mathsf{W}} = |e|$$

and θ_{W} is the weak mixing (Weinberg) angle ($\sin^2\theta_{\mathsf{W}}(M_Z) = 0.23120$).

The leptonic charged current and neutrino neutral current are given by the expressions:

$$j_\alpha^{\mathsf{CC}}(x) = 2 \sum_{\ell=e,\mu,\tau,\ldots} \overline{\nu}_{\ell,L}(x)\gamma_\alpha \ell_L(x) \quad \text{and} \quad j_\alpha^{\mathsf{NC}}(x) = \sum_{\ell=e,\mu,\tau,\ldots} \overline{\nu}_{\ell,L}(x)\gamma_\alpha \nu_{\ell,L}(x).$$

The currents may include (yet unknown) heavy neutrinos and corresponding charged leptons. The left- and right-handed fermion fields are defined as usually:

$$\nu_{\ell,L/R}(x) = \left(\frac{1 \pm \gamma_5}{2}\right) \nu_\ell(x) \quad \text{and} \quad \ell_{L/R}(x) = \left(\frac{1 \pm \gamma_5}{2}\right) \ell(x).$$

Note that the kinetic term of the Lagrangian includes both L and R handed neutrinos and moreover, it can include other sterile neutrinos:

$$\begin{aligned}\mathcal{L}_0 =& \frac{i}{2}\left[\overline{\nu}(x)\gamma^\alpha\partial_\alpha\nu(x) - \partial_\alpha\overline{\nu}(x)\gamma^\alpha\nu(x)\right] \equiv \frac{i}{2}\overline{\nu}(x)\overleftrightarrow{\boldsymbol{\partial}}\nu(x) \\ =& \frac{i}{2}\left[\overline{\nu}_L(x)\overleftrightarrow{\boldsymbol{\partial}}\nu_L(x) + \overline{\nu}_R(x)\overleftrightarrow{\boldsymbol{\partial}}\nu_R(x)\right],\end{aligned}$$

$$\boldsymbol{\nu}(x) = \boldsymbol{\nu}_L(x) + \boldsymbol{\nu}_R(x) = \begin{pmatrix}\nu_e(x)\\ \nu_\mu(x)\\ \nu_\tau(x)\\ .\\ .\\ .\end{pmatrix}, \quad \boldsymbol{\nu}_{L/R}(x) = \begin{pmatrix}\nu_{e,L/R}(x)\\ \nu_{\mu,L/R}(x)\\ \nu_{\tau,L/R}(x)\\ .\\ .\\ .\end{pmatrix} = \frac{1\pm\gamma_5}{2}\begin{pmatrix}\nu_e(x)\\ \nu_\mu(x)\\ \nu_\tau(x)\\ .\\ .\\ .\end{pmatrix}.$$

Neutrino chirality: $\gamma_5\nu_L = -\nu_L$ and $\gamma_5\nu_R = +\nu_R$.

The Lagrangian of the theory with massless neutrinos is invariant with respect to the global gauge transformations $\nu_\ell(x) \to e^{i\Lambda_\ell}\nu_\ell(x)$, $\ell(x) \to e^{i\Lambda_\ell}\ell(x)$ with $\Lambda_\ell = \text{const}$. This leads to conservation of the individual lepton flavor numbers L_ℓ (electron, muon, tauon,...). It is not the case for massive neutrinos.

There are two types of possible neutrino mass terms: Dirac and Majorana.

3.2 Dirac neutrinos

The Dirac mass term has the form

$$\mathcal{L}_{\mathrm{D}}(x) = -\overline{\boldsymbol{\nu}}_R(x)\mathbf{M}_{\mathrm{D}}\boldsymbol{\nu}_L(x) + \mathrm{H.c.},$$

where $\mathbf{M}_{\mathrm{D}}$ is a $N \times N$ complex *nondiagonal* matrix. In general, $N \geq 3$ that is the column $\boldsymbol{\nu}_L$ may include the heavy *active* neutrino fields as well as *sterile* neutrino fields which do not enter into the standard charged and neutral currents.

An arbitrary complex matrix can be diagonalized by means of an appropriate *biunitary* transformation. One has

$$\mathbf{M}_{\mathrm{D}} = \tilde{\mathbf{V}}\mathbf{m}\mathbf{V}^{\dagger}, \quad \mathbf{m} = ||m_{kl}|| = ||m_k\delta_{kl}||,$$

where $\mathbf{V}$ and $\tilde{\mathbf{V}}$ are unitary matrices and $m_k \geq 0$. Therefore

$$\mathcal{L}_{\mathrm{D}}(x) = -\overline{\boldsymbol{\nu}'}_R(x)\mathbf{m}\boldsymbol{\nu}'_L(x) + \mathrm{H.c.} = -\overline{\boldsymbol{\nu}'}(x)\mathbf{m}\boldsymbol{\nu}'(x) = -\sum_{k=1}^{N} m_k\overline{\nu}_k(x)\nu_k(x),$$

$$\boldsymbol{\nu}'_L(x) = \mathbf{V}^{\dagger}\boldsymbol{\nu}_L(x), \quad \boldsymbol{\nu}'_R(x) = \tilde{\mathbf{V}}^{\dagger}\boldsymbol{\nu}_R(x), \quad \boldsymbol{\nu}'(x) = (\nu_1, \nu_2, \ldots, \nu_N)^T.$$

It is easy to prove that the kinetic term in the neutrino Lagrangian is transformed to

$$\mathcal{L}_0 = \frac{i}{2}\,\overline{\boldsymbol{\nu}'}(x)\overleftrightarrow{\boldsymbol{\partial}}\boldsymbol{\nu}'(x) = \frac{i}{2}\sum_k \overline{\nu}_k(x)\overleftrightarrow{\boldsymbol{\partial}}\nu_k(x).$$

Hence, one can conclude that $\nu_k(x)$ is the field of a Dirac neutrino with the mass m_k and the flavor LH neutrino fields $\nu_{\ell,L}(x)$ present in the standard weak lepton currents are linear combinations of the LH components of the fields of neutrinos with definite masses:

$$\boldsymbol{\nu}_L = \mathbf{V}\boldsymbol{\nu}'_L \quad \text{or} \quad \nu_{\ell,L} = \sum_k V_{\ell k}\nu_{k,L}.$$

The matrix $\mathbf{V}$ is sometimes referred to as the Pontecorvo-Maki-Nakagawa-Sakata (PMNS) neutrino (vacuum) mixing matrix.[a]

It can be proved that the Lagrangian of the theory with the Dirac mass term is invariant with respect to the global gauge transformation

$$\nu_k(x) \to e^{i\Lambda}\nu_k(x), \quad \ell(x) \to e^{i\Lambda}\ell(x), \quad \Lambda = \text{const}.$$

This means that the lepton charge

$$L = \sum_{\ell=e,\mu,\tau,\ldots} L_\ell$$

common to all charged leptons and all neutrinos ν_k is conserved. However

the individual lepton flavor numbers L_ℓ are no longer conserved.

[a] Of course it is not the same as the Cabibbo-Kobayashi-Maskawa (CKM) quark mixing matrix. It seems however that the PMNS and CKM matrices are, in a sense, *complementary* (see below).

3.2.1 Parametrization of mixing matrix for Dirac neutrinos

It is well known that a complex $n \times n$ unitary matrix depends on n^2 *real* parameters. The classical result by Murnagham[a] states that the matrices from the unitary group $U(n)$ are products of a diagonal phase matrix

$$\boldsymbol{\Gamma} = \text{diag}\left(e^{i\alpha_1}, e^{i\alpha_2}, \ldots, e^{i\alpha_n}\right),$$

containing n phases α_k, and $n(n-1)/2$ matrices whose main building blocks have the form

$$\begin{pmatrix} \cos\theta & \sin\theta\, e^{-i\phi} \\ -\sin\theta\, e^{+i\phi} & \cos\theta \end{pmatrix} = \begin{pmatrix} 1 & 0 \\ 0 & e^{+i\phi} \end{pmatrix} \underbrace{\begin{pmatrix} \cos\theta & \sin\theta \\ -\sin\theta & \cos\theta \end{pmatrix}}_{\text{Euler rotation}} \begin{pmatrix} 1 & 0 \\ 0 & e^{-i\phi} \end{pmatrix}.$$

Therefore any $n \times n$ unitary matrix can be parametrized in terms of

$$n(n-1)/2 \text{ "angles" (taking values within } [0, \pi/2])$$

and

$$n(n+1)/2 \text{ "phases" (taking values within } [0, 2\pi)).$$

The usual parametrization of both the CKM and PMNS matrices is of this type.

[a] F. D. Murnagham, "The unitary and rotation groups," Washington, DC: Sparta Books (1962).

One can reduce the number of the phases further by taking into account that the Lagrangian with the Dirac mass term is invariant with respect to the transformation

$$\ell \mapsto e^{ia_\ell}\ell, \quad \nu_k \mapsto e^{ib_\ell}\nu_k, \quad V_{\ell k} \mapsto e^{i(b_k - a_\ell)}V_{\ell k},$$

and to the global gauge transformation

$$\ell \mapsto e^{i\Lambda}\ell, \quad \nu_k \mapsto e^{i\Lambda}\nu_k.$$

Therefore $2N-1$ phases are unphysical and the number of physical (*Dirac*) phases is

$$n_{\mathsf{D}} = \frac{N(N+1)}{2} - (2N-1) = \frac{N^2-3N+2}{2} = \frac{(N-1)(N-2)}{2} \qquad (N \geq 2);$$

$$n_{\mathsf{D}}(2) = 0, \quad n_{\mathsf{D}}(3) = 1, \quad n_{\mathsf{D}}(4) = 3, \ldots$$

The nonzero phases lead to the CP and T violation in the neutrino sector.

Three-neutrino case

In the most interesting (today!) case of three lepton generations one defines the orthogonal rotation matrices in the ij-planes which depend upon the mixing angles θ_{ij}:

$$\mathbf{O}_{12} = \underbrace{\begin{pmatrix} c_{12} & s_{12} & 0 \\ -s_{12} & c_{12} & 0 \\ 0 & 0 & 1 \end{pmatrix}}_{\text{Solar matrix}}, \quad \mathbf{O}_{13} = \underbrace{\begin{pmatrix} c_{13} & 0 & s_{13} \\ 0 & 1 & 0 \\ -s_{13} & 0 & c_{13} \end{pmatrix}}_{\text{Bona vacantia (as yet)}}, \quad \mathbf{O}_{23} = \underbrace{\begin{pmatrix} 1 & 0 & 0 \\ 0 & c_{23} & s_{23} \\ 0 & -s_{23} & c_{23} \end{pmatrix}}_{\text{Atmospheric matrix}},$$

(where $c_{ij} \equiv \cos\theta_{ij}$, $s_{ij} \equiv \sin\theta_{ij}$) and the diagonal matrix with the Dirac phase factor:

$$\boldsymbol{\Gamma}_{\mathsf{D}} = \mathsf{diag}\left(1, 1, e^{i\delta}\right).$$

The parameter δ is commonly referred to as the Dirac CP-violation phase.

Finally, by taking into account the Murnagham theorem, the PMNS mixing matrix for the Dirac neutrinos can be parametrized as[a]

$$\begin{aligned} \mathbf{V}_{(\mathsf{D})} &= \mathbf{O}_{23}\boldsymbol{\Gamma}_{\mathsf{D}}\mathbf{O}_{13}\boldsymbol{\Gamma}_{\mathsf{D}}^{\dagger}\mathbf{O}_{12} \\ &= \begin{pmatrix} c_{12}c_{13} & s_{12}c_{13} & s_{13}e^{-i\delta} \\ -s_{12}c_{23} - c_{12}s_{23}s_{13}e^{i\delta} & c_{12}c_{23} - s_{12}s_{23}s_{13}e^{i\delta} & s_{23}c_{13} \\ s_{12}s_{23} - c_{12}c_{23}s_{13}e^{i\delta} & -c_{12}s_{23} - s_{12}c_{23}s_{13}e^{i\delta} & c_{23}c_{13} \end{pmatrix}. \end{aligned}$$

[a] This is the *Chau–Keung presentation* advocated by the PDG for both CKM and PMNS matrices.

Since the Dirac mass term violates conservation of the individual lepton numbers L_e, L_μ and L_τ, it allows many lepton family number violating processes, like

$$\mu^\pm \to e^\pm + \gamma, \quad \mu^\pm \to e^\pm + e^+ + e^-,$$
$$K^+ \to \pi^+ + \mu^\pm + e^\mp, \quad K^- \to \pi^- + \mu^\pm + e^\mp,$$
$$\mu^- + (A,Z) \to e^- + (A,Z), \quad \tau^- + (A,Z) \to \mu^- + (A,Z), \ldots$$

However the neutrinoless double beta decay[a] $(A,Z) \to (A,Z+2) + 2e^-$ and the processes like $K^+ \to \pi^- + \mu^+ + e^+$, $K^- \to \pi^+ + \mu^- + e^-$, etc. are forbidden as a consequence of the total lepton charge conservation.

Table 1: Current limits on the simplest lepton family number violating μ and τ decays.
[From S. Eidelman *et al.* (Particle Data Group), "Review of particle physics," Phys. Lett. B **592** (2004) 1–1109.].

Decay Modes	Fraction	C.L.		Decay Modes	Fraction	C.L.
$\mu^- \to \nu_e \overline{\nu}_\mu$	$< 1.2\%$	90%		$\tau^- \to e^- \gamma$	$< 2.7 \times 10^{-6}$	90%
$\mu^- \to e^- \gamma$	$< 1.2 \times 10^{-11}$	90%		$\tau^- \to \mu^- \gamma$	$< 1.1 \times 10^{-6}$	90%
$\mu^- \to e^- e^+ e^-$	$< 1.0 \times 10^{-12}$	90%		$\tau^- \to e^- \pi^0$	$< 3.7 \times 10^{-6}$	90%
$\mu^- \to 2\gamma$	$< 7.2 \times 10^{-11}$	90%		$\tau^- \to \mu^- \pi^0$	$< 4.0 \times 10^{-6}$	90%

[a] Hereafter abbreviated as $(\beta\beta)_{0\nu}$.

3.2.2 Neutrinoless muon decay in SM

The L_μ and L_e violating muon decay $\mu^- \to e^-\gamma$ is allowed if $V^*_{\mu k}V_{ek} \neq 0$ for $k = 1, 2$ or 3. The corresponding Feynman diagrams include W loops and thus the decay width is strongly suppressed by the neutrino to W boson mass ratios:

$$R = \frac{\Gamma(\mu^- \to e^-\gamma)}{\Gamma(\mu^- \to e^-\nu_\mu\overline{\nu}_e)} = \frac{3\alpha}{32\pi}\left|\sum_k V^*_{\mu k}V_{ek}\frac{m_k^2}{m_W^2}\right|^2.$$

Since $m_k/m_W = 1.24 \times 10^{-11}\,(m_k/1\text{ eV})$, the ratio can be estimated as

$$R \approx 5.2 \times 10^{-48}\left|\sum_k V^*_{\mu k}V_{ek}\left(\frac{m_k}{1\text{ eV}}\right)^2\right|^2,$$

while the current experimental upper limit is (at least!) 36 orders of magnitude larger (see Table 1):

$$R_{(\text{exp})} < 1.2 \times 10^{-11} \text{ at } 90\% \text{ C.L.} \quad (\textbf{NO GO!})$$

Some nonstandard models are more optimistic.

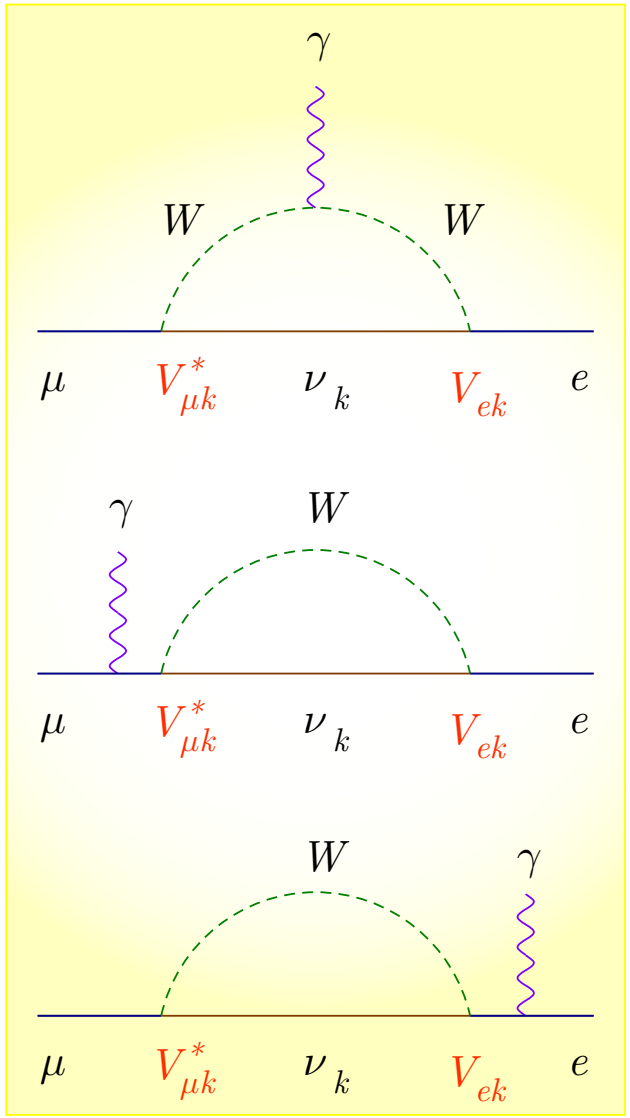

3.2.3 Nuclear beta decay

The method of measurement of the (anti)neutrino mass through the investigation of the high-energy part of the β-spectrum was proposed by Perrin (1933) and Fermi (1934).
The first experiments on the measurement of the neutrino mass with this method have been done by Curran, Angus and Cockcroft (1948) and Hanna and Pontecorvo (1949).

The energy spectrum of electrons in the decay $(A, Z) \to (A, Z+1) + e^- + \overline{\nu}_e$ is[a]

$$\frac{d\Gamma}{dT} = \sum_k |V_{ek}|^2 \frac{d\Gamma_k}{dT}, \tag{1}$$

$$\frac{d\Gamma_k}{dT} = \frac{(G_F \cos\theta_C)^2}{2\pi^3} pp_k (T + m_e)(Q - T) |\mathcal{M}|^2 F(T)\theta(Q - T - m_k). \tag{2}$$

Here G_F is the Fermi constant, θ_C is the Cabibbo angle, m_e, p and T are the mass, magnitude of the momentum and kinetic energy of the electron, respectively,

$$p_k = \sqrt{E_k^2 - m_k^2} = \sqrt{(Q - T)^2 - m_k^2}$$

is the magnitude of the neutrino momentum, Q is the energy released in the decay (the endpoint of the β spectrum in case of zero neutrino mass), $\mathcal{M}$ is the nuclear matrix element, and $F(T)$ is the Fermi function, which describes the Coulomb interaction of the final particles. The step function in Eq. (2) ensures that a neutrino

[a] The recoil of the final nucleus and radiative corrections (luckily small) are neglected.

state ν_k is only produced if its total energy is larger than its mass: $E_k = Q - T \geq m_k$. As it is seen from Eq. (1), the largest distortion of the β-spectrum due to neutrino masses can be observed in the region

$$Q - T \sim m_k. \tag{3}$$

However, for $\max(m_k) \simeq 1$ eV only a very small part (about 10^{-13}) of the decays give contribution to the region (3). This is the reason why in the analysis of the results of the measurement of the β-spectrum a relatively large part of the spectrum is used.[b] Taking this into account and applying unitarity of the mixing matrix, we can write

$$\sum_k |V_{ek}|^2 p_k \approx \sum_k |V_{ek}|^2 (Q-T)\left[1 - \frac{m_k^2}{2(Q-T)^2}\right]$$

$$= (Q-T)\left[1 - \frac{1}{2(Q-T)^2}\sum_k |V_{ek}|^2 m_k^2\right] \approx \sqrt{(Q-T)^2 - m_\beta^2},$$

where the effective neutrino mass m_β is defined by

$$m_\beta^2 = \sum_k |V_{ek}|^2 m_k^2$$

and it was assumed that $\max\left(m_k^2\right) \ll 4(Q-T)^2$.

[b] For example, in the Mainz tritium experiment (see below) the last 70 eV of the spectrum is used.

Finally, the β-spectrum that is used for fitting the data can be presented as

$$\frac{d\Gamma}{dT} \propto p\,(T+m_e)\,|\mathcal{M}|^2\,F(T)K^2(T),$$

where

$$K(T) \propto \sqrt{\frac{d\Gamma/dT}{p\,(T+m_e)\,|\mathcal{M}|^2\,F(T)}}$$

$$\approx (Q-T)\left[1-\frac{m_\beta^2}{(Q-T)^2}\right]^{1/4}$$

is the so-called *Kurie plot*.

Unfortunately, the real situation is much more complicated.

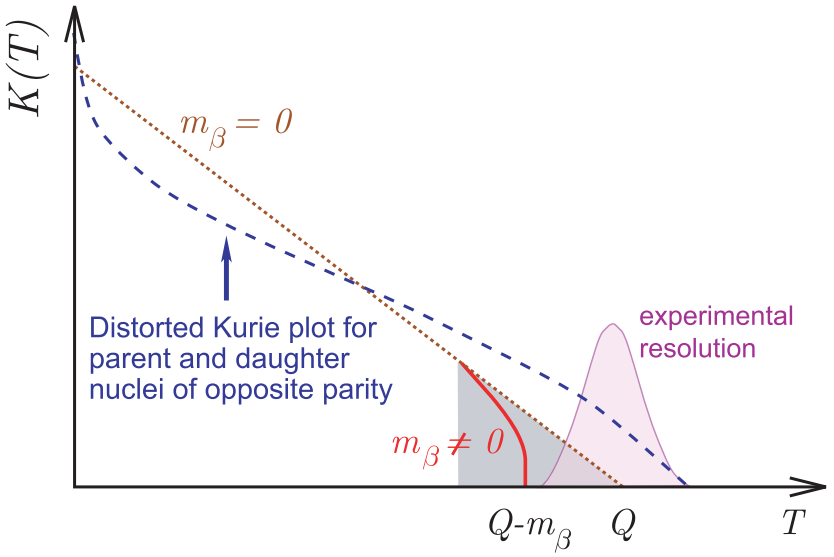

Kurie plot for allowed processes is a sensitive test of the effective neutrino mass m_β while the first order forbidden processes should have a distorted Kurie plot.

In an actual experiment, the measurable quantity is a sum of β spectra, leading each with probability $P_n = P_n(E_0 - V_n - E)$ to a final state n of excitation energy V_n:

$$\frac{d\Gamma(T,Q)}{dT} \longmapsto \sum_n P_n\,(E_0 - V_n - E)\,\frac{d\Gamma\,(T, E_0 - V_n)}{dT}.$$

Here $E_0 = Q - \mathcal{E}$ and $\mathcal{E}$ is the recoil energy of the daughter nucleus.

Example: Tritium beta decay. [a]

An important issue is the decay of molecular tritium $\mathrm{T}_2 \to \left({}^3\mathrm{HeT}\right)^+ + e^- + \overline{\nu}_e$. Considering the most precise direct determination of the mass difference

$$m(\mathrm{T}) - m\left({}^3\mathrm{He}\right) = (18590.1 \pm 1.7)\ \mathrm{eV}/c^2$$

and taking into account the recoil and apparative effects (these are taken for the Mainz experiment) one derives an endpoint energy of the molecular ion $\left({}^3\mathrm{HeT}\right)^+$ ground state:

$$E_0 = (18574.3 \pm 1.7)\ \mathrm{eV}.$$

The excitation spectrum is shown in the figure. The first group concerns rotational and vibrational excitation of the molecule in its electronic ground state; it comprises a fraction of $P_g = 57.4\%$ of the total rate.

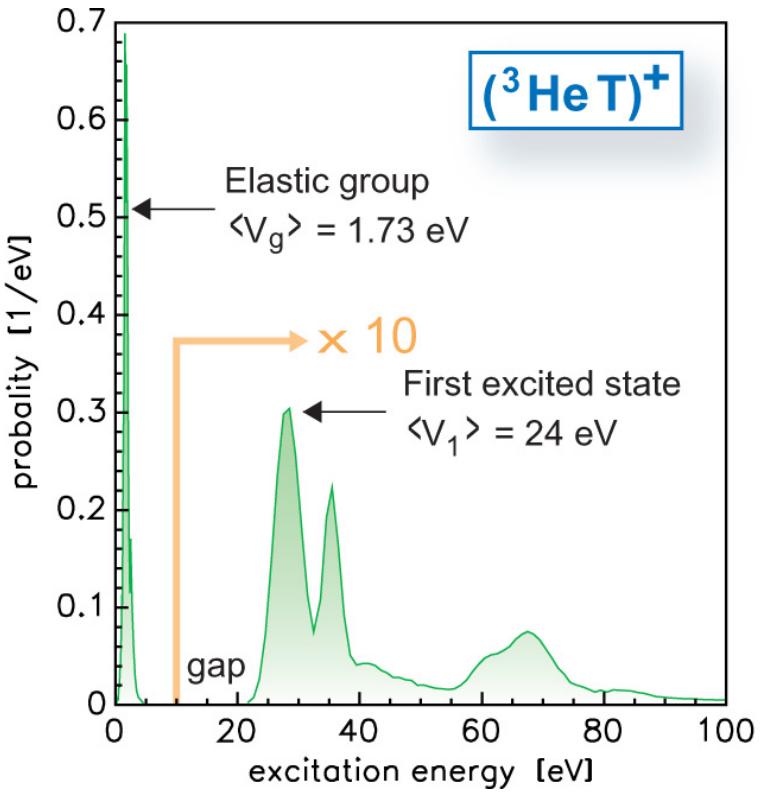

Excitation spectrum of the daughter molecular ion $\left({}^3\mathrm{HeT}\right)^+$ in β decay of molecular tritium.

[a] For more details, see C. Kraus *et al.*, "Final results from phase II of the Mainz neutrino mass search in tritium β decay," Eur. Phys. J. C **40** (2005) 447–468 (hep-ex/0412056).

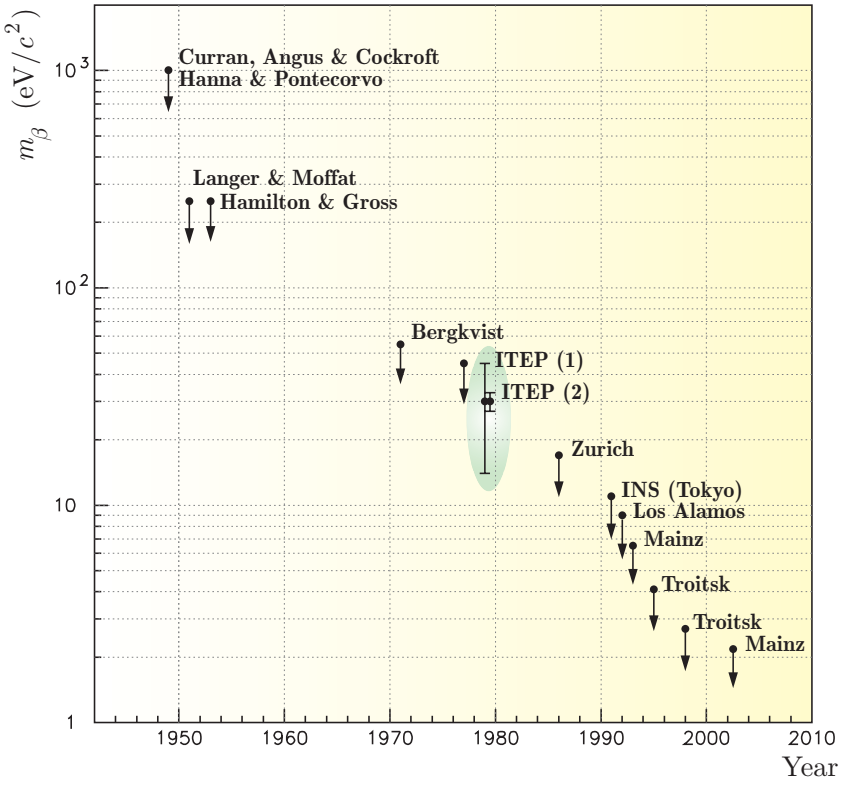

Progress of the neutrino mass measurements in tritium β decay, including the final Mainz phase II upper limit (see below).

[The compilation is taken from V. M. Lobashev, "Direct search for mass of neutrino," in Proceedings of the 18th International Conference on Physics in Collision ("PIC 98"), Frascati, June 17–19, 1998, pp. 179–194.]

The history of the search for the neutrino mass in the tritium β decay counts almost 55 years (see figure). In 1980, the steady improvement of the upper limit was suddenly speeded up by a report of the ITEP group (Moscow) on the observation of the nonzero neutrino mass effect in the β-spectrum in the valine molecule ($C_5H_{11}NO_2$). The reported result was[a]

$$14 \leq m_\beta \leq 46 \text{ eV}/c^2 \quad (99\% \text{ C.L.})$$

This research stimulated more than 20 experimental proposals with an intention to check this clime. Alas!... in several years the experimental groups from Zurich, Tokyo, Los Alamos, and then Livermore refuted the ITEP result.

[a] V. A. Lyubimov *et al.*, "An estimate of the ν_e mass from the β-spectrum of tritium in the valine molecule," Phys. Lett. B **94** (1980) 266–268 (327 citations in SPIRES!)

The top figure shows the data points from the tail of the β-spectrum measured in the Los Alamos tritium experiment compared with the expected values (the straight line) for $m_\beta = 30$ eV. The data wander from the line, ruling out the possibility of a 30-eV neutrino. The bottom figure shows the same data points compared with the expectation for $m_\beta = 0$. While the data clearly favor a neutrino mass of zero, the best fit is actually for a slightly negative m_β. (Note that in the bottom plot, the data points lie, on average, slightly above the line, so this is not a perfect fit.) Both plots display "residuals," which indicate how many standard deviations each data point is from a particular hypothesis.

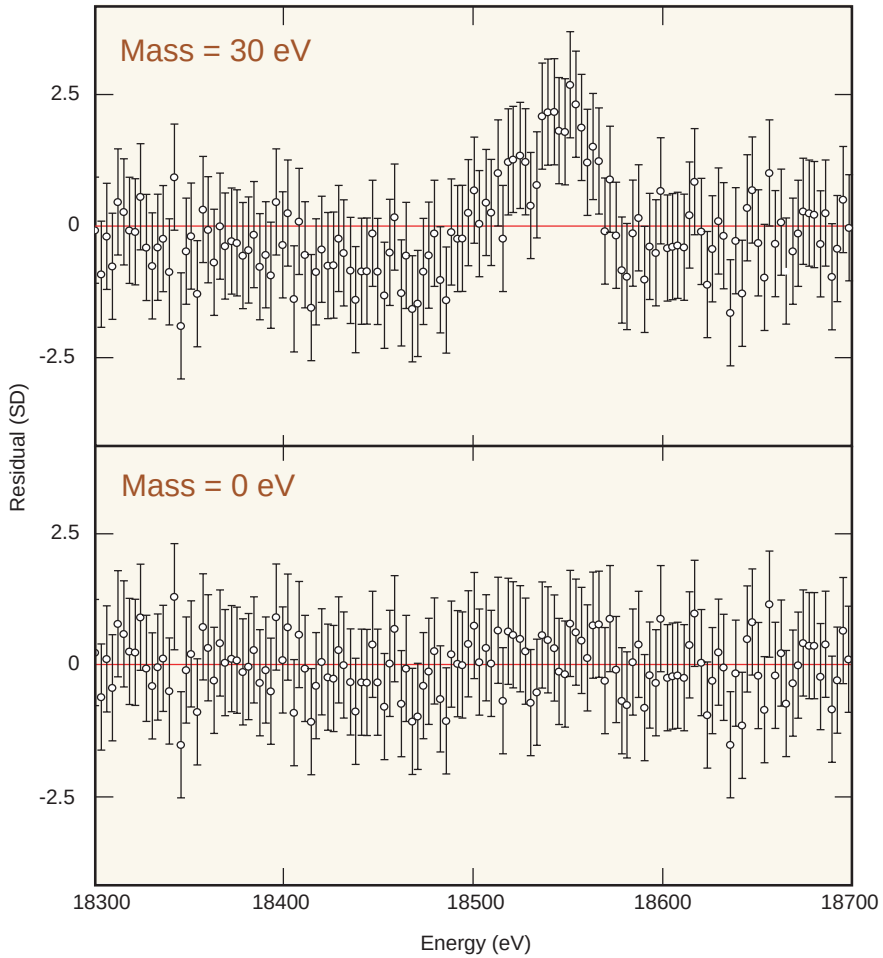

Did the neutrino weigh 30 electron volts?

[Borrowed from T. J. Bowles and R. G. H. Robertson (as told to D. Kestenbaum), "Tritium beta decay and the search for neutrino mass," Los Alamos Science, Nu. **25** (1997) 6-11.]

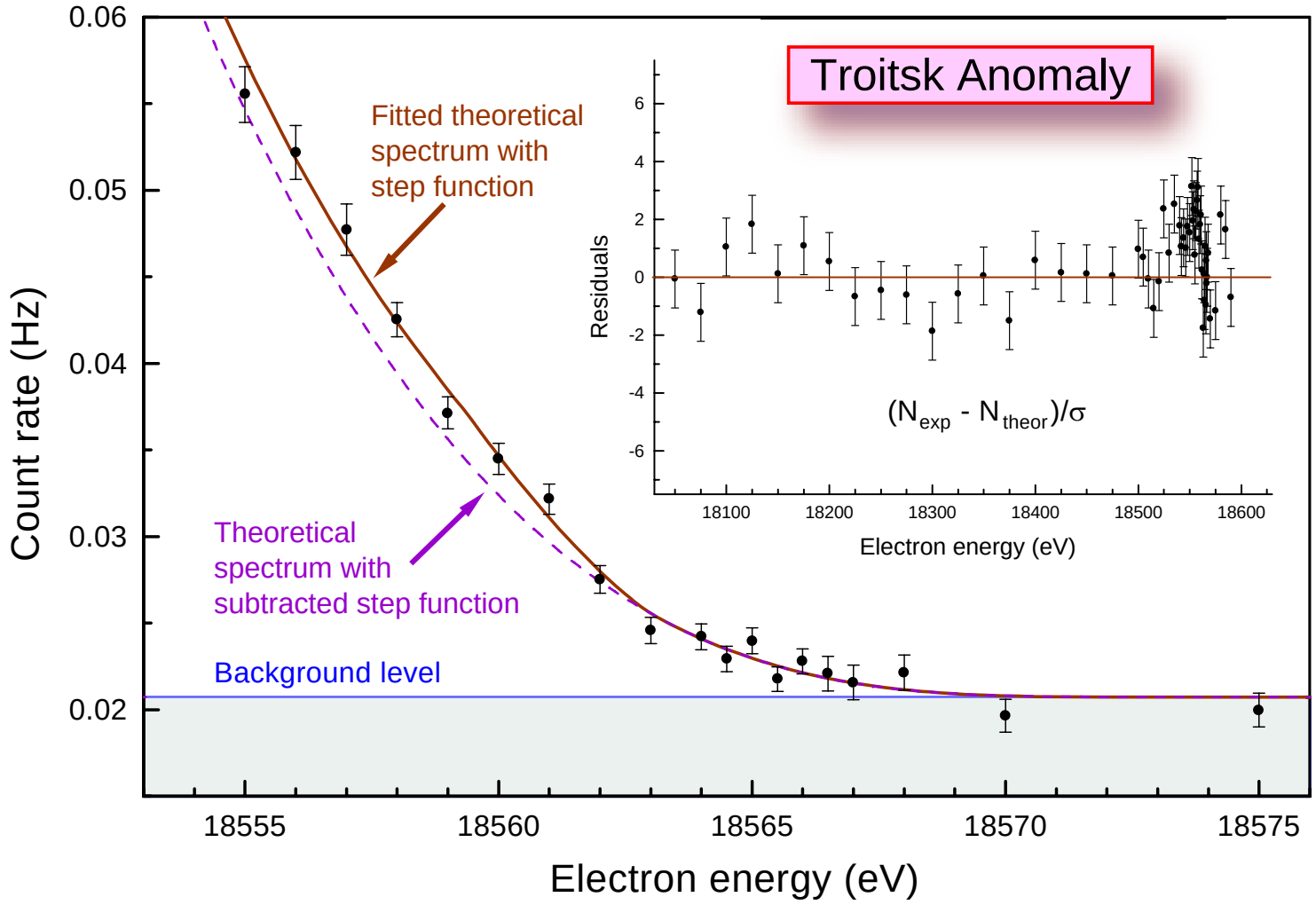

Part of experimental β-spectrum in the Troitsk ν-mass experiment near the end-point.

[V. M. Lobashev *et al.*, "Direct search for mass of neutrino and anomaly in the tritium beta-spectrum," Phys. Lett. B **460** (1999) 227–235.]

The Troitsk group reported on a step like anomaly which appeared in their integral spectra with an amplitude of about 6×10^{-11} of the total decay rate and at variable positions in the range from 5 to 15 eV below the endpoint.

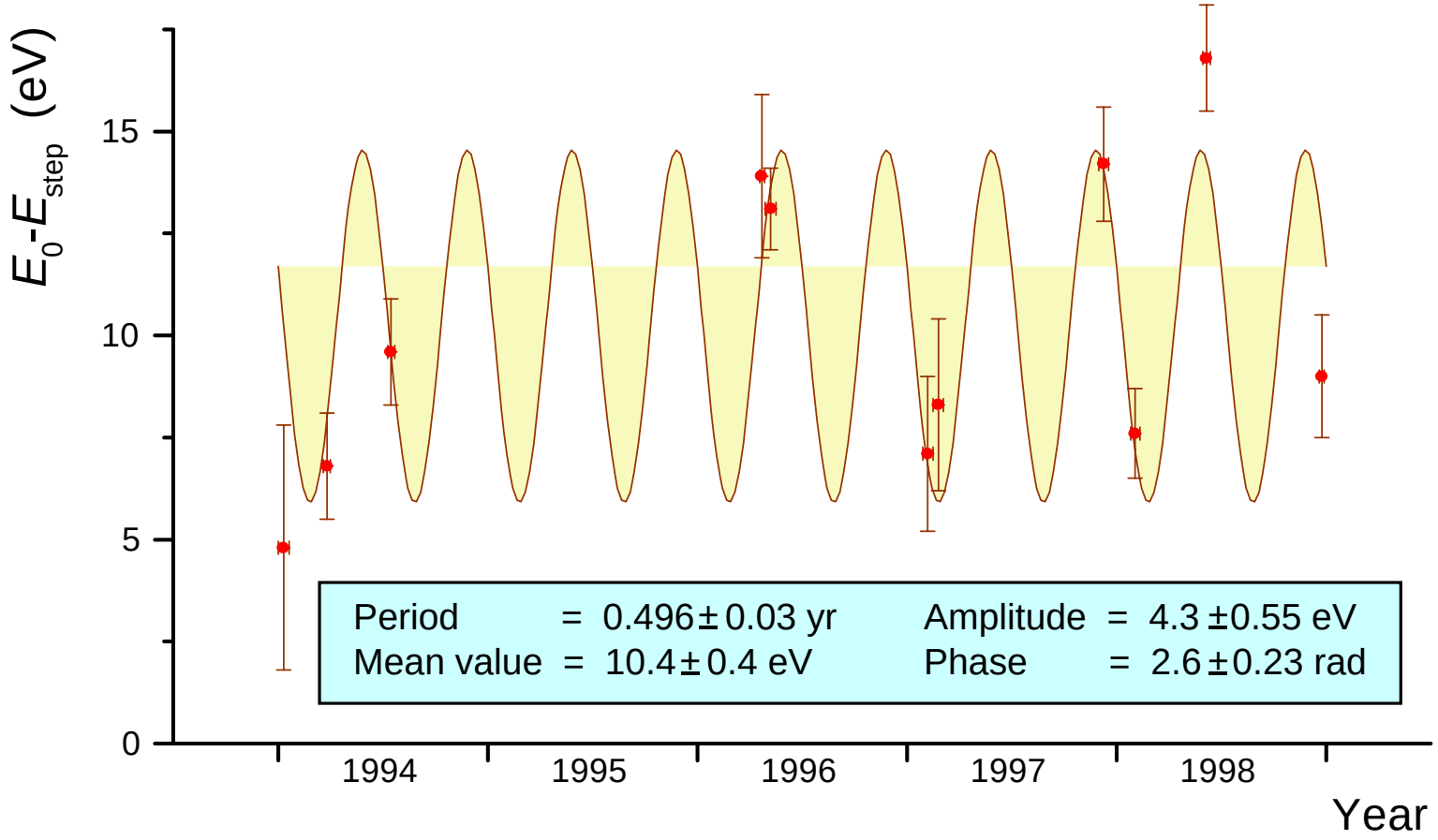

The change in time of the positions of these steps seemed to be compatible with a half year period. The phenomenology and origin of the Troitsk anomaly are barely known.

Published results of the squared neutrino mass values m_β^2 obtained from tritium decay since 1990 are shown in figure. The already finished experiments at Los Alamos, Zürich, Tokyo, Beijing and Livermore used magnetic spectrometers, the experiments at Troitsk and Mainz are using electrostatic filters with magnetic adiabatic collimation. The progress in the observable m_β of the final Mainz result as compared to the most sensitive earlier experiments using momentum analysing spectrometers approaches 2 orders of magnitude.

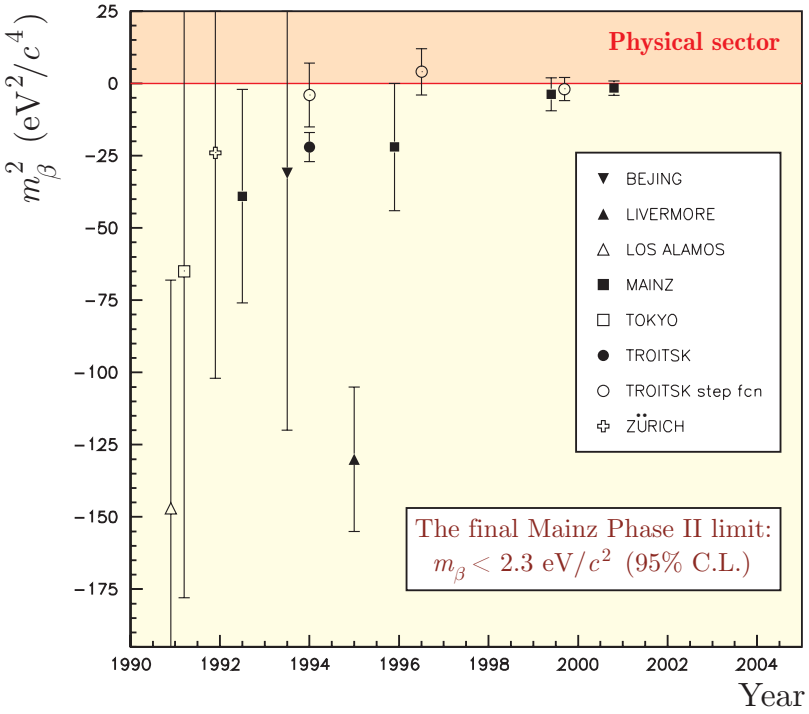

[From C. Kraus *et al.*, "Final results from phase II of the Mainz neutrino mass search in tritium β decay," Eur. Phys. J. C **40** (2005) 447–468 (hep-ex/0412056).]

The Mainz experiment does not confirm the Troitsk anomaly being however compatible with the main Troitsk result $m_\beta^2 = (-2.3 \pm 2.5_{\text{stat}} \pm 2.0_{\text{syst}})$ eV$^2/c^4$.

The negative m_β^2 sector is not necessarily unphysical and might also be fitted by a model with *tachyonic neutrinos*. But this point would come up only in case of an unambiguous experimental negative m_β^2 result.

3.3 Majorana neutrinos

The charge conjugated bispinor field ψ^c is defined by the transformation

$$\psi \longmapsto \psi^c = C\overline{\psi}^T, \quad \overline{\psi} \longmapsto \overline{\psi^c} = -\psi^T C,$$

where C is the charge-conjugation matrix which satisfies the conditions

$$C\gamma_\alpha^T C^\dagger = -\gamma_\alpha, \quad C\gamma_5^T C^\dagger = \gamma_5, \quad C^\dagger = C^{-1} = C, \quad C^T = -C,$$

and thus coincides (up to a phase factor) with the inversion of the axes x^0 and x^2:

$$C = \gamma_0\gamma_2 = \begin{pmatrix} 0 & \sigma_2 \\ \sigma_2 & 0 \end{pmatrix}$$

Reminder:

The Pauli matrices:

$$\sigma_0 \equiv 1 = \begin{pmatrix} 1 & 0 \\ 0 & 1 \end{pmatrix}, \quad \sigma_1 = \begin{pmatrix} 0 & 1 \\ 1 & 0 \end{pmatrix}, \quad \sigma_2 = \begin{pmatrix} 0 & -i \\ i & 0 \end{pmatrix}, \quad \sigma_3 = \begin{pmatrix} 1 & 0 \\ 0 & -1 \end{pmatrix}.$$

The Dirac matrices:

$$\gamma^0 = \gamma_0 = \begin{pmatrix} \sigma_0 & 0 \\ 0 & -\sigma_0 \end{pmatrix}, \quad \gamma^k = -\gamma_k = \begin{pmatrix} 0 & \sigma_k \\ -\sigma_k & 0 \end{pmatrix}, \quad k = 1, 2, 3, \quad \gamma^5 = \gamma_5 = -\begin{pmatrix} 0 & \sigma_0 \\ \sigma_0 & 0 \end{pmatrix}.$$

Clearly a charged fermion field $\psi(x)$ is different from the charge conjugated field $\psi^c(x)$.

But for a *neutral* fermion field $\nu(x)$ the equality $\boxed{\nu^c(x) = \nu(x)}$ is not forbidden.

This is the *Majorana condition*[a] (Majorana neutrino and antineutrino coincide).

In the chiral representation

$$\nu = \begin{pmatrix} \phi \\ \chi \end{pmatrix}, \quad \nu^c = C\overline{\nu}^T = \begin{pmatrix} -\sigma_2\chi^* \\ +\sigma_2\phi^* \end{pmatrix}.$$

According to the Majorana condition

$$\phi = -\sigma_2\chi^* \quad \text{and} \quad \chi = \sigma_2\phi^* \quad \Longrightarrow \quad \phi + \chi = \sigma_2\,(\phi - \chi)^*.$$

(The Majorana neutrino is two-component, i.e. needs only one chiral projection). Then

$$\nu_L = \left(\frac{1+\gamma_5}{2}\right)\nu = \begin{pmatrix} \phi - \chi \\ \chi - \phi \end{pmatrix} \quad \text{and} \quad \nu_R = \left(\frac{1-\gamma_5}{2}\right)\nu = \begin{pmatrix} \phi + \chi \\ \phi + \chi \end{pmatrix} = \nu_L^c.$$

Therefore

$$\boxed{\nu = \nu_L + \nu_R = \nu_L + \nu_L^c.}$$

Now we can construct the Majorana mass term in the general N-neutrino case. It is

$$\mathcal{L}_{\mathsf{M}}(x) = -\frac{1}{2}\overline{\boldsymbol{\nu}}_L^c(x)\mathbf{M}_{\mathsf{M}}\boldsymbol{\nu}_L(x) + \mathsf{H.c.},$$

[a] More generally, $\nu^c(x) = e^{i\phi}\nu(x)$ ($\phi = \text{const}$).

where $\mathbf{M}_{\mathsf{M}}$ is a $N \times N$ complex *nondiagonal* matrix and, in general, $N \geq 3$.

It can be proved that the $\mathbf{M}_{\mathsf{M}}$ should be symmetric,

$$\mathbf{M}_{\mathsf{M}}^{T} = \mathbf{M}_{\mathsf{M}}.$$

If one assume for a simplification that its spectrum is nondegenerated, the mass matrix can be diagonalized by means of the following transformation

$$\mathbf{M}_{\mathsf{M}} = \mathbf{V}^{*}\mathbf{m}\mathbf{V}^{\dagger}, \quad \mathbf{m} = ||m_{kl}|| = ||m_k \delta_{kl}||,$$

where $\mathbf{V}$ is a unitary matrix and $m_k \geq 0$. Therefore

$$\mathcal{L}_{\mathsf{M}}(x) = -\frac{1}{2}\left[(\overline{\boldsymbol{\nu}'}_L)^c \mathbf{m} \boldsymbol{\nu}'_L + \overline{\boldsymbol{\nu}'}_L \mathbf{m} (\boldsymbol{\nu}'_L)^c\right] = -\frac{1}{2}\,\overline{\boldsymbol{\nu}'}\mathbf{m}\boldsymbol{\nu}' = -\frac{1}{2}\sum_{k=1}^{N} m_k \overline{\nu}_k \nu_k,$$

$$\boldsymbol{\nu}'_L = \mathbf{V}^{\dagger}\boldsymbol{\nu}_L, \quad (\boldsymbol{\nu}'_L)^c = C\left(\overline{\boldsymbol{\nu}'_L}\right)^T, \quad \boldsymbol{\nu}' = \boldsymbol{\nu}'_L + (\boldsymbol{\nu}'_L)^c.$$

The last equality means that the fields $\nu_k(x)$ are Majorana neutrino fields.

Considering that the kinetic term in the neutrino Lagrangian is transformed to

$$\mathcal{L}_0 = \frac{i}{4}\,\overline{\boldsymbol{\nu}'}(x)\overleftrightarrow{\boldsymbol{\partial}}\,\boldsymbol{\nu}'(x) = \frac{i}{4}\sum_k \overline{\nu}_k(x)\overleftrightarrow{\boldsymbol{\partial}}\,\nu_k(x),$$

one can conclude that $\nu_k(x)$ is the field with the definite mass m_k.

The flavor LH neutrino fields $\nu_{\ell,L}(x)$ present in the standard weak lepton currents are linear combinations of the LH components of the fields of neutrinos with definite masses:

$$\boldsymbol{\nu}_L = \mathbf{V}\boldsymbol{\nu}'_L \quad \text{or} \quad \nu_{\ell,L} = \sum_k V_{\ell k}\nu_{k,L}.$$

Of course neutrino mixing matrix $\mathbf{V}$ is not the same as in the case of Dirac neutrinos.

There is no global gauge transformations under which the Majorana mass term (in its most general form) could be invariant. This implies that there are no conserved lepton charges that could allow us to distinguish Majorana νs and $\overline{\nu}$s. In other words,

the Majorana neutrinos are truly neutral fermions.

3.3.1 Parametrization of mixing matrix for Majorana neutrinos

Since the Majorana neutrinos are not rephasable, there may be a lot of extra phase factors in the mixing matrix. The Lagrangian with the Majorana mass term is invariant with respect to the transformation

$$\ell \mapsto e^{ia_\ell}\ell, \quad V_{\ell k} \mapsto e^{-ia_\ell}V_{\ell k}$$

Therefore N phases are unphysical and the number of the physical phases now is

$$\frac{N(N+1)}{2} - N = \frac{N(N-1)}{2} = \underbrace{\frac{(N-1)(N-2)}{2}}_{\text{Dirac phases}} + \underbrace{(N-1)}_{\text{Majorana phases}} = n_{\mathsf{D}} + n_{\mathsf{M}};$$

$$n_{\mathsf{M}}(2) = 1, \quad n_{\mathsf{M}}(3) = 2, \quad n_{\mathsf{M}}(4) = 3, \ldots$$

In the case of three lepton generations one defines the diagonal matrix with the extra phase factors: $\boldsymbol{\Gamma}_{\mathsf{M}} = \mathrm{diag}\left(e^{i\alpha_1/2}, e^{i\alpha_2/2}, 1\right)$, where $\alpha_{1,2}$ are commonly referred to as the Majorana CP-violation phases. Then the PMNS matrix can be parametrized as

$$\mathbf{V}_{(\mathsf{M})} = \mathbf{O}_{23}\boldsymbol{\Gamma}_{\mathsf{D}}\mathbf{O}_{13}\boldsymbol{\Gamma}_{\mathsf{D}}^{\dagger}\mathbf{O}_{12}\boldsymbol{\Gamma}_{\mathsf{M}} = \mathbf{V}_{(\mathsf{D})}\boldsymbol{\Gamma}_{\mathsf{M}}$$

$$= \begin{pmatrix} c_{12}c_{13} & s_{12}c_{13} & s_{13}e^{-i\delta} \\ -s_{12}c_{23} - c_{12}s_{23}s_{13}e^{i\delta} & c_{12}c_{23} - s_{12}s_{23}s_{13}e^{i\delta} & s_{23}c_{13} \\ s_{12}s_{23} - c_{12}c_{23}s_{13}e^{i\delta} & -c_{12}s_{23} - s_{12}c_{23}s_{13}e^{i\delta} & c_{23}c_{13} \end{pmatrix} \begin{pmatrix} e^{i\alpha_1/2} & 0 & 0 \\ 0 & e^{i\alpha_2/2} & 0 \\ 0 & 0 & 1 \end{pmatrix},$$

Neither L_ℓ nor $L = \sum_\ell L_\ell$ is conserved allowing a lot of new processes, for example, $\tau^- \to e^+(\mu^+)\pi^-\pi^-$, $\tau^- \to e^+(\mu^+)\pi^- K^-$, $\pi^- \to \mu^+\overline{\nu}_e$, $K^+ \to \pi^-\mu^+e^+$, $K^+ \to \pi^0 e^+\overline{\nu}_e$, $D^+ \to K^-\mu^+\mu^+$, $B^+ \to K^- e^+\mu^+$, $\Xi^- \to p\mu^-\mu^-$, $\Lambda_c^+ \to \Sigma^-\mu^+\mu^+$, etc.

No one was discovered yet but (may be!?) the $(\beta\beta)_{0\nu}$ decay. Thus we have to discuss this issue with some details.

3.3.2 Neutrinoless double beta decay

The theory with Majorana neutrinos allows the decay $(A, Z) \to (A, Z+2) + 2e^-$ with $\Delta L = 2$. The decay rate for this process is expressed as follows:

$$\left[T^{0\nu}_{1/2}\right]^{-1} = G^{0\nu}_Z \left|m_{\beta\beta}\right|^2 \left|\mathcal{M}^{0\nu}_{\mathsf{F}} - (g_A/g_V)^2 \mathcal{M}^{0\nu}_{\mathsf{GT}}\right|^2,$$

where $G^{0\nu}_Z$ is the two-body phase-space factor including coupling constant, $\mathcal{M}^{0\nu}_{\mathsf{F/GT}}$ are the Fermi/Gamow-Teller nuclear matrix elements. The constants g_V and g_A are the vector and axial-vector relative weak coupling constants, respectively. The complex parameter $m_{\beta\beta}$ is the *effective Majorana electron neutrino mass* given by

$$\begin{aligned} m_{\beta\beta} &= \sum_k V^2_{ek} m_k \\ &= \left|V_{e1}\right|^2 m_1 + \left|V_{e2}\right|^2 m_2 e^{i\phi_2} + \left|V_{e3}\right|^2 m_3 e^{i\phi_3}, \end{aligned}$$

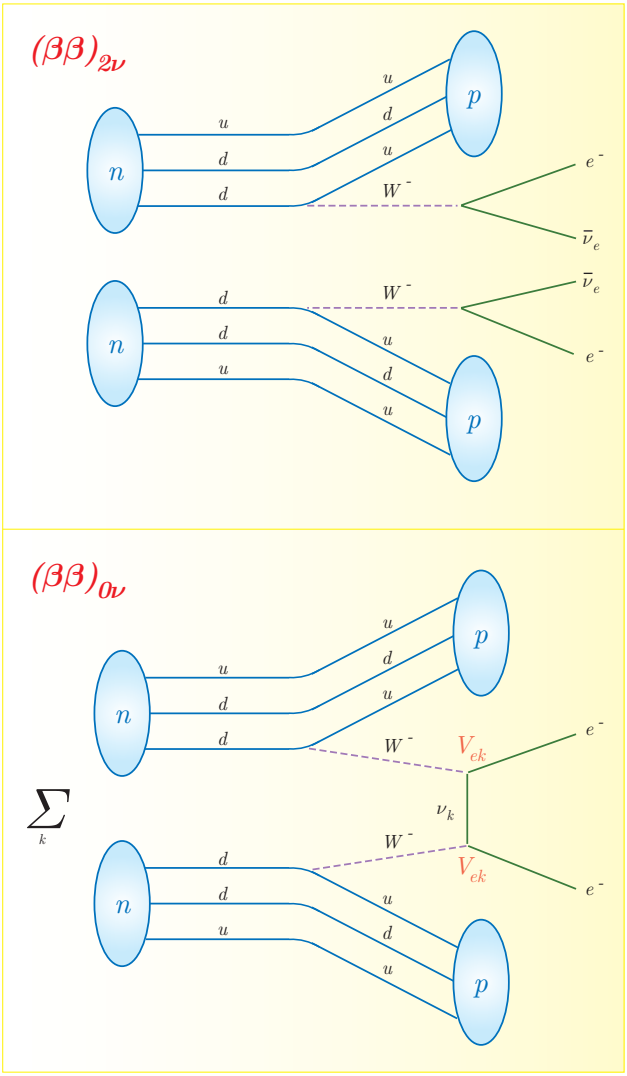

Here $\phi_2 = \alpha_2 - \alpha_1$ (pure Majorana phase) and $\phi_3 = -(\alpha_2 + 2\delta)$ (mixture of Dirac and Majorana CP-violation phases).

The electron sum energy spectrum of the $(\beta\beta)_{2\nu}$ mode as well as of the exotic modes with one or two majorons in final state,

$$(A, Z) \to (A, Z+2) + 2e^- + \chi,$$
$$(A, Z) \to (A, Z+2) + 2e^- + 2\chi,$$

is *continuous* because the available energy release ($Q_{\beta\beta}$) is shared between the electrons and other final state particles. In contrast, the two electrons from the $(\beta\beta)_{0\nu}$ decay carry the full available energy, and hence the electron sum energy spectrum has a sharp peak at the $Q_{\beta\beta}$ value. This feature allows one to distinguish the $(\beta\beta)_{0\nu}$ decay signal from the background.

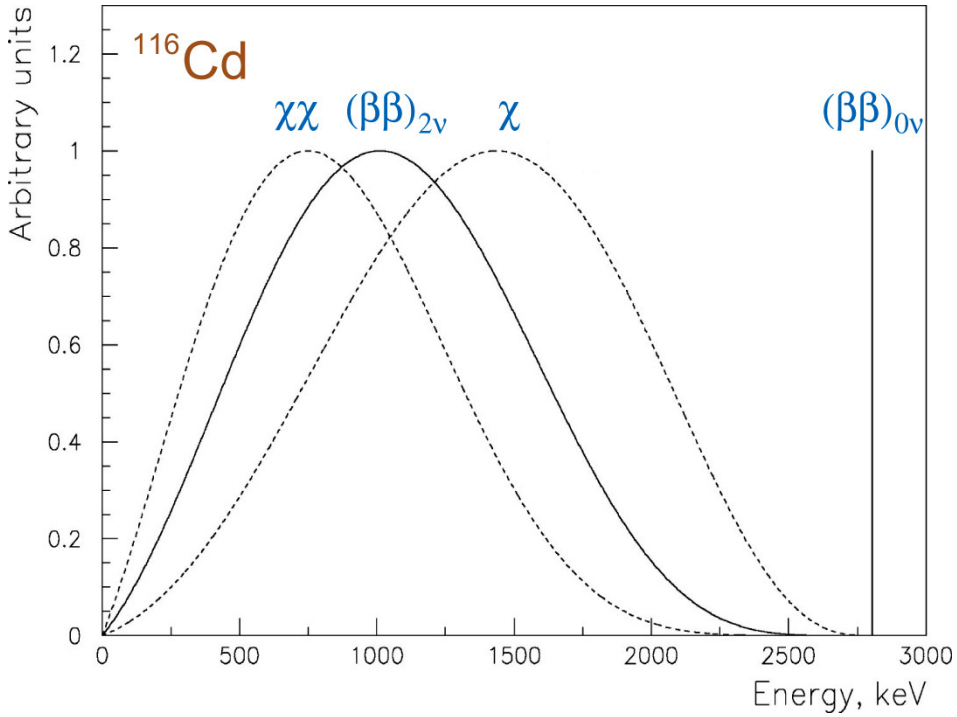

The electron sum energy spectra calculated for the different β decay modes of cadmium-116.

[From Y. Zdesenko, "Colloquium: The future of double beta decay research," Rev. Mod. Phys. **74** (2003) 663–684.]

Majoron is a Nambu-Goldstone boson, – a hypothetical neutral pseudoscalar zero-mass particle which couples to Majorana neutrinos and may be emitted in the neutrinoless β decay. It is a consequence of the spontaneous breaking of the global $B - L$ symmetry.

Table 2: Summary of the most recent $\beta\beta_{2\nu}$ experiments and calculations.

[From E. Fiorini, "Experimental prospects of neutrinoless double beta decay," Phys. Scripta **T121** (2005) 86–93].

Element	Isotope	$T^{2\nu}_{1/2}$ (years)	
		Measured	**Calculated**
Calcium	$^{48}_{20}$Ca	$4.2^{+2.1}_{-1.0} \times 10^{19}$	$6 \times 10^{18} - 5 \times 10^{20}$
Germanium	$^{76}_{32}$Ge	$1.42^{+0.09}_{-0.07} \times 10^{21}$	$7 \times 10^{19} - 6 \times 10^{22}$
Selenium	$^{82}_{34}$Se	$(0.9 \pm 0.1) \times 10^{20}$	$3 \times 10^{18} - 6 \times 10^{21}$
Zirconium	$^{96}_{40}$Zr	$2.1^{+0.8}_{-0.4} \times 10^{19}$	$3 \times 10^{17} - 6 \times 10^{20}$
Molybdenum	$^{100}_{42}$Mo	$(8.0 \pm 0.7) \times 10^{18}$	$1 \times 10^{17} - 2 \times 10^{22}$
Molybdenum	$^{100}_{42}$Mo (0^{+*})	$(6.8 \pm 1.2) \times 10^{20}$	$5 \times 10^{19} - 2 \times 10^{21}$
Cadmium	$^{116}_{48}$Cd	$3.3^{+0.4}_{-0.3} \times 10^{19}$	$3 \times 10^{18} - 2 \times 10^{21}$
Tellurium	$^{128}_{52}$Te	$(2.5 \pm 0.4) \times 10^{24}$	$9 \times 10^{22} - 3 \times 10^{25}$
Tellurium	$^{130}_{52}$Te	$(9.0 \pm 1.5) \times 10^{20}$	$2 \times 10^{19} - 7 \times 10^{20}$
Neodymium	$^{150}_{60}$Nd	$(7.0 \pm 1.7) \times 10^{18}$	$6 \times 10^{16} - 4 \times 10^{20}$
Uranium	$^{238}_{92}$U	$(2.0 \pm 0.6) \times 10^{21}$	$1.2 \times 10^{19} - ? \times 10^{21}$

The standard $(\beta\beta)_{2\nu}$ is observed for 10 isotopes with $T^{2\nu}_{1/2} \sim 10^{19-25}$ years (see table).

The figure summarizes the present knowledge of the absolute Majorana mass scale. Shown are the 99% CL regions allowed by the neutrino oscillation data in the plane of $m_{\beta\beta}$ and m_L – the mass of lightest neutrino. The two bands marked with $\Delta m^2_{23} > 0$ and $\Delta m^2_{23} < 0$ correspond to the *normal mass hierarchy* (i.e. $m_1 \ll m_2 \ll m_3$) and *inverted mass hierarchy* (i.e. $m_3 \ll m_1 \approx m_2$), respectively.
For a given m_L the range of $m_{\beta\beta}$ is determined by variations of the Majorana phase and uncertainties in the neutrino oscillation parameters.

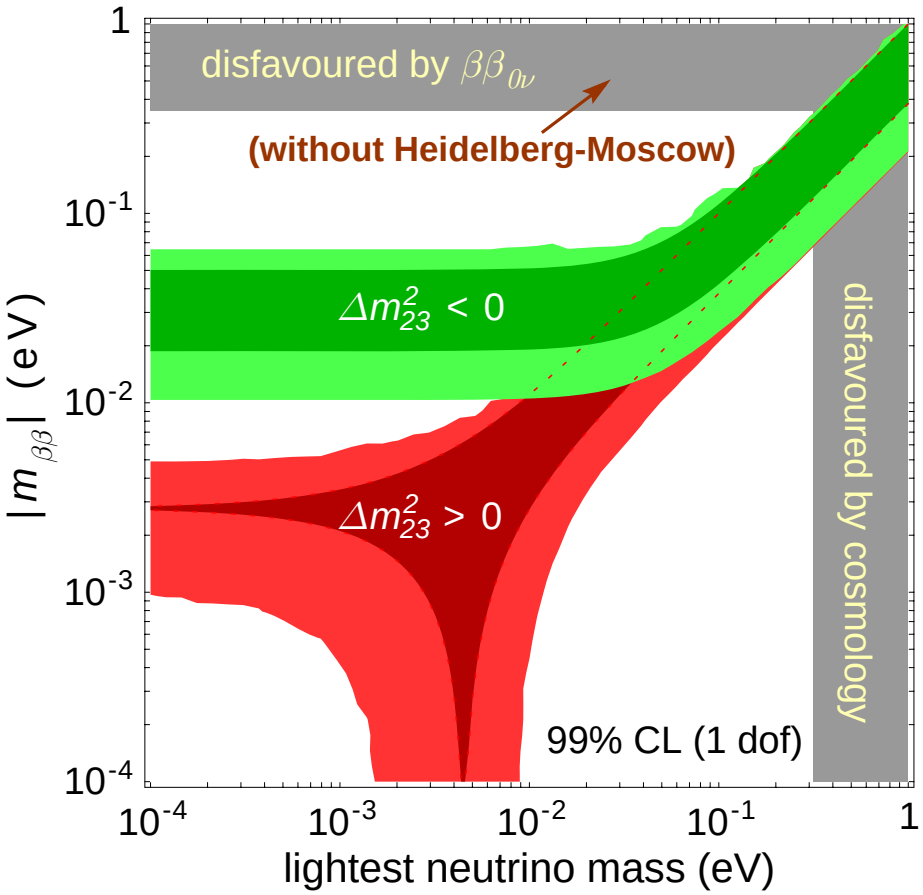

The darker regions show how the $m_{\beta\beta}$ range would shrink if the present best-fit values of the oscillation parameters were confirmed with negligible error.

[From A. Strumia and F. Vissani, "Implications of neutrino data circa 2005," Nucl. Phys. B **726** (2005) 294–316 (hep-ph/0503246).]

The only evidence for the $(\beta\beta)_{0\nu}$ decay has been obtained by the Heidelberg-Moscow (HM) (**sub**)collaboration in the Gran Sasso lab. The HM best value of the effective neutrino mass is $|m_{\beta\beta}| = 0.4$ eV. Allowing conservatively for an uncertainty of the nuclear matrix element of $\pm 50\%$ the 3σ confidence range may widen to $(0.1 - 0.9)$ eV.

The bars in the figure denote allowed ranges of $|m_{\beta\beta}|$ in different neutrino mass scenarios, still allowed by neutrino oscillation experiments. All models except the *degenerate* one are excluded by the new $(\beta\beta)_{0\nu}$ decay result. Also shown is the exclusion line from WMAP, plotted for $\sum_k m_k < 1.0$ eV (which is perhaps too strict). WMAP does not rule out any of the neutrino mass schemes.

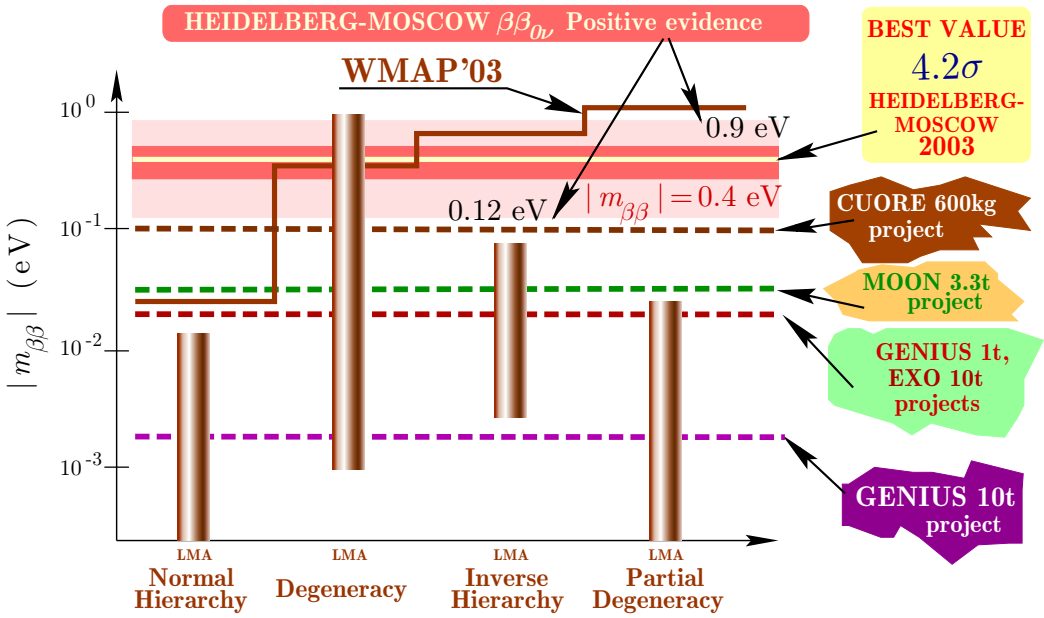

Further shown are the expected sensitivities for the future potential $(\beta\beta)_{0\nu}$ decay experiments CUORE, MOON, EXO and GENIUS.

[From H. V. Klapdor-Kleingrothaus, "First evidence for neutrinoless double beta decay and world status of double beta experiments," hep-ph/0512263.]

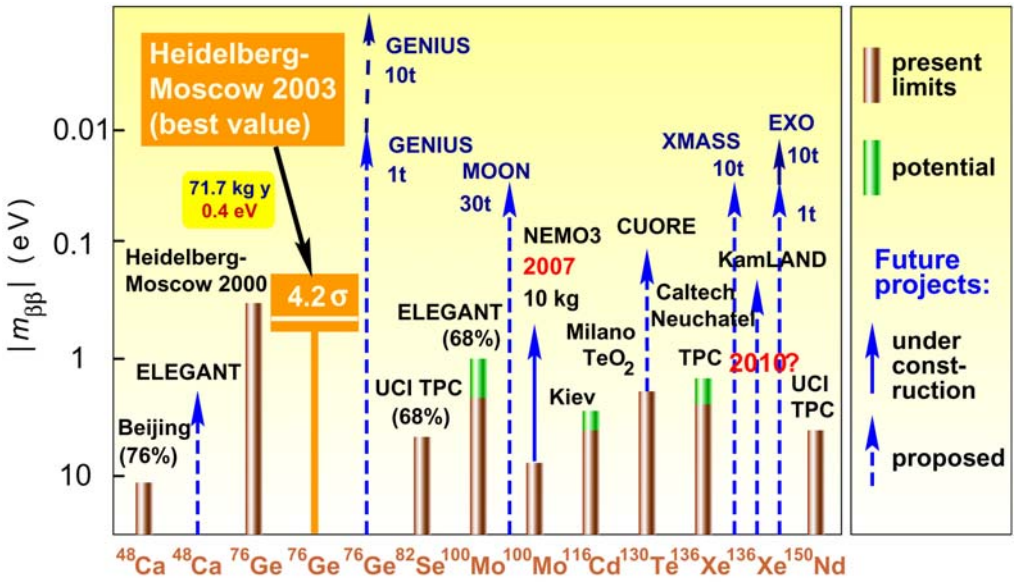

Figure shows the HM-2000 and HM-2003 results in comparison with the potential of the most promising other $(\beta\beta)_{0\nu}$ experiments as well as the expected potential of several future projects. Given are limits for $|m_{\beta\beta}|$, except for the HM-2003 experiment where the measured *value* is given (confidence range and best value).

[The histogram is built by combining the data from papers H. V. Klapdor-Kleingrothaus *et al.*, "Latest results from the Heidelberg-Moscow double beta decay experiment," Eur. Phys. J. A **12** (2001) 147–154 (hep-ph/0103062) and H. V. Klapdor-Kleingrothaus, "First evidence for neutrinoless double beta decay and world status of double beta experiments," in Proceedings of the 11th International Workshop on Neutrino Telescopes, Venice, Feb. 22–25, 2005, edited by M. Baldo-Ceolin, pp. 215–237 (hep-ph/0512263).]

New approaches and considerably enlarged experiments are required to fix the $(\beta\beta)_{0\nu}$ half life with higher accuracy. This will, however, only marginally improve the precision of the deduced effective neutrino mass $|m_{\beta\beta}|$ (or its upper limit), because of the uncertainties in the nuclear matrix elements, which probably hardly can be reduced to less than 50%.

3.4 See-saw mechanism

3.4.1 Dirac-Majorana mass term for one generation

It is possible to consider mixed models in which both Majorana and Dirac mass terms are present. For simplicity sake we'll start with a toy model for one lepton generation.

Let us consider a theory containing two independent neutrino fields ν_L and ν_R:

$\left\{ \begin{array}{l} \nu_L \text{ would generally represent any active neutrino (e.g., } \nu_L = \nu_{eL}), \\ \nu_R \text{ can represents a right handed field unrelated to any of these or} \\ \quad \text{it can be charge conjugate of any of the active neutrinos (e.g., } \nu_R = (\nu_{\mu L})^c). \end{array} \right.$

We can write the following generic mass term between ν_L and ν_R:

$$\mathcal{L}_m = - \underbrace{m_D \, \overline{\nu}_L \nu_R}_{\text{Dirac mass term}} - \underbrace{(1/2) \left[m_L \, \overline{\nu}_L \nu_L^c + m_R \, \overline{\nu}_R^c \nu_R \right]}_{\text{Majorana mass term}} + \text{H.c.} \qquad (4)$$

- ⋆ As we know, the Dirac mass term respects L while the Majorana mass term violates it.
- ⋆ The parameter m_D in Eq. (4) is in general complex but we'll assume it to be real (but not necessarily positive).
- ⋆ The parameters m_L, and m_R in Eq. (4) can be chosen real and (by an appropriate rephasing the fields ν_L and ν_R) non-negative, but the latter is not assumed.
- ⋆ Obviously, neither ν_L nor ν_R is a mass eigenstate.

In order to obtain the *mass basis* we can apply the useful identity[a]

$$\overline{\nu}_L \nu_R = (\overline{\nu}_R)^c (\nu_L)^c$$

which allows us to rewrite Eq. (4) as follows

$$\mathcal{L}_m = -\frac{1}{2} \left(\overline{\nu}_L, (\overline{\nu}_R)^c\right) \begin{pmatrix} m_L & m_D \\ m_D & m_R \end{pmatrix} \begin{pmatrix} (\nu_L)^c \\ \nu_R \end{pmatrix} + \text{H.c.} \equiv -\frac{1}{2} \overline{\boldsymbol{\nu}}_L \mathbf{M} \left(\boldsymbol{\nu}_L\right)^c + \text{H.c.}$$

If (for simplicity) CP conservation is assumed the matrix $\mathbf{M}$ can be diagonalized through the standard orthogonal transformation

$$\mathbf{V} = \begin{pmatrix} \cos\theta & \sin\theta \\ -\sin\theta & \cos\theta \end{pmatrix} \quad \text{with} \quad \theta = \frac{1}{2} \arctan\left(\frac{2m_D}{m_R - m_L}\right).$$

and we have

$$\mathbf{V}^T \mathbf{M} \mathbf{V} = \text{diag}(m_1, m_2),$$

where $m_{1,2}$ are eigenvalues of $\mathbf{M}$ given by

$$m_{1,2} = \frac{1}{2} \left(m_L + m_R \pm \sqrt{(m_L - m_R)^2 + 4m_D^2}\right).$$

---

[a] A particular case of a more general relation $\overline{\psi}_1 \Gamma \psi_2 = \overline{\psi}_2^c C \Gamma^T C^{-1} \psi_1^c$, where $\psi_{1,2}$ are Dirac spinors and Γ represents a product of the Dirac γ matrices.

The eigenvalues are real if (as we assume) $m_{D,L,R}$ are real, but not necessarily positive. Let us define $\zeta_k = \mathrm{sign}\, m_k$ and rewrite the mass term in the new basis:

$$\mathcal{L}_m = -\frac{1}{2}\left[\zeta_1 |m_1| \overline{\nu}_{1L} \left(\nu_{1L}\right)^c + \zeta_2 |m_2| \left(\overline{\nu}_{2R}\right)^c \nu_{2R}\right] + \text{H.c.}, \tag{5}$$

The new fields ν_{1L} and ν_{2R} represent chiral components of two different neutrino states with "masses" m_1 and m_2, respectively:

$$\begin{pmatrix} \nu_L \\ \nu_R^c \end{pmatrix} = \mathbf{V} \begin{pmatrix} \nu_{1L} \\ \nu_{2R}^c \end{pmatrix} \quad \Longrightarrow \quad \begin{cases} \nu_{1L} = \cos\theta\, \nu_L - \sin\theta\, \nu_R^c, \\ \nu_{2R} = \sin\theta\, \nu_L^c + \cos\theta\, \nu_R. \end{cases}$$

Now we define two 4-component fields

$$\nu_1 = \nu_{1L} + \zeta_1 \left(\nu_{1L}\right)^c \quad \text{and} \quad \nu_2 = \nu_{2R} + \zeta_2 \left(\nu_{2R}\right)^c.$$

Certainly, these fields are self-conjugate,

$$\nu_k^c = \zeta_k \nu_k \quad (k = 1, 2)$$

and therefore they describe Majorana neutrinos. In terms of these fields Eq. (6) is

$$\mathcal{L}_m = -\frac{1}{2}\left(|m_1|\, \overline{\nu}_1 \nu_1 + |m_2|\, \overline{\nu}_2 \nu_2\right). \tag{6}$$

We can conclude therefore that $\nu_k(x)$ is the Majorana neutrino field with the definite (physical) mass $|m_k|$.

There are several special cases of the Dirac-Majorana mass matrix $\mathbf{M}$ which are of considerable phenomenological importance, in particular,

(A): $\mathbf{M} = \begin{pmatrix} 0 & m \\ m & 0 \end{pmatrix} \quad \Longrightarrow \quad |m_{1,2}| = m, \quad \theta = \frac{\pi}{4}$ (maximal mixing)

two Majorana fields are equivalent to one Dirac field;

(B): $\mathbf{M} = \begin{pmatrix} m_L & m \\ m & m_L \end{pmatrix} \quad \Longrightarrow \quad m_{1,2} = m_L \pm m_D, \quad \theta = \frac{\pi}{4}$ (maximal mixing);

(C): $\mathbf{M} = \begin{pmatrix} 0 & m \\ m & M \end{pmatrix}$ or, more generally, $|m_L| \ll |m_R|, \quad m_D > 0.$

A generalization of case (A), $|m_{L,R}| \ll |m_D|$, leads to the so-called "Pseudo-Dirac neutrinos" and to the ν_L (active) $\leftrightarrow$ ν_R (sterile) oscillations with almost maximal mixing ($\tan 2\theta \gg 1$).

3.4.2 The See-saw

The case (C) with $m \ll M$ is the simplest example of the seesaw mechanism. It leads to two masses, one very large $m_1 \approx M$ other $m_2 \approx m^2/M \ll m$, suppressed compared to entries in $\mathbf{M}$. In particular, one can assume

$m \sim m_\ell$ or m_q (0.5 MeV to 200 GeV) and $M \sim M_{\mathsf{GUT}} \sim 10^{15-16}$ GeV.

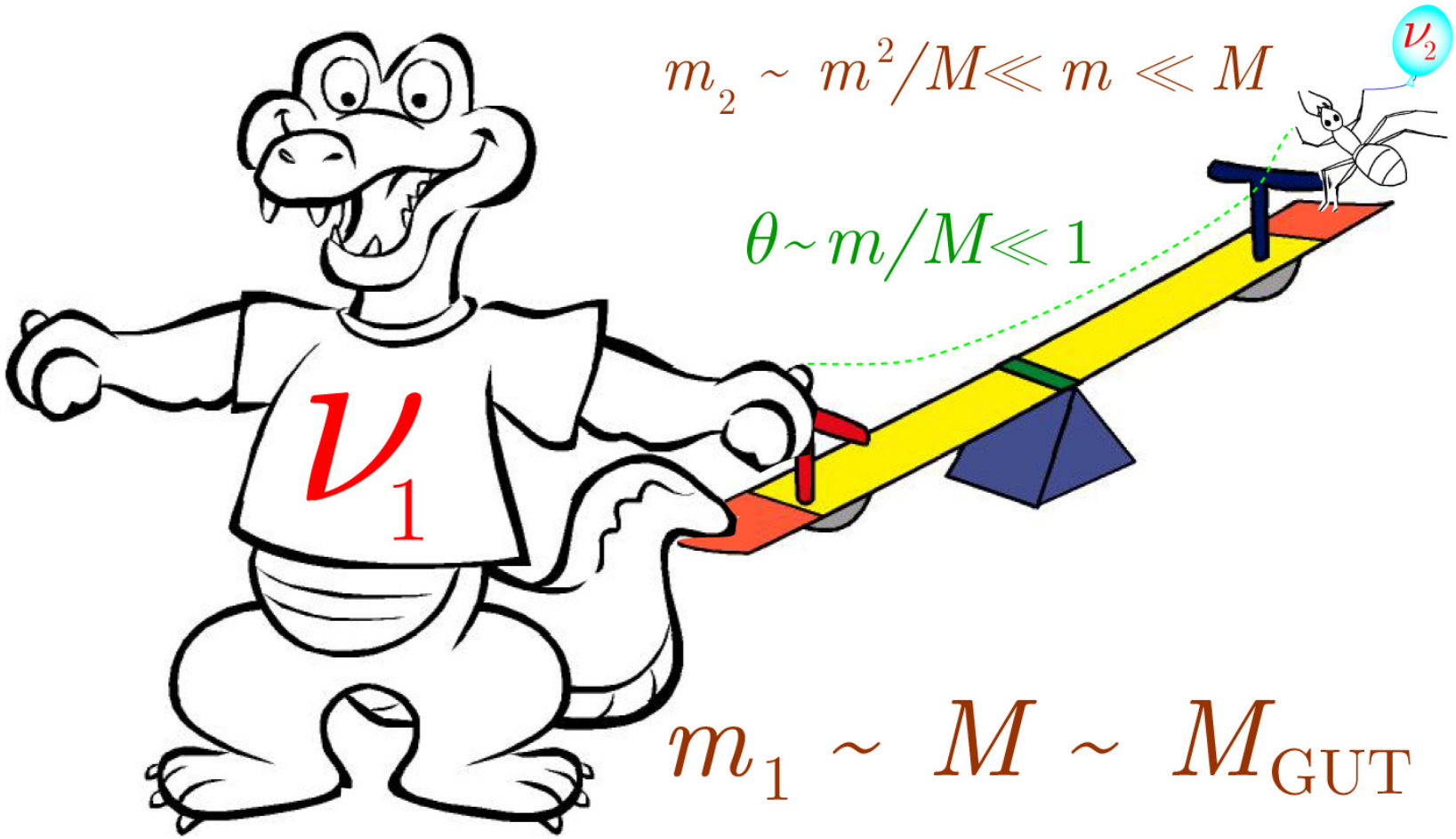

Then, m_2 can ranges from $\sim 10^{-14}$ eV to ~ 0.04 eV. The mixing between the heavy and light neutrinos is extremely small: $\theta \approx m/M \sim 10^{-20} - 10^{-13} \ll 1$.

3.4.3 More neutral fermions

A generalization of the above scheme to N generations is almost straightforward but technically cumbersome. Let's consider it schematically for $N = 3$.

- If neutral fermions are added to the SM fields, then the flavour neutrinos can acquire mass by mixing with them.
- The additional neutrinos can be
  - $SU(2) \times U(1)$ singlets (e.g., right-handed neutrinos), or
  - $SU(2) \times U(1)$ doublets (e.g., Higgsino in SUSY), or
  - $SU(2) \times U(1)$ triplets (e.g., Wino in SUSY).
- Addition of three right-handed neutrinos $\mathcal{N}_{iR}$ leads to the see-saw mechanism with the following mass terms:

$$\mathcal{L}_m = -\sum_{ij} \left[\overline{\nu}_{iL} M^D_{ij} \mathcal{N}_{jR} - \frac{1}{2} \left(\mathcal{N}_{iR}\right)^c M^R_{ij} \mathcal{N}_{jR} + \text{H.c.} \right].$$

- The above equation gives the see-saw 6×6 mass matrix

$$\mathbf{M} = \begin{pmatrix} \mathbf{0} & \mathbf{m}_D \\ \mathbf{m}_D^T & \mathbf{M}_R \end{pmatrix}.$$

  Both $\mathbf{m}_D$ and $\mathbf{m}_R$ are 3×3 matrices in the generation space.

When $\mathbf{M}_R$ is nonsingular and its scale M is much larger than that in $\mathbf{m}_R$,[a] one get

$$\mathbf{m}_\nu \sim -\mathbf{m}_D \mathbf{M}_R^{-1} \mathbf{m}_D^T.$$

All the neutrino masses are automatically suppressed due to the large scale $M \sim M_{\rm GUT}$ in $\mathbf{M}_R$. One gets the following mass hierarchy for a diagonal $\mathbf{M}_R$

$$m_1 : m_2 : m_3 \propto m_{D1}^2 : m_{D2}^2 : m_{D3}^2$$

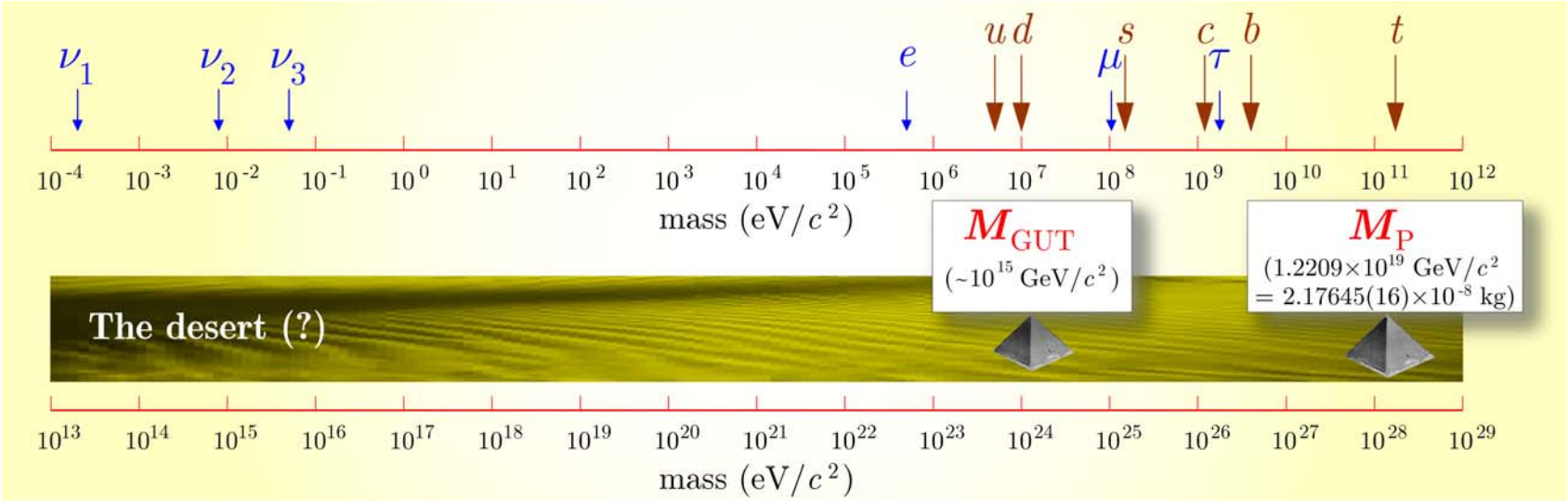

Here m_{Dk} are eigenvalues of $\mathbf{m}_D$. As long as these eigenvalues are hierarchical, the Majorana neutrino masses also display the hierarchy.

---

[a] A large M is natural in, e.g., grand unified $SO(10)$ theories which therefore provide a nice framework to understand small neutrino masses.

4 Neutrino oscillations in vacuum

4.1 Macroscopic Feynman diagrams

Let us consider two reactions

$$\underbrace{\pi^+ n \to \mu^+ \mu^- p}_{\text{allowed in SM}} \quad \text{and} \quad \underbrace{\pi^+ n \to \mu^+ \tau^- p}_{\text{forbidden in SM}}.$$

The first one is allowed in the SM while the second reaction is forbidden by conservation of the individual lepton numbers $L_{\mu,\tau}$. However, our previous consideration suggests that in a model extended by inclusion of a Dirac or Majorana mass term these numbers are no longer conserved and the second process becomes also possible through the Feynman diagrams like one shown in the figure. The diagram describes the process of a pion decay with subsequent quasielastic neutrino scattering off a neutron with production of a τ lepton. The 4-momenta of the particles are shown in parentheses.

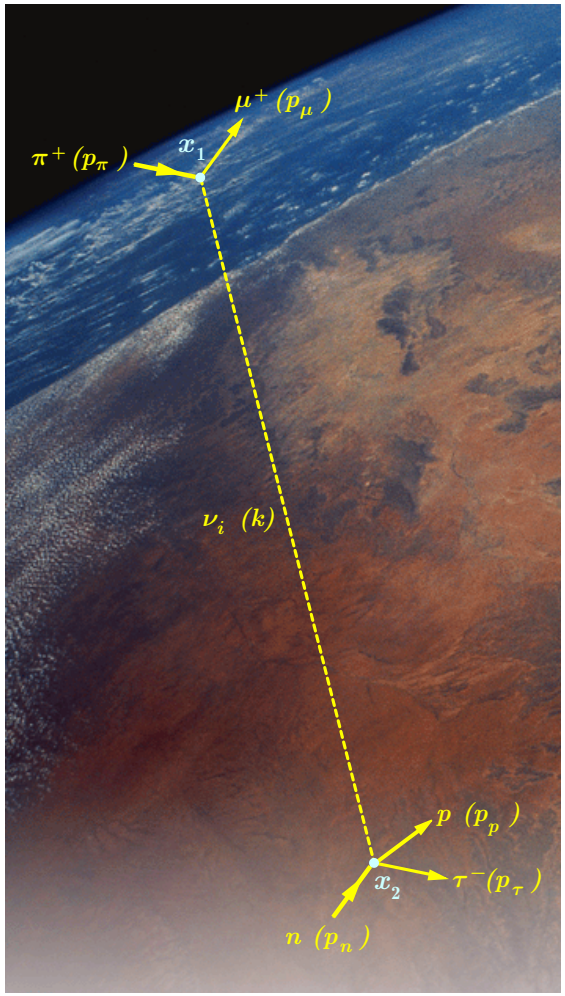

The mass eigenstate neutrino ν_k is in a virtual state between the space-time points of its production ($x_1 = (t_1, \mathbf{x}_1)$) and absorption ($x_2 = (t_2, \mathbf{x}_2)$).

The amplitude of the process under consideration,

$$\mathcal{M}(x_1, x_2) = \langle \text{out}|\text{in}\rangle = \langle \mu^+, \tau^-, p|\pi^+, n\rangle,$$

is given by the sum of N diagrams with $i = 1, 2, \ldots, N$ ($N = 3$ from here on).

The diagrams are quite unusual considering that the points x_1 and x_2 are separated by a macroscopic spatial interval $|\mathbf{x}_1 - \mathbf{x}_2|$. However, there are solid evidences that just the processes of this kind were already detected in the underground experiments Kamiokande, IMB, SOUDAN 2, Super-Kamiokande, and MACRO exploring atmospheric neutrinos crossing the Earth (see Part I of these lectures). Moreover, these results are confirmed by two accelerator experiments – K2K and (very recently) MINOS (FNAL, NuMI Beam).[a]

A careful consideration demonstrates that the situation is even more nontrivial.
Neglecting the matter effects, the general structure of the amplitude can be written as

$$\mathcal{M}(x_1, x_2) = \sum_j \int d^4y_1 d^4y_2 \, A_2(x_2 - y_2) \, V^*_{\tau j} \, G_j(y_2 - y_1) \, V_{\mu j} \, A_1(y_1 - x_1),$$

where $A_1(y_1 - x_1)$ and $A_2(x_2 - y_2)$ are the matrices describing the vertices x_1 and x_2 (decay and interaction) and

[a] D. A. Petyt (for the MINOS Collaboration), "First MINOS results from the NuMI Beam," report in the University of Minnesota Joint Experimental/Theoretical Physics Seminar, Fermilab March 30,2006.

$$G_j(y_2 - y_1) = \langle 0|T\left[\nu_j(y_1)\overline{\nu}_j(y_2)\right]|0\rangle = i\int \frac{d^4q}{(2\pi)^4}\,\frac{\hat{q} - m_j}{q^2 - m_j^2 + i0}\,e^{iq(y_2-y_1)}$$

is the Green function describing the propagation of the virtual neutrino ν_j between the space-time points y_1 and y_2 ($T[\cdots]$ denotes the standard T-ordering operator).

The following simple but important statements can be proved:

- $\star$ $\mathcal{M}(x_1, x_2) \equiv 0$ if the neutrino mass spectrum is degenerate ($m_1 = m_2 = m_3$). This is an obvious consequence of the unitarity of the mixing matrix which in particular provides $\sum_j V_{\mu j}V^*_{\tau j} = 0$.
- $\star$ If the wave functions of any of the "colliding" particles (pion or neutron) are plane waves that is

  $$\Phi_\pi(x) = e^{-ip_\pi x} = e^{-i(E_\pi t - \mathbf{p}_\pi \mathbf{x})} \quad \text{or} \quad \Psi_n(x) = e^{-ip_n x} = e^{-i(E_n t - \mathbf{p}_n \mathbf{x})},$$

  the amplitude is suppressed by the factor

  $$\sum_j V_{\mu j}V^*_{\tau j}\left(\frac{m_j}{E_\nu}\right)^2 = 10^{-20}\sum_j V_{\mu j}V^*_{\tau j}\left(\frac{m_j}{1\ \text{eV}/c^2}\right)^2\left(\frac{10\ \text{GeV}}{E_\nu}\right)^2,$$

  where $E_\nu \equiv k_0 = E_\pi - E_\mu$ is the virtual neutrino energy (independent of m_j). This is a consequence of the energy-momentum conservation in each vertex.

A nontrivial (but not the most general) situation occurs when both wave functions $\Phi_\pi(x)$ and $\Psi_n(x)$ are localized within neighborhoods of the points $\mathbf{x_1}$ and $\mathbf{x_2}$:

$$\Phi_\pi(x) = e^{-iE_\pi t}\varphi_\pi(\mathbf{x}-\mathbf{x_1}) \quad \text{and} \quad \Psi_n(x) = e^{-iE_n t}\psi_n(\mathbf{x}-\mathbf{x_2}).$$

According to the uncertainty principle this means that there is a spread in the momenta of these particles. In this case, by applying the crucial Grimus-Stockinger theorem[a] one can prove that in the asymptotic limit $L = |\mathbf{x}_1 - \mathbf{x}_2| \to \infty$, $\mathcal{M}(x_1, x_2) \to \mathcal{M}_\infty(L)$ and

$$\mathcal{M}_\infty(L) = \frac{\mathcal{M}_1\mathcal{M}_2}{L}\sum_j V_{\mu j}V^*_{\tau j}e^{iq_jL}, \quad \text{where} \quad q_j = \sqrt{E_\nu^2 - m_j^2}, \quad E_\nu = E_\pi - E_\mu.$$

[a] See W. Grimus and P. Stockinger, "Real oscillations of virtual neutrinos," Phys. Rev. D **54** (1996) 3414–3419 (hep-ph/9603430).

The theorem states: Let $\Phi = \Phi(\mathbf{q})$ be a 3 times continuously differentiable function such that Φ itself and all its first and second derivatives decrease at least like $|\mathbf{q}|^{-2}$ for $|\mathbf{q}| \to \infty$, a a real number, and

$$J(\mathbf{L}) \equiv \int d^3q\, \frac{\Phi(\mathbf{q})}{a - |\mathbf{q}|^2 + i0}\, \exp\left(-i\mathbf{q}\mathbf{L}\right).$$

Then in the asymptotic limit $L = |\mathbf{L}| \to \infty$ one obtains, for $a > 0$,

$$J(\mathbf{L}) \to -\frac{2\pi^2}{L}\Phi\left(-\sqrt{a}\,\mathbf{l}\right)\exp\left(i\sqrt{a}L\right) + \mathcal{O}\left(L^{-3/2}\right), \qquad \mathbf{l} \equiv \frac{\mathbf{L}}{L},$$

whereas for $a < 0$ the integral $J(\mathbf{L})$ decreases like L^{-2}.

To calculate the factors $\mathcal{M}_1$ and $\mathcal{M}_2$ as functions of the momenta of the initial and final particles, respectively, one have to "decipher" the vertices of our macro-diagram by applying an interaction model (like that shown in the figure on right). *It is by no means a simple or straightforward task.* One can prove however that after quadrating the amplitude we will arrive at something like

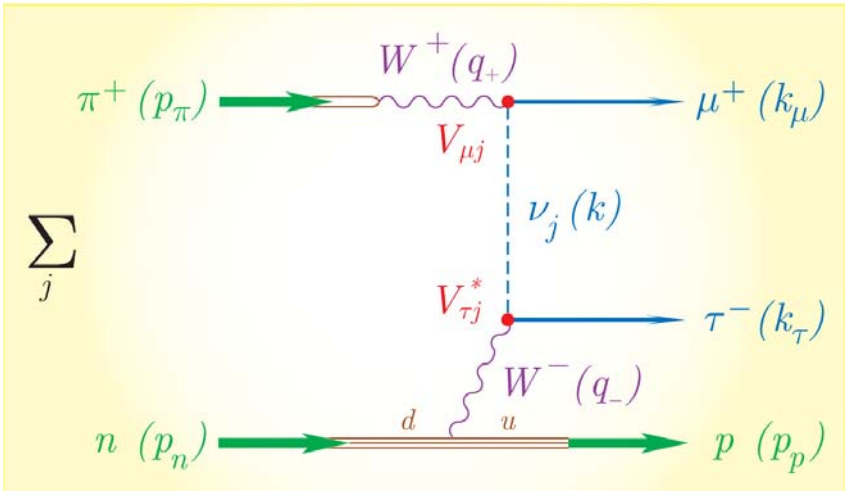

$$L^{-2}\, d\Gamma(\pi^+ \to \mu^+ \nu_\mu) \times P(\nu_\mu \to \nu_\tau) \times d\sigma(\nu_\tau + n \to p + \tau),$$

where $d\Gamma$ is the differential width of standard pion decay, $d\sigma$ is the differential cross section for the quasielastic $\nu_\tau\, n$ interaction, the factor L^2 accounts for the geometrical decrease of the neutrino flux, and

$$P(\nu_\mu \to \nu_\tau) \equiv \left| \sum_j V_{\mu j} V^*_{\tau j} e^{i q_j L} \times \sqrt{S_j} \right|^2 \tag{7}$$

where S_j is a suppression factor (see below). Equation (7) can be *interpreted* as the probability of the transition of **real** muon neutrino to **real** tauon neutrino (both having energy $E_\nu = E_\pi - E_\mu$) on the path L between the neutrino source and detector.

The obtained result is almost independent of the specific process. This allows us to generalize it quite straightforwardly and write out the formula for the transition probability between any neutrino pair:

$$P(\nu_\alpha \to \nu_\beta) = \sum_{jk} V_{\alpha j} V_{\beta k} \left(V_{\alpha k} V_{\beta j}\right)^* \exp\left[i(q_j - q_k)L\right] \times S_{jk}. \tag{8}$$

The suppression factor S_{jk} in Eq. (8) is given by

$$S_{jk} \approx \exp\left[-\left(\frac{L}{L^{\mathsf{coh}}_{jk}}\right)^2 - \left(\frac{L^{\mathsf{loc}}}{L^{\mathsf{osc}}_{jk}}\right)^2\right], \tag{9}$$

where

$$L^{\mathsf{coh}}_{jk} = \frac{E_\nu}{\sqrt{2}\sigma_p} L^{\mathsf{osc}}_{jk}$$

are the coherence lengths defined through the uncertainty σ_p in the momentum of the source (pion in our particular case) and the neutrino oscillation lengths,

$$L^{\mathsf{osc}}_{jk} = \frac{2\pi E_\nu}{q_j - q_k};$$

L^{loc} is the measure of fuzziness of the detector (neutron in our case).

According to Eq. (9), the factor S_{jk} suppresses the neutrino oscillations if

- $L \gtrsim L^{\mathrm{coh}}_{jk}$ ("blooming" of the neutrino wave packets) and/or
- $L^{\mathrm{osc}}_{jk} \lesssim L^{\mathrm{loc}}$.

In other words, the oscillations are not suppressed when at least one of the oscillation lengths is large enough.

Ultrarelativistic neutrinos

In the ultrarelativistic limit $E_\nu^2 \gg m_k^2$, which is valid for almost all interesting circumstances (except for the relic neutrinos),[a]

$$q_j = \sqrt{E_\nu^2 - m_j^2} \approx E_\nu - \frac{m_j^2}{2E_\nu}$$

and, assuming in addition that the neutrino oscillation lengths are large enough, we can write

$$P(\nu_\alpha \to \nu_\beta) = P_{\alpha\beta}(L) \approx \sum_{jk} V_{\alpha j} V_{\beta k} \left(V_{\alpha k} V_{\beta j}\right)^* \exp\left(\frac{2i\pi L}{L_{jk}}\right), \tag{10}$$

$$L^{\mathrm{osc}}_{jk} \equiv L_{jk} = \frac{4\pi E_\nu}{\Delta m^2_{jk}} \quad \text{and} \quad \Delta m^2_{jk} = m_k^2 - m_j^2. \tag{11}$$

[a] Note that decay of any known particle produces ultrarelativistic neutrinos even if the particle is at rest (with the uncertainty of σ_p).

Important notes

- ⋆ In order to obtain $\mathcal{M}_\infty$ we have performed the asymptotic limit $L \to \infty$. From the proof of the Grimus-Stockinger theorem it follows that "large L" means

$$L \gg 2 \times 10^{-16}\ \text{m} \times \left(1\ \text{GeV}/\overline{E}_\nu\right),$$

  where $\overline{E}_\nu$ is an average neutrino energy. For every thinkable neutrino experiment this is very well fulfilled and corrections to $\mathcal{M}_\infty$ are suppressed by $1/\sqrt{\overline{E}_\nu}$.

- ⋆ The factor $1/L$ in the asymptotic amplitude corresponds to the geometrical decrease of the neutrino "flux" by $1/L^2$ in the "cross section".

- ⋆ From the derivation one can conclude that neutrino oscillations between the neutrino with masses m_j and m_k can only take place if

$$|q_j - q_k| \lesssim \sigma,$$

  where σ is the minimum of the widths of the Fourier transformations of the involved wave functions. In coordinate space this simply means that corresponding widths must be smaller than the oscillation lengths defined by

$$L_{jk} = \frac{4\pi E_\nu}{m_j^2 - m_k^2} \equiv \frac{4\pi E_\nu}{\Delta m_{jk}^2} \approx 2.48\ \text{m} \times \frac{E_\nu\ (\text{MeV})}{\Delta m_{jk}^2\ (\text{eV}^2)}.$$

- ⋆ The nature of neutrinos (Dirac or Majorana) was not specified in our schematic consideration. It can be shown however that the difference between $\mathcal{M}_\infty^{\text{Dirac}}$ and $\mathcal{M}_\infty^{\text{Majorana}}$ is of the order of m_j/E_ν.

4.2 Quantum mechanical approach

The flavor neutrino eigenstates which can be written as a vector

$$|\boldsymbol{\nu}\rangle_f = (|\nu_e\rangle, |\nu_\mu\rangle, |\nu_\tau\rangle, \ldots)^T \equiv (|\nu_\alpha\rangle)^T$$

are defined as the states which correspond to the charge leptons $\alpha = e, \mu, \tau$. The correspondence is established through the charged current interactions of active neutrinos and charged leptons. In general, the flavor states have no definite masses.

The neutrino mass eigenstates

$$|\boldsymbol{\nu}\rangle_m = (|\nu_1\rangle, |\nu_2\rangle, |\nu_3\rangle, \ldots)^T \equiv (|\nu_k\rangle)^T$$

are, by definition, the states with the definite masses m_k, $k = 1, 2, 3, \ldots$.

Since $|\nu_\alpha\rangle$ and $|\nu_k\rangle$ are not identical, they are related to each other through a unitary transformation

$$|\nu_\alpha\rangle = \sum_k \hat{V}_{\alpha k}|\nu_k\rangle \quad \text{or} \quad |\boldsymbol{\nu}\rangle_f = \hat{\mathbf{V}}|\boldsymbol{\nu}\rangle_m,$$

where $\hat{\mathbf{V}} = \| \hat{V}_{\alpha k} \|$ is a unitary (in general, $N \times N$) matrix. In order to find out the correspondence between $\hat{\mathbf{V}}$ and the PMNS mixing matrix $\mathbf{V}$ we can normalize the "f" and "m" states by the following conditions

$$\langle 0|\nu_{\alpha L}(x)|\nu_{\alpha'}\rangle = \delta_{\alpha\alpha'} \quad \text{and} \quad \langle 0|\nu_{kL}(x)|\nu_{k'}\rangle = \delta_{kk'}.$$

From these conditions we obtain

$$\sum_k V_{\alpha k}\hat{V}_{\alpha' k} = \delta_{\alpha\alpha'} \quad \text{and} \quad \sum_\alpha V_{\alpha k}\hat{V}_{\alpha k'} = \delta_{kk'}.$$

Therefore

$$\hat{\mathbf{V}} \equiv \mathbf{V}^\dagger$$

and

$$|\boldsymbol{\nu}\rangle_f = \mathbf{V}^\dagger|\boldsymbol{\nu}\rangle_m \quad \Longleftrightarrow \quad |\boldsymbol{\nu}\rangle_m = \mathbf{V}|\boldsymbol{\nu}\rangle_f.$$

The time evolution of a single mass eigenstate $|\nu_k\rangle$ with momentum p_ν is trivial,

$$i\frac{d}{dt}|\nu_k(t)\rangle = E_k|\nu_k(t)\rangle \quad \Longrightarrow \quad |\nu_k(t)\rangle = e^{-iE_2(t-t_0)}|\nu_k(t_0)\rangle,$$

where $E_k = \sqrt{p_\nu^2 + m_k^2}$ is the total energy in the state $|\nu_k\rangle$. Therefore, assuming that all the components of the neutrino wave packet have the same momenta, one can write

$$i\frac{d}{dt}|\boldsymbol{\nu}(t)\rangle_m = \mathbf{H}_0|\boldsymbol{\nu}(t)\rangle_m, \quad \text{where} \quad \mathbf{H}_0 = \text{diag}\,(E_1, E_2, E_3, \ldots). \tag{12}$$

($\mathbf{H}_0$ is the vacuum Hamiltonian.) From Eqs. (61) and (12) we have

$$i\frac{d}{dt}|\boldsymbol{\nu}(t)\rangle_f = \mathbf{V}^\dagger\mathbf{H}_0\mathbf{V}|\boldsymbol{\nu}(t)\rangle_f. \tag{13}$$

Solution to this equation is obvious:

$$\begin{aligned} |\boldsymbol{\nu}(t)\rangle_f &= \mathbf{V}^\dagger e^{-i\mathbf{H}_0(t-t_0)}\mathbf{V}\,|\boldsymbol{\nu}(t_0)\rangle_f \\ &= \mathbf{V}^\dagger \,\mathrm{diag}\left(e^{-iE_1(t-t_0)}, e^{-iE_2(t-t_0)}, \ldots\right)\,\mathbf{V}\,|\boldsymbol{\nu}(t_0)\rangle_f. \end{aligned} \tag{14}$$

In the ultrarelativistic limit $p_\nu^2 \gg m_k^2$,

$$E_k = \sqrt{p_\nu^2 + m_k^2} \approx p_\nu + \frac{m_k^2}{2p_\nu} \approx E_\nu + \frac{m_k^2}{2E_\nu}.$$

By applying this approximation and Eq. (14) one can derive the survival and transition probabilities

$$\begin{aligned} P\left[\nu_\alpha(t_0) \to \nu_\beta(t)\right] \equiv P_{\alpha\beta}(t-t_0) &= \left|\langle\nu_\beta(t)|\nu_\alpha(t_0)\rangle\right|^2 \\ &= \left|\sum_k V_{\alpha k}V_{\beta k}^*\,\exp\left[iE_k(t-t_0)\right]\right|^2 \\ &= \sum_{jk} V_{\alpha j}V_{\beta k}\left(V_{\alpha k}V_{\beta j}\right)^*\,\exp\left[i(E_j-E_k)(t-t_0)\right] \\ &\approx \sum_{jk} V_{\alpha j}V_{\beta k}\left(V_{\alpha k}V_{\beta j}\right)^*\,\exp\left[i\Delta m_{jk}^2(t-t_0)/2E_\nu\right]. \end{aligned}$$

The next standard approximation is

$$v_k = p_\nu / E_k \approx c = 1$$

from which it follows that

$$t - t_0 \approx L \; = \; \text{source–detector distance}.$$

This approximation is in fact contradictory since the corresponding corrections are also of the order of m_k/E_ν. However, only with this approximation we arrive at the formula[a]

$$\begin{aligned} P_{\alpha\beta}(L) &\approx \sum_{jk} V_{\alpha j} V_{\beta k} \left(V_{\alpha k} V_{\beta j}\right)^* \exp\left(\frac{i\Delta m^2_{jk} L}{2E_\nu}\right) \\ &= \sum_{jk} V_{\alpha j} V_{\beta k} \left(V_{\alpha k} V_{\beta j}\right)^* \exp\left(\frac{2i\pi L}{L_{jk}}\right), \end{aligned} \tag{15}$$

which marvelously and enigmatically fits the field-theoretical ("diagrammatic") result (10) written in the ultrarelativistic limit.

The range of applicability of the standard quantum-mechanical approach is very limited but enough for the interpretation of essentially all modern experiments.

---

[a] As above, $L_{jk} = 4\pi E_\nu / \Delta m^2_{jk}$ are the neutrino oscillation lengths.

4.2.1 Simplest case: two flavor vacuum oscillations

Let us now consider the simplest 2-flavor case with $i = 2, 3$ and $\alpha = \mu, \tau$ (the most favorable due to the SK and other underground experiments). The 2×2 vacuum mixing matrix can be parametrized (due to the unitarity) with a single parameter, $\theta = \theta_{23}$, the vacuum mixing angle,

$$\mathbf{V} = \begin{pmatrix} \cos\theta & \sin\theta \\ -\sin\theta & \cos\theta \end{pmatrix}, \qquad 0 \leq \theta \leq \pi/2.$$

Equation (15) then becomes very simple:

$$P_{\alpha\alpha'}(L) = \frac{1}{2}\sin^2 2\theta \left[1 - \cos\left(\frac{2\pi L}{L_\nu}\right)\right],$$

$$L_\nu \equiv L_{23} = \frac{4\pi E_\nu}{\Delta m^2_{23}} \approx 2R_\oplus \left(\frac{E_\nu}{10\ \text{GeV}}\right)\left(\frac{0.002\ \text{eV}^2}{\Delta m^2_{23}}\right)$$

where $R_\oplus$ is the mean radius of the Earth. Since 10 GeV is a typical energy for the atmospheric neutrinos, the Earth is surprisingly very suitable for studying the atmospheric neutrino oscillations in rather wide range of the parameter Δm^2_{23}.

5 Neutrino oscillations in matter

5.1 Neutrino refraction

It has been noted by Wolfenstein[a] that neutrino oscillations in a medium are affected by interactions even if the thickness of the medium is negligible in comparison with the neutrino mean free path.

Let us forget for the moment about the inelastic collisions and consider the simplest case of a ultrarelativistic neutrino which moves in an external (effective) potential W formed by the matter background. If the neutrino momentum in vacuum was $\mathbf{p}$ then its energy was $\simeq p = |\mathbf{p}|$. When the neutrino enters into the medium, its energy becomes $E = p + W$. Let us now introduce the index of refraction $n = p/E$ which is a positive value in the absence of inelastic collisions. Therefore

$$W = (1 - n)E \simeq (1 - n)p. \tag{16}$$

In the last step, we took into account that neutrino interaction with matter is very weak, $|W| \ll E$, and thus $E \simeq p$ is a good approximation.

The natural generalization of Eq. (13) for the time evolution of neutrino flavor states in matter then follows from this simple consideration and the quantum-mechanical correspondence principle.

[a] L. Wolfenstein, Phys. Rev. D **17** (1978) 2369.

This is the famous Wolfenstein equation:

$$i\frac{d}{dt}|\boldsymbol{\nu}(t)\rangle_f = \left[\mathbf{V}\mathbf{H}_0\mathbf{V}^\dagger + \mathbf{W}(t)\right]|\boldsymbol{\nu}(t)\rangle_f, \tag{17}$$

where

$$\mathbf{W}(t) = \mathrm{diag}\left(1-n_{\nu_e}, 1-n_{\nu_\mu}, 1-n_{\nu_\tau}, \ldots\right) p \tag{18}$$

is the interaction Hamiltonian.

It will be useful for the following to introduce the *time-evolution operator* for the flavor states defined by

$$|\boldsymbol{\nu}(t)\rangle_f = \mathbf{S}(t)|\boldsymbol{\nu}(0)\rangle_f.$$

Taking into account that $|\boldsymbol{\nu}(t)\rangle_f$ must satisfy Eq. (17) for any initial condition $|\boldsymbol{\nu}(t=0)\rangle_f = |\boldsymbol{\nu}(0)\rangle_f$, the Wolfenstein equation can be immediately rewritten in terms of the evolution operator:

$$i\dot{\mathbf{S}}(t) = \left[\mathbf{V}\mathbf{H}_0\mathbf{V}^\dagger + \mathbf{W}(t)\right]\mathbf{S}(t), \quad \mathbf{S}(0) = \mathbf{1}. \tag{19}$$

This equation (or its equivalent (17)) cannot be solved analytically in the general case of a medium with a varying (along the neutrino pass) density. But for a medium with a slowly (adiabatically) varying density distribution the approximate solution can be obtained by a diagonalization of the effective Hamiltonian. Below we will consider this method for a rather general 2-flavor case but now let us illustrate (without derivation) the simplest situation with a matter of constant density.

5.1.1 Matter of constant density

In the 2-flavor case, the transition probability is given by the formula very similar to that for vacuum:

$$P_{\alpha\alpha'}(L) = \frac{1}{2}\sin^2 2\theta_{\mathsf{m}}\left[1-\cos\left(\frac{2\pi L}{L_{\mathsf{m}}}\right)\right],$$

$$L_{\mathsf{m}} = L_{\mathsf{v}}\left[1-2\kappa\left(L_{\mathsf{v}}/L_0\right)\cos\theta+\left(L_{\mathsf{v}}/L_0\right)^2\right]^{-1/2}.$$

The L_{m} is called the oscillation length in matter and is defined through the following quantities:

$$L_{\mathsf{v}} \equiv L_{23} = \frac{4\pi E}{\Delta m^2}, \quad L_0 = \frac{\sqrt{2}\pi A}{G_F N_A Z\rho} \approx 2R_\oplus\left(\frac{A}{2Z}\right)\left(\frac{2.5\ \mathrm{g/cm}^3}{\rho}\right),$$

$$\kappa = \mathsf{sign}\left(m_3^2-m_2^2\right), \quad \Delta m^2 = \left|m_3^2-m_2^2\right|.$$

The parameter θ_{m} is called the mixing angle in matter and is given by

$$\sin 2\theta_{\mathsf{m}} = \sin 2\theta\left(\frac{L_{\mathsf{m}}}{L_{\mathsf{v}}}\right), \quad \cos 2\theta_{\mathsf{m}} = \left(\cos 2\theta - \kappa\frac{L_{\mathsf{v}}}{L_0}\right)\left(\frac{L_{\mathsf{m}}}{L_{\mathsf{v}}}\right).$$

The solution for antineutrinos is the same but with the replacement $\kappa \mapsto -\kappa$. The closeness of the value of L_0 to the Earth's diameter is even more surprising than that for L_{v}. The matter effects are important for atmospheric neutrinos.

5.2 Propagation of high-energy mixed neutrinos through matter

"The matter doesn't matter"

Lincoln Wolfenstein, lecture given at 28th SLAC Summer Institute on Particle Physics "Neutrinos from the Lab, the Sun, and the Cosmos", Stanford, CA, Aug. 14-25, 2000.

When neutrinos propagate through vacuum there is a phase change

$$\exp\left(-im_i^2 t/2p_\nu\right).$$

For two mixed flavors there is a resulting oscillation with length

$$L_{\text{vac}} = \frac{4\pi E_\nu}{\Delta m^2} \approx D_\oplus \left(\frac{E_\nu}{10\ \text{GeV}}\right)\left(\frac{0.002\ \text{eV}^2}{\Delta m^2}\right).$$

In matter there is an additional phase change due to refraction associated with forward scattering

$$\exp\left[ip_\nu(\text{Re}\, n - 1)t\right]$$

and the characteristic length (for a normal medium) is

$$L_{\text{ref}} = \frac{\sqrt{2}A}{G_F N_A Z \rho} \approx D_\oplus \left(\frac{A}{2Z}\right)\left(\frac{2.5\ \text{g/cm}^2}{\rho}\right).$$

It is generally believed that the imaginary part of the index of refraction n which describes the neutrino absorption due to inelastic interactions *does not affect the oscillation probabilities* or at the least inelastic interactions can be someway *decoupled* from oscillations.

The conventional arguments are

- $\mathrm{Re}\, n - 1 \propto G_F$ while $\mathrm{Im}\, n \propto G_F^2$;
- Only Δn may affect the oscillations and $\Delta \mathrm{Im}\, n$ is all the more negligible.

It will be shown that these arguments do not work for sufficiently high neutrino energies and/or for thick media $\Longrightarrow$ in general absorption cannot be decoupled from refraction and mixing.

By using another cant phrase of Wolfenstein, one can say that

"In some circumstances the matter could matter."

5.2.1 Generalized MSW equation

Let $f_{\nu_\alpha A}(0)$ be the amplitude for the ν_α zero-angle scattering from particle A of the matter background ($A = e, p, n, \ldots$),
$\rho(t)$ – the matter density (in g/cm^3),
$Y_A(t)$ – the number of particles A per amu in the point t of the medium,
$N_0 = 6.02214199 \times 10^{23}$ cm^{-3} – the reference particle number density (numerically equal to the Avogadro's number).

Then the index of refraction of ν_α for small $|n-1|$ is given by

$$n_\alpha(t) = 1 + \frac{2\pi N_0 \rho(t)}{p_\nu^2} \sum_A Y_A(t) f_{\nu_\alpha A}(0),$$

where p_ν is the neutrino momentum. Since the amplitude $f_{\nu_\alpha A}(0)$ is in general a complex number, the index of refraction is also complex. Its real part is responsible for neutrino refraction while the imaginary part – for absorption. From the optical theorem of quantum mechanics we have

$$\mathrm{Im}\left[f_{\nu_\alpha A}(0)\right] = \frac{p_\nu}{4\pi} \sigma^{\mathrm{tot}}_{\nu_\alpha A}\left(p_\nu\right).$$

This implies that

$$p_\nu \mathrm{Im}\left[n_\alpha(t)\right] = \frac{1}{2} N_0 \rho(t) \sum_A Y_A(t) \sigma^{\mathrm{tot}}_{\nu_\alpha A}\left(p_\nu\right) = \frac{1}{2\Lambda_\alpha\left(p_\nu, t\right)},$$

where $\Lambda_\alpha\left(p_\nu, t\right)$ is the mean free path of ν_α in the point t of the medium.

Note:

The dimension of Λ_α is cm,

$$\Lambda_\alpha\left(p_\nu, t\right) = \frac{1}{\Sigma_\alpha^{\text{tot}}\left(p_\nu, t\right)} = \frac{\lambda_a^{\text{tot}}\left(p_\nu, t\right)}{\rho(t)}.$$

Since the neutrino momentum, p_ν, is an extrinsic variable in Eq. (20), we will sometimes omit this argument to simplify formulas.

The generalized MSW equation for the time-evolution operator

$$\mathbf{S}(t) = \begin{pmatrix} S_{\alpha\alpha}(t) & S_{\alpha\beta}(t) \\ S_{\beta\alpha}(t) & S_{\beta\beta}(t) \end{pmatrix}$$

of two mixed stable neutrino flavors ν_α and ν_β propagating through an absorbing medium can be written as

$$\boxed{i\frac{d}{dt}\mathbf{S}(t) = \left[\mathbf{V}\mathbf{H}_0\mathbf{V}^T + \mathbf{W}(t)\right]\mathbf{S}(t), \quad (\mathbf{S}(0) = \mathbf{1})\,.} \tag{20}$$

Here

$$\mathbf{V}=\begin{pmatrix}\cos\theta & \sin\theta\\ -\sin\theta & \cos\theta\end{pmatrix}$$ is the vacuum mixing matrix ($0\le\theta\le\pi/2$),

$$\mathbf{H}_0=\begin{pmatrix}E_1 & 0\\ 0 & E_2\end{pmatrix}$$ is the vacuum Hamiltonian for ν mass eigenstates,

$$E_i=\sqrt{p_\nu^2+m_i^2}\simeq p_\nu+m_i^2/2p_\nu$$ is the energy of the ν_i eigenstate,

$$\mathbf{W}(t)=-p_\nu\begin{pmatrix}n_\alpha(t)-1 & 0\\ 0 & n_\beta(t)-1\end{pmatrix}$$ is the interaction Hamiltonian.

5.2.2 Master equation

It is useful to transform MSW equation into the one with a traceless Hamiltonian. For this purpose we define the matrix

$$\widetilde{\mathbf{S}}(t)=\exp\left\{\frac{i}{2}\int_0^t \mathrm{Tr}\left[\mathbf{H}_0+\mathbf{W}(t')\right]dt'\right\}\mathbf{S}(t).$$

The master equation (ME) for this matrix then is

$$\boxed{i\frac{d}{dt}\widetilde{\mathbf{S}}(t)=\mathbf{H}(t)\widetilde{\mathbf{S}}(t),\quad \widetilde{\mathbf{S}}(0)=\mathbf{1}.} \tag{21}$$

The effective Hamiltonian is defined by

$$\mathbf{H}(t) = \begin{pmatrix} q(t) - \Delta_c & \Delta_s \\ \Delta_s & -q(t) + \Delta_c \end{pmatrix},$$

$$\Delta_c = \Delta \cos 2\theta, \quad \Delta_s = \Delta \sin 2\theta, \quad \Delta = \frac{m_2^2 - m_1^2}{4p_\nu},$$

$$q(t) = q_R(t) + iq_I(t) = \frac{1}{2} p_\nu \left[n_\beta(t) - n_\alpha(t) \right].$$

The Hamiltonian for antineutrinos is of the same form as $\mathbf{H}(t)$ but

$$\mathrm{Re}\left[f_{\overline{\nu}_\alpha A}(0) \right] = -\mathrm{Re}\left[f_{\nu_\alpha A}(0) \right] \quad \text{and} \quad \mathrm{Im}\left[f_{\overline{\nu}_\alpha A}(0) \right] \neq \mathrm{Im}\left[f_{\nu_\alpha A}(0) \right].$$

The neutrino oscillation probabilities are

$$P\left[\nu_\alpha(0) \to \nu_{\alpha'}(t) \right] \equiv P_{\alpha\alpha'}(t) = \left| S_{\alpha'\alpha}(t) \right|^2 = A(t) \left| \widetilde{S}_{\alpha'\alpha}(t) \right|^2, \tag{22}$$

where

$$A(t) = \exp\left[-\int_0^t \frac{dt'}{\Lambda(t')} \right], \quad \frac{1}{\Lambda(t)} = \frac{1}{2} \left[\frac{1}{\Lambda_\alpha(t)} + \frac{1}{\Lambda_\beta(t)} \right].$$

Owing to the complex potential q, the Hamiltonian $\mathbf{H}(t)$ is non-Hermitian and the new evolution operator $\widetilde{\mathbf{S}}(t)$ is nonunitary. As a result, there are no conventional relations between $P_{\alpha\alpha'}(t)$.

Since

$$q_I(t) = \frac{1}{4}\left[\frac{1}{\Lambda_\beta(t)} - \frac{1}{\Lambda_\alpha(t)}\right],$$

the matrix $\mathbf{H}(t)$ becomes Hermitian when $\Lambda_\alpha = \Lambda_\beta$. If this is the case at any t, the ME reduces to the standard MSW equation and inelastic scattering results in the common exponential attenuation of the probabilities. probabilities. From here, we shall consider the more general and more interesting case, when $\Lambda_\alpha \neq \Lambda_\beta$.

5.2.3 Examples

$\nu_\alpha - \nu_s$

This is the extreme example. Since $\Lambda_s = \infty$, we have $\Lambda = 2\Lambda_\alpha$ and $q_I = -1/4\Lambda_\alpha$. So $q_I \neq 0$ at any energy. Even without solving the evolution equation, one can expect the penetrability of active neutrinos to be essentially modified in this case because, roughly speaking, they spend a certain part of life in the sterile state. In other words, sterile neutrinos "tow" their active companions through the medium as a tugboat. On the other hand, the active neutrinos "retard" the sterile ones, like a bulky barge retards its tugboat. As a result, the sterile neutrinos undergo some absorption.

$\nu_{e,\mu} - \nu_\tau$

Essentially at all energies, $\sigma^{\mathsf{CC}}_{\nu_{e,\mu}N} > \sigma^{\mathsf{CC}}_{\nu_\tau N}$. This is because of large value of the τ lepton mass, m_τ, which leads to several consequences:

1. high neutrino energy threshold for τ production;
2. sharp shrinkage of the phase spaces for CC $\nu_\tau N$ reactions;
3. kinematic correction factors ($\propto m_\tau^2$) to the nucleon structure functions (the corresponding structures are negligible for e production and small for μ production).

The neutral current contributions are canceled out from q_I. Thus, in the context of the master equation, ν_τ can be treated as (almost) sterile within the energy range for which $\sigma^{\mathsf{CC}}_{\nu_{e,\mu}N} \gg \sigma^{\mathsf{CC}}_{\nu_\tau N}$ (see Figs. 6–7 below).

$\overline{\nu}_e - \overline{\nu}_\alpha$

A similar situation, while in quite a different and narrow energy range, holds in the case of mixing of $\overline{\nu}_e$ with some other flavor. This is a particular case for a normal C asymmetric medium, because of the W boson resonance formed in the neighborhood of $E_\nu^{\mathsf{res}} = m_W^2/2m_e \approx 6.33$ PeV through the reactions

$$\overline{\nu}_e e^- \to W^- \to \text{hadrons} \quad \text{and} \quad \overline{\nu}_e e^- \to W^- \to \overline{\nu}_\ell \ell^- \quad (\ell = e, \mu, \tau).$$

Let's remind that $\sigma^{\mathsf{tot}}_{\overline{\nu}_e e} \approx 250\ \sigma^{\mathsf{tot}}_{\overline{\nu}_e N}$ just at the resonance peak (see Fig. 5 and Table 3 below).

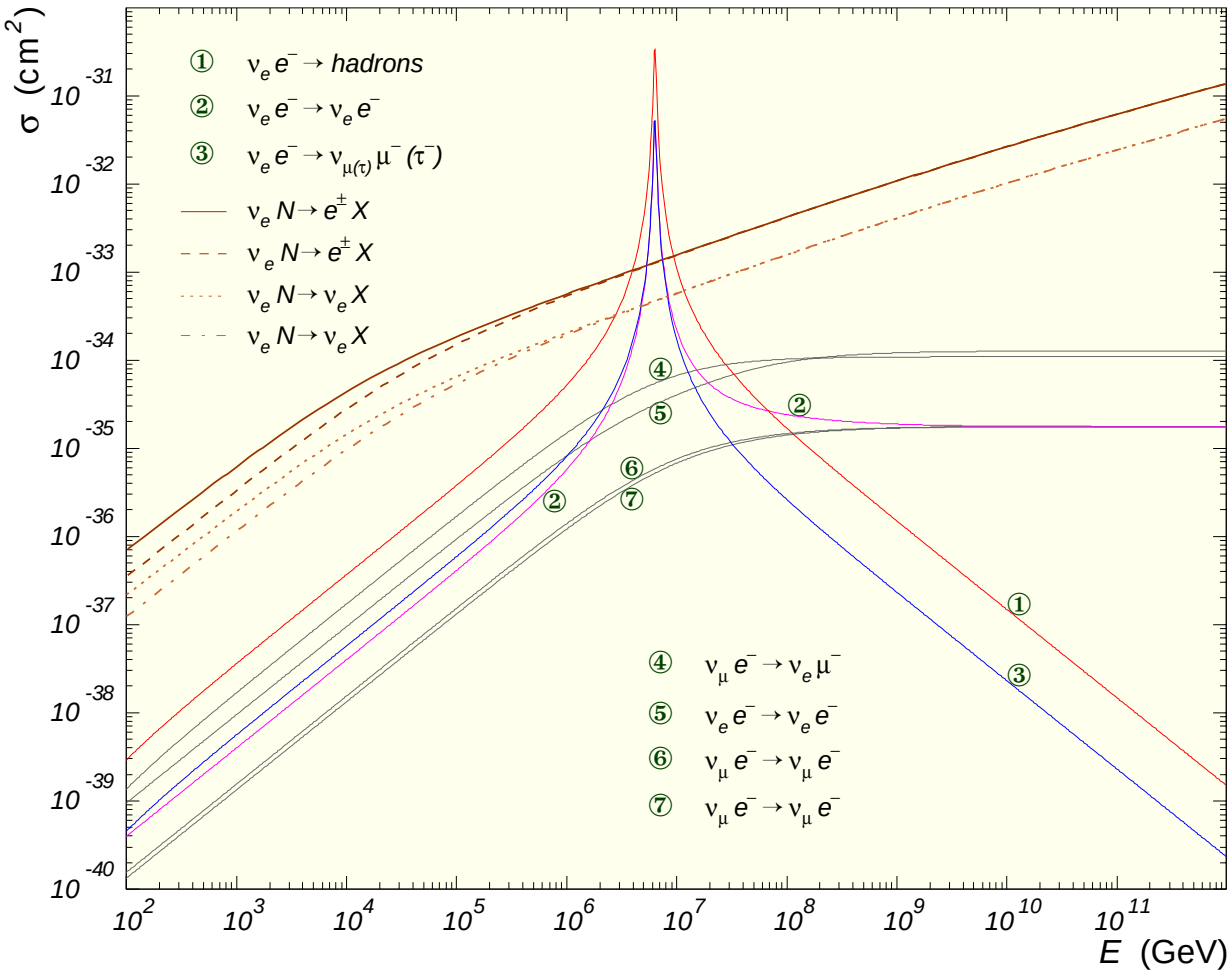

Figure 5: Total cross sections for (anti)neutrino interactions on electron targets. The cross sections for (anti)neutrino CC and NC interactions on isoscalar nucleon are also shown for a comparison.

Table 3: Integrated cross sections for neutrino-electron and neutrino-nucleon scattering at $E_\nu = m_W^2/2m_e \approx 6.331$ PeV.

Reaction	σ (cm^2)	Reaction	σ (cm^2)
$\nu_\mu e \to \nu_\mu e$	5.86×10^{-36}	$\nu_\mu N \to \mu^- +$ anything	1.43×10^{-33}
$\overline{\nu}_\mu e \to \overline{\nu}_\mu e$	5.16×10^{-36}	$\nu_\mu N \to \nu_\mu +$ anything	6.04×10^{-34}
$\nu_\mu e \to \mu \nu_e$	5.42×10^{-35}	$\overline{\nu}_\mu N \to \mu^+ +$ anything	1.41×10^{-33}
$\nu_e e \to \nu_e e$	3.10×10^{-35}	$\overline{\nu}_\mu N \to \overline{\nu}_\mu +$ anything	5.98×10^{-34}
$\overline{\nu}_e e \to \overline{\nu}_e e$	5.215×10^{-32}		
$\overline{\nu}_e e \to \overline{\nu}_\mu \mu$	5.214×10^{-32}		
$\overline{\nu}_e e \to \overline{\nu}_\tau \tau$	5.208×10^{-32}		
$\overline{\nu}_e e \to$ hadrons	3.352×10^{-31}		
$\overline{\nu}_e e \to$ anything	4.917×10^{-31}		

Just at the resonance peak, $\sigma^{\rm tot}_{\overline{\nu}_e e} \approx 250\, \sigma^{\rm tot}_{\overline{\nu}_e N}$.

Note:

The cross sections for electron targets listed in Table 3 were calculated using the formulas given by Gandhi *et al.*, [a] but some numerical values are different since the input parameters were updated.

[a] R. Gandhi, C. Quigg, M. H. Reno, and I. Sarcevic, "Ultrahigh-energy neutrino interactions," Astropart. Phys. **5** (1996) 81–110 (hep-ph/9512364).

5.2.4 Total cross sections

According to Albright and Jarlskog[a]

$$\frac{d\sigma^{\mathrm{CC}}_{\nu,\overline{\nu}}}{dxdy} = \frac{G_F^2 m_N E_\nu}{\pi}\left(A_1F_1 + A_2F_2 \pm A_3F_3 + A_4F_4 + A_5F_5\right),$$

where $F_i = F_i(x, Q^2)$ are the nucleon structure functions and A_i are the kinematic factors $i = 1, \ldots, 5$). These factors were calculated by many authors[b] and the most accurate formulas were given by Paschos and Yu:

$$A_1 = xy^2 + \frac{m_l^2 y}{2m_N E_\nu}, \quad A_2 = 1 - y - \frac{m_N}{2E_\nu}xy - \frac{m_l^2}{4E_\nu^2}, \quad A_3 = xy\left(1 - \frac{y}{2}\right) - \frac{m_l^2 y}{4m_N E_\nu},$$

$$A_4 = \frac{m_l^2}{2m_N E_\nu}\left(xy + \frac{m_l^2}{2m_N E_\nu}\right), \quad A_5 = -\frac{m_l^2}{2m_N E_\nu}.$$

The contributions proportional to m_ℓ^2 must vanish as $E_\nu \gg m_\ell$. However they remain surprisingly important even at very high energies.

---

[a] C. H. Albright and C. Jarlskog, Nucl. Phys. B**84** (1975) 467. See also I. Ju, Phys. Rev. D**8** (1973) 3103 and V. D. Barger *et al.*, Phys. Rev. D**16** (1977) 2141.

[b] See previous footnote and also the more recent papers: S. Dutta, R. Gandhi, and B. Mukhopadhyaya, Eur. Phys. J. C **18** (2000) 405 (hep–ph/9905475); N. I. Starkov, J. Phys. G: Nucl. Part. Phys. **27** (2001) L81; E. A. Paschos and J. Y. Yu, Phys. Rev. D**65** (2002) 033002 (hep–ph/0107261).

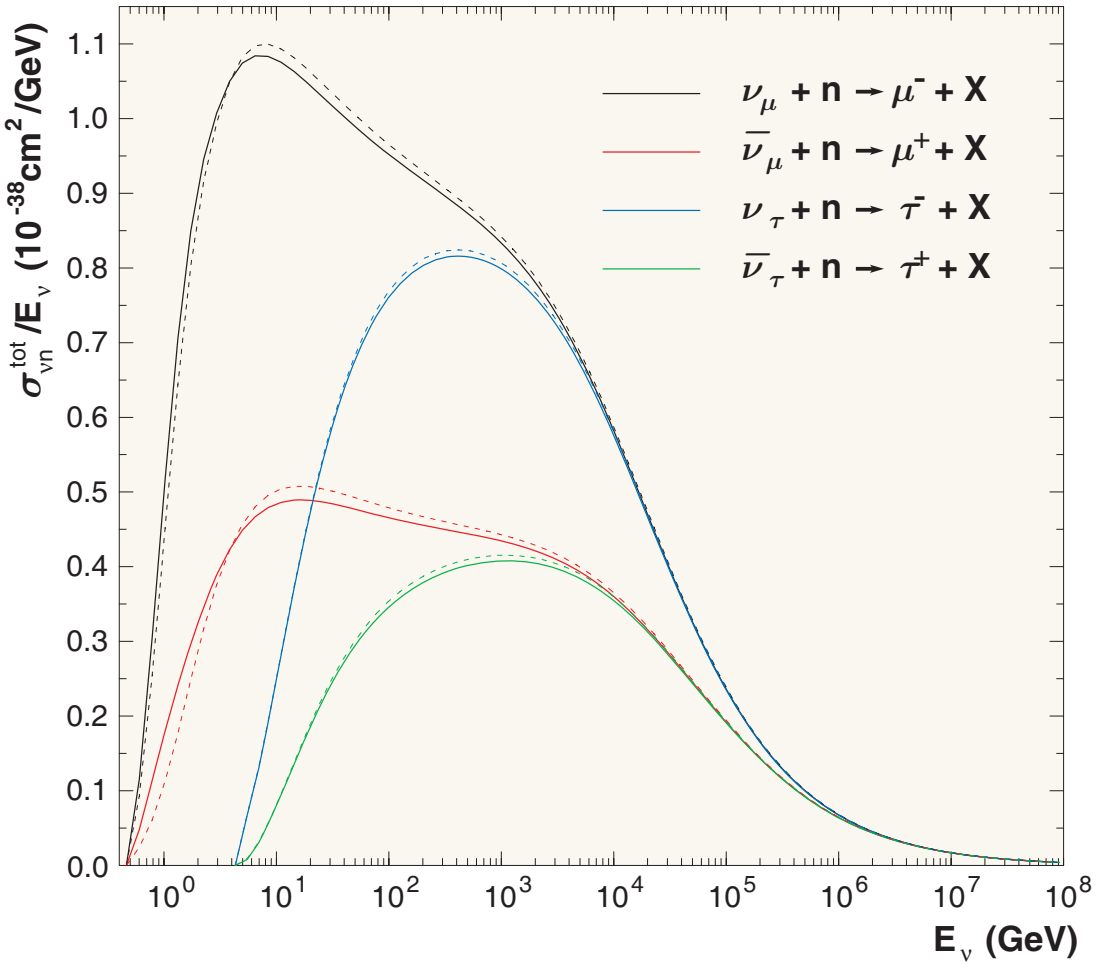

Figure 6: Total inelastic νn cross sections evaluated with the MRST 2002 NNLO PDF model modified according to Bodek–Yang prescription (solid lines) and unmodified (dashed lines).

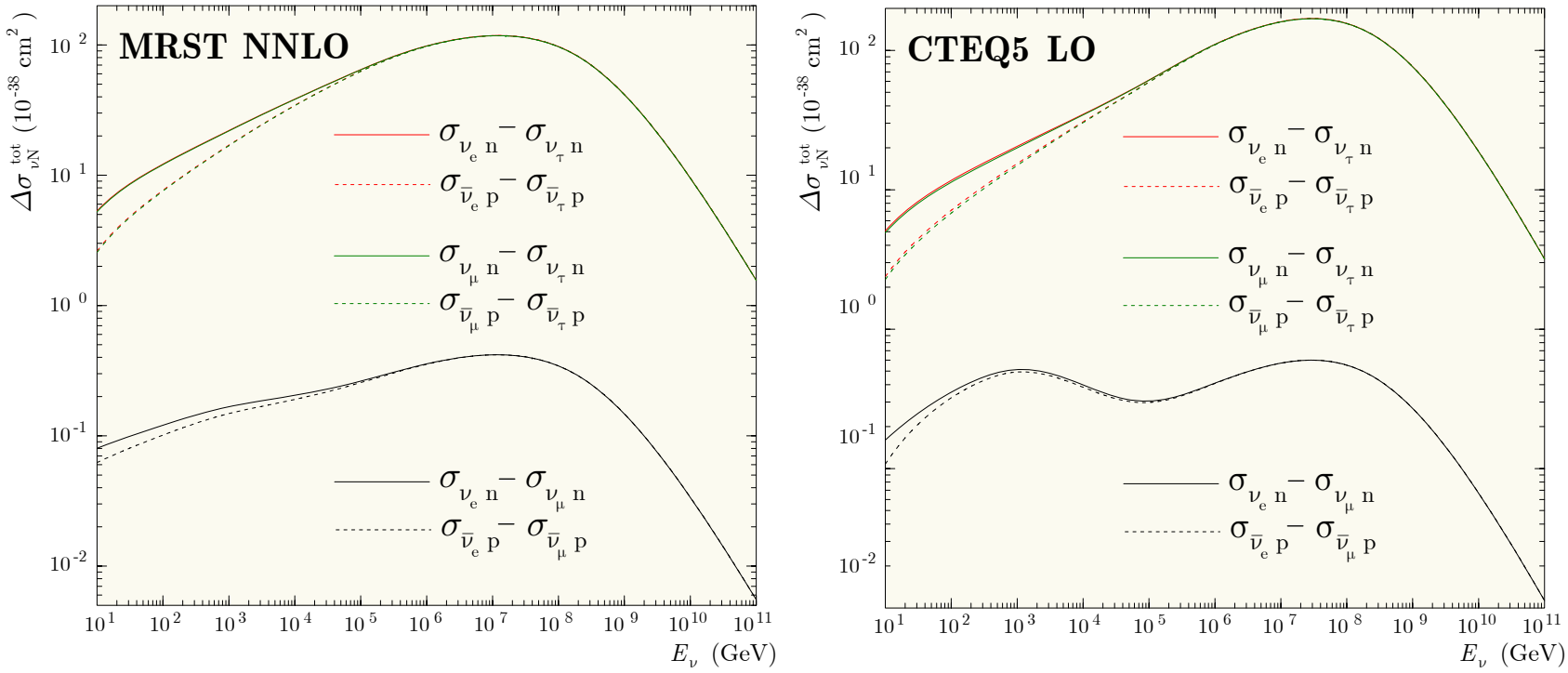

Figure 7: Differences between the total neutrino cross sections for proton and neutron targets evaluated with the MRST 2002 NNLO (left) and CTEQ 5-DIS LO (right) PDF models.

5.2.5 Indices of refraction

For $E_\nu \ll \min\left(m_{W,Z}^2/2m_A\right)$ and for an electroneutral nonpolarized cold medium, the q_R is energy independent. In the leading orders of the standard electroweak theory it is

$$q_R = \begin{cases} \frac{1}{2}V_0 Y_p \rho & \text{for } \alpha = e \text{ and } \beta = \mu \text{ or } \tau, \\ -\frac{1}{2}a_\tau V_0 \left(Y_p + b_\tau Y_n\right)\rho & \text{for } \alpha = \mu \text{ and } \beta = \tau, \\ \frac{1}{2}V_0 \left(Y_p - \frac{1}{2}Y_n\right)\rho & \text{for } \alpha = e \text{ and } \beta = s, \\ \frac{1}{4}V_0 Y_n \rho & \text{for } \alpha = \mu \text{ or } \tau \text{ and } \beta = s, \end{cases}$$

where

$$V_0 = \sqrt{2}G_F N_0 \simeq 7.63 \times 10^{-14} \text{ eV} \quad \left(L_0 = \frac{2\pi}{V_0} \simeq 1.62 \times 10^4 \text{ km} \sim D_\oplus\right),$$

$$a_\tau = \frac{3\alpha r_\tau \left[\ln(1/r_\tau) - 1\right]}{4\pi \sin^2\theta_W} \simeq 2.44 \times 10^{-5}, \quad b_\tau = \frac{\ln(1/r_\tau) - 2/3}{\ln(1/r_\tau) - 1} \simeq 1.05,$$

α is the fine-structure constant, θ_W is the weak-mixing angle and $r_\tau = (m_\tau/m_W)^2$.

Notes:

- For an isoscalar medium the $|q_R|$ is of the same order of magnitude for any pair of flavors but $\nu_\mu - \nu_\tau$.
- For an isoscalar medium $q_R^{(\nu_\mu - \nu_\tau)}/q_R^{(\nu_e - \nu_\mu)} \approx -5 \times 10^{-5}$.

- For certain regions of a neutron-rich medium the value of $q_R^{(\nu_e - \nu_s)}$ may become vanishingly small. In this case, the one-loop radiative corrections must be taken into account.
- For very high energies the q_R have to be corrected for the gauge boson propagators and strong-interaction effects.

One can expect $|q_R|$ to be either an energy-independent or decreasing function for any pair of mixed neutrino flavors. On the other hand, there are several cases of much current interest when $|q_I|$ either increases with energy without bound (mixing between active and sterile neutrino states) or has a broad or sharp maximum (as for $\nu_\mu - \nu_\tau$ or $\overline{\nu}_e - \overline{\nu}_\mu$ mixings, respectively).

Numerical estimations suggest that for every of these cases there is an energy range in which q_R and q_I are comparable in magnitude. Since $q_R \propto \rho$ and $q_I \propto$ and are dependent upon the composition of the medium (Y_A) there may exist some more specific situations, when

$$|q_R| \sim |q_I| \sim |\Delta|$$

or even

$$|q_R| \sim |\Delta_c| \quad \text{and} \quad |q_I| \sim |\Delta_s| \,.$$

If this is the case, the refraction, absorption and mixing become interestingly superimposed.

5.2.6 Eigenproblem and mixing matrix in matter

Eigenvalues

The matrix $\mathbf{H}(t)$ has two complex instantaneous eigenvalues, $\varepsilon(t)$ and $-\varepsilon(t)$, with $\varepsilon = \varepsilon_R + i\varepsilon_I$ satisfying the characteristic equation

$$\varepsilon^2 = (q - q_+)\,(q - q_-)\,,$$

where $q_\pm = \Delta_c \pm i\Delta_s = \Delta e^{\pm 2i\theta}$. The solution is

$$\varepsilon_R^2 = \frac{1}{2}\left(\varepsilon_0^2 - q_I^2\right) + \frac{1}{2}\sqrt{\left(\varepsilon_0^2 - q_I^2\right)^2 + 4q_I^2\left(\varepsilon_0^2 - \Delta_s^2\right)},$$

$$\varepsilon_I = \frac{q_I\,(q_R - \Delta_c)}{\varepsilon_R} \quad \text{(provided } q_R \neq \Delta_c\text{)}\,,$$

with

$$\varepsilon_0 = \sqrt{\Delta^2 - 2\Delta_c q_R + q_R^2} \geq |\Delta_s|, \qquad \text{sign}\,(\varepsilon_R) \stackrel{\text{def}}{=} \text{sign}(\Delta) \equiv \zeta.$$

(At that choice $\varepsilon = \Delta$ for vacuum and $\varepsilon = \zeta\varepsilon_0$ if $q_I = 0$.)

In the vicinity of the MSW resonance, $q_R = q_R(t_\star) = \Delta_c$

$$\lim_{q_R \to \Delta_c \pm 0} \varepsilon_R = \Delta_s \sqrt{\max\left(1 - \Delta_I^2/\Delta_s^2, 0\right)},$$

$$\lim_{q_R \to \Delta_c \pm 0} \varepsilon_I = \pm\zeta\Delta_I \sqrt{\max\left(1 - \Delta_s^2/\Delta_I^2, 0\right)},$$

where $\Delta_I = q_I(t_\star)$. Therefore the resonance value of $|\varepsilon_R|$ (which is inversely proportional to the neutrino oscillation length in matter) is always smaller than the conventional MSW value $|\Delta_s|$ and *vanishes* if $\Delta_I^2 < \Delta_s^2$ (ε_I remains finite in this case). In neutrino transition through the region of resonance density $\rho = \rho(t_\star)$, ε_I undergoes discontinuous jump while ε_R remains continuous. The corresponding cuts in the q plane are placed outside the circle $|q| \leq |\Delta|$. If $\Delta_I^2 > \Delta_s^2$, the imaginary part of ε vanishes while the real part remains finite.

A distinctive feature of the characteristic equation is the existence of two mutually conjugate "super-resonance" points $q_\pm$ in which ε vanishes giving rise to the total degeneracy of the levels of the system (impossible in the "standard MSW" solution). Certainly, the behavior of the system in the vicinity of these points must be dramatically different from the conventional pattern.

The "super-resonance" conditions are physically realizable for various meaningful mixing scenarios.

Some useful relations

$$\varepsilon_R^2 = \frac{2q_I^2\left(\varepsilon_0^2-\Delta_s^2\right)}{\sqrt{\left(\varepsilon_0^2-q_I^2\right)^2+4q_I^2\left(\varepsilon_0^2-\Delta_s^2\right)}-\varepsilon_0^2+q_I^2},$$

$$\varepsilon_I = \frac{\sqrt{\left(\varepsilon_0^2-q_I^2\right)^2+4q_I^2\left(\varepsilon_0^2-\Delta_s^2\right)}-\varepsilon_0^2+q_I^2}{2q_I\left(q_R-\Delta_c\right)},$$

$$\frac{\partial\varepsilon_R}{\partial q_R}=\frac{\partial\varepsilon_I}{\partial q_I}=\frac{q_I\varepsilon_I+\left(q_R-\Delta_c\right)\varepsilon_R}{\varepsilon_R^2+\varepsilon_I^2},$$

$$\frac{\partial\varepsilon_I}{\partial q_R}=-\frac{\partial\varepsilon_R}{\partial q_I}=\frac{q_I\varepsilon_R-\left(q_R-\Delta_c\right)\varepsilon_I}{\varepsilon_R^2+\varepsilon_I^2},$$

$$\mathrm{Re}\left[\frac{q(t)-\Delta_c}{\varepsilon}\right]=\left(\frac{q_R-\Delta_c}{\varepsilon_R}\right)\left(\frac{\varepsilon_R^2+q_I^2}{\varepsilon_R^2+\varepsilon_I^2}\right),$$

$$\mathrm{Im}\left[\frac{q(t)-\Delta_c}{\varepsilon}\right]=\left(\frac{q_I}{\varepsilon_R}\right)\left(\frac{\varepsilon_R^2-\varepsilon_0^2+\Delta_s^2}{\varepsilon_R^2+\varepsilon_I^2}\right),$$

$$\left(q_R-\Delta_c\right)^2=\varepsilon_0^2-\Delta_s^2.$$

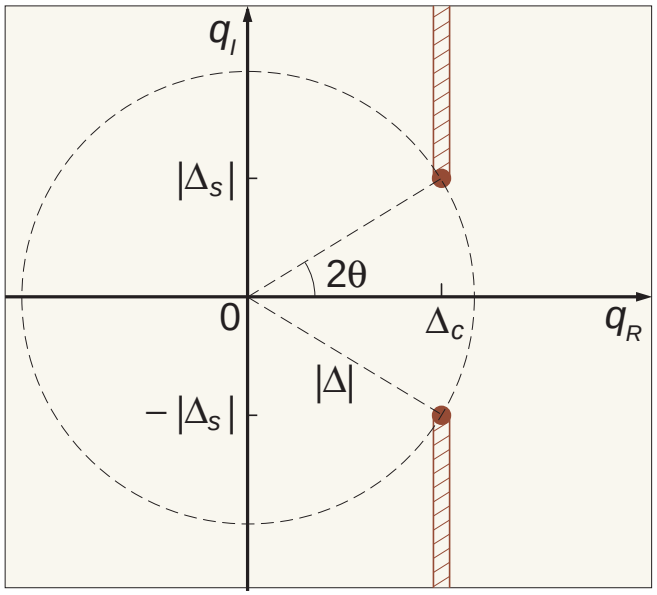

Figure 8: Zeros and cuts of ε in the q plane for $\Delta_c > 0$. The cuts are placed outside the circle $|q| \le |\Delta|$ parallel to axis $q_R = 0$. The MSW resonance point is $(\Delta_c, 0)$ and the two "super-resonance" points are $(\Delta_c, \pm\Delta_s)$.

Eigenstates

In order to simplify the solution to the eigenstate problem we'll assume that the phase trajectory $q = q(t)$ does not cross the points $q_\pm$ at any t. In non-Hermitian quantum dynamics one has to consider the two pairs of instantaneous eigenvectors $|\Psi_\pm\rangle$ and $|\overline{\Psi}_\pm\rangle$ which obey the relations

$$\mathbf{H}|\Psi_\pm\rangle = \pm\varepsilon|\Psi_\pm\rangle \quad \text{and} \quad \mathbf{H}^\dagger|\overline{\Psi}_\pm\rangle = \pm\varepsilon^*|\overline{\Psi}_\pm\rangle. \tag{23}$$

and (for $q \neq q_\pm$) form a complete biorthogonal and biorthonormal set,

$$\langle\overline{\Psi}_\pm|\Psi_\pm\rangle = 1, \quad \langle\overline{\Psi}_\pm|\Psi_\mp\rangle = 0, \quad |\Psi_+\rangle\langle\overline{\Psi}_+| + |\Psi_-\rangle\langle\overline{\Psi}_-| = \mathbf{1}.$$

Therefore, the eigenvectors are defined up to a gauge transformation

$$|\Psi_\pm\rangle \mapsto e^{if_\pm}|\Psi_\pm\rangle, \quad |\overline{\Psi}_\pm\rangle \mapsto e^{-if_\pm^*}|\overline{\Psi}_\pm\rangle,$$

with arbitrary complex functions $f_\pm(t)$ such that $\mathrm{Im}\,(f_\pm)$ vanish as $q = 0$.[a] Thus it is sufficient to find any particular solution of Eqs. (23). Taking into account that $\mathbf{H}^\dagger = \mathbf{H}^*$, we may set $|\overline{\Psi}_\pm\rangle = |\Psi_\pm^*\rangle$ and hence the eigenvectors can be found from the identity

$$\mathbf{H} = \varepsilon|\Psi_+\rangle\langle\Psi_+^*| - \varepsilon|\Psi_-\rangle\langle\Psi_-^*|.$$

[a] For our aims, the class of the gauge functions may be restricted without loss of generality by the condition $f_\pm|_{q=0} = 0$.

Setting $|\Psi_\pm\rangle = (v_\pm, \pm v_\mp)^T$ we arrive at the equations

$$v_\pm^2 = \frac{\varepsilon \pm (q - \Delta_c)}{2\varepsilon}, \quad v_+ v_- = \frac{\Delta_s}{2\varepsilon},$$

a particular solution of which can be written as

$$v_+ = \sqrt{\left|\frac{\varepsilon + q - \Delta_c}{2\varepsilon}\right|}\, e^{i(\varphi-\psi)/2},$$

$$v_- = \zeta\sqrt{\left|\frac{\varepsilon - q + \Delta_c}{2\varepsilon}\right|}\, e^{i(-\varphi-\psi)/2}.$$

where

$$\varphi = \arg(\varepsilon + q - \Delta_c) = -\arg(\varepsilon - q + \Delta_c) = \arctan\left(\frac{q_I}{\varepsilon_R}\right),$$

$$\psi = \arg(\varepsilon) = \arctan\left(\frac{\varepsilon_I}{\varepsilon_R}\right),$$

and we have fixed the remaining gauge ambiguity by a comparison with the vacuum case.

Mixing angle in matter

It may be sometimes useful to define the complex mixing angle in matter $\Theta = \Theta_R + i\Theta_I$ by the relations

$$\sin\Theta = v_+ \quad \text{and} \quad \cos\Theta = v_-$$

or, equivalently,

$$\sin 2\Theta = \frac{\Delta_s}{\varepsilon}, \quad \cos 2\Theta = \frac{\Delta_c - q}{\varepsilon},$$

The real and imaginary parts of Θ are found to be

$$\mathrm{Re}(\Theta) \equiv \Theta_R = \frac{1}{2}\arctan\left[\frac{(q_I - \Delta_s)\,\varepsilon_R - (q_R - \Delta_c)\,\varepsilon_I}{(q_R - \Delta_c)\,\varepsilon_R + (q_I - \Delta_s)\,\varepsilon_I}\right],$$

$$\mathrm{Im}(\Theta) \equiv \Theta_I = \frac{1}{4}\ln\left[\frac{\varepsilon_R^2 + \varepsilon_I^2}{(q_R - \Delta_c)^2 + (q_I - \Delta_s)^2}\right].$$

$$\cos\Theta = \cos\Theta_R \cosh\Theta_I - i\sin\Theta_R \sinh\Theta_I,$$
$$\sin\Theta = \sin\Theta_R \cosh\Theta_I + i\cos\Theta_R \sinh\Theta_I.$$

Having regard to the prescription for the sign of ε_R, one can verify that $\Theta = \theta$ if $q = 0$ (vacuum case) and $\Theta = 0$ if $\Delta_s = 0$ (no mixing or $m_1^2 = m_2^2$). It is also clear that Θ becomes the standard MSW mixing angle with $\mathrm{Im}(\Theta) = 0$ when $q_I = 0$ ($\Lambda_\alpha = \Lambda_\beta$).

Mixing matrix in matter

In order to build up the solution to ME for the nondegenerated case one has to diagonalize the Hamiltonian. Generally a non-Hermitian matrix cannot be diagonalized by a single unitary transformation. But in our simple case this can be done by a complex orthogonal matrix (extended mixing matrix in matter)

$$\mathbf{U}_f = \mathbf{U}\exp(i\mathbf{f}),$$

where $\mathbf{f} = \mathrm{diag}\,(f_-, f_+)$ and

$$\mathbf{U} = (|\Psi_-\rangle, |\Psi_+\rangle) = \begin{pmatrix} v_- & v_+ \\ -v_+ & v_- \end{pmatrix} = \begin{pmatrix} \cos\Theta & \sin\Theta \\ -\sin\Theta & \cos\Theta \end{pmatrix}.$$

Properties of $\mathbf{U}$:

$$\mathbf{U}^T\mathbf{H}\mathbf{U} = \mathrm{diag}\,(-\varepsilon, \varepsilon),$$
$$\mathbf{U}^T\mathbf{U} = \mathbf{1},$$
$$\mathbf{U}|_{q=0} = \mathbf{V}.$$

From CE it follows that

$$\partial\varepsilon/\partial q = (q - \Delta_c)/\varepsilon$$

and thus

$$\frac{\partial v_\pm}{\partial q} = \pm\frac{\Delta_s^2 v_\mp}{2\varepsilon^2}.$$

We therefore have

$$i\mathbf{U}^T\dot{\mathbf{U}} = -\Omega\begin{pmatrix} 0 & -i \\ i & 0 \end{pmatrix} = -\Omega\boldsymbol{\sigma}_2,$$

where

$$\Omega = \frac{\dot{q}\Delta_s}{2\varepsilon^2} = \frac{i}{4}\frac{d}{dt}\ln\left(\frac{q - q_+}{q - q_-}\right).$$

Properties of $\mathbf{U}_f$:

$$\mathbf{U}_f^T\mathbf{H}\mathbf{U}_f = \mathsf{diag}\,(-\varepsilon, \varepsilon),$$
$$\mathbf{U}_f^T\mathbf{U}_f = \mathbf{1},$$
$$\mathbf{U}_f|_{q=0} = \mathbf{V},$$
$$i\mathbf{U}_f^T\dot{\mathbf{U}}_f = -\Omega e^{-i\mathbf{f}}\boldsymbol{\sigma}_2 e^{i\mathbf{f}} - \dot{\mathbf{f}}.$$

5.2.7 Adiabatic solution

Formal solution to ME in the most general form:

$$\widetilde{\mathbf{S}}(t) = \mathbf{U}_f(t) \exp\left[-i\mathbf{\Phi}(t)\right] \mathbf{X}_f(t) \mathbf{U}_f^T(0). \tag{24}$$

Here $\mathbf{\Phi}(t) = \mathrm{diag}\left(-\Phi(t), \Phi(t)\right)$ and $\Phi(t) = \Phi_R(t) + i\Phi_I(t)$ is the complex dynamical phase, defined by

$$\Phi_R(t) = \int_0^t \varepsilon_R(t')dt', \quad \Phi_I(t) = \int_0^t \varepsilon_I(t')dt',$$

and $\mathbf{X}_f(t)$ must satisfy the equation

$$i\dot{\mathbf{X}}_f(t) = \left[\Omega(t) e^{-i\mathbf{f}(t)} \mathbf{F}(t) e^{i\mathbf{f}(t)} + \dot{\mathbf{f}}(t)\right] \mathbf{X}_f(t), \quad \mathbf{X}_f(0) = \mathbf{1},$$

where

$$\mathbf{F}(t) = e^{i\mathbf{\Phi}(t)} \boldsymbol{\sigma}_2 e^{-i\mathbf{\Phi}(t)} = \begin{pmatrix} 0 & -ie^{-2i\Phi(t)} \\ ie^{2i\Phi(t)} & 0 \end{pmatrix}.$$

It can be proved now that the right side of Eq. (24) is gauge-invariant i.e. it does not depend on the unphysical complex phases $f_\pm(t)$. This crucial fact is closely related to the absence of the Abelian topological phases in the system under consideration.

Finally, we can put $f_\pm = 0$ in Eq. (24) and the result is

$$\widetilde{\mathbf{S}}(t) = \mathbf{U}(t) \exp\left[-i\mathbf{\Phi}(t)\right] \mathbf{X}(t)\mathbf{U}^T(0), \tag{25a}$$

$$i\dot{\mathbf{X}}(t) = \Omega(t)\mathbf{F}(t)\mathbf{X}(t), \quad \mathbf{X}(0) = \mathbf{1}. \tag{25b}$$

These equations, being equivalent to the ME, have nevertheless a restricted range of practical usage on account of poles and cuts as well as decaying and increasing exponents in the "Hamiltonian" $\Omega\mathbf{F}$.

Adiabatic theorem

The adiabatic theorem of Hermitian quantum mechanics can almost straightforwardly be extended to ME under the requirements:

(a) the potential q is a sufficiently smooth and slow function of t;

(b) the imaginary part of the dynamical phase is a bounded function i.e. $\lim_{t\to\infty} |\Phi_I(t)|$ is finite;

(c) the phase trajectory $q = q(t)$ is placed far from the singularities for any t.

The first requirement breaks down for a condensed medium with a sharp boundary or layered structure (like the Earth). If however the requirement (a) is valid inside each layer (t_i, t_{i+1}), the problem reduces to Eqs. (25) by applying the rule

$$\widetilde{\mathbf{S}}(t) \equiv \widetilde{\mathbf{S}}(t,0) = \widetilde{\mathbf{S}}\,(t,t_n)\ldots\widetilde{\mathbf{S}}\,(t_2,t_1)\,\widetilde{\mathbf{S}}\,(t_1,0),$$

where $\widetilde{\mathbf{S}}\,(t_{i+1},t_i)$ is the time-evolution operator for the i-th layer.

The requirement (b) alone is not too restrictive considering that for many astrophysical objects (like stars, galactic nuclei, jets and so on) the density ρ exponentially disappears to the periphery and, on the other hand, $\varepsilon_I \to 0$ as $\rho \to 0$. In this instance, the function $\Phi_I(t)$ must be t independent for sufficiently large t. But, in the case of a steep density profile, the requirements (a) and (b) may be inconsistent.

The important case of violation of the requirement (c) is the subject of a special study which is beyond the scope of this study.

It is interesting to note in this connection that, in the Hermitian case, a general adiabatic theorem has been proved without the traditional gap condition [J. E. Avron and A. Elgart, Commun. Math. Phys. **203** (1999) 445].

The solution

Presume that all necessary conditions do hold for $0 \le t \le T$. Then, in the adiabatic limit, we can put $\Omega = 0$ in Eq. (25b). Therefore $\mathbf{X} = \mathbf{1}$ and Eq. (25a) yields

$$\widetilde{S}_{\alpha\alpha}(t) = v_+(0)v_+(t)e^{-i\Phi(t)} + v_-(0)v_-(t)e^{i\Phi(t)},$$
$$\widetilde{S}_{\alpha\beta}(t) = v_-(0)v_+(t)e^{-i\Phi(t)} - v_+(0)v_-(t)e^{i\Phi(t)},$$
$$\widetilde{S}_{\beta\alpha}(t) = v_+(0)v_-(t)e^{-i\Phi(t)} - v_-(0)v_+(t)e^{i\Phi(t)},$$
$$\widetilde{S}_{\beta\beta}(t) = v_-(0)v_-(t)e^{-i\Phi(t)} + v_+(0)v_+(t)e^{i\Phi(t)},$$

Taking into account Eq. (22) we obtain the survival and transition probabilities:

$$
\begin{aligned}
P_{\alpha\alpha}(t) &= A(t)\left\{\left[I_+^+(t)e^{\Phi_I(t)} + I_-^-(t)e^{-\Phi_I(t)}\right]^2 - I^2(t)\sin^2\left[\Phi_R(t) - \varphi_+(t)\right]\right\},\\
P_{\alpha\beta}(t) &= A(t)\left\{\left[I_+^-(t)e^{\Phi_I(t)} - I_-^+(t)e^{-\Phi_I(t)}\right]^2 + I^2(t)\sin^2\left[\Phi_R(t) - \varphi_-(t)\right]\right\},\\
P_{\beta\alpha}(t) &= A(t)\left\{\left[I_-^+(t)e^{\Phi_I(t)} - I_+^-(t)e^{-\Phi_I(t)}\right]^2 + I^2(t)\sin^2\left[\Phi_R(t) + \varphi_-(t)\right]\right\},\\
P_{\beta\beta}(t) &= A(t)\left\{\left[I_-^-(t)e^{\Phi_I(t)} + I_+^+(t)e^{-\Phi_I(t)}\right]^2 - I^2(t)\sin^2\left[\Phi_R(t) + \varphi_+(t)\right]\right\},
\end{aligned}
\tag{26}
$$

where we have denoted for compactness

$$
I_\varsigma^{\varsigma'}(t) = |v_\varsigma(0)v_{\varsigma'}(t)| \qquad (\varsigma,\varsigma' = \pm),
$$

$$
\varphi_\pm(t) = \frac{\varphi(0) \pm \varphi(t)}{2},
$$

$$
I^2(t) = 4I_+^+(t)I_-^-(t) = 4I_+^-(t)I_-^+(t) = \frac{\Delta_s^2}{|\varepsilon(0)\varepsilon(t)|}.
$$

Limiting cases

In the event that the conditions

$$\left|\frac{1}{\Lambda_\beta(t)}-\frac{1}{\Lambda_\alpha(t)}\right| \ll 4\varepsilon_0(t) \quad \text{and} \quad t \ll \min\left[\Lambda_\alpha(t),\Lambda_\beta(t)\right]$$

are satisfied for any $t \in [0,T]$, the formulas (26) reduce to the standard MSW adiabatic solution

$$\left.\begin{aligned} P_{\alpha\alpha}(t) = P_{\beta\beta}(t) &= \frac{1}{2}\left[1+J(t)\right] - I_0^2(t)\sin^2\left[\Phi_0(t)\right], \\ P_{\alpha\beta}(t) = P_{\beta\alpha}(t) &= \frac{1}{2}\left[1-J(t)\right] + I_0^2(t)\sin^2\left[\Phi_0(t)\right], \end{aligned}\right\} \qquad \text{(MSW)}$$

where

$$J(t) = \frac{\Delta^2 - \Delta_c\left[q_R(0)+q_R(t)\right]+q_R(0)q_R(t)}{\varepsilon_0(0)\varepsilon_0(t)},$$

$$I_0^2(t) = \frac{\Delta_s^2}{\varepsilon_0(0)\varepsilon_0(t)}, \quad \Phi_0(t) = \int_0^t \varepsilon_0(t')dt'.$$

Needless to say either of the above conditions or both may be violated for sufficiently high neutrino energies and/or for thick media, resulting in radical differences between the two solutions. These differences are of obvious interest to high-energy neutrino astrophysics.

It is perhaps even more instructive to examine the distinctions between the general adiabatic solution (26) and its "classical limit"

$$\left.\begin{aligned} P_{\alpha\alpha}(t) &= \exp\left[-\int_0^t \frac{dt'}{\Lambda_\alpha(t')}\right], \quad P_{\alpha\beta}(t) = 0, \\ P_{\beta\beta}(t) &= \exp\left[-\int_0^t \frac{dt'}{\Lambda_\beta(t')}\right], \quad P_{\beta\alpha}(t) = 0, \end{aligned}\right\} \qquad (\Delta_s = 0)$$

which takes place either in the absence of mixing or for $m_1^2 = m_2^2$.

Note:

Considering that $\Omega \propto \Delta_s$, the classical limit is the exact solution to the master equation (for $\Delta_s = 0$). Therefore it can be derived directly from Eq. (21). To make certain that the adiabatic solution has correct classical limit, the following relations are useful:

$$\lim_{\Delta_s \to 0} \varepsilon(t) = \zeta\zeta_R \left[q(t) - \Delta_c\right]$$

and

$$\lim_{\Delta_s \to 0} |v_\pm(t)|^2 = \frac{1}{2}\left(\zeta\zeta_R \pm 1\right),$$

where

$$\zeta_R = \mathsf{sign}\left[q_R(t) - \Delta_c\right].$$

5.2.8 Matter of constant density and composition

In this simple case, the adiabatic approximation becomes exact and thus free from the above-mentioned conceptual difficulties. For definiteness sake we assume $\Lambda_\alpha < \Lambda_\beta$ (and thus $q_I < 0$) from here. The opposite case can be considered in a similar way. Let's denote

$$\frac{1}{\Lambda_\pm} = \frac{1}{2}\left(\frac{1}{\Lambda_\alpha} + \frac{1}{\Lambda_\beta}\right) \pm \frac{\xi}{2}\left(\frac{1}{\Lambda_\alpha} - \frac{1}{\Lambda_\beta}\right),$$

$$I_\pm^2 = \frac{1}{4}\left(1 + \frac{\varepsilon_0^2 + q_I^2 - \Delta_s^2}{\varepsilon_R^2 + \varepsilon_I^2}\right) \pm \frac{\xi}{2}\left(\frac{\varepsilon_R^2 + q_I^2}{\varepsilon_R^2 + \varepsilon_I^2}\right),$$

$$L = \frac{\pi}{|\varepsilon_R|} \quad \text{and} \quad \xi = \left|\frac{q_R - \Delta_c}{\varepsilon_R}\right|.$$

As is easy to see,

$$I_\pm^\pm = \begin{cases} I_\pm & \text{if} \quad \text{sign}\,(q_R - \Delta_c) = +\zeta, \\ I_\mp & \text{if} \quad \text{sign}\,(q_R - \Delta_c) = -\zeta, \end{cases}$$

$$I_+^- = I_-^+ = \sqrt{I_+ I_-} = \frac{I}{2} = \left|\frac{\Delta_s}{2\varepsilon}\right| \quad \text{and} \quad \text{sign}(\varphi) = -\zeta.$$

By applying these identities the neutrino oscillation probabilities can be written as

$$P_{\alpha\alpha}(t) = \left(I_+ e^{-t/2\Lambda_+} + I_- e^{-t/2\Lambda_-}\right)^2 - I^2 e^{-t/\Lambda} \sin^2\left(\frac{\pi t}{L} + |\varphi|\right),$$

$$P_{\beta\beta}(t) = \left(I_- e^{-t/2\Lambda_+} + I_+ e^{-t/2\Lambda_-}\right)^2 - I^2 e^{-t/\Lambda} \sin^2\left(\frac{\pi t}{L} - |\varphi|\right),$$

$$P_{\alpha\beta}(t) = P_{\beta\alpha}(t) = \frac{1}{4} I^2 \left(e^{-t/2\Lambda_-} - e^{-t/2\Lambda_+}\right)^2 + I^2 e^{-t/\Lambda} \sin^2\left(\frac{\pi t}{L}\right).$$

The difference between the survival probabilities for ν_α and ν_β is

$$P_{\alpha\alpha}(t) - P_{\beta\beta}(t) = -\zeta \mathsf{Re}\left(\frac{q - \Delta_c}{\varepsilon}\right)\left(e^{-t/2\Lambda_-} - e^{-t/2\Lambda_+}\right)$$
$$+ I^2 e^{-t/\Lambda} \sin\varphi \sin\left(\frac{2\pi t}{L}\right).$$

Case $|q| \gtrsim |\Delta_s|$

Let's examine the case when Λ_+ and Λ_- are vastly different in magnitude. This will be true when $\Lambda_\beta \gg \Lambda_\alpha$ and the factor ξ is not too small. The second condition holds if q_R is away from the MSW resonance value Δ_c and the following dimensionless parameter

$$\varkappa = \frac{\Delta_s}{|q|} \approx 0.033 \times \sin 2\theta \left(\frac{\Delta m^2}{10^{-3}\ \text{eV}^2}\right)\left(\frac{100\ \text{GeV}}{E_\nu}\right)\left(\frac{V_0}{|q|}\right)$$

is sufficiently small. In fact we assume $|\varkappa| \lesssim 1$ and impose no specific restriction for the ratio q_R/q_I. This spans several possibilities:

- $\star$ small Δm^2,
- $\star$ small mixing angle,
- $\star$ high energy,
- $\star$ high matter density.

The last two possibilities are of special interest because the inequality $|\varkappa| \lesssim 1$ may be fulfilled for a wide range of the mixing parameters Δm^2 and θ by changing E_ν and/or ρ. In other words, this condition is by no means artificial or too restrictive.

After elementary while a bit tedious calculations we obtain

$$\xi = 1 - \frac{1}{2}\varkappa^2 + \mathcal{O}\left(\varkappa^3\right), \quad I^2 = \varkappa^2 + \mathcal{O}\left(\varkappa^3\right),$$

$$I_+ = 1 + \mathcal{O}\left(\varkappa^2\right), \quad I_- = \frac{1}{4}\varkappa^2 + \mathcal{O}\left(\varkappa^3\right);$$

$$\Lambda \approx 2\Lambda_\alpha,$$
$$\Lambda_+ \approx \left(1 + \frac{\varkappa^2}{4}\right)\Lambda_\alpha \approx \Lambda_\alpha,$$
$$\Lambda_- \approx \left(\frac{4}{\varkappa^2}\right)\Lambda_\alpha \gg \Lambda_\alpha.$$

Due to the wide spread among the length/time scales $\Lambda_\pm$, Λ and L as well as among the amplitudes $I_\pm$ and I, the regimes of neutrino oscillations are quite diverse for different ranges of variable t.

With reference to Figs. 9–12, one can see a regular gradation from slow (at $t \lesssim \Lambda_\mu$) to very fast (at $t \gtrsim \Lambda_\mu$) neutrino oscillations followed by the asymptotic nonoscillatory behavior:

$$P_{\mu\mu}(t) \simeq \frac{\varkappa^4}{16} e^{-t/\Lambda_-},$$
$$P_{ss}(t) \simeq e^{-t/\Lambda_-},$$
$$P_{\mu s}(t) = P_{s\mu}(t) \simeq \frac{\varkappa^2}{4} e^{-t/\Lambda_-}.$$

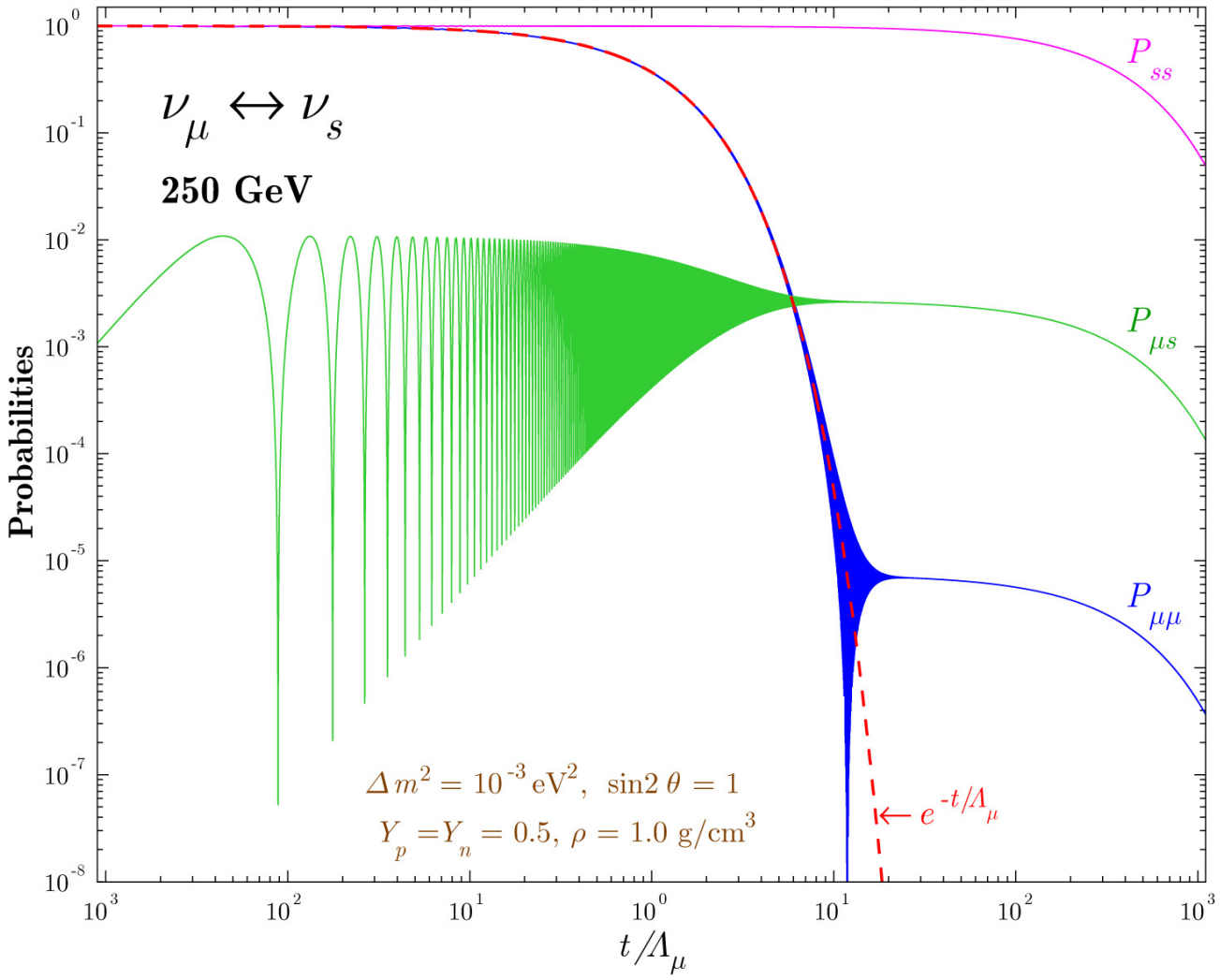

Figure 9: Survival and transition probabilities for $\nu_\mu \leftrightarrow \nu_s$ oscillations ($E_\nu = 250$ GeV, $\rho = 1$ g/cm^3).

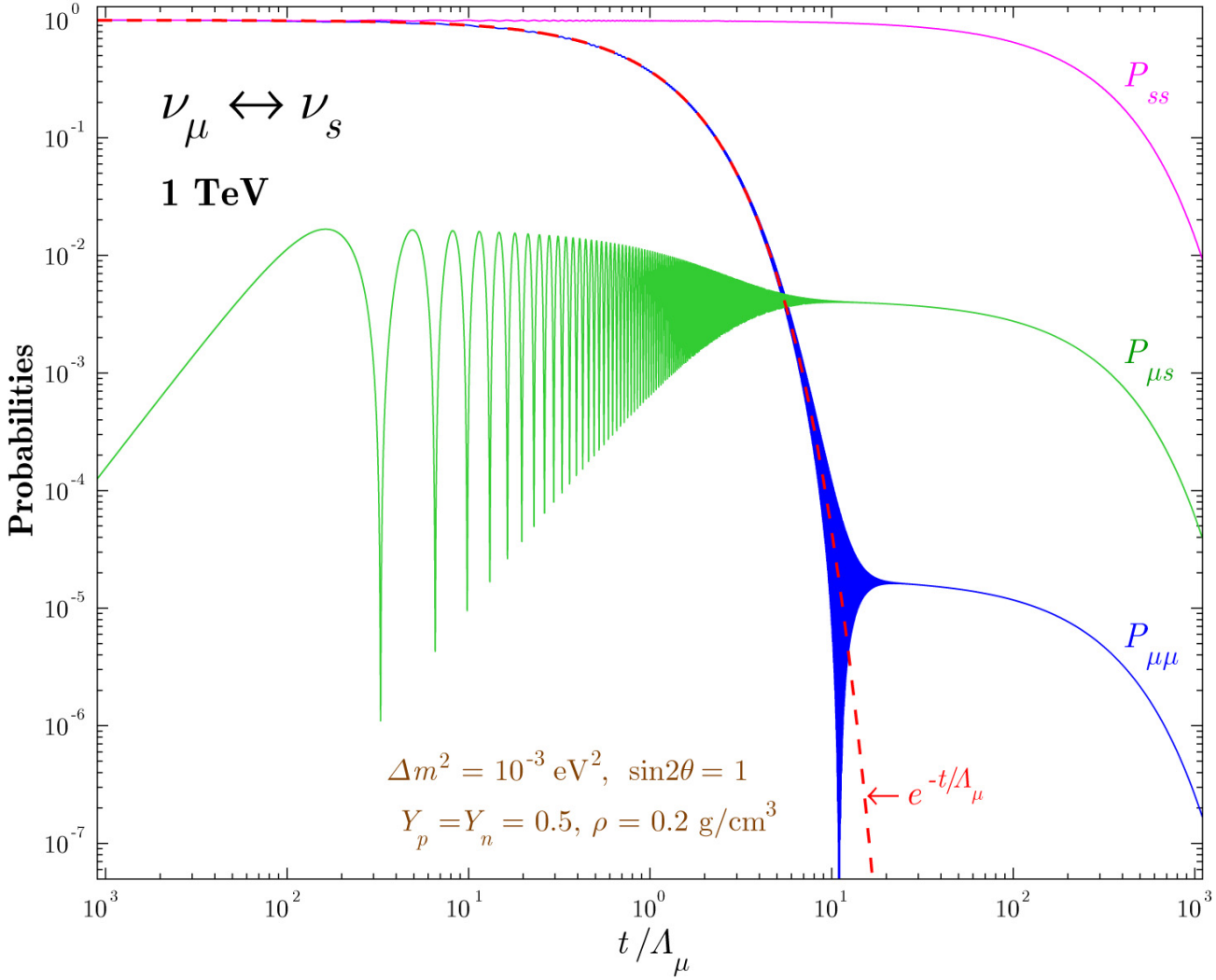

Figure 10: Survival and transition probabilities for $\nu_\mu \leftrightarrow \nu_s$ oscillations ($E_\nu = 1000$ GeV, $\rho = 0.2$ g/cm^3).

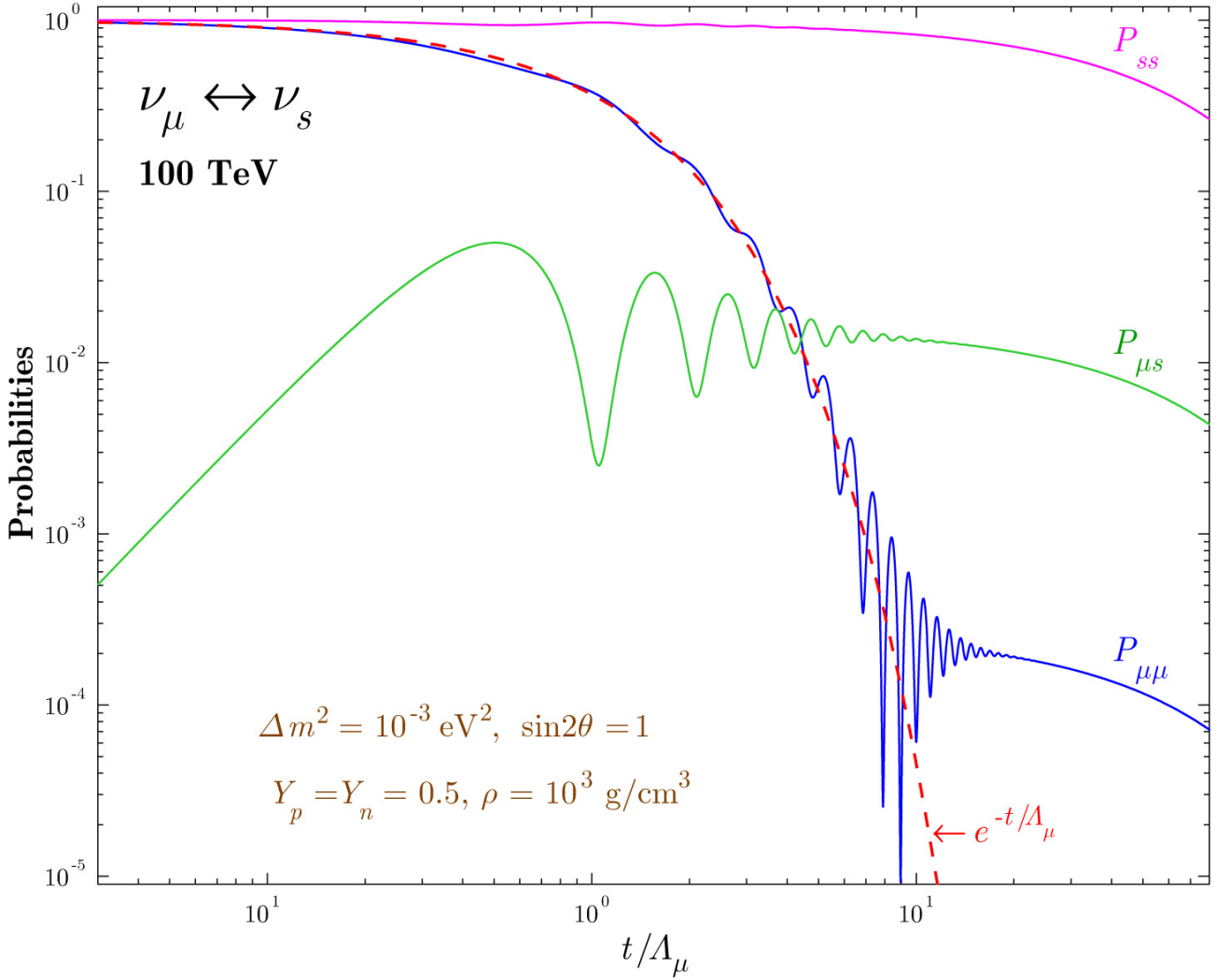

Figure 11: Survival and transition probabilities for $\nu_\mu \leftrightarrow \nu_s$ oscillations ($E_\nu = 100$ TeV, $\rho = 10^{-3}$ g/cm^3).

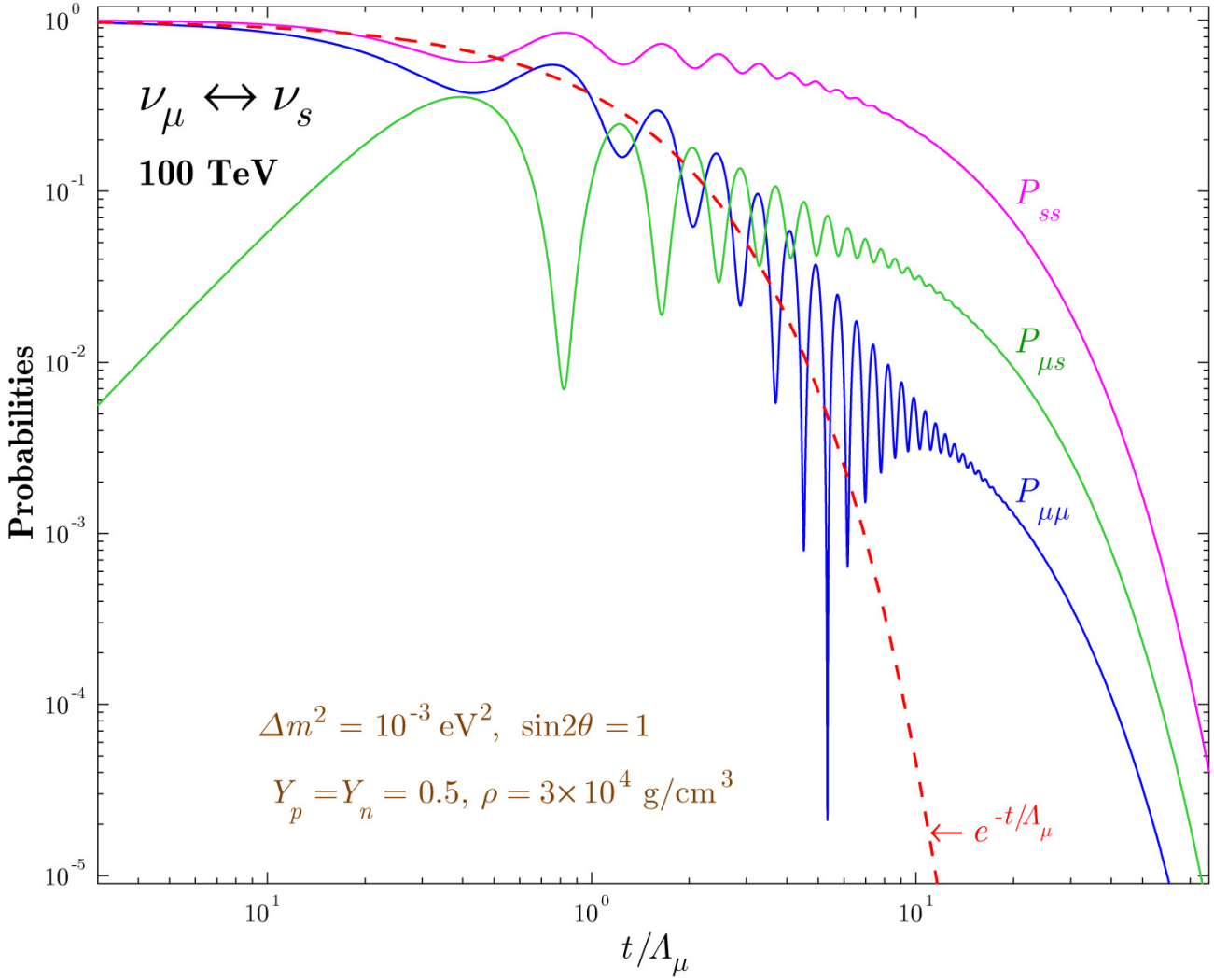

Figure 12: Survival and transition probabilities for $\nu_\mu \leftrightarrow \nu_s$ oscillations ($E_\nu = 100$ TeV, $\rho = 3 \times 10^{-4}$ g/cm^3).

Degenerate case

The consideration must be completed for the case of degeneracy. Due to the condition $q_I < 0$, the density and composition of the "degenerate environment" are fine-tuned in such a way that

$$q = q_{-\zeta} = \Delta_c - i\,|\Delta_s|.$$

The simplest way is in coming back to the master equation. Indeed, in the limit of $q = q_{-\zeta}$, the Hamiltonian reduces to

$$\mathbf{H} = |\Delta_s| \begin{pmatrix} -i & \zeta \\ \zeta & i \end{pmatrix} \equiv |\Delta_s|\,\mathbf{h}_\zeta.$$

Considering that $\mathbf{h}_\zeta^2 = \mathbf{0}$, we promptly arrive at the solution of ME:

$$\widetilde{\mathbf{S}}(t) = \mathbf{1} - it\,|\Delta_s|\,\mathbf{h}_\zeta$$

and thus

$$\begin{aligned} P_{\alpha\alpha}(t) &= (1 - |\Delta_s|\,t)^2\, e^{-t/\Lambda}, \\ P_{\beta\beta}(t) &= (1 + |\Delta_s|\,t)^2\, e^{-t/\Lambda}, \\ P_{\alpha\beta}(t) &= P_{\beta\alpha}(t) = (\Delta_s t)^2\, e^{-t/\Lambda}. \end{aligned}$$

Since $1/\Lambda_\beta = 1/\Lambda_\alpha - 4\,|\Delta_s|$, the necessary condition for the total degeneration is

$$4\Lambda_\alpha\,|\Delta_s| \leq 1$$

and thus

$$1/\Lambda = 1/\Lambda_\alpha - 2\,|\Delta_s| \geq 2\,|\Delta_s|.$$

The equality only occurs when ν_β is sterile.

The degenerate solution must be compared with the standard MSW solution

$$\left.\begin{aligned} P_{\alpha\alpha}(t) = P_{ss}(t) &= \frac{1}{2}\,[1+\cos\,(2\Delta_s t)], \\ P_{\alpha s}(t) = P_{s\alpha}(t) &= \frac{1}{2}\,[1-\cos\,(2\Delta_s t)], \end{aligned}\right\} \qquad \text{(MSW)}$$

and with the classical penetration coefficient

$$\exp\,(-t/\Lambda_\alpha)$$

(with $1/\Lambda_\alpha$ numerically equal to $4\,|\Delta_s|$) relevant to the transport of unmixed active neutrinos through the same environment.

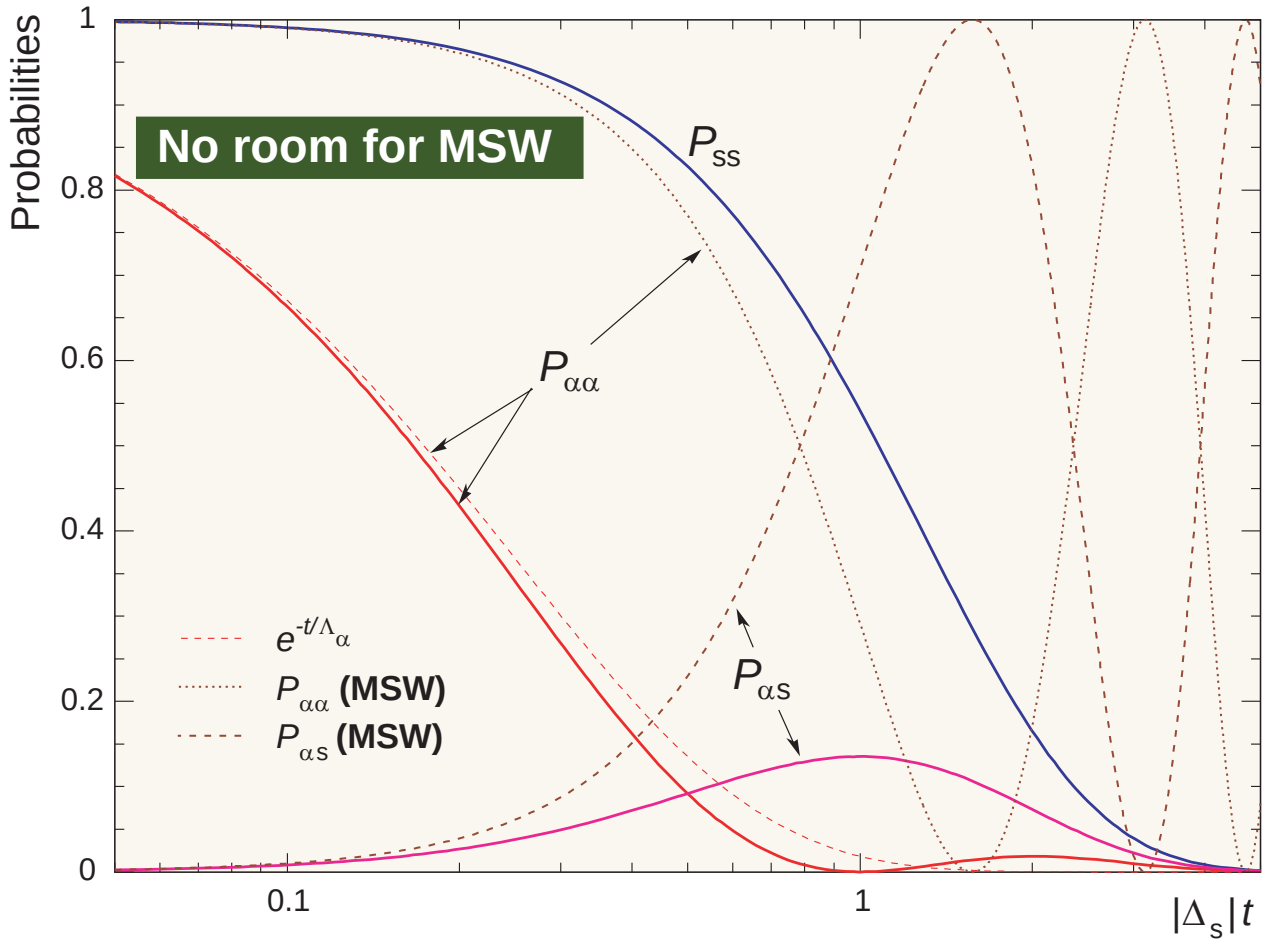

Figure 13: Survival and transition probabilities for $\nu_\alpha \leftrightarrow \nu_s$ oscillations in the case of degeneracy ($q = q_{-\zeta}$). The standard MSW probabilities (dotted and dash-dotted curves) together with the penetration coefficient for unmixed ν_α (dashed curve) are also shown.

5.2.9 Conclusions

We have considered, on the basis of the MSW evolution equation with complex indices of refraction, the conjoint effects of neutrino mixing, refraction and absorption on high-energy neutrino propagation through matter. The adiabatic solution with correct asymptotics in the standard MSW and classical limits has been derived. In the general case the adiabatic behavior is very different from the conventional limiting cases.

A noteworthy example is given by the active-to-sterile neutrino mixing. It has been demonstrated that, under proper conditions, the survival probability of active neutrinos propagating through a very thick medium of constant density may become many orders of magnitude larger than it would be in the absence of mixing. The quantitative characteristics of this phenomenon are highly responsive to changes in density and composition of the medium as well as to neutrino energy and mixing parameters.

Considering a great variety of latent astrophysical sources of high-energy neutrinos, the effect may open a new window for observational neutrino astrophysics.

Part II

SOLAR NEUTRINOS

6 The pp fusion step by step

The evidence is strong that the overall fusion reaction is "burning" hydrogen to make helium:

$$4\ {}^{1}\mathrm{H} + 2\ e^{-} \rightarrow\ {}^{4}\mathrm{He} + 2\ \nu_e + 6\ \gamma.$$

In this reaction, the final particles have less internal energy than the starting particles. Since energy is conserved, the extra energy is released as

- ⋆ energy of motion of the nuclei and electrons in the solar gas,
- ⋆ the production of lots of low energy photons and, finally,
- ⋆ the energy of the neutrinos, which easily shoot out of the Sun.

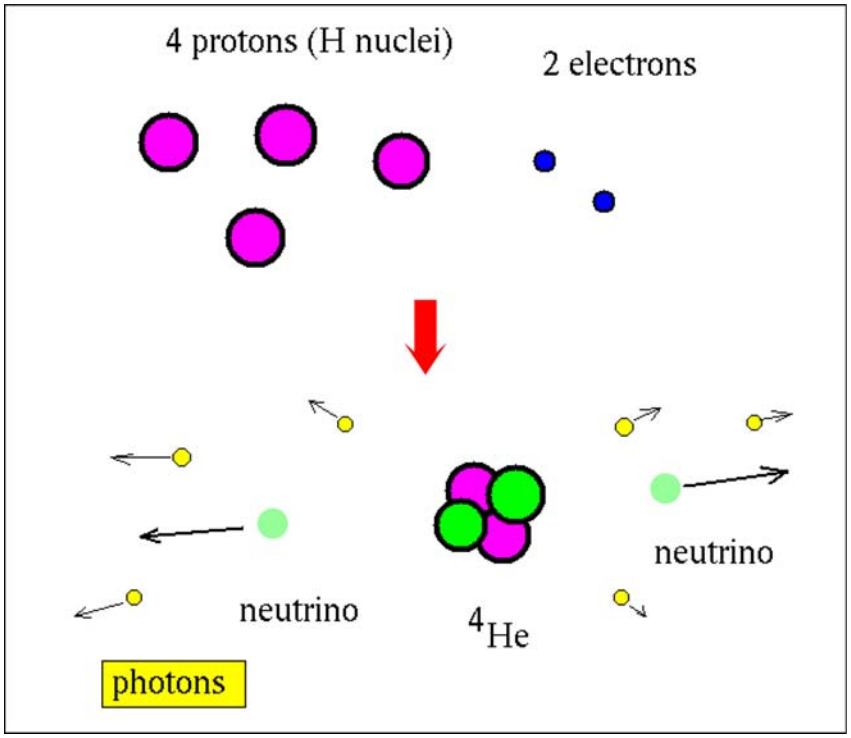

That is the gas gets hotter and has lots of photons (and neutrinos). The energy release in this reaction is $\Delta E = (4 \times 1.007825u - 4.002603u) \times 931\ \mathrm{MeV}/u = 26.7\ \mathrm{MeV}$ each time the reaction happens.

The fusion reaction as given above is a summary. Really it may only occur in several steps since the temperature in the Sun is too low and, as a result,

---

an inelastic collision of *two* nuclei in the Sun is *nearly impossible*.

The two nuclei have to get within $r_p \sim 10^{-13}$ cm for the strong interactions to hold them together but they repel each other. For example, the potential energy for Coulomb interaction of two protons is

$$U_{\text{Coulomb}} = \frac{e^2}{r_p} \approx 2 \times 10^{-6} \text{ erg} \approx 1.2 \text{ MeV}.$$

Since $T_\odot \lesssim 1.5 \times 10^7$ K (the helioseismology confirms this!)

$$\langle E_p^{\text{kin}} \rangle = \frac{3}{2} k T_\odot \lesssim 2 \text{ keV}.$$

Assuming Maxwellian distribution, the fraction of protons with $E_p^{\text{kin}} > U_{\text{Coulomb}}$ is

$$\exp\left(-E_p^{\text{kin}} / \langle E_p^{\text{kin}} \rangle\right) < e^{-600} \sim 10^{-260}.$$

Considering that the number of protons in the Sun is about 10^{57} we can conclude that

the classical probability of the fusion is ZERO.

Let's estimate the quantum probability. The nucleus wave function can be written

$$\psi \propto \exp\left(i\int p dx\right).$$

$$E_p^{\text{kin}} = \frac{p^2}{2m} = E_0 - U; \qquad \Rightarrow \qquad p = \sqrt{2m\left(E_0 - U\right)}$$

The repulsion energy of two nuclei with charges $Z_1 e$ and $Z_2 e$ is $U = Z_1 Z_2 e^2/r$ and the classical turning point ($p = 0$) is given by

$$r_1 = Z_1 Z_2 e^2/E_0.$$

In quantum theory

$$p = i\sqrt{2m\left(U - E_0\right)} \quad \text{for} \quad r < r_1$$

and thus the probability of the barrier penetration (tunnel effect) can be estimated as

$$\psi^2(r) \propto \exp\left[-2\int_r^{r_1} \sqrt{2m\left[U(r') - E_0\right]}\, dr'\right].$$

where $r \sim r_p$ is the radius of nuclear interaction. It is assumed here that one of the nuclei is in rest ($m_2 = \infty$). To take into account its finite mass one have to replace m with the effective dynamic mass of the colliding particles:

$$m \longmapsto M = \frac{m_1 m_2}{m_1 + m_2} = \frac{A_1 A_2}{A_1 + A_2} m_p = A m_p.$$

Considering that usually $r_p \ll r_1$, for rough estimation we can put $r = 0$. Than the barrier penetration probability is given by

$$\psi^2(r) \approx \psi^2(0) = e^{-\phi},$$

where ($\hbar = c = 1 \Longrightarrow e^2/\hbar c = \alpha$)

$$\phi = 2r_1\sqrt{2ME_0}\int_0^1 \sqrt{1/x - 1}\; dx = \pi r_1\sqrt{2ME_0} = \pi Z_1 Z_2 \alpha\sqrt{2M/E_0}.$$

In thermal equilibrium with the temperature T the number of particles with energy E_0 is proportional to $exp\,(-E_0/kT)$. Therefore the full probability is proportional to

$$\int e^{-\chi(E_0)} dE_0, \quad \text{where} \quad \chi = \sqrt{\frac{E_1}{E_0}} + \frac{E_0}{kT} \quad \text{and} \quad E_1 = 2\pi^2 Z_1^2 Z_2^2 \alpha^2 M.$$

The integral can be evaluated by using the saddle-point technique considering that the function χ has a sharp minimum (and thus $e^{-\chi}$ has a sharp maximum, – *Gamov's peak*). The minimum is given by

$$\frac{d\chi}{dE_0} = -\frac{1}{2E_0}\sqrt{\frac{E_1}{E_0}} + \frac{1}{kT} = 0.$$

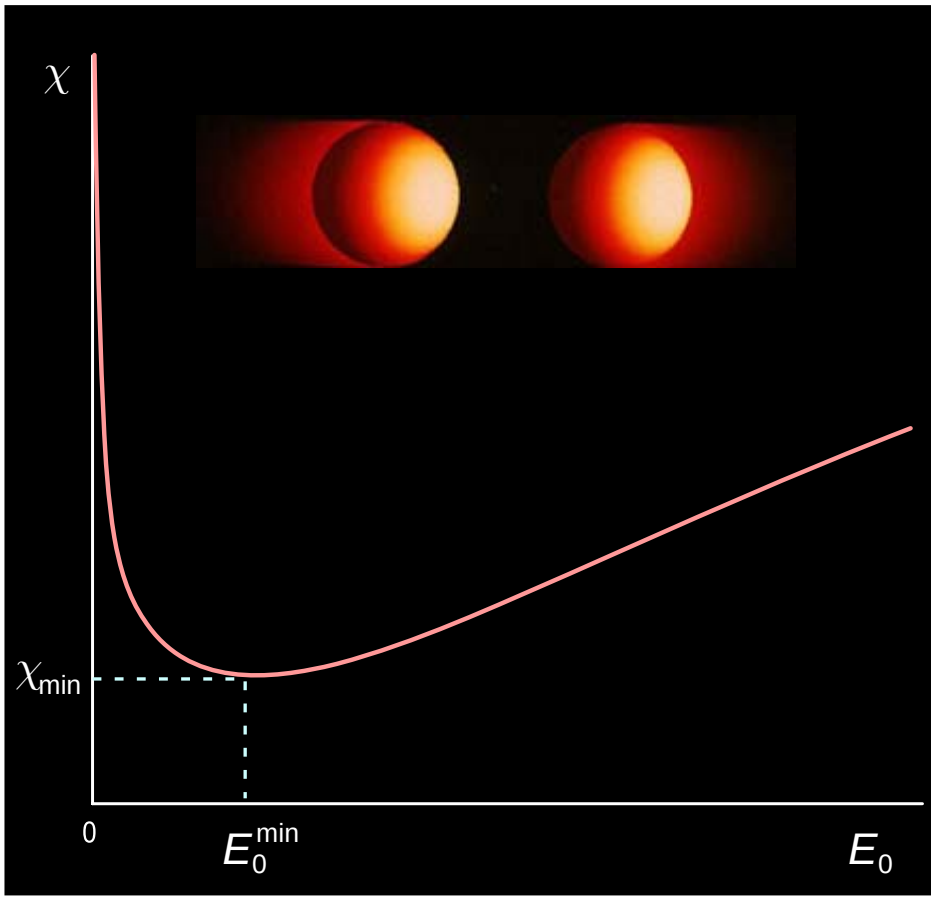

The Gamov's peak is given by

$$E_0^{\min} = E_1^{1/3} \left(kT/2\right)^{2/3}$$
$$\simeq 0.122 \left(A Z_1^2 Z_2^2 T_9^2\right)^{1/3} \text{ MeV},$$
$$\chi_{\min} = 3 \left(\frac{E_1}{4kT}\right)^{1/3}$$
$$\simeq 4.25 \left(\frac{A Z_1^2 Z_2^2}{T_9}\right)^{1/3},$$

where $T_9 = T/(10^9 \text{ K})$. Now one can approximate $\chi(E_0)$ by

$$\chi(E_0) \simeq \chi_{\min} + \kappa \left(1 - E_0/E_0^{\min}\right)^2,$$
$$\kappa = (3/8) \left(2E_1/kT\right)^{1/3}.$$

Finally, the full probability is estimated by $C(T) \exp\left[-\chi_{\min}(T)\right]$. In particular, for the pp fusion in the center of the Sun ($T_9 \simeq 0.015$)

$$E_0^{\min} \simeq 5.9 \text{ keV}, \quad \chi_{\min} \simeq 13.7, \quad \exp\left(-\chi_{\min}\right) \simeq 1.15 \times 10^{-6}.$$

6.1 The pp I branch

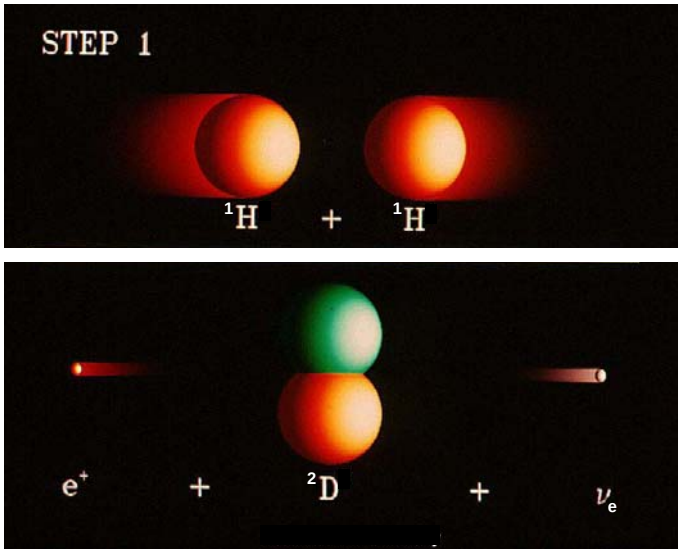

Note: the secondary positron very quickly encounters a free electron in the Sun and both particles annihilate, their mass energy appearing as two 511 KeV γs: $e^+e^- \rightarrow \gamma\gamma$.

The energy liberation in this reaction is $Q = 1.442$ MeV, including ~ 250 keV taking away by neutrinos ($E_\nu \leq 420$ keV). The number of deuterium nuclei generated in 1 cm^3 per 1 sec is

$$\frac{d[\mathrm{D}]}{dt} = C_D \frac{n_p^2}{N_A T_9^{2/3}} \exp\left(-\frac{3.38}{T_9^{1/3}}\right),$$

$$C_\mathrm{D} \approx 2.1 \times 10^{-15}\ \mathrm{cm}^{-3}\mathrm{s}^{-1}.$$

By introducing the weight concentrations for the chemical elements

$$X(i) = \frac{m_\mathrm{H} n_i A_i}{\rho} = \frac{n_i A_i}{N_A \rho},$$

we can write the reaction rate:

$$\dot{X}(\mathrm{D}) = C_1 \rho \left[X(\mathrm{H})\right]^2 T_9^{-2/3} e^{-3.38/T_9^{1/3}}$$

$$(C_1 \approx 2.1 \times 10^{-15}\ \mathrm{s}^{-1}).$$

The characteristic time is $\tau_1 \approx 1.3 \times 10^{10}$ yr at $\rho = 100$ g/cm^3 and $T = 1.3 \times 10^7$ K. The reaction is very rare. That's why the Sun is still burning after $\sim 4.6 \times 10^9$ years!

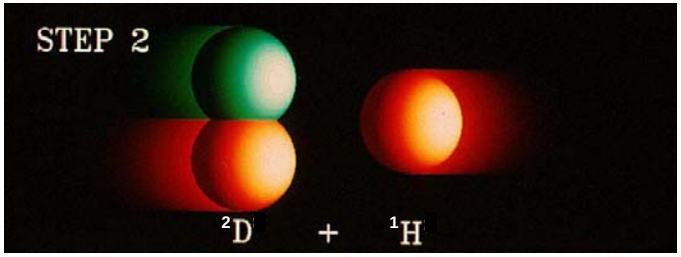

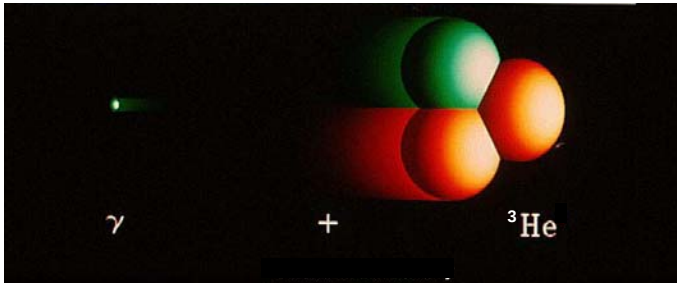

The energy liberation: $Q = 5.493$ MeV;
the reaction rate:

$$\dot{X}(^3\mathrm{He}) = C_2 \rho X(^1\mathrm{H}) X(^2\mathrm{D}) T_9^{-2/3} e^{-3.72/T_9^{1/3}},$$

$$C_2 \approx 3.98 \times 10^3 \ \mathrm{s}^{-1} \approx 2 \times 10^{18} C_1,$$

and $\tau_2 \approx 6$ s.

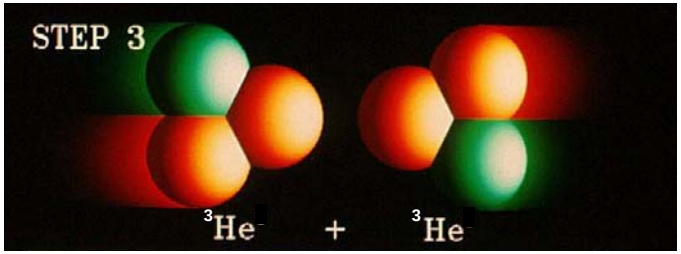

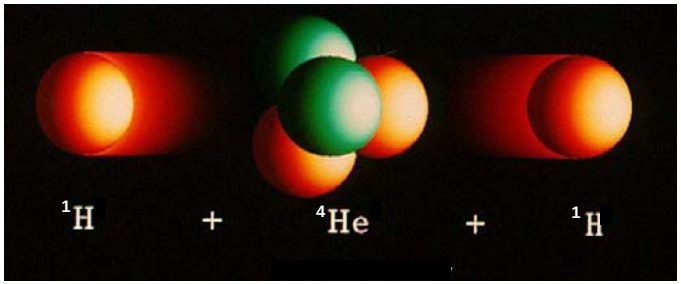

The energy liberation: $Q = 12.859$ MeV;
the reaction rate:

$$\dot{X}(^4\mathrm{He}) = C_3 \rho \left[X(^3\mathrm{He})\right]^2 T_9^{-2/3} e^{-12.28/T_9^{1/3}},$$

$$C_3 \approx 1.3 \times 10^{10} \ \mathrm{s}^{-1} \approx 6 \times 10^6 C_2,$$

and $\tau_3 \approx 10^6$ yr.

Even at temperatures in the Sun's core, 1.5×10^7 K, the average lifetime of a proton against pp fusion is about $\sim 10^{10}$ yr. It is an extremely slow reaction, and it is this time scale that sets the stellar clock, so to speak, by determining how long the star will remain a stable main sequence object.

In contrast, the deuteron created will only last about a few seconds before it hits into another proton and fusion creates a ^{3}He nucleus. Therefore it cannot accrue and its stationary concentration is given by $X(\mathrm{D}) = (\tau_2/\tau_1)X(\mathrm{H}) \approx 10^{-17}X(\mathrm{H})$. The ^{3}He nucleus will last about 250,000 years before it hits another ^{3}He nucleus hard enough for the two to stick together.

6.2 The pep fusion

The deuterium can also be produced in the reaction

$$^1\mathrm{H} + ^1\mathrm{H} + e^- \rightarrow ^2\mathrm{D} + \nu_e \quad (E_\nu = 1.44 \text{ MeV})$$

which has a characteristic time scale $\sim 10^{12}$ yr that is rather larger than the age of the Universe at this time. So it is *insignificant* in the Sun as far as energy generation is concerned. Nevertheless, the pep fusion accounts for about 0.25% of the deuterons created in the pp chain.

Enough pep fusions happen to produce a detectable number of neutrinos, so the reaction must be accounted for by those interested in the *solar neutrino problem*.

6.3 The pp II branch

The ^{3}He does not always have to hit another ^{3}He nucleus. It could hit a ^{4}He forming stable ^{7}Be. But ^{7}Be has an affinity for electron capture, and can absorb free electrons. The electron turns one of the Be protons into a neutron, changing the ^{7}Be into ^{7}Li, while tossing out a neutrino. The ^{7}Li will then quickly fuse with a free proton, resulting in unstable ^{8}Be which immediately falls apart into two stable ^{4}He nuclei.

$^3\text{He}+^4\text{He} \rightarrow {}^7\text{Be}+\gamma$	$+1.586$ MeV	$(9.7\times10^5$ yr)
$^7\text{Be}+e^- \rightarrow {}^7\text{Li}(+\gamma)+\nu_e$	$+862/384$ keV	(142 d)
$^7\text{Li}+^1\text{H} \rightarrow {}^4\text{He}+{}^4\text{He}$	$+17.347$ MeV	(9.5 min)

$\sim 14\,\%$ of ^{3}He goes out this way avoiding the pp I chain,

$\sim 99.89\,\%$ of ^{7}Be goes the ^{7}Li route.

$\sim 90\%$ of ^{7}Li nuclei are in the ground state and thus $E_\nu = 862$ keV; the rest lithium is created in an excited state and $E_\nu = 384$ keV.

Note: Fusion with ^{4}He is less likely, because there is more ^{3}He around deep inside the stellar core. But in heavier stars, where the temperatures exceed about 2.4×10^7 K, the pp II chain can rival the pp I chain for energy production inside the star. This is because at higher temperatures the ^{3}He gets used up faster, driving down its abundance compared to ^{4}He.

6.4 The pp III branch

The ^{7}Be has two ways to go – it can either absorb an electron, as in pp II (99.89%), or absorb a proton, as in pp III (0.11%). Absorbing a proton raises the nucleus from beryllium to boron, and the ^{7}Be becomes ^{8}B. But ^{8}B is unstable and takes < 1 second, fairly independent of temperature, to spit out a positron and a neutrino to become beryllium again, only this time it's ^{8}Be. But ^{8}Be falls apart in a hurry into two ^{4}He nuclei, and once again we have turned hydrogen into helium.

$^7\text{Be} + ^1\text{H} \rightarrow ^8\text{B} + \gamma$	$+135$ keV	$(66$ years$)$
$^8\text{B} \rightarrow ^8\text{Be} + e^+ + \nu_e$	≤ 14.06 MeV	$(0.9$ sec$)$
$^8\text{Be} \rightarrow ^4\text{He} + ^4\text{He}$	$+18.074$ MeV	$(9.7 \times 10^{-17}$ sec$)$

$\sim 0.11\,\%$ of ^{7}Be goes this route.

Of course, $e^+e^- \rightarrow \gamma\gamma$.

Note: In low mass stars the internal temperature is not high enough to finish the pp cycle. They produce the first stage of pp fusion up to ^{3}He, but are unable to force the last stage of ^{3}He fusion, either with another ^{3}He or an ^{4}He. So they fuse hydrogen into ^{3}He instead of ^{4}He. This fact is confirmed by the observation that low mass stars are often anomalously rich in ^{3}He compared to ^{4}He.

6.5 The pp IV branch (hep reaction)

The low-energy cross section for the "hep reaction"

$$^3\mathrm{He} + {}^1\mathrm{H} \rightarrow {}^4\mathrm{He} + e^+ + \nu_e$$

is uncertain. While the probability of the pp IV branch is estimated to be about $3 \times 10^{-5}\%$, the hep produces highest-energy solar neutrinos,

$$E_\nu \leq 18.77 \text{ MeV},$$

which can at some level influence the electron energy spectrum produced by solar neutrino interactions and measured in the high-threshold detectors like Super-Kamiokande and SNO.

6.6 The full pp chain

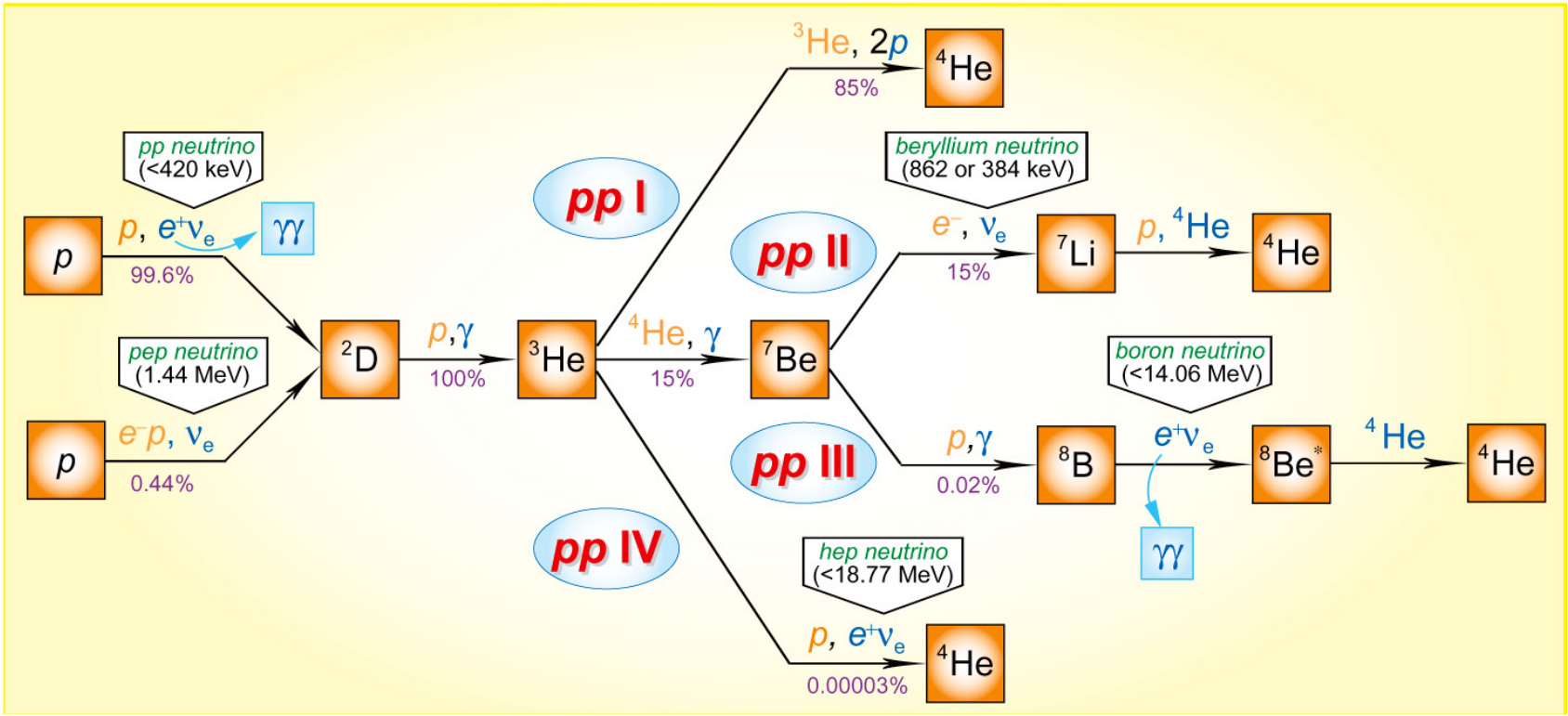

The diagram shows the full pp chain responsible for production of about 98.4% of the solar energy. The neutrinos export 3%, 4%, and 28% of the energy in pp I, pp II, pp III, respectively. All four pp chains are active simultaneously in a H-burning star containing significant ^{4}He. The details depend on density, temperature and composition but in the SUN the pp I dominates.

7 An excursus: the elemental abundance in the Sun

The matter that formed the Sun had already been cycled through one or more generations of stars. We can see elements up to and beyond ^{56}Fe in the heliosphere.

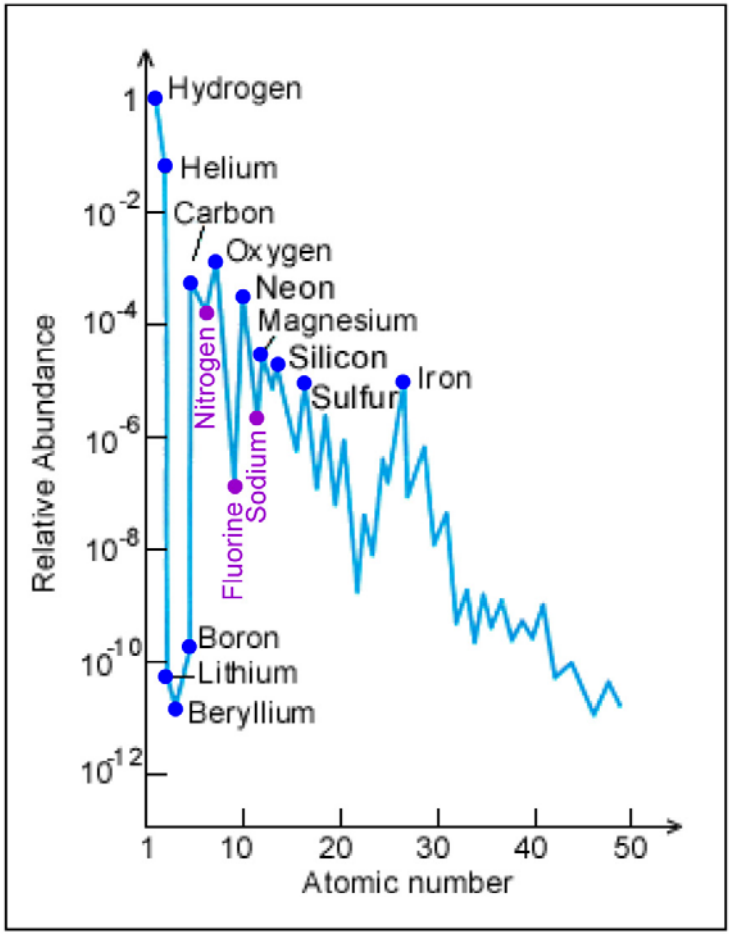

ELEMENTAL ABUNDANCE IN THE SUN

Element	% by mass	% by number
Hydrogen	73.4	92.0
Helium	25.0	7.8
Oxygen	0.80	0.06
Carbon	0.20	0.02
Neon	0.16	0.01
Iron	0.14	0.003
Nitrogen	0.09	0.008
Silicon	0.09	0.004
Magnesium	0.06	0.003
Sulfur	0.05	0.002

The current solar abundance curve is shown in the figure (the ordinate compares all elements to Hydrogen) and the relative abundances of the elements (by mass and by number) are shown in the table.

Comments:

1. The general trend is towards ever decreasing abundances as the atomic number increases.
2. There is a distinct zig-zag (up-down) pattern to the whole curve. For example,
   - between Carbon and Oxygen there is a decrease (the element is Nitrogen);
   - between Neon and Magnesium the decrease element is Sodium;
   - the largest drop is between Oxygen and Neon, the element that thus decreases notably is Fluorine.

   The reason for this fluctuating pattern is just this: elements with *odd* numbers of nucleons are less stable, resulting in one unpaired (odd) proton or neutron – those that pair these particles result in offsetting spins in opposite directions that enhance stability.
3. There is a huge drop in abundance for the Lithium-Beryllium-Boron triplet. This results from two factors:
   - at the Big Bang, nuclear processes that could fuse the proper H or He isotopes into Li and/or the other two were statistically very rare and hence inefficient, and
   - some of the Li-Be-B that formed and survived may be destroyed in processes with stars.

8 The CNO cycle

The presence of the "impurities" in the solar core opens the door to another fusion reaction. The most important (after the pp) is the CNO bi-cycle, which is responsible for as much as 1.6% of the Sun's total output. The main CNO reactions ("cycle I") are

$^{12}\mathrm{C}+^{1}\mathrm{H} \rightarrow {}^{13}\mathrm{N}+\gamma$	$+1.944$ MeV	$(1.3\times10^{7}$ years$)$
$^{13}\mathrm{N}\rightarrow {}^{13}\mathrm{C}+e^{+}+\nu_e$	$+2.221$ MeV	$(7$ min$)$
$^{13}\mathrm{C}+^{1}\mathrm{H} \rightarrow {}^{14}\mathrm{N}+\gamma$	$+7.550$ MeV	$(2.7\times10^{6}$ years$)$
$^{14}\mathrm{N}+^{1}\mathrm{H} \rightarrow {}^{15}\mathrm{O}+\gamma$	$+7.293$ MeV	$(3.2\times10^{8}$ years$)$
$^{15}\mathrm{O}\rightarrow {}^{15}\mathrm{N}+e^{+}+\nu_e$	$+2.761$ MeV	$(82$ sec$)$
$^{15}\mathrm{N}+^{1}\mathrm{H} \rightarrow {}^{12}\mathrm{C}+{}^{4}\mathrm{He}$	$+4.965$ MeV	$(1.1\times10^{5}$ years$)$

- The cycle uses carbon, nitrogen, and oxygen as catalysts to suck up four protons and build a ^{4}He nucleus out of them. The relative abundances of C, N, and O do not change.
- The cycle does not start until the pp fusion has begun, and provides the energy necessary to allow a low level of proton fusions onto the heavier nuclei.
- The cycle timescale is determined by the slowest reaction ($^{14}\mathrm{N}+{}^{1}\mathrm{H}$) while the approach to equilibrium is determined by the second slowest reaction ($^{12}\mathrm{C}+{}^{1}\mathrm{H}$).

The second minor branch ("cycle II") is a similar type of cycle, and it joins onto the first. Starting with ^{14}N, the process steps through two of the last-three reactions given above until ^{15}N is produced. It then proceeds as follows to convert ^{15}N back into ^{14}N, with the production of ^{17}F (fluorine-17) occurring in one of the steps:

$^{15}\mathrm{N} + {}^{1}\mathrm{H} \rightarrow {}^{16}\mathrm{O} + \gamma$	$+12.126$ MeV
$^{16}\mathrm{O} + {}^{1}\mathrm{H} \rightarrow {}^{17}\mathrm{F} + \gamma$	$+0.601$ MeV
$^{17}\mathrm{F} \rightarrow {}^{17}\mathrm{O} + e^{+} + \nu_e$	$+2.726$ MeV
$^{17}\mathrm{O} + {}^{1}\mathrm{H} \rightarrow {}^{14}\mathrm{N} + {}^{4}\mathrm{He}$	$+1.193$ MeV

The latter cycle is much less frequent, with the first reaction having a probability of about 4×10^{-4} relative to the last reaction of the cycle I.

The fractions of the nuclear energy loss from the core through neutrino emission in the first and second branches of the CNO process are 6% and 4%, respectively.

Note: The CNO cycle lacks significance at the low temperatures in the Sun. For abundances characteristic of the Sun, the CNO process becomes important for core temperatures of roughly 1.5×10^7 K (1.3 keV), and it provides virtually all of the conversion of hydrogen into helium in the later stages of the solar lifetime when the temperature exceed 2.5×10^7 K (2.2 keV).

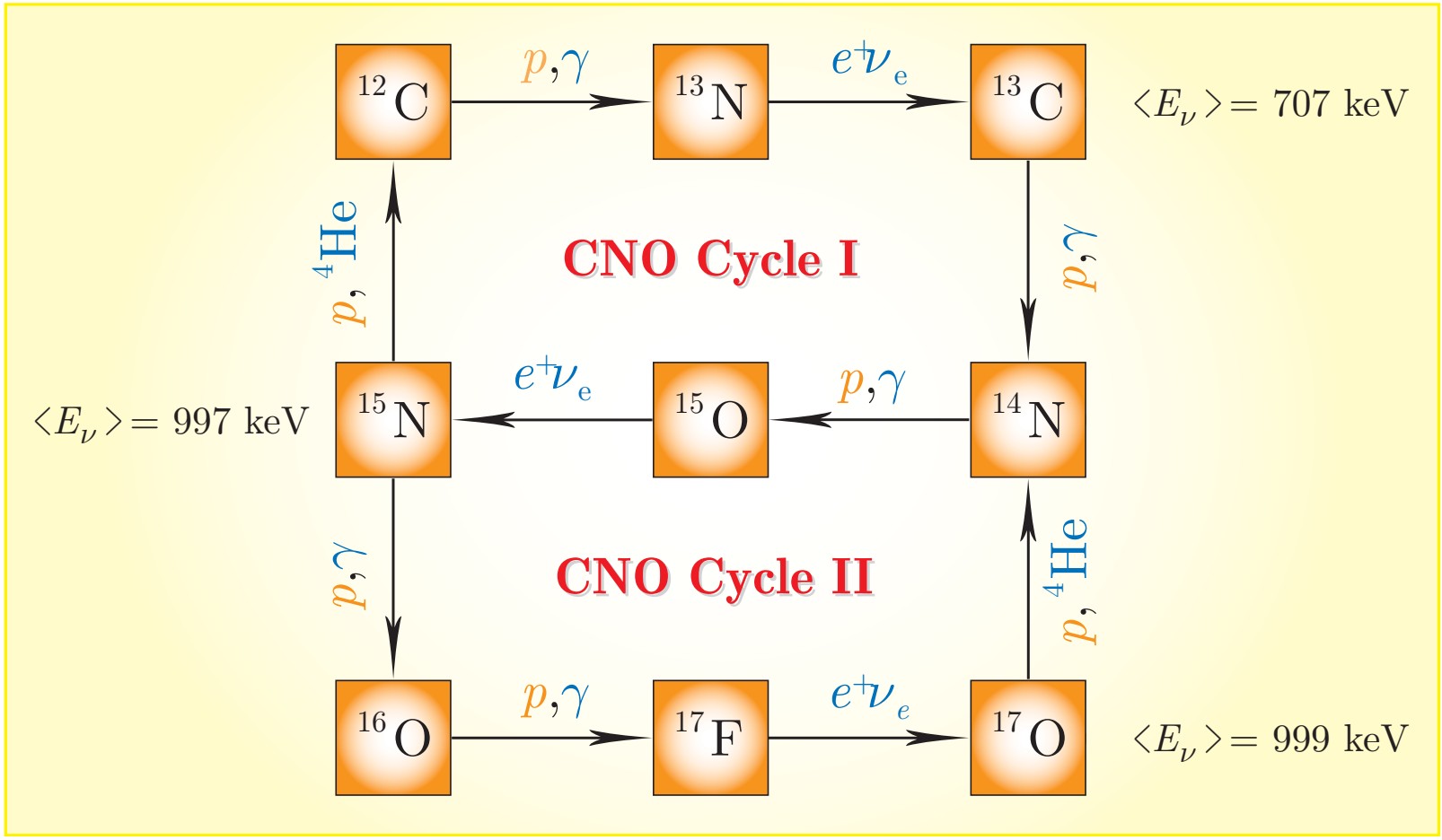

The diagram of the full CNO bi-cycle responsible for production of about 1.5-1.6% of the solar energy. The cycle I dominates.

Note: The CNO cycles III and IV are essential for the hydrogen burning in massive stars. The full net includes ^{18}F, ^{18}O, and ^{19}F.

9 Solar neutrino spectrum

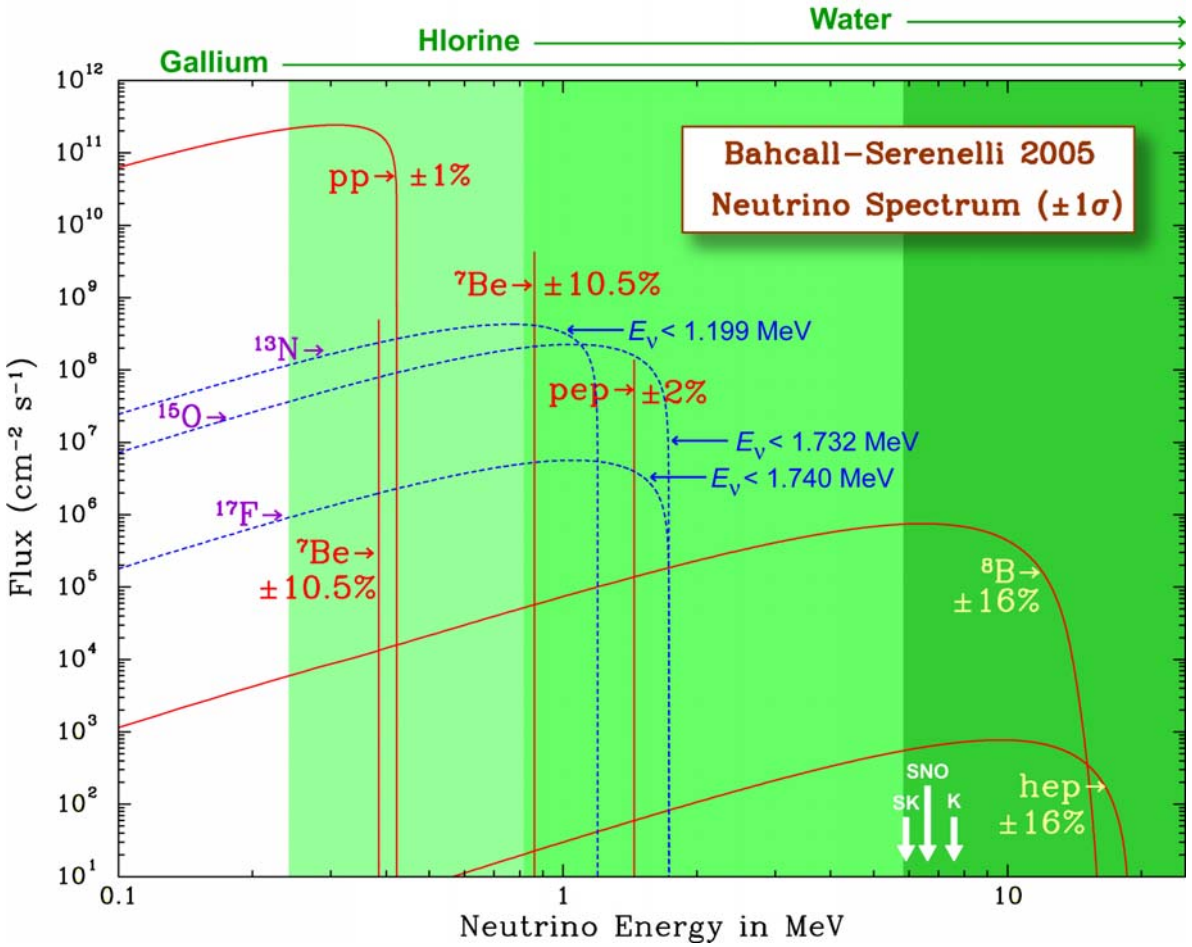

Solar neutrino energy spectrum at Earth calculated in the Bahcall-Serenelli solar model "BS05(OP)".
Also shown the uncertainties of the neutrino flux calculation (on the $1\ \sigma$ level) and the threshold neutrino energies for the gallium, chlorine and water detectors.

[From J. N. Bahcall, A. M. Serenelli, and S. Basu, "New solar opacities, abundances, helioseismology, and neutrino fluxes," Astrophys. J. **621** (2005) L85–L88 (astro-ph/0412440).]

Comparison between the "Standard Solar Models" of Bahcall & Pinsonneult (1995) [BP95] and of Dar & Shaviv (1996) [DS96].[a]

Parameter/Effect	**BSP98**	**DS96**
$M_\odot$	1.9899×10^{33} g	1.9899×10^{33} g
$L_\odot$	3.844×10^{33} erg s^{-1}	3.844×10^{33} erg s^{-1}
$R_\odot$	6.9599×10^{10} cm	6.9599×10^{10} cm
$t_\odot$	4.566×10^{9} yr	4.57×10^{9} yr
Rotation	Not Included	Not Included
Magnetic Field	Not Included	Not Included
Mass Loss	Not Included	Not Included
Angular Momentum Loss	Not Included	Not Included
Premain Sequence Evolution	Not Included	Included
Initial Abundances :		
^{4}He	Adjusted	Adjusted
C, N, O, Ne	Adjusted	Adjusted
All Other Elements	Adjusted	Meteoritic

[a]From A. Dar and G. Shaviv, "The solar neutrino problem: An update," Phys. Rept. **311** (1999) 115–141 (astro-ph/9808098).

Continued

Parameter/Effect	**BSP98**	**DS96**
Photospheric Abundances :		
^{4}He	Predicted	Predicted
C, N, O, Ne	Photospheric	Photospheric
All Other Elements	Meteoritic	Predicted
Radiative Opacities	OPAL 1996	OPAL 1996
Equation of State	Straniero 1996?	Dar – Shaviv 1996
Partial Ionization Effects	Not Included	Included
Diffusion of Elements :		
H, ^{4}He	Included	Included
Heavier Elements	Approximated by Fe	All Included
Partial Ionization Effects	Not Included	Included
Nuclear Reaction Rates :		
$S_{11}(0)$ eV · b	4.00×10^{-19}	4.07×10^{-19}
$S_{33}(0)$ MeV · b	5.3	5.6
$S_{34}(0)$ keV · b	0.53	0.45
$S_{17}(0)$ eV · b	19	17
Screening Effects	Included	Included
Nuclear Equilibrium	Imposed	Not Assumed

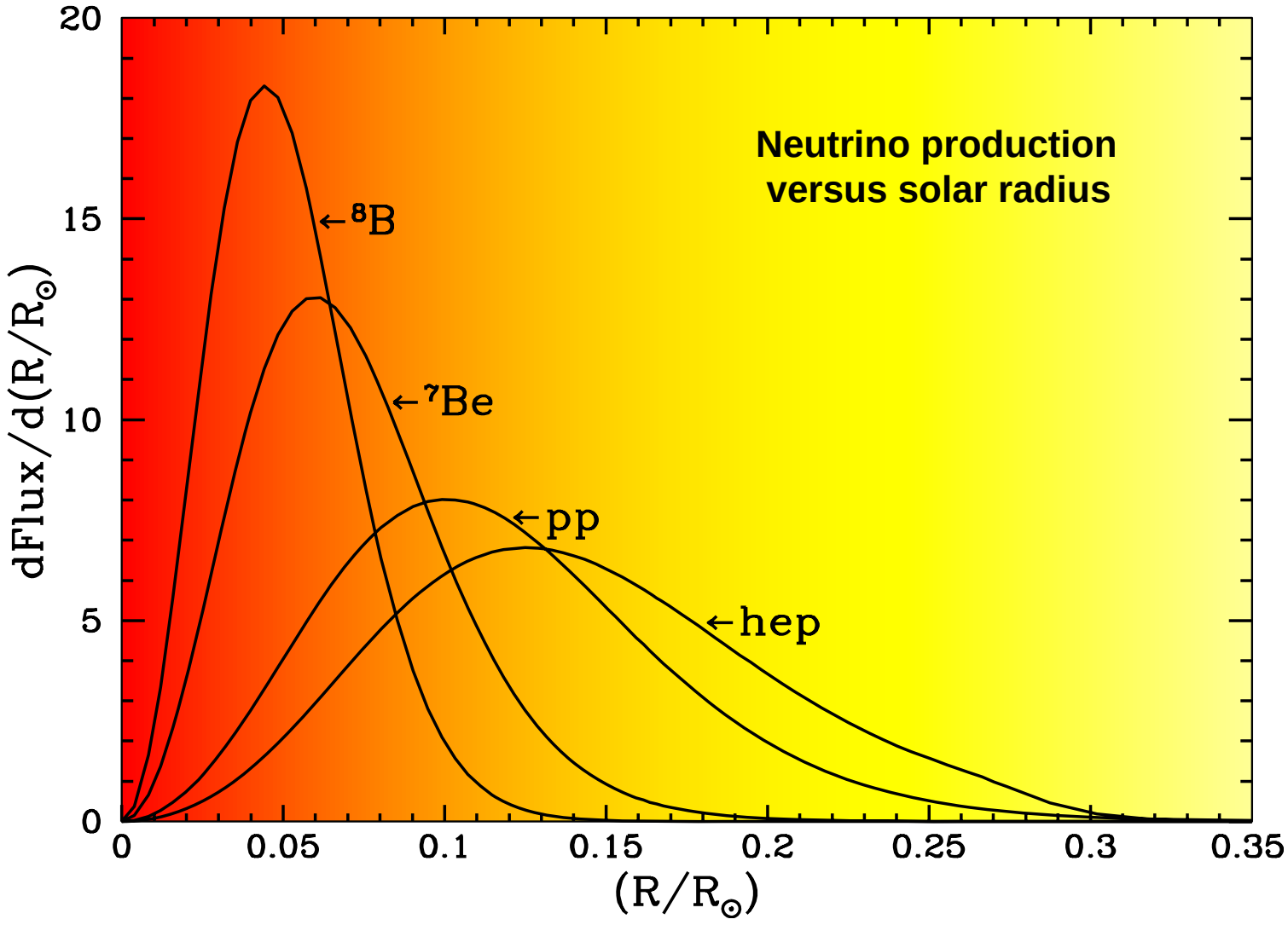

Figure shows where the different neutrino fluxes originate in the Sun according to SSM.
[From John Bahcall's homepage, URL: <http://www.sns.ias.edu/~jnb/>.]

Part III

SOLAR NEUTRINO EXPERIMENTS

10 Current status

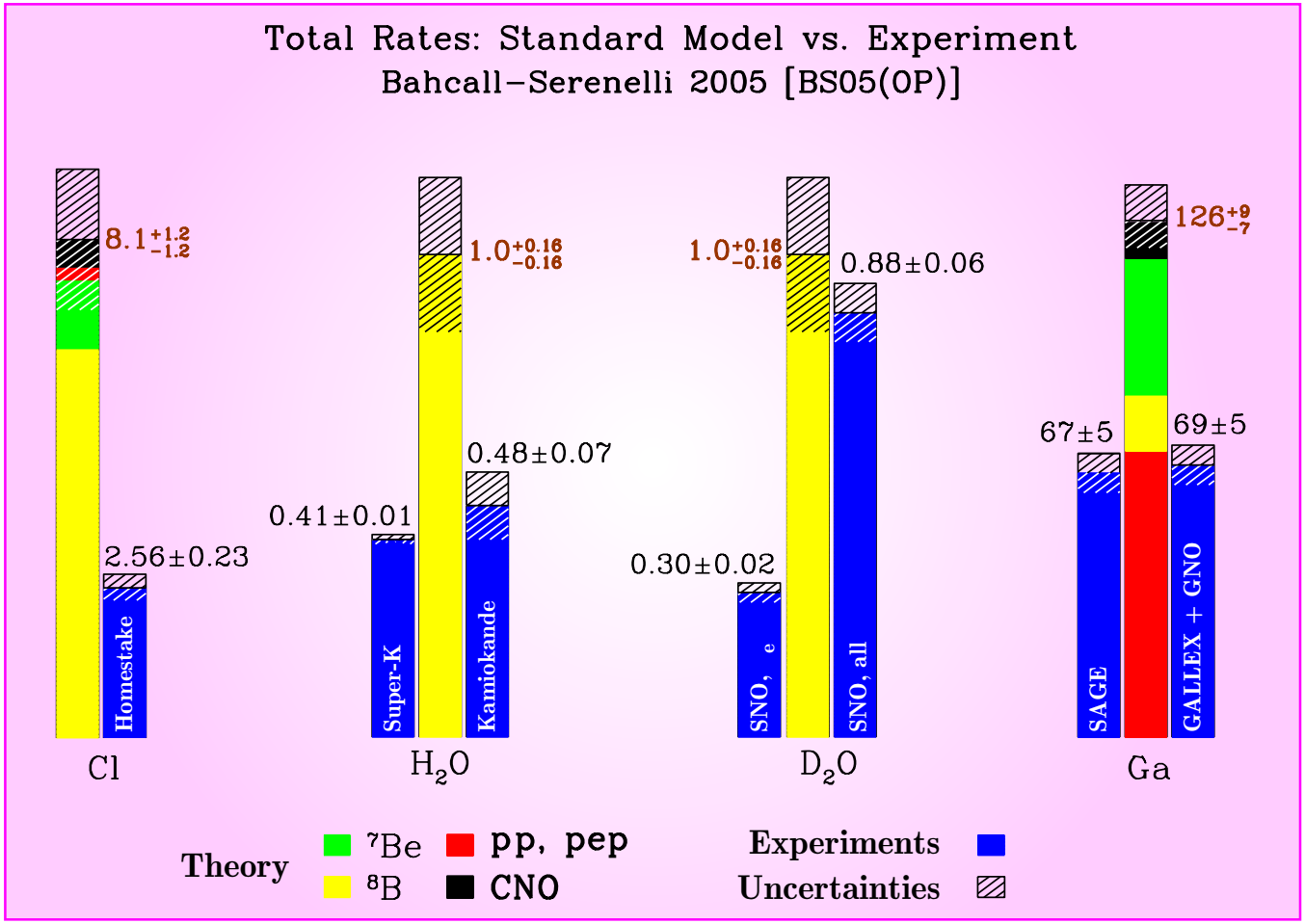

Current (Oct. 2005) status of the standard solar model and solar neutrino problem.
[Borrowed from John Bahcall's Home Page, URL: <http://www.sns.ias.edu/~jnb/> (slightly modified).]

Table 4: Current status of the solar neutrino data (2005).

Experiment	Measured flux (SNU / 10^{10} count/m^{2}s)	Ratio experiment/theory	Threshold energy	Years of running
Homestake	$2.56 \pm 0.16 \pm 0.16$	$0.33 \pm 0.03 \pm 0.05$	814 keV	1970-1995
Kamiokande	$2.80 \pm 0.19 \pm 0.33$	$0.54 \pm 0.08^{+0.10}_{-0.07}$	7.5 MeV	1986-1995
SAGE	$75 \pm 7 \pm 3$	$0.58 \pm 0.06 \pm 0.03$	233 keV	1990-2006
GALLEX	$78 \pm 6 \pm 5$	$0.60 \pm 0.06 \pm 0.04$	233 keV	1991-1996
Super-K	$2.35 \pm 0.02 \pm 0.08$	$0.465 \pm 0.005^{+0.016}_{-0.015}$	5.5 (6.5) MeV	from 1996
GNO	$66 \pm 10 \pm 3$	$0.51 \pm 0.08 \pm 0.03$	233 keV	from 1998
SNO (CC)	$1.68 \pm 0.06^{+0.08}_{-0.09}$		6.75 MeV	from 1999
SNO (ES)	$2.35 \pm 0.22 \pm 0.15$			
SNO (NC)	$4.94 \pm 0.21^{+0.38}_{-0.34}$			

- The values are given in SNU (defined as 10^{-36} capture per second per target atom) for the radiochemical experiments and in units of 10^{10} counts/m^{2}s for the water-Cherenkov experiments.
- The first and errors for the relative values correspond to experimental and theoretical errors, respectively, with the statistical and systematic errors added quadratically. The models by Bahcall and Pinsonneault BP98 and BP00 were used in the calculations.

[The data are borrowed from the *Ultimate Neutrino Page* maintained by Juha Peltoniemi and Juho Sarkamo, of Oulu University, URL: <http://cupp.oulu.fi/neutrino/> (last modified 10.4.2005).]

11 Cl-Ar detector at Homestake

[From URL: <http://www.bnl.gov/bnlweb/raydavis/research.htm>.]

The Homestake Neutrino Trap is a tank 20 feet (6.1 m) in diameter and 48 feet (14.6 m) long filled with 100,000 gallons (378,520 liters) of a common cleaning fluid, tetrachloroethylene (C_2Cl_4). On the average each molecule of C_2Cl_4 contains one atom of the desired isotope, ${}^{37}_{17}Cl$. The other three chlorine atoms ${}^{35}_{17}Cl$ contain two less neutrons. When a neutrino of the right energy reacts with an atom of ${}^{37}_{17}Cl$, it produces an atom of ${}^{37}_{18}Ar$ and an electron (B. Pontecorvo, 1946, L. V. Alvarez, 1949):

$$\nu_e + {}^{37}_{17}Cl \to {}^{37}_{18}Ar + e^- \quad (E_\nu^{\text{th}} \approx 814 \text{ keV}).$$

Then the radioactive argon decays back to chlorine:

$${}^{37}_{18}Ar \to {}^{37}_{17}Cl + e^+ + \nu_e \quad (T_{1/2} \approx 35 \text{ days}).$$

The idea is to tell that the reaction happened by seeing the positron.

The argon-37 is allowed to build up for several months, then is removed by purging the tank with helium gas. The argon is adsorbed in a cold trap and assayed for radioactivity.

The chlorine-argon experiment has been run by Raymond Davis, Jr., Kenneth C. Hoffman and Don S. Harmer of Brookhaven National Laboratory. The detector is located nearly a mile underground, in a rock cavity at the 4,850 foot level (1.48 km) below the surface in the Homestake Gold Mine in the town of Lead, South Dakota.

Suggested in 1964 by John Bahcall and Raymond Davis, the experiment was begun on 1967 and continued to measure the solar neutrino flux until the late 1990s, when the Homestake Mine ceased operating.

The first results of the experiment showed that the Sun's output of neutrinos from the isotope boron-8 was less than expected.

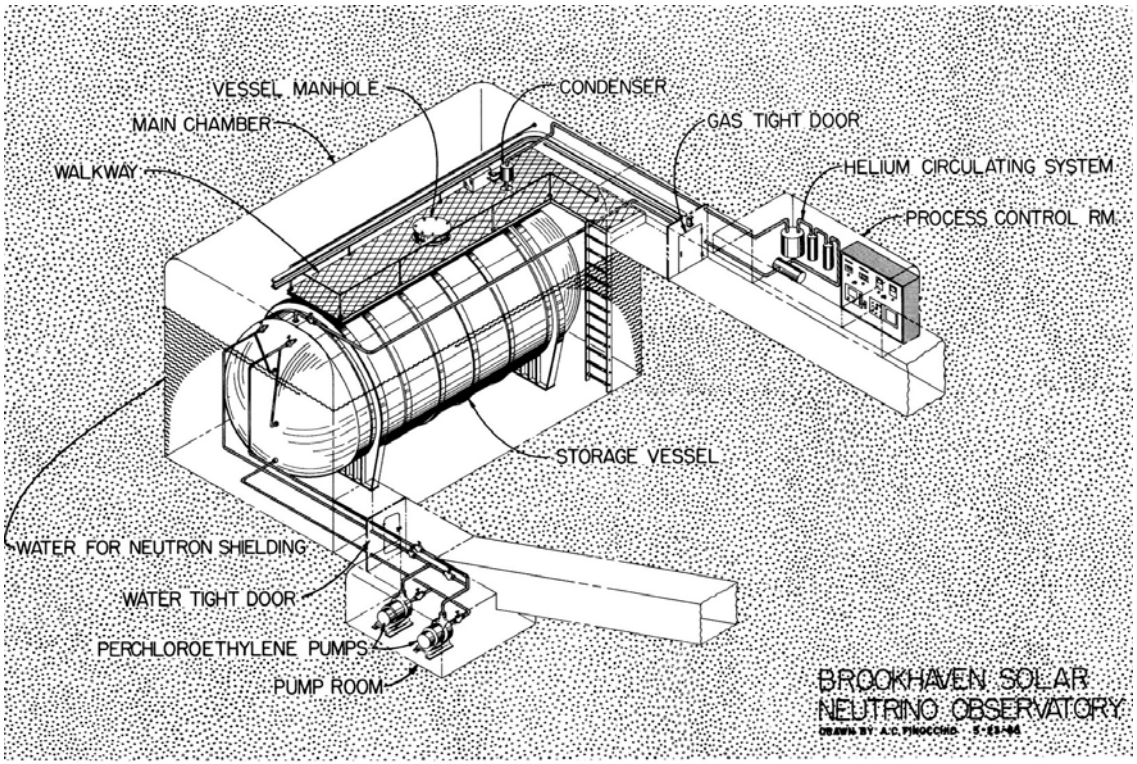

[From J. N. Bahcall, "Neutrinos from the Sun," Sci. Am. **221**, No. 1 (1969) 28–37.]

Figure on the right shows the argon extraction system which is deep underground next to the 100,000-gallon neutrino trap. Helium is circulated through the tank to sweep up any atoms of ^{37}Ar that have been formed from ^{37}Cl.
The efficiency of the extraction is determined by previously inserting in the tank a small amount of ^{36}Ar, a rare, nonradioactive isotope of argon. The helium and argon pass through the apparatus at left, where the argon condenses in a charcoal trap cooled by liquid nitrogen.

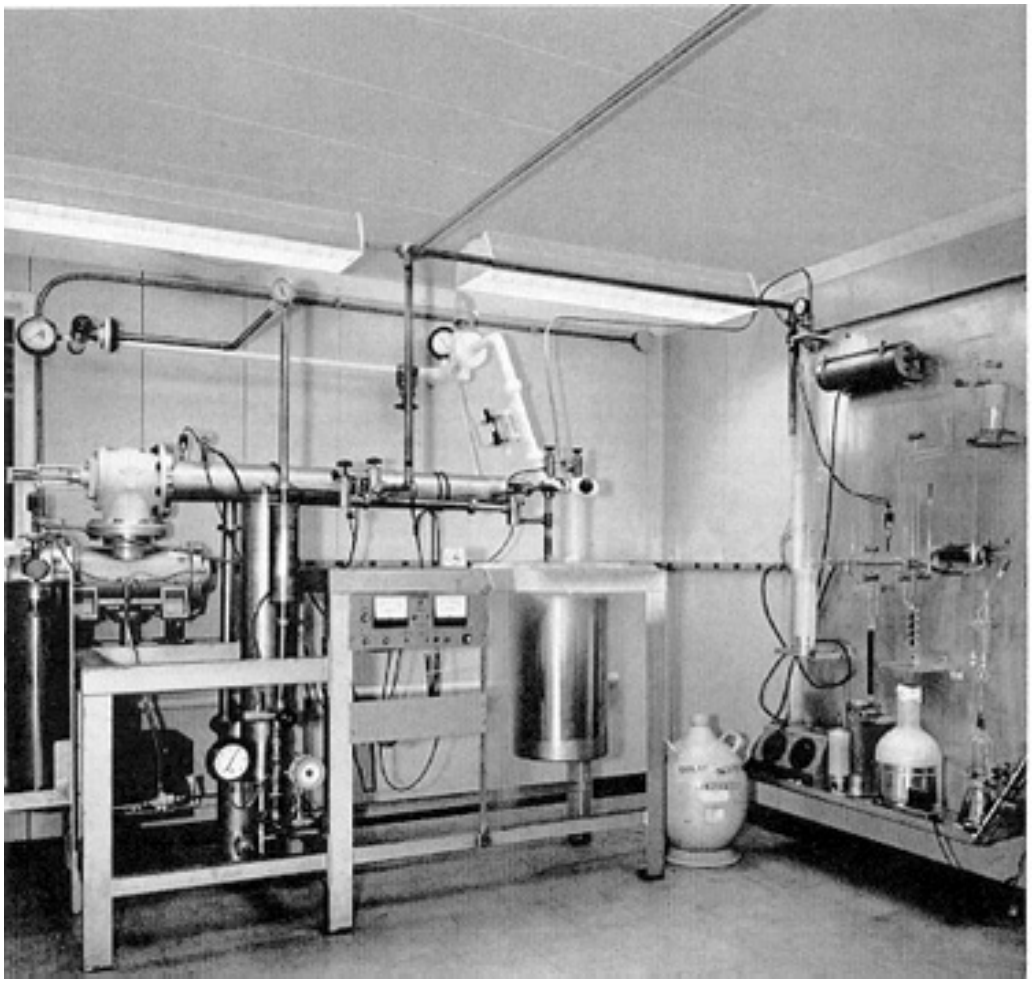

This argon fraction is purified in the apparatus at the right. The purified sample is then shipped to Brookhaven, where the content of ^{37}Ar is determined in shielded counters.

[From J. N. Bahcall, "Neutrinos from the Sun," Sci. Am. **221**, No. 1 (1969) 28–37.]

Deep-mine location shields the solar-neutrino detector from the intense flux of cosmic-ray (atmospheric) muons. Being very penetrating, the muons can knock protons out of atomic nuclei well below the earth's surface.

If a muon-induced proton entered the neutrino detector, it could mimic the entry of a solar neutrino by converting an atom of ^{37}Cl into an atom of radioactive ^{37}Ar.

Figure on the right shows the ^{37}Ar production rate in 3.8×10^5 liters of perchloroethylene as a function of the depth below the surface. The corresponding background effect is about 0.2 atoms per day in 10^5 gal. Other sources of the background are estimated to be on the same level or less, in particular,

- fast neutrons from (α, n) reactions and spontaneous fission of U in the rock wall: 0.1–0.3;
- internal contamination (U, Th, Ca): $\lesssim 0.1$;
- atmospheric neutrino interactions: $\lesssim 0.01$.

[From R. Davis, Jr. and D. S. Harmer, "Solar neutrino detection by the ^{37}Cl – ^{37}Ar method," in Proc. of the Informal Conference on Experimental Neutrino Physics (CERN, January 20–22, 1965), CERN 65-32, pp. 201–212.]

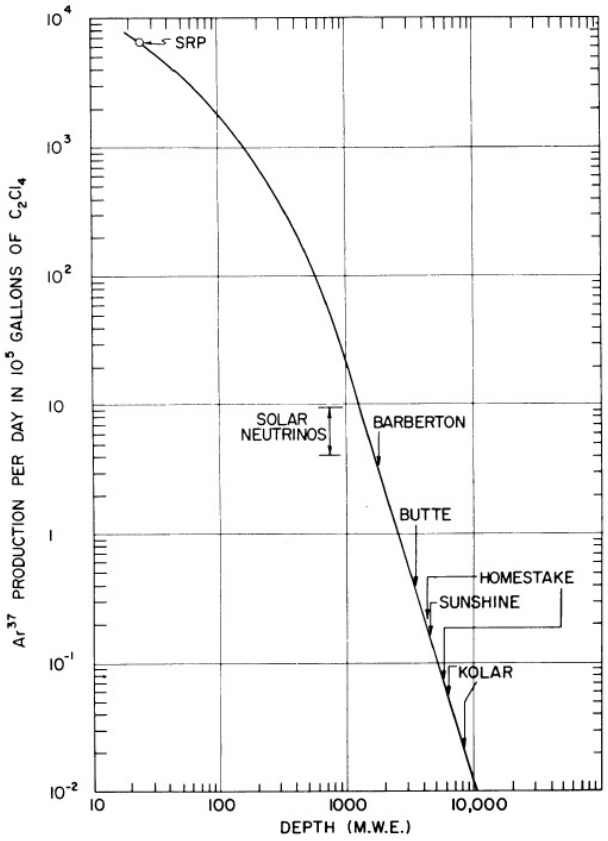

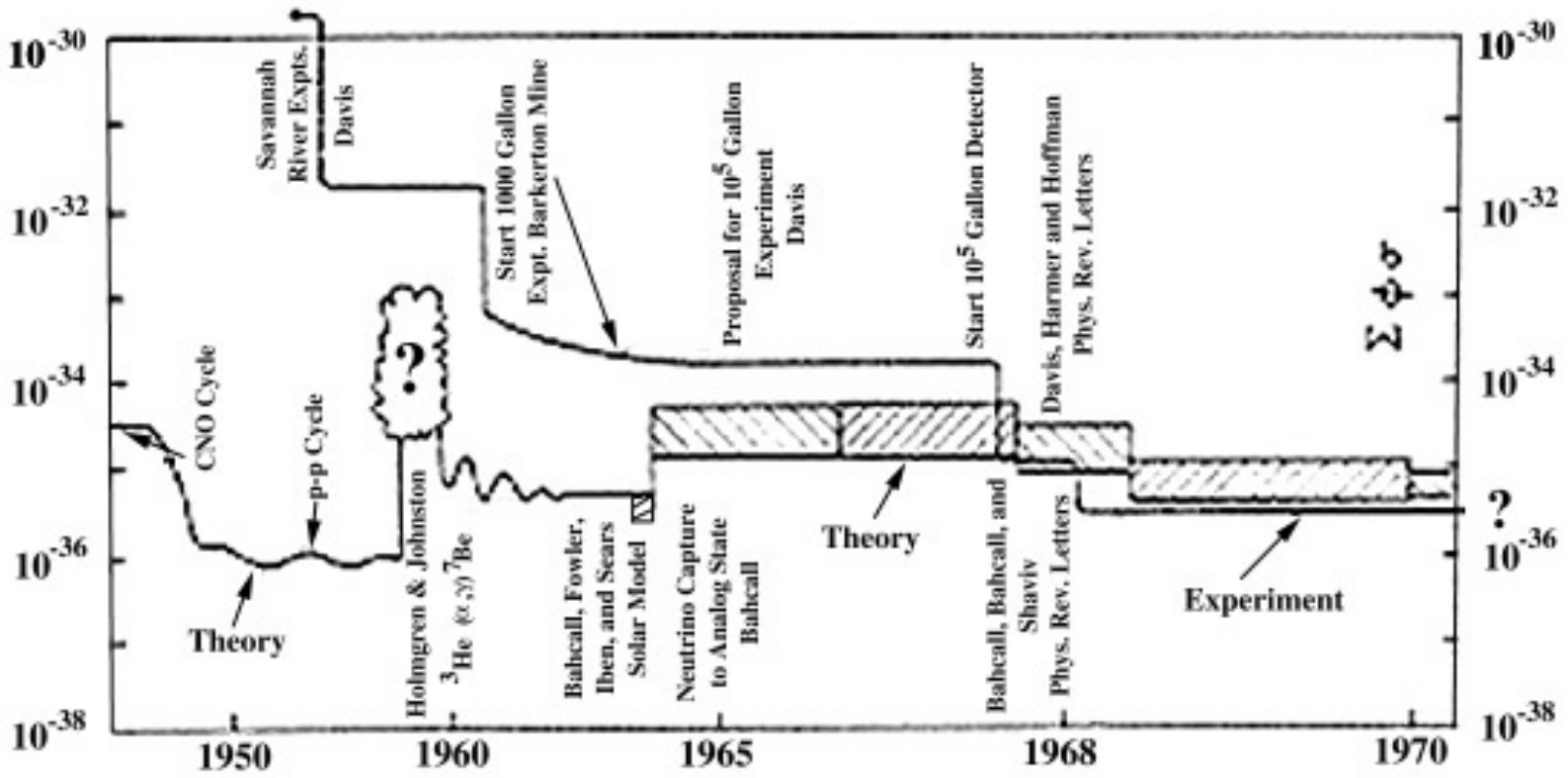

This figure is an overall pictorial history of the subject as it looked in 1970. The experimental upper limit is indicated by the thin curve and the range of theoretical values (after 1964) by the cross-hatched region. The units are captures per target atom per second (10^{-36} captures/atom/s $\equiv$ 1 SNU). A few of the major events are indicated on the figure at the period corresponding to the time they occurred.

[From J. N. Bahcall and R. Davis, Jr., "An account of the development of the solar neutrino problem," in Essays in Nuclear Astrophysics, edited by C. A. Barnes *et al.* (Cambridge University Press, 1982), pp. 243–285.]

Figure on the right shows the observed (Davis & coauthors) and predicted (Bahcall & co-authors) neutrino capture rates published within the period from 1964 to 1980. The earliest observational upper limits of 4000 and 160 SNU (obtained in 1955 and 1964, respectively) are not shown since these would not fit conveniently in the plot [see previous slide].
The theoretical uncertainties are more "experimental" than "theoretical" since the basic theory has not changed since 1964. What have changed are the best estimates for many different input parameters. The error bars shown for the theoretical points represent the range of capture rates that were obtained from standard solar models when the various nuclear and atomic parameters were allowed to vary over the range conventionally regarded as acceptable at the time the calculations were made.

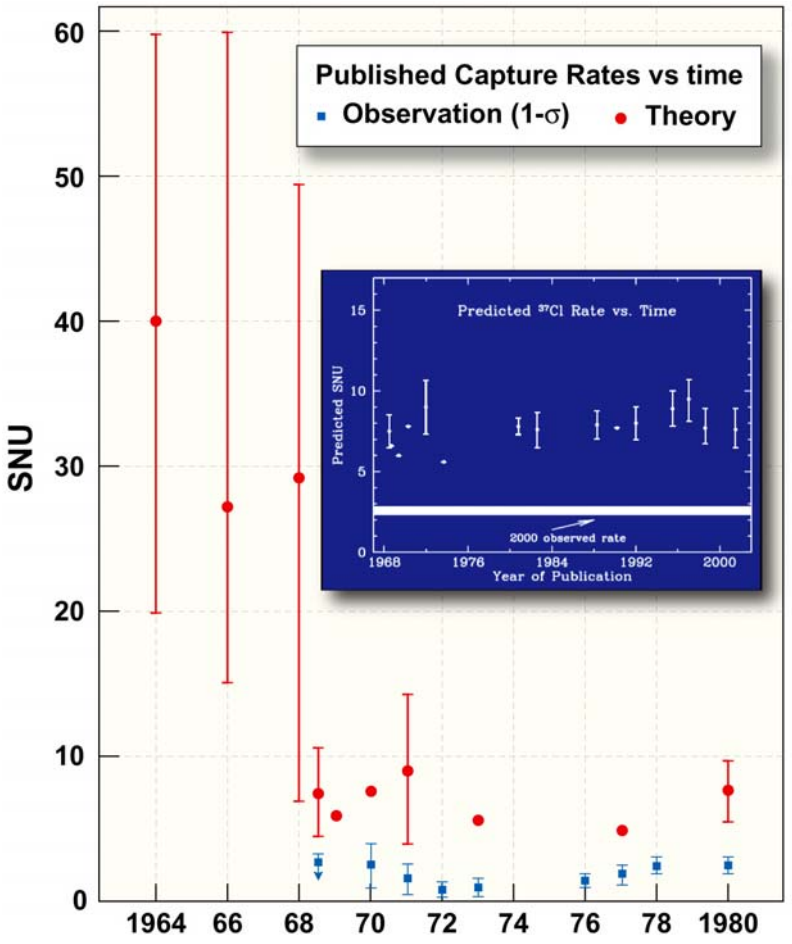

[From J. N. Bahcall and R. Davis, Jr., "An account of the development of the solar neutrino problem," in Essays in Nuclear Astrophysics, edited by C. A. Barnes *et al.* (Cambridge University Press, 1982), pp. 243–285.]

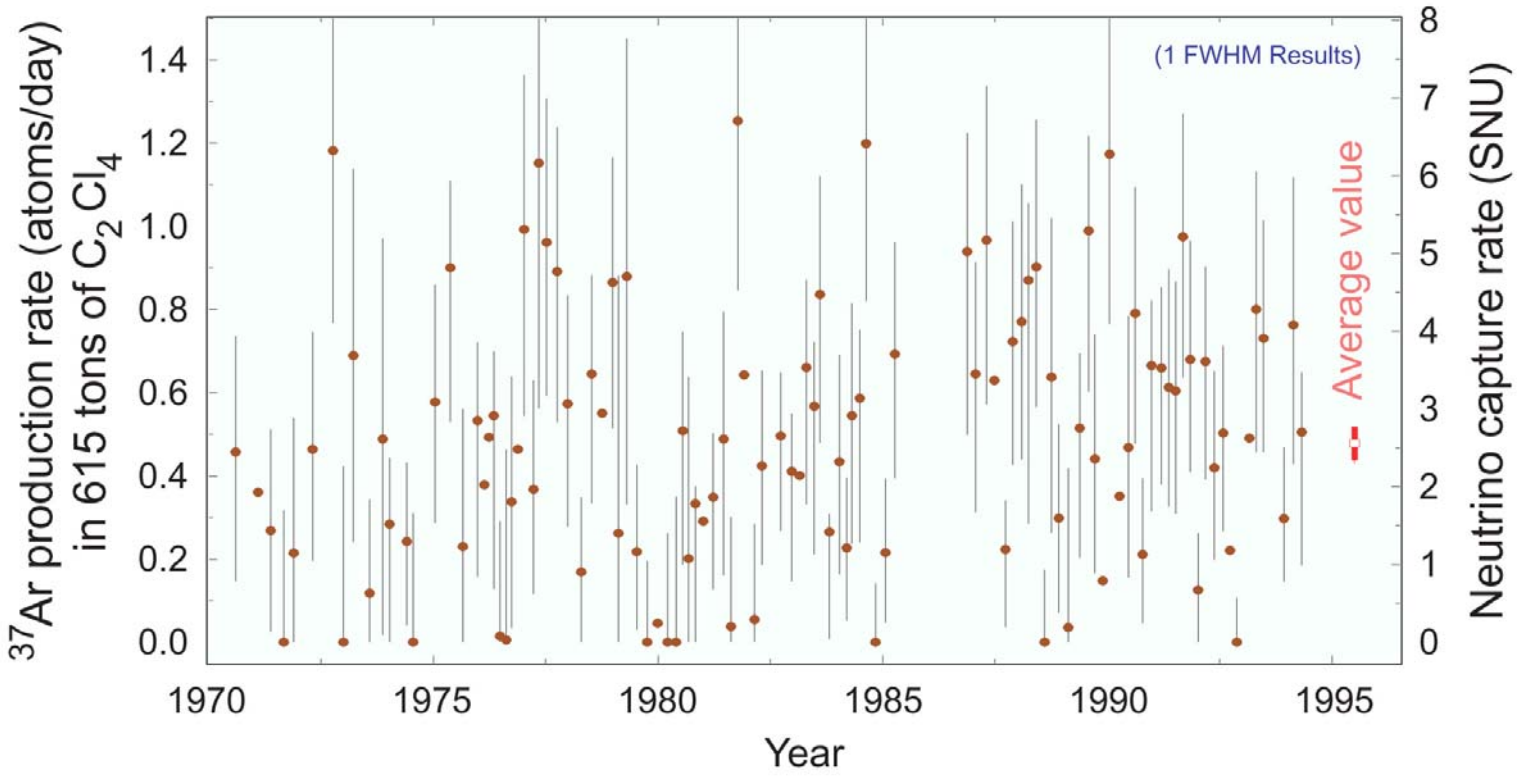

The final Homestake chlorine experiment one-FWHM (full width at half maximum) results for 108 individual solar neutrino observations (no. 18 to 133). All known sources of nonsolar ^{37}Ar production are subtracted. The errors of individual measurements are statistical errors only and are significantly non-Gaussian for near zero rates. The error of the cumulative result is the combination of the statistical and systematic errors in quadrature. [From B. T. Cleveland *et al.*, "Measurement of the solar electron neutrino flux with the Homestake chlorine detector," Astrophys. J. **496** (1998) 505–526. (1119 citations in SPIRES!)]

11.1 Solar Neutrino Puzzle, Number I'

The average solar neutrino induced ^{37}Ar production rate in the Homestake detector is

$$0.478 \pm 0.030_{\text{stat}} \pm 0.029_{\text{syst}} \text{ day}^{-1}.$$

Since the detector contains 2.16×10^{30} ^{37}Cl atoms, this gives a neutrino capture rate of

$$\boxed{\langle \sigma \Phi_{\nu_e} \rangle = 2.56 \pm 0.16_{\text{stat}} \pm 0.16_{\text{syst}} \text{ SNU}.}$$

This measurement is to be compared with the SM predictions for the chlorine detector:

$$\langle \sigma \Phi_{\nu_e} \rangle_{\text{theor}} = \begin{cases} 7.63 \text{ SNU} & \text{(Sackman, Boothroyd \& Fowler, 1990)} \\ 6.36 \text{ SNU} & \text{(Turck-Chièze \& Lopes, 1993)} \\ (4.2 \pm 1.2) \text{ SNU} & \text{(Dar \& Shaviv, 1994)} \\ (9.3 \pm 1.3) \text{ SNU} & \text{(Bahcall \& Pinsonneault, 1995)} \\ (4.1 \pm 1.2) \text{ SNU} & \text{(Dar \& Shaviv, 1996)} \\ (7.7 \pm 1.2) \text{ SNU} & \text{(Bahcall, Basu \& Pinsonneault, 1998)} \\ (8.1 \pm 1.2) \text{ SNU} & \text{(Bahcall \& Serenelli, 2005).} \end{cases}$$

The observed flux is much lower than that predicted (except for the Dar and Shaviv result). This discrepancy between observation and prediction has existed since the early 1970s when the observations of the Homestake detector were first reported.

11.2 Solar Neutrino Puzzle, Number II'

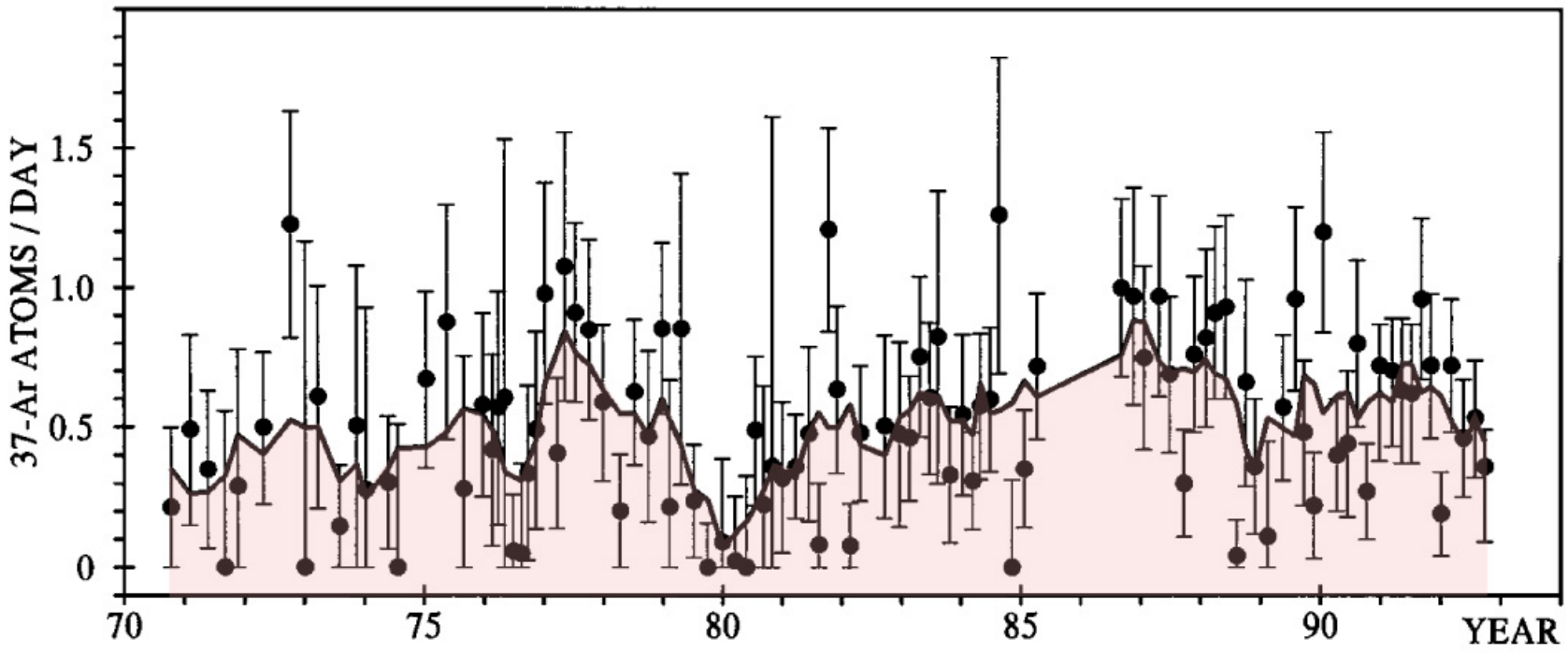

Homestake neutrino data with error bars and 5-point running-averaged values (solid line) from runs No. 18 to No. 126. The 5-point running-average values (Q5) are used to illustrate better the long-term behaviour considering that the original neutrino data are very scattered. Other choices for the smoothing, for instance 3- or 7-point running averages, do not alter qualitatively the results.

[This and next figures are borrowed from S. Massetti, M. Storini, and N. Iucci, "Correlative analyses for Homestake neutrino data," Nuovo Cim. **20 C** (1997) 1021–1026.]

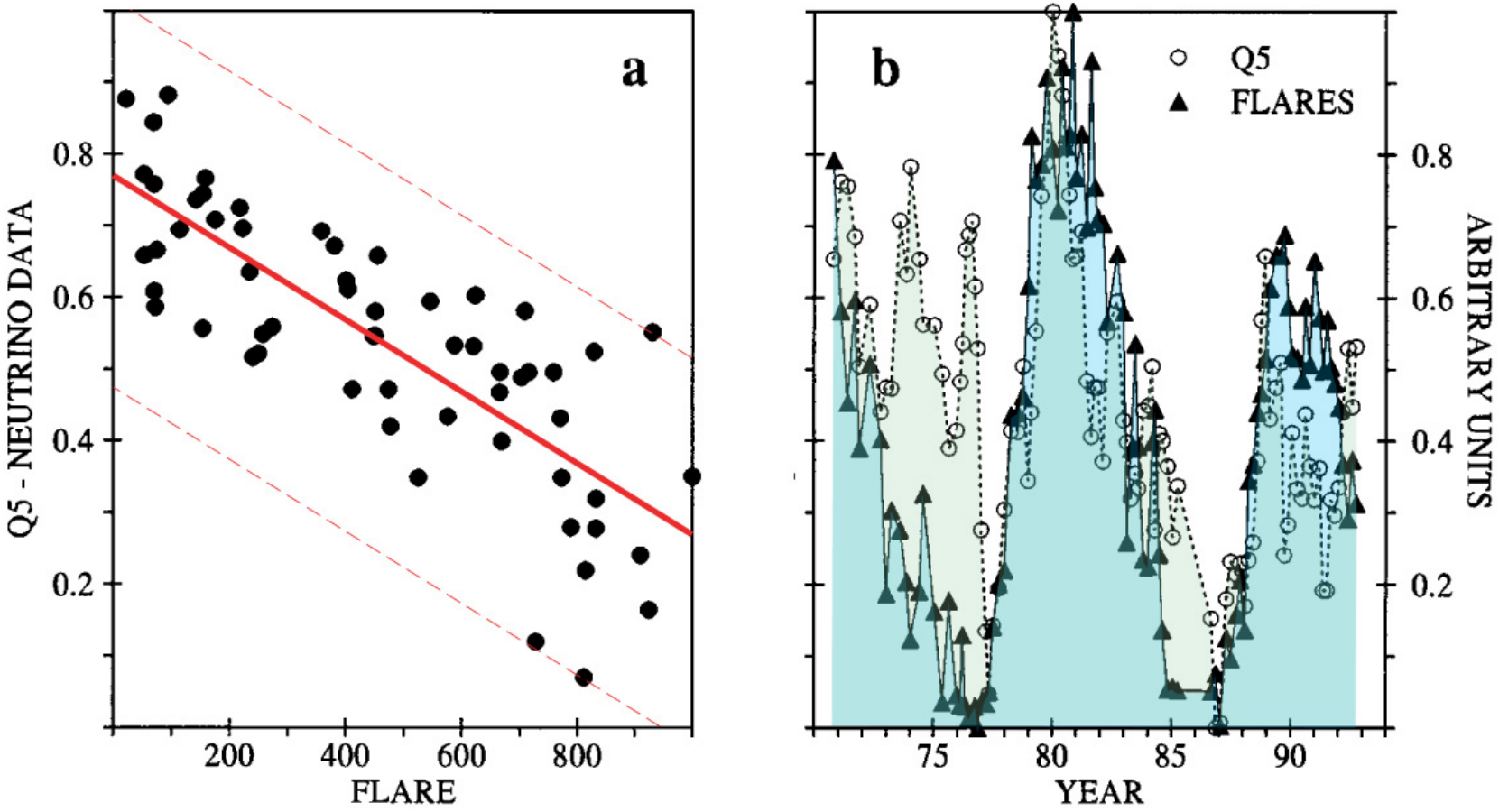

Scatter plot of solar flares counts vs. 5-point running averages of Homestake neutrino values in the period 1977 to 1989 (a) and the above data sets plotted as a function of time in the period 1970 to 1992 (b); the neutrino data in (b) are reported with an inverted scale and both data sets are normalized in a way that minimum = 0 and maximum = 1.

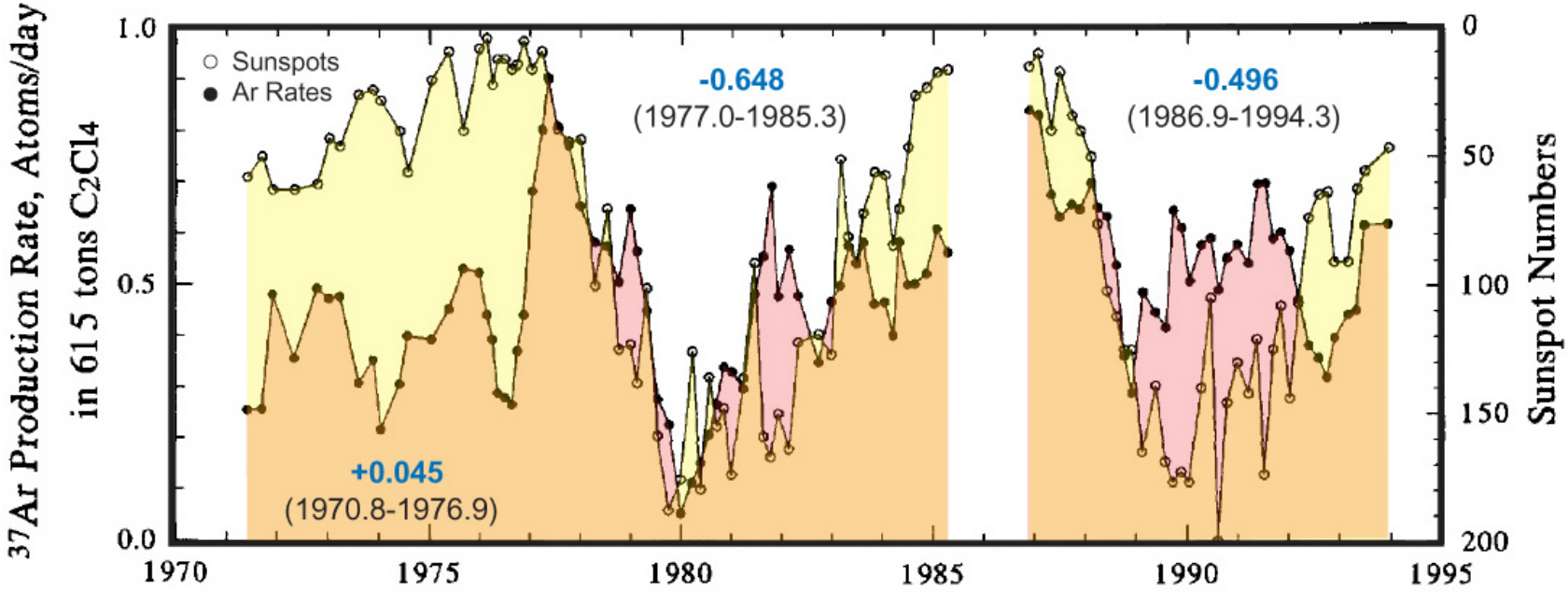

The plot shows the 5-point running averages of the Homestake data compared to sunspot numbers; the sunspots are plotted on an inverted scale.

[R. Davis Jr., "A review of measurements of the solar neutrino flux and their variation," Nucl. Phys. B (Proc. Suppl.) **48** (1996) 284–298.]

Some of the conclusions of the authors are:

The Homestake data:

i) Exhibit a clear modulation of the neutrino signal, almost on the long term.

ii) Are badly correlated with geomagnetic indices, supporting the hypothesis that the source of the modulation is on the Sun.

iii) Are correlated with cosmic-rays intensity only in the period 1970-1982, whereas over the total period the correlation is near zero.

iv) Are better correlated with flare counts than with sunspot numbers. Note that flare phenomena are intimately related to the toroidal component of the heliomagnetic field. The best correlated period (1977-1989) corresponds to that characterized by a reinforcement of the interplanetary magnetic-field intensity, suggesting again an enhancement of the global heliomagnetic field.

More or less similar conclusions were found in the regression analyses reported by many authors. These results suggest a pulsating character of the Homestake data and their anticorrelation with the solar magnetic activity (sunspot or flare numbers).

A veritable host of new ideas was brought forth to resolve the solar neutrino puzzles. Let's consider a (very incomplete) list of these solutions.

11.3 Solutions

11.3.1 Astrophysics and/or Nuclear Physics

- Models with convective mixing of the solar core [*Ezer & Cameron, 1968; Shaviv & Salpeter, 1968; Bahcall, Bahcall & Ulrich, 1968*]
- Models with turbulent diffusion of ^{3}He [*Schatzman 1969*]
- An overabundance of ^{3}He in the present Sun [*Kocharov & Starbunov 1970*]
- Models with the strong central magnetic field (the energy density of the Sun's central magnetic field $|\mathbf{B}|^2/8\pi$ is a few percent of the gas pressure) [*Abraham & Iben 1971; Bahcall & Ulrich 1971; Bartenwerfer 1973; Parker 1974; Ulrich 1974*]
- A secular instability such that the presently observed solar luminosity does not equal the current energy-generation rate [*Fowler 1968, 1972; Sheldon 1969*]
- Models with low heavy elements ("low Z") abundances in the solar interior [*Bahcall & Ulrich 1971; Schatzman 1981; Maeder 1990*].
- An instability of the Sun that makes now a special time [*Fowler 1972; Dilke & Gough 1972*]
- A low-energy resonance in the $^3\mathrm{He} + {}^3\mathrm{He} \rightarrow {}^4\mathrm{He} + 2{}^1\mathrm{H}$ reaction [*Fowler 1972; Fetisov & Kopysov 1972*]
- Helium core (the Sun is assumed to be in a later stage of stellar evolution, such that hydrogen is burned-out and the core is made of helium) [*Prentice 1973*]

- Models with a rapidly rotating solar interior (the rotation is lowering the central pressure and temperature) [*Demarque, Mengel & Sweigert 1973; Roxburgh 1974; Rood & Ulrich 1974*]
- Rotation plus magnetic fields [*Snell, Wheeler & Wilson 1976*]
- A half-solar mass core of large heavy element abundance that survived the big bang and subsequently accreted another half solar mass at the time of the formation of the solar system [*Hoyle 1975*]
- A departure from the Maxwellian distribution [*Clayton* et al. *1975*]
- A fractionation of the primordial hydrogen and helium [*Wheeler & Cameron 1975*]
- Models with hydrogen mixing into the core by turbulent diffusion [*Schatzman 1981; Maeder 1990*]
- Mixing of ^{3}He due to rapid filamental flow downward [*Cummings & Haxton, 1996*]
- Temporal and spatial variations in temperature [*Dar & Shaviv, 1998*]
- Collective plasma processes [*Salpeter & Van Horne, 1969; . . . ; Tsytovich* et al. *1995, Dar & Shaviv, 1998*]
- A new solar model in which the Sun is formed by accretion of fresh SN debris on the collapsed core of a supernova; neutron emission from the SN remnant at the solar core; neutron decay major elements are Iron, nickel, oxygen, silicon [*Manuel, Miller & Katragada, 2003*]

11.3.2 Nonstandard Neutrino Properties

- Vacuum neutrino oscillations [*Gribov & Pontecorvo 1969*]
- An appreciable (anomalous) magnetic moment for the neutrino [*Cisneros 1971; Okun, Voloshin & Vysotsky, 1986*]
- Neutrino instability [*Bahcall, Cabibbo & Yahil 1972*]
- Goldstone neutrinos resulting from a spontaneous breakdown of supersymmetry [*Das 1984*].
- Matter enhanced neutrino oscillations [*Wolfenstein 1978; . . .; Mikheev & Smirnov, 1985*] $\Longrightarrow \gtrsim 10,000$ papers, 100s of alterations, 10s of innovations;
- Matter-induced neutrino decay $\nu \longrightarrow \overline{\nu} +$ Majoron [*Berezhiani & Vysotsky 1987*]
- Resonant neutrino spin–flavor precession in the solar magnetic field [*Akhmedov 1987; Lim & Marciano 1988*]
- Nonstandard (in particular, flavor-changing) neutrino interactions with matter [*Roulet, 1991; Guzzo, Masiero & Petcov 1991, Barger, Phillips & Whisnant 1991*]
- A nonstandard (strong enough) $\nu_e\gamma$ interaction that would cause the neutrinos to disappear before they leave the Sun or make them lose energy towards detection thresholds [*Dixmier, 1994*]

11.3.3 Exotics and Science Fiction

- Quark catalysis [*Libby & Thomas 1969; Salpeter 1970*]
- Accretion onto a central black hole (the model assumes that the Sun's energy did not come from fusion, rather from release of energy from accretion onto a black hole at the center of the Sun) [*Clayton, Newman & Talbot 1975*]
- Multiplicative mass creation [*Maeder 1977*]
- WIMPs as a source of solar energy [*Faulkner & Gilliland 1985; Spergel & Press 1985; Press & Spergel 1985; Faulkner, Gough & Vahia 1986; Gilliland* et al. *1986*]
- Violation of equivalence principle [*Gasperini, 1988, 1989; Halprin & Leung 1991*]
- Daemon[a] catalysis (it is assumed that daemons are capable of catalyzing proton-fusion reactions, which may account for the observed solar neutrino deficiency) [*Drobyshevski 1996, 2002*]

[a] **Daemon** = **D**ark **E**lectric **M**atter **O**bject, a hypothetical Planckian particle carrying a negative electric charge of up to $Z = 10$.

12 Ga-Ge detector SAGE

These solar neutrino experiments are based on the reaction (originally proposed by V. A. Kuzmin in 1965)

$$\nu_e + {}^{71}_{31}\mathrm{Ga} \rightarrow {}^{71}_{32}\mathrm{Ge} + e^- \quad (E_\nu^{\mathrm{th}} \approx 232.696 \pm 0.15 \text{ keV})^{\mathrm{a}}.$$

Then the radioactive germanium decays back to gallium:

$${}^{71}_{32}\mathrm{Ge} \rightarrow {}^{71}_{31}\mathrm{Ga} + e^+ + \nu_e \quad (T_{1/2} \approx 11.4 \text{ days}).$$

Backgrounds for the gallium experiments are caused by ^{71}Ge production through non-neutrino mechanisms

$$p + {}^{71}_{31}\mathrm{Ga} \rightarrow {}^{71}_{32}\mathrm{Ge} + n \quad (E_p^{\mathrm{th}} \approx 1.02 \text{ MeV}).$$

Like in the chlorine experiment, the protons may be produced by cosmic muon interactions, fast neutrons or residual radioactivity. Radon gas and its daughter products are also a large cause of background; the radon half-life is about 3.8 days.

[a] This is the weighted average of all the available measurements for the neutrino energy threshold of this reaction computed (including estimates of systematic errors) by G. Audi and A. H. Wapstra.

In the SAGE (Soviet–American Gallium solar neutrino Experiment), the ^{71}Ge atoms are chemically extracted from a 50-metric ton target of gallium metal and concentrated in a sample of germane gas (GeH_4) mixed with xenon.

The the ^{71}Ge atoms are then individually counted by observing their decay back to ^{71}Ga in a small proportional counter.

The SAGE collaboration regularly performs solar neutrino extractions, every four weeks, reducing the statistical error, and explores further possibilities for reducing the systematic uncertainties.

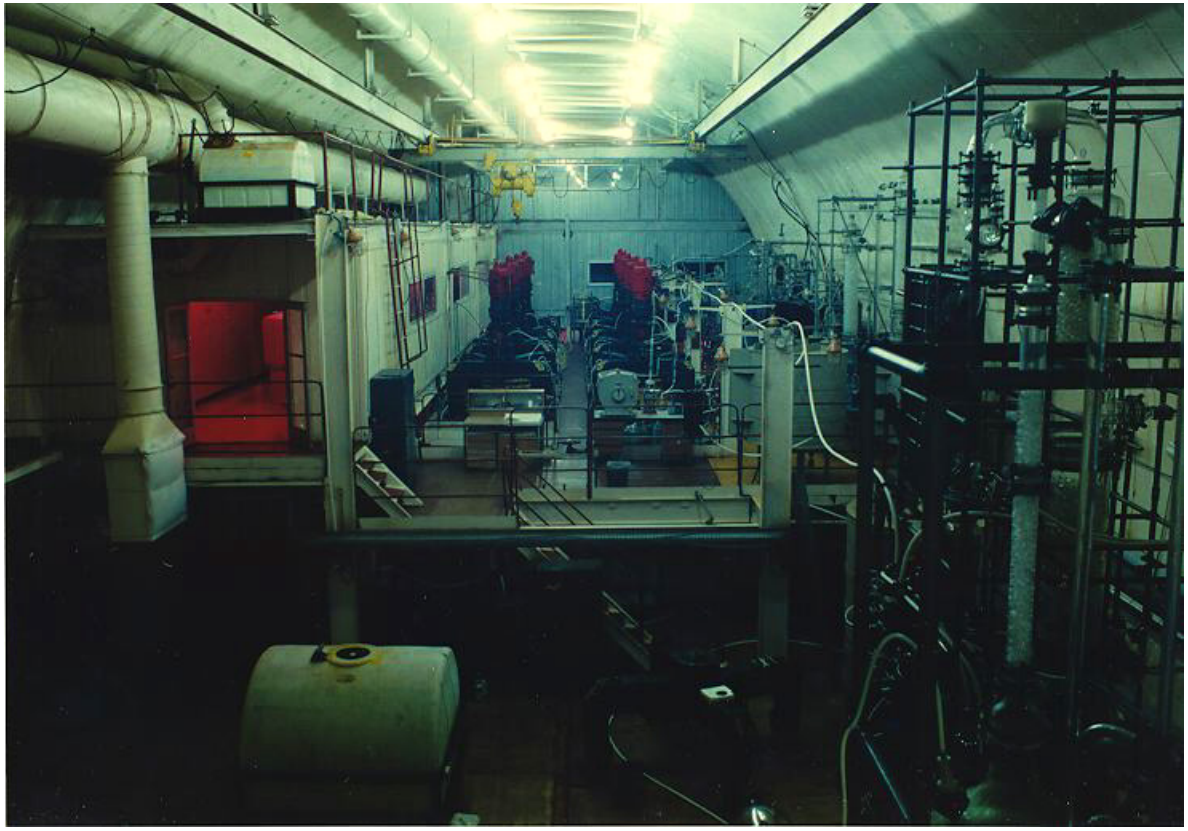

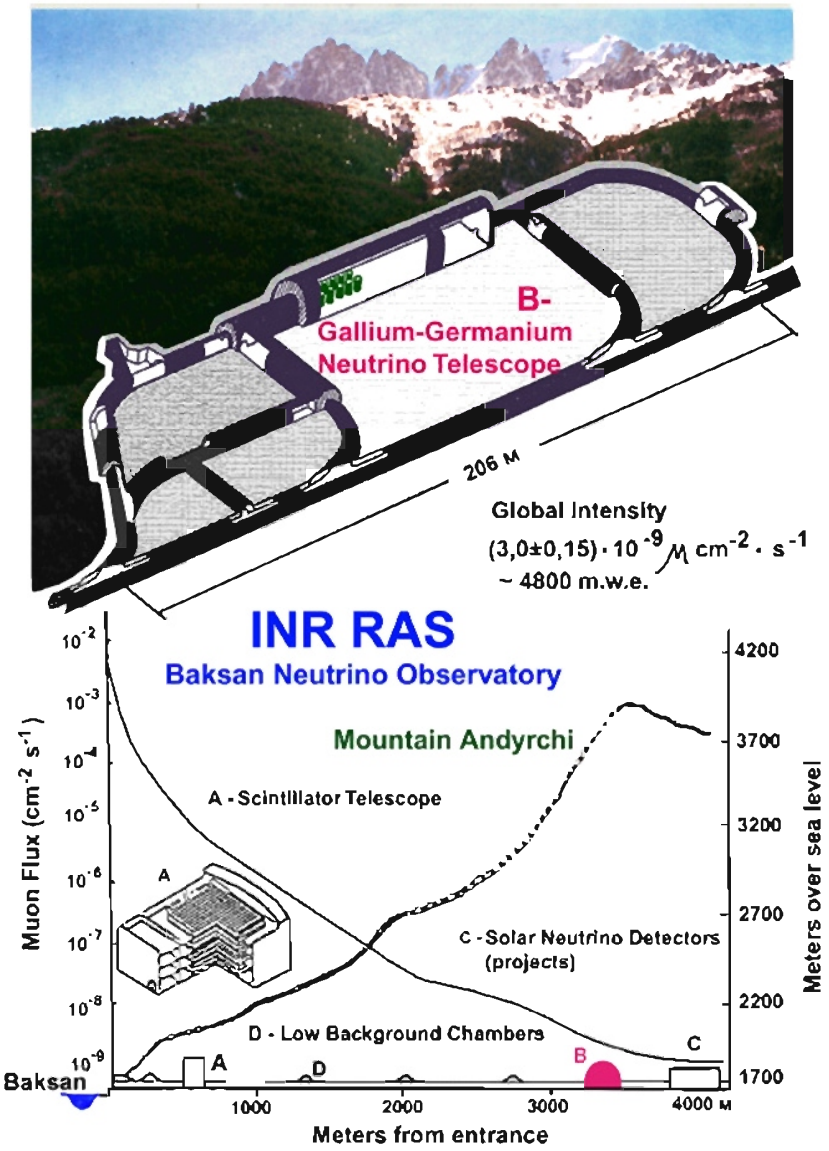
B-
Gallium-Germanium
Neutrino Telescope
206 м
Global Intensity
(3,0±0,15)·10⁻⁹ μ cm⁻²·s⁻¹
~ 4800 m.w.e.
INR RAS
Baksan Neutrino Observatory
Mountain Andyrchi
A - Scintillator Telescope
C - Solar Neutrino Detectors
(projects)
D - Low Background Chambers
Muon Flux (cm⁻² s⁻¹)
Meters over sea level
Meters from entrance
Baksan
A
B
C
D
1000
2000
3000
4000 м
4200
3700
3200
2700
2200
1700

To check the response of the SAGE experiment to low-energy neutrinos, a source of ^{51}Cr was produced by irradiating 512.7 g of 92.4%-enriched ^{50}Cr in a high-flux fast neutron reactor.

This source, which mainly emits monoenergetic 747-keV neutrinos, was placed at the center of a 13.1 ton target of liquid gallium and the cross section for the production of ^{71}Ge by the inverse beta decay reaction $^{71}\mathrm{Ga}(\nu_e, e^-)^{71}\mathrm{Ga}$ was measured to be

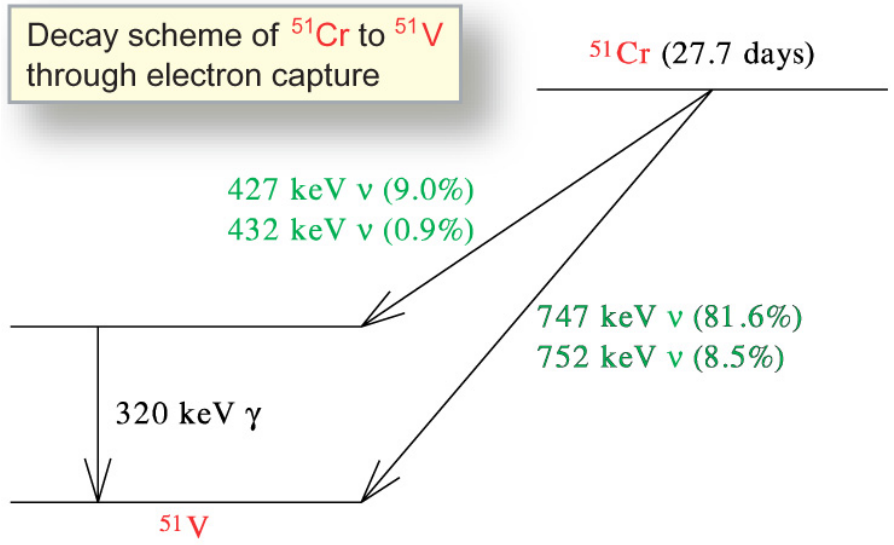

[From J. N. Abdurashitov *et al.*, "Measurement of the response of a gallium metal solar neutrino experiment to neutrinos from a ^{51}Cr source," Phys. Rev. C **59** (1999) 2246–2263.]

$$(5.55 \pm 0.60_{\mathrm{stat}} \pm 0.32_{\mathrm{stat}}) \times 10^{45}\ \mathrm{cm}^2.$$

The ratio of this result to the theoretical cross section of Bahcall and of Haxton are

$$0.95 \pm 0.12\,(\mathrm{exp})\,{}^{+0.035}_{-0.027}\,(\mathrm{theor}) \quad \text{and} \quad 0.87 \pm 0.11\,(\mathrm{exp}) \pm 0.09\,(\mathrm{theor}),$$

respectively. This good agreement between prediction and observation implies that the overall experimental efficiency is correctly determined and provides considerable evidence for the reliability of the solar neutrino measurement.

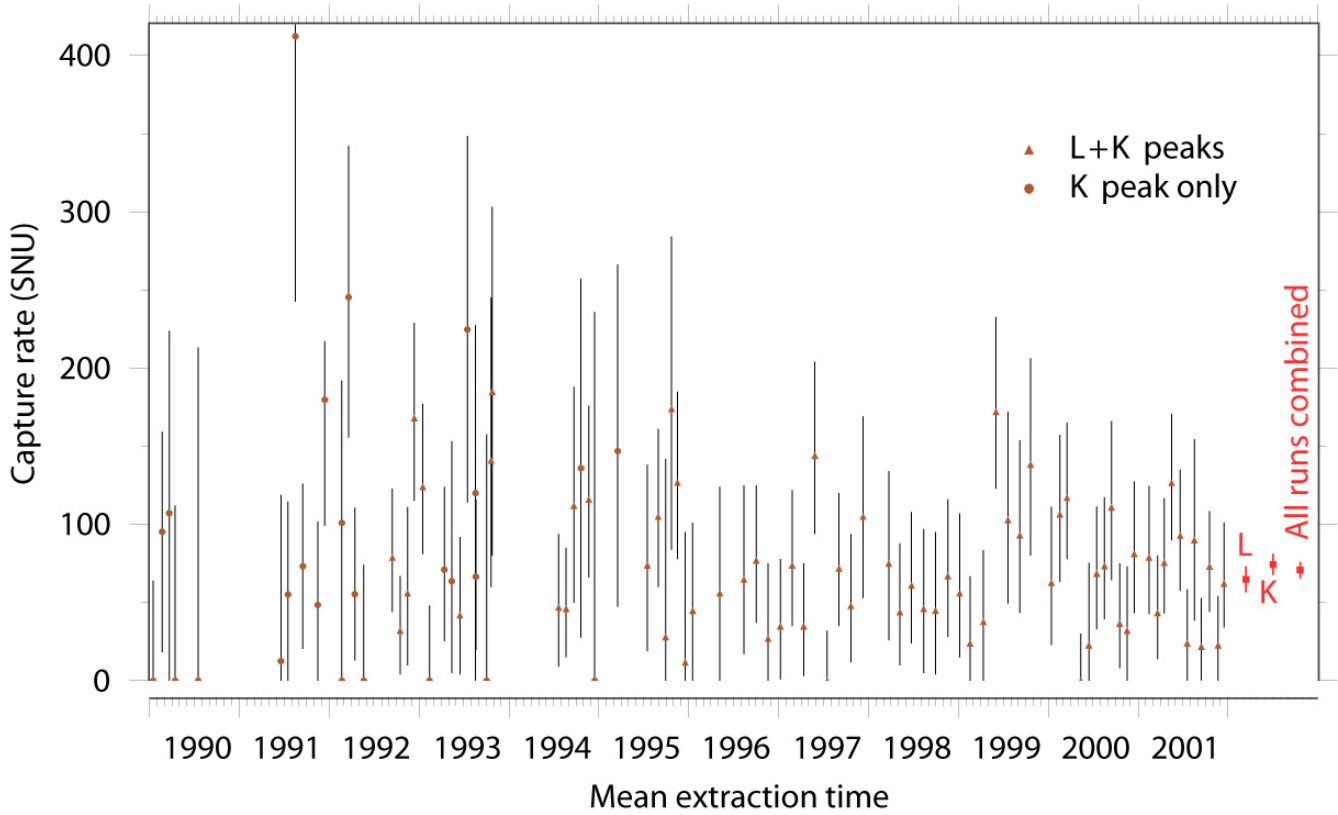

The capture rate from all SAGE extractions versus time: the triangles are for the L and K peaks and the circles are for the K peak alone; the vertical bars near each point correspond to a statistical error of 68%. The average rates for the L, K, and $L + K$ peaks are also shown.

[This and next figures are borrowed from J. N. Abdurashitov *et al.*, "Solar neutrino flux measurements by the Soviet-American Gallium Experiment (SAGE) for half the 22-Year Solar Cycle," Zh. Eksp. Teor. Fiz. **122** (2002) 211–226 [J. Exp. Theor. Phys. **95** (2002) 181–193] (astro–ph/0204245).]

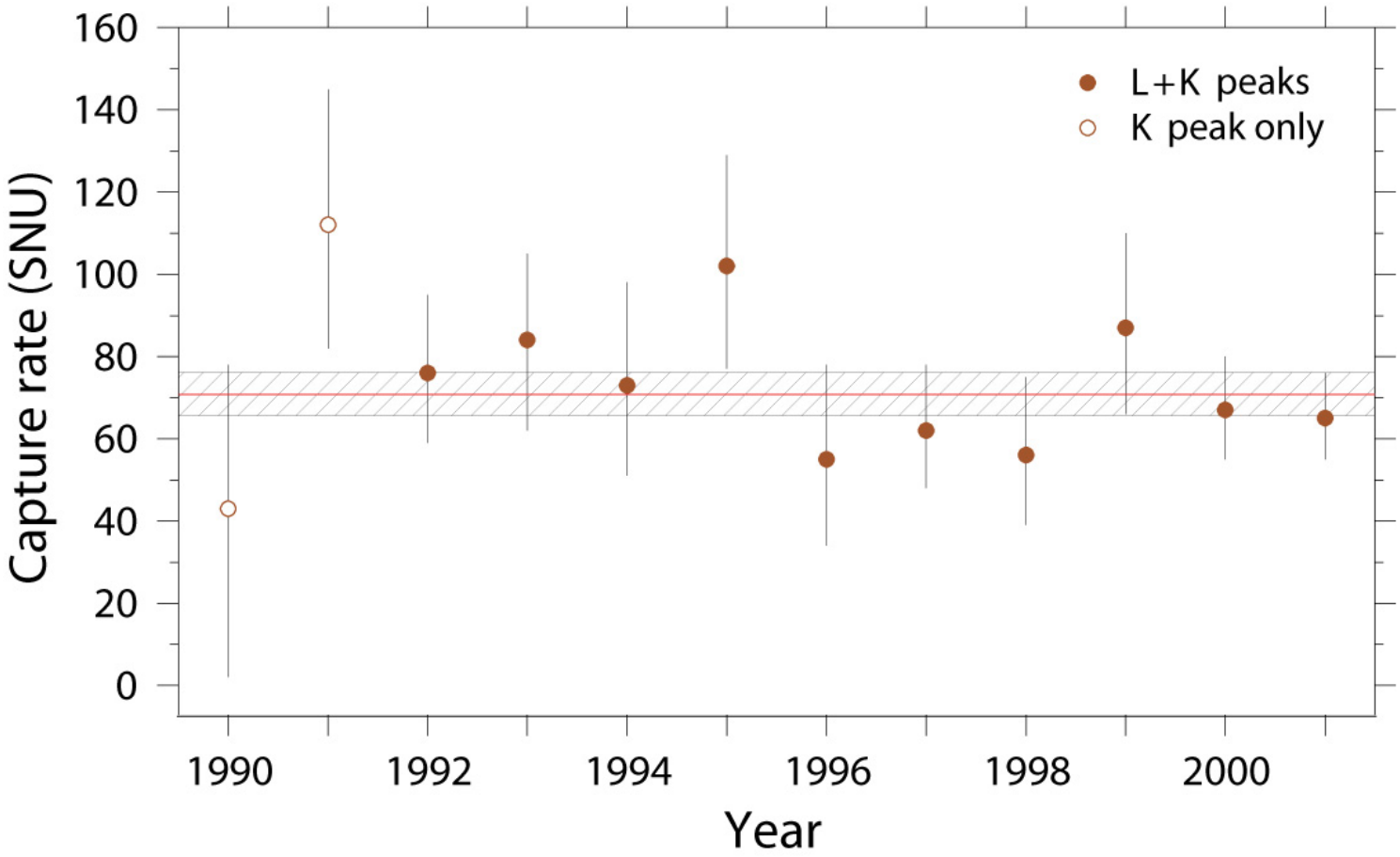

Results of the measurements combined by years; open and filled symbols refer to K and $K + L$ peaks, respectively; the hatched region corresponds to the SAGE result of $70.8^{+5.3}_{-5.2}\,(\text{stat})\ ^{+3.7}_{-3.2}\,(\text{syst})$ SNU. The data shown have a statistical error of 68%. The neutrino capture rate was constant during the entire data acquisition period with a 83% probability.

13 Ga-Ge detectors GALLEX and GNO

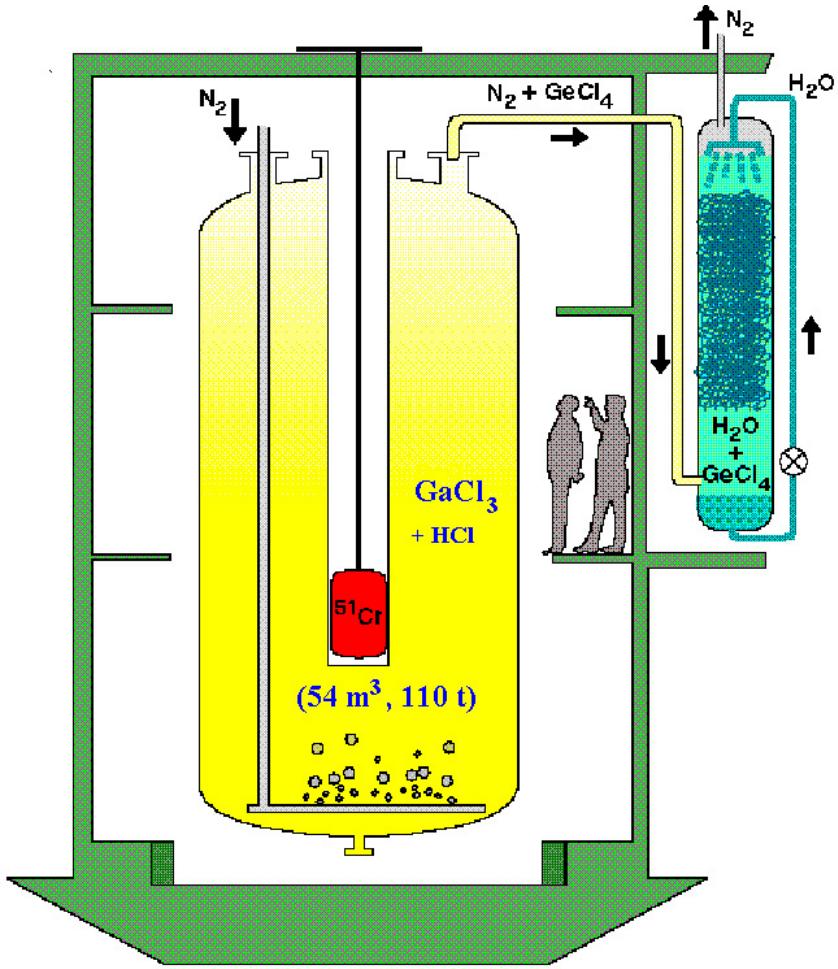

Figure on the left shows a scheme of the GALLEX detector tank with the absorber system and the Chromium source inserted inside the thimble.

The experimental procedure for GALLEX is as follows: 30.3 tons of gallium in form of a concentrated $GaCl_3$-HCl solution are exposed to solar neutrinos. In $GaCl_3$-HCl solution, the neutrino induced ^{71}Ge atoms (as well as the inactive Ge carrier atoms added to the solution at the beginning of a run) form the volatile compound $GeCl_4$, which at the end of an exposure is swept out of the solution by means of a gas stream (nitrogen). The nitrogen is then passed through a gas scrubber where the $GeCl_4$ is absorbed in water.

The $GeCl_4$ is finally converted to GeH_4, which together with xenon is introduced into a proportional counter in order to determine the number of ^{71}Ge atoms by observing their radioactive decay. [From URL: <http://www.mpi-hd.mpg.de/nuastro/gallex/detector.htm>.]

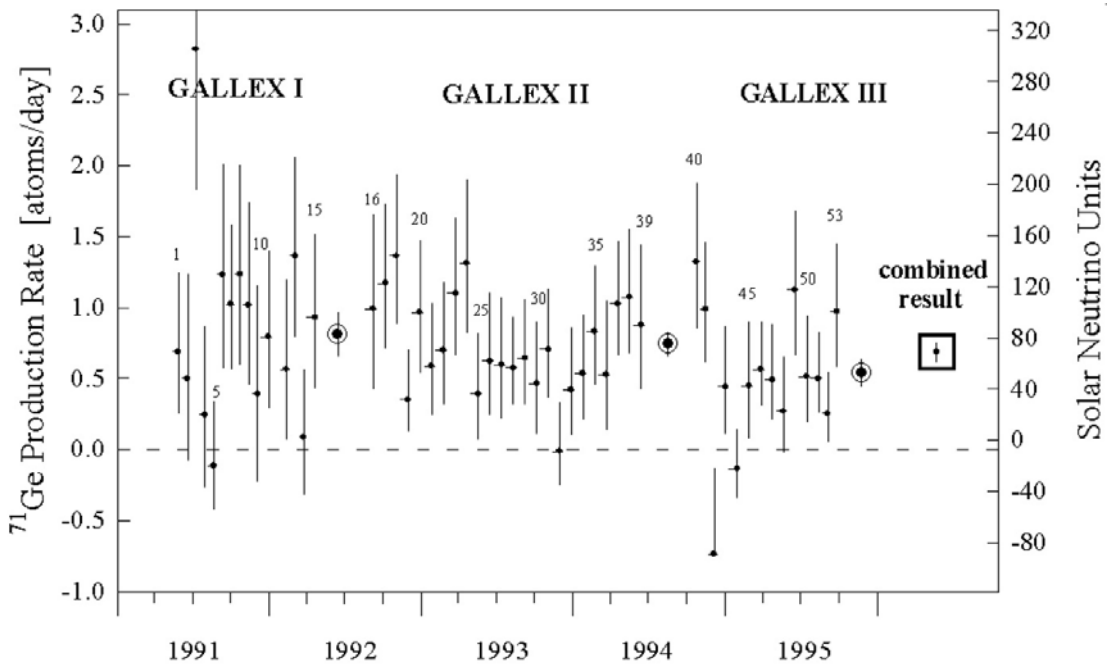

GALLEX I, II, and III single run overview.
Results for the 14 solar neutrino runs of GALLEX III (labels 40-53), shown together with the earlier results from GALLEX I (labels 1-15) and from GALLEX II (labels 16-39).

The left hand scale is the measured ^{71}Ge production rate; the right hand scale, the net solar neutrino production rate (SNU) after subtraction of side reaction contributions.

Error bars are $\pm 1\sigma$, statistical only. The label "combined" applies to the mean global value for the total of all 53 runs. The visibility is enhanced by a square box, but its error is the small bar inside the box. Horizontal bars represent run duration; their asymmetry reflects the "mean age" of the ^{71}Ge produced.

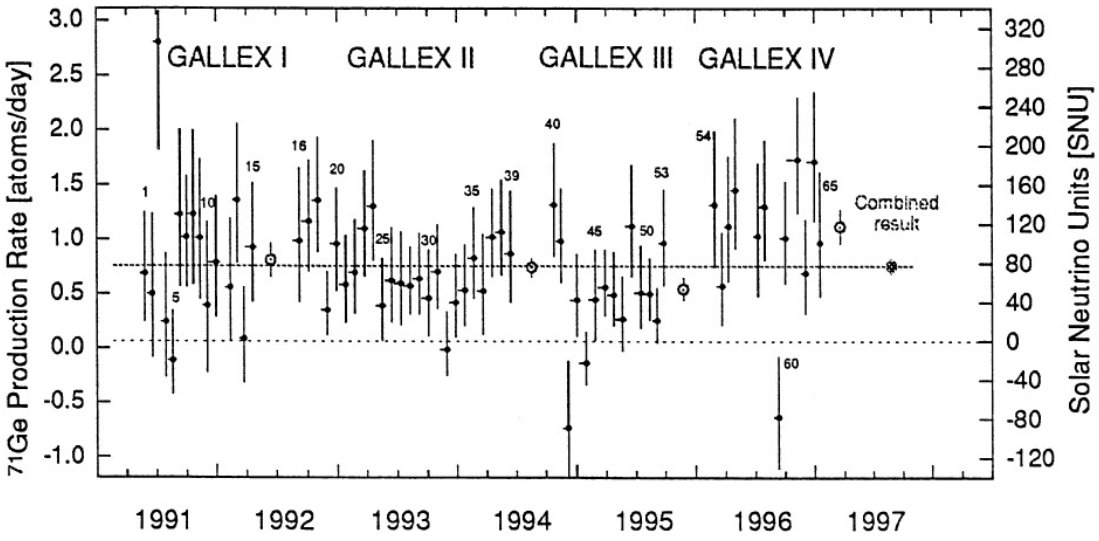

Summary of the results of GALLEX individual solar runs closed points. The left hand scale is the measured ^{71}Ge production rate; the right hand scale, the net solar neutrino production rate SNU after subtraction of side reaction contributions.

Error bars are $\pm 1\sigma$ statistical only. Open circles are the combined results for each of the measuring periods, GALLEX I, II, III and IV. The label "combined" applies to the mean global value for the total of all 65 runs. Horizontal bars represent run duration; their asymmetry reflects the "mean age" of the ^{71}Ge produced. The combined result which comprises 65 solar runs, is $77.5 \pm 6.2^{+4.3}_{-4.7}\,(1\sigma)$ SNU. The GALLEX experimental program to register solar neutrinos has now been completed.

In April 1998, GALLEX was succeeded by a new project, the Gallium Neutrino Observatory (GNO), with newly defined motives and goals.

[From W. Hampel *et al.* (GALLEX Collaboration), "GALLEX solar neutrino observations: Results for GALLEX IV," Phys. Lett. B **447** (1999) 127–133.]

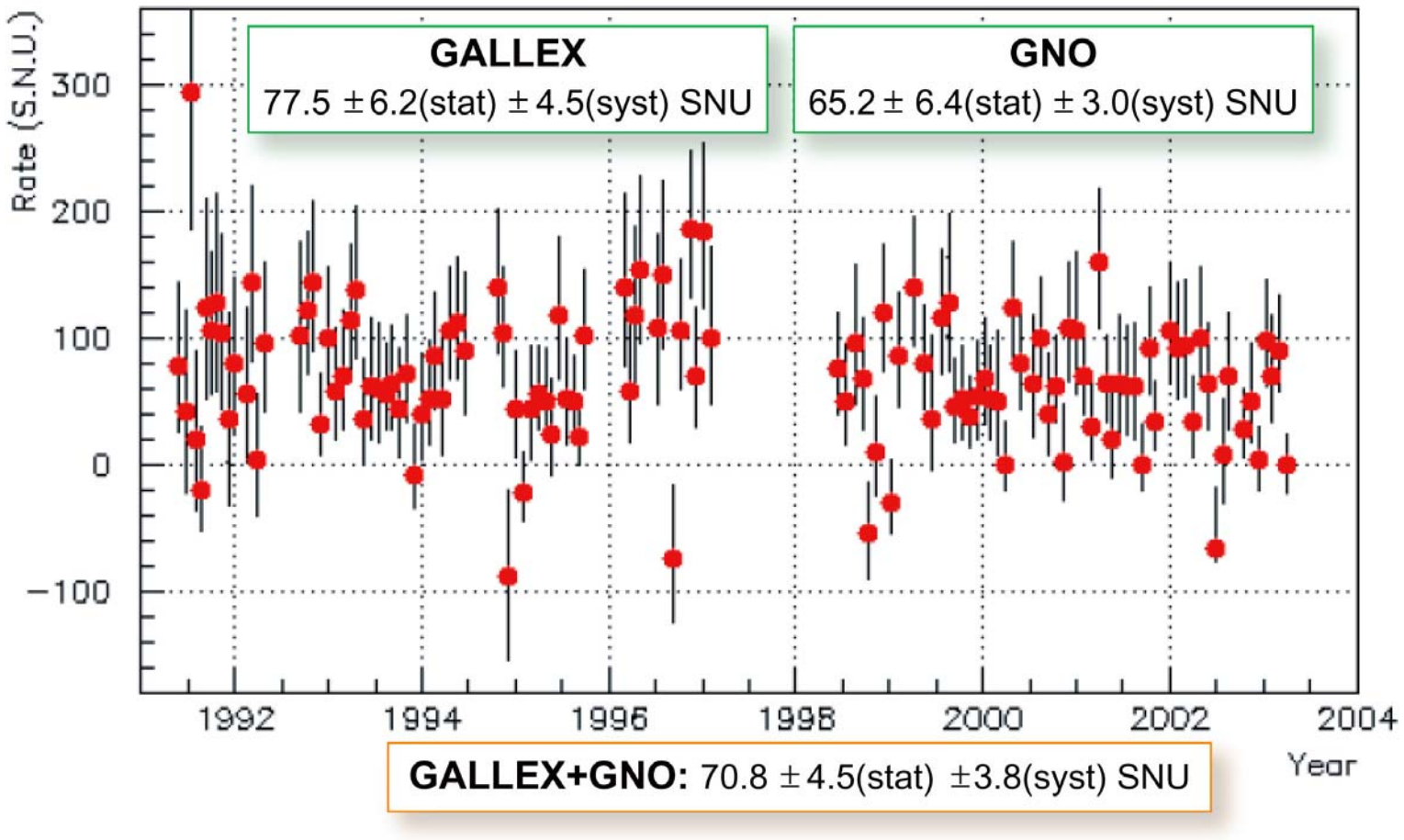

Single run results for GNO and GALLEX during a full solar cycle. Plotted is the net solar neutrino production rate in SNU after subtraction of side reaction contributions. Error bars are $\pm 1\sigma$, statistical only. [From M. Altmann *et al.* (GNO Collaboration), "Complete results for five years of GNO solar neutrino observations," Phys. Lett. B **616** (2005) 174–190 (hep-ex/0504037)]

14 H_2O Cherenkov detectors (Kamiokande and Super-Kamiokande)

Super-Kamiokande (SK), as well as its precursor Kamiokande (K), is an underground ring-imaging water-Cherenkov neutrino detector located in the Kamioka mine, Japan (137.32° E longitude, 36.43° N latitude).[a]

SK is a cylindrical tank (41.4 m in height, 39.3 m in diameter) filled with 50 kton of ultra-pure water, and situated under about 1 km of rock (2700 m.w.e.). The rock provides a shield against the cosmic-ray muons: the muon count rate in the detector is reduced to 2.2. Hz.

The outer walls of the tank are constructed from 5 cm thick stainless steel sheets, which are attached to the rock cavity and backed by concrete. About 2 m in from the walls is a 1 m wide structure of stainless beams that provide the backbone for the mounting PMTs. The structure divides the whole detector tank into an inner detector (ID) and outer detector (OD).

The 11,146 inward-facing ID PMTs that are used in event detection are mounted on the inside of the steel beam structure and are surrounded with black polyethylene sheets to minimize light reflection within the ID region. They provide a photo-coverage of 40%.

[a] See Part I of these lectures for the details relevant to the atmospheric neutrino studies with K and SK detectors.

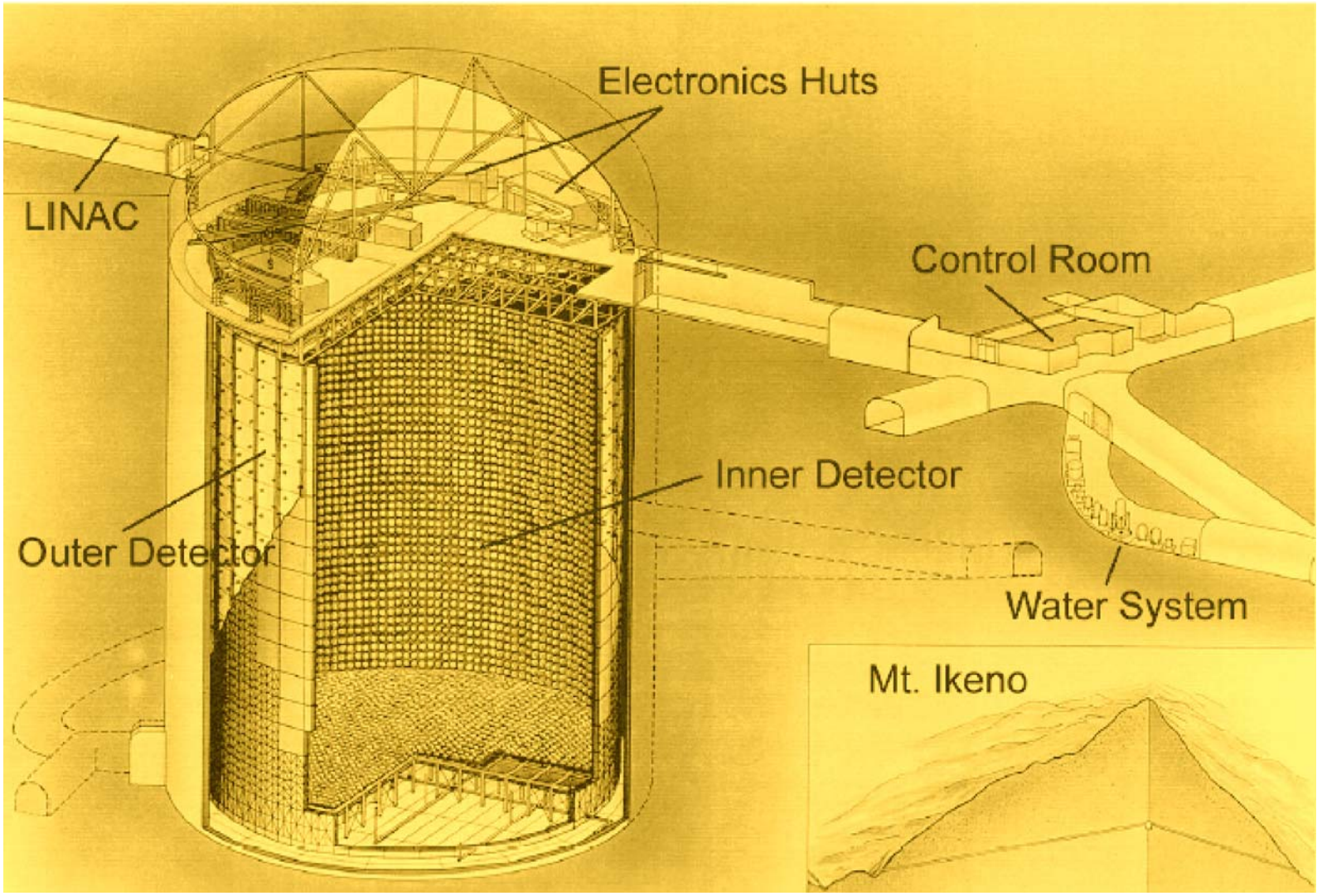

[This and next figures are borrowed from D. Turčan, "Solar neutrino at Super-Kamiokande solving the solar neutrino puzzle via neutrino flavor oscillations," Ph. D. Thesis, Faculty of the Graduate School, Maryland University, 2003.]

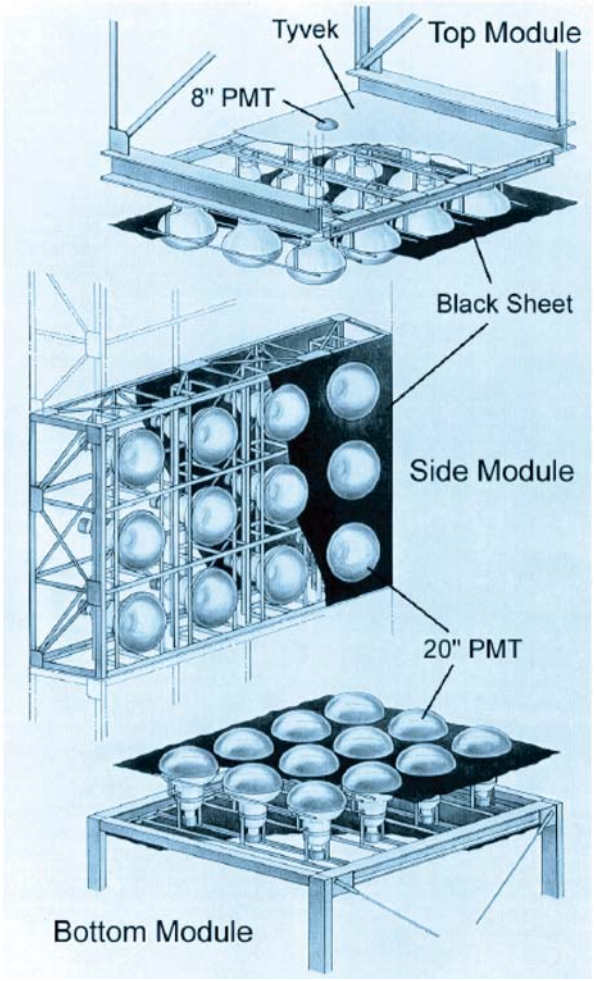

The entire ID region is a volume of 32.5 kt while the region actually used in the analysis is 2 m inside the PMT structure and represents a fiducial volume of 22.5 kt. There are at the least two reasons for excluding the 10 kt volume:

1) It is necessary to reduce the background from radioactive decays of radon which is particularly prominent near the PMTs and beams. The radon is still the main source of background in the fiducial volume, but the 2 m reduction brings the background to a manageable level.

2) There is a need for multiple PMT hits: if an event happens very near a PMT, all the light will be collected by that same PMT, and there will not be sufficient information for reconstructing that event. The PMTs used in SK's ID are 50 cm in diameter; they are largest PMTs in the world, designed and constructed especially for the SK experiment.

The OD, which surrounds the steel structure, has 1885 outward-facing 20 cm PMTs.

The top of the tank is a flat sheet that covers the entire are of the detector. It is under a dome, which lined with a polyurethane material ("Mineguard"), to reduce the radon emanation and erosion from the rock walls.

Cherenkov method of particle detection

In a transparent medium with an index of refraction $n > 1$ the light velocity is $v_c = c/n < c$. When a charged particle traverses the medium with velocity $v > v_c$, the Cherenkov light is emitted in a cone of half angle $\theta_C = \arccos(c/nv)$ from the direction of the particle's track.

This may easily be understood from the Huygens' principle (Fig. 14):

$$AB/v = AC/v_c$$

$$\Downarrow$$

$$\cos\theta_C = AC/AB = v_c/v.$$

The refractive index of pure water is about 4/3 for a wavelength region 300 to 700 nm (where the PMTs are sensitive). Therefore the Cherenkov light is emitted by ultrarelativistic particles under about $42°$.

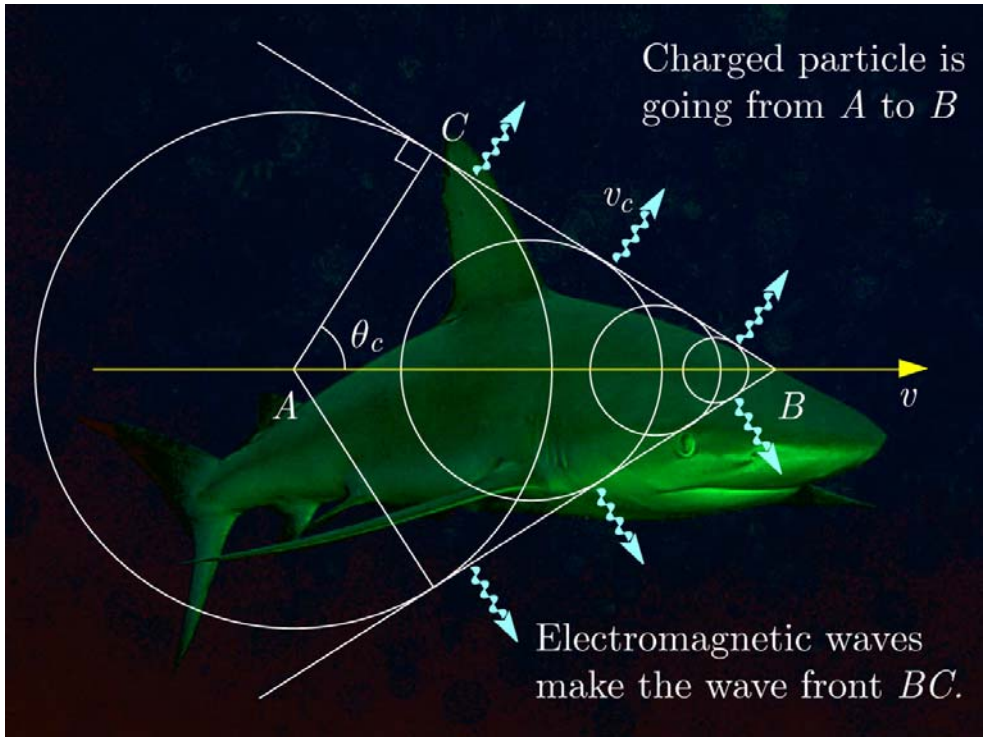

Figure 14: Cherenkov cone construction using the Huygens' principle.

The number of photons produced along a flight path dx in a wave length bin $d\lambda$ for a particle carrying charge ze is

$$\frac{d^2 N_\gamma}{d\lambda dx} = \frac{2\pi\alpha z^2 \sin^2\theta_C}{\lambda^2},$$

where $\alpha \approx 1/137$ is the fine structure constant. The number of Cherenkov photons emitted per unit path length with wavelength between λ_1 and λ_2 is

$$\frac{dN_\gamma}{dx} = 2\pi\alpha z^2 \int_{\lambda_1}^{\lambda_2} \left[\frac{d^2 N_\gamma}{d\lambda dx}\right] \frac{d\lambda}{\lambda^2} \approx 2\pi\alpha z^2 \sin^2\theta_C \left(\frac{1}{\lambda_1} - \frac{1}{\lambda_2}\right)$$

(neglecting the dispersion of the medium). In particular, for the optical range (400–700 nm)

$$\frac{dN_\gamma}{dx} = \frac{491.3\, z^2 \sin^2\theta_C}{1 \text{ cm}}.$$

A single charged particle emits about 214 (380) photons per 1 cm of the path length in water within the optical range (the PMT sensitive range).

For $v \approx c$ the Cherenkov light yield is independent of the energy of the charged particle. This means the light output of a single particle does not allow its energy to be measured.

The energies E_C and momenta p_C of some particles with $v = v_c$ in water (Cherenkov thresholds) are shown in Table 5, assuming $n(H_2O) = 1.33$).

Table 5: Cherenkov thresholds in total energy and momentum for water.

Particle	E_C (MeV)	p_C (MeV/c)
$e^{\pm}$	0.775	0.583
$\mu^{\pm}$	160.3	120.5
$\pi^{\pm}$	211.7	159.2
p	1423	1070

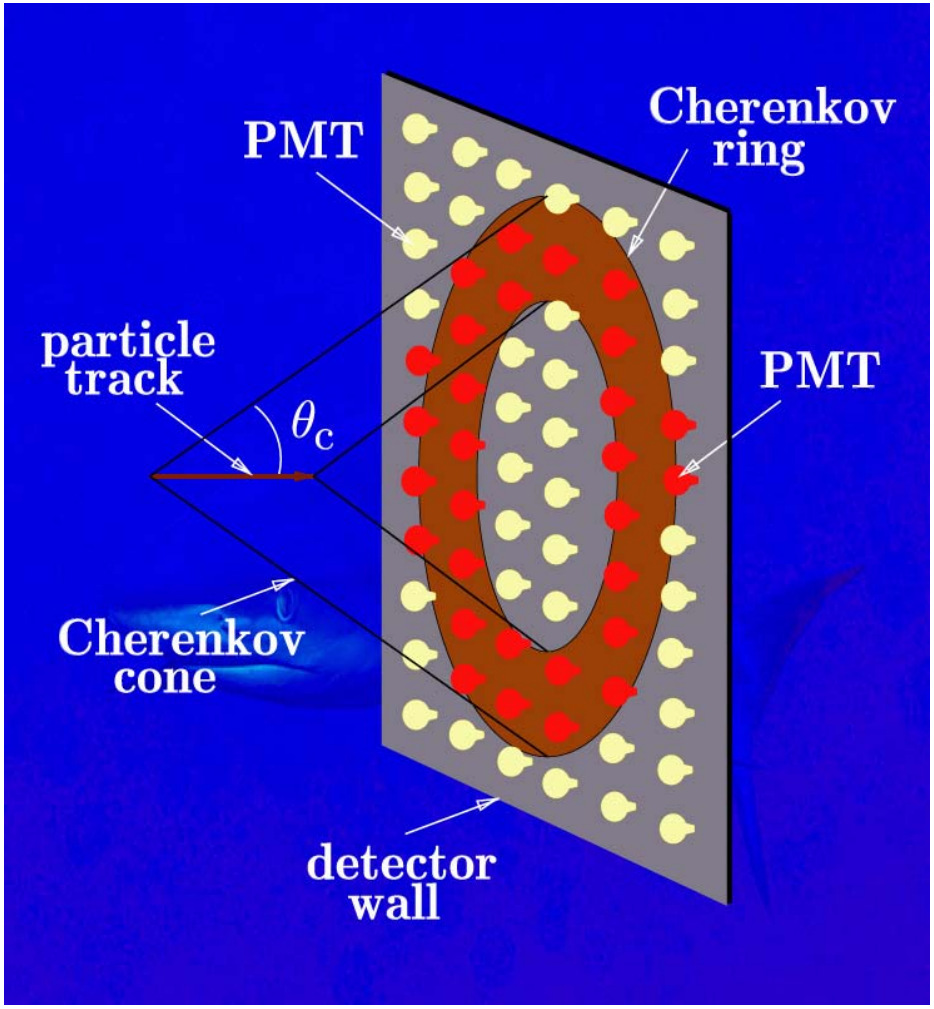

Figure 15: Cherenkov ring.

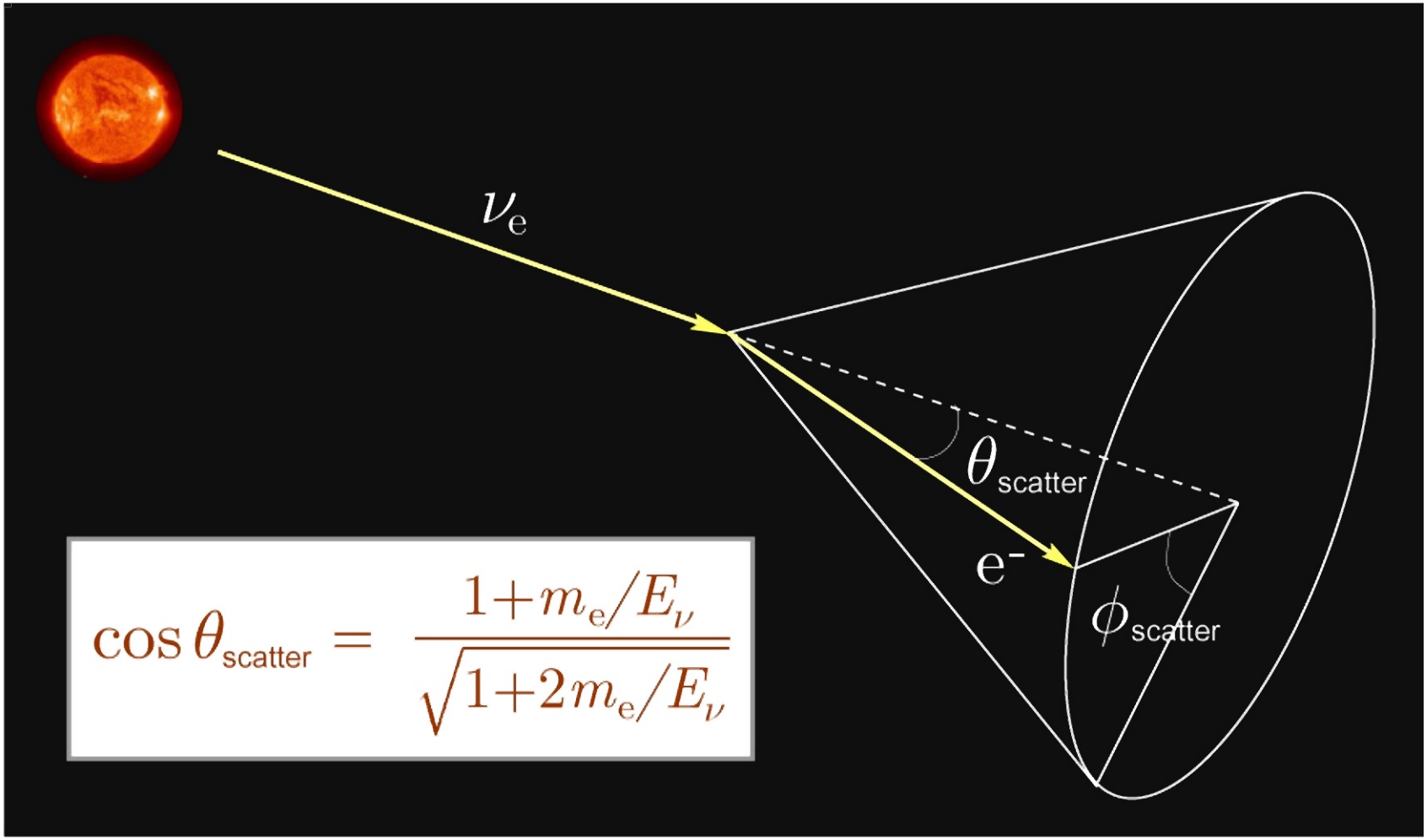
ν_e
$\theta_{scatter}$
e^-
$\phi_{scatter}$
$\cos\theta_{scatter} = \frac{1+m_e/E_\nu}{\sqrt{1+2m_e/E_\nu}}$

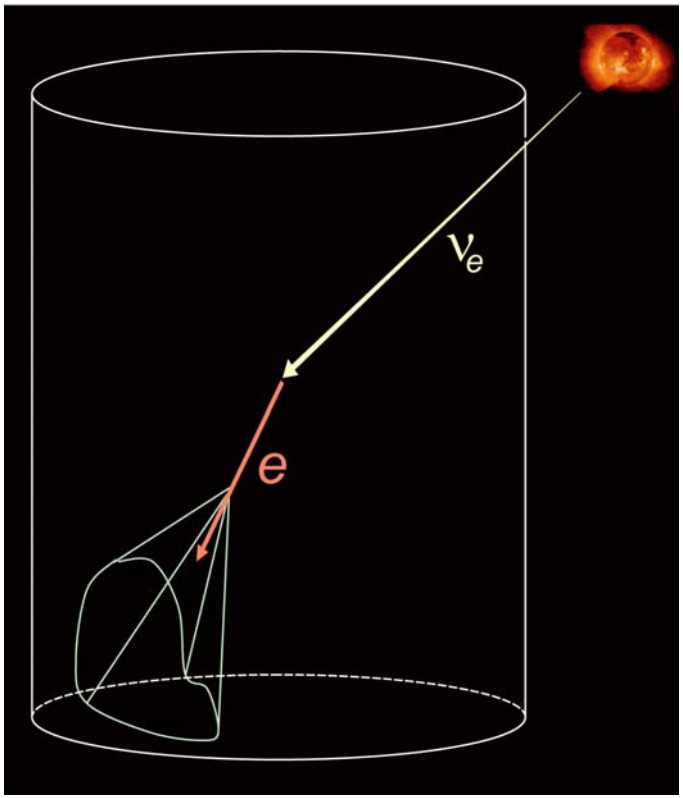

Super-Kamiokande uses elastic scattering of neutrinos from electrons. Cherenkov radiation emitted by the electron is detected by phototubes. The image looks like a diffuse ring on the detector walls.

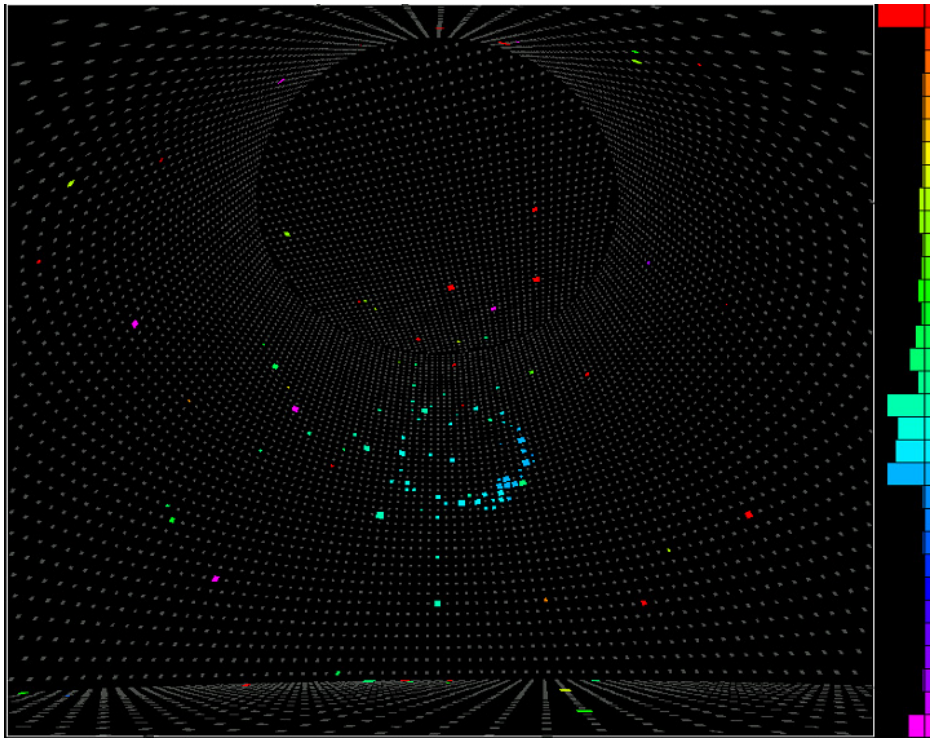

A real event recorded in the Super-Kamiokande detector on 1998-03-12 14:08:40. It is about 12.5 MeV and has an unusually nice, well-defined ring. The color scale is time. This event was found by Mark Vagins. [From I. Semeniuk, "Feature – Astronomy and the New Neutrino," Sky & Telescope, September 2004, pp. 42-48; see also Tomasz Barszczak, URL: <http://www.ps.uci.edu/~tomba/sk/tscan/pictures.html>.]

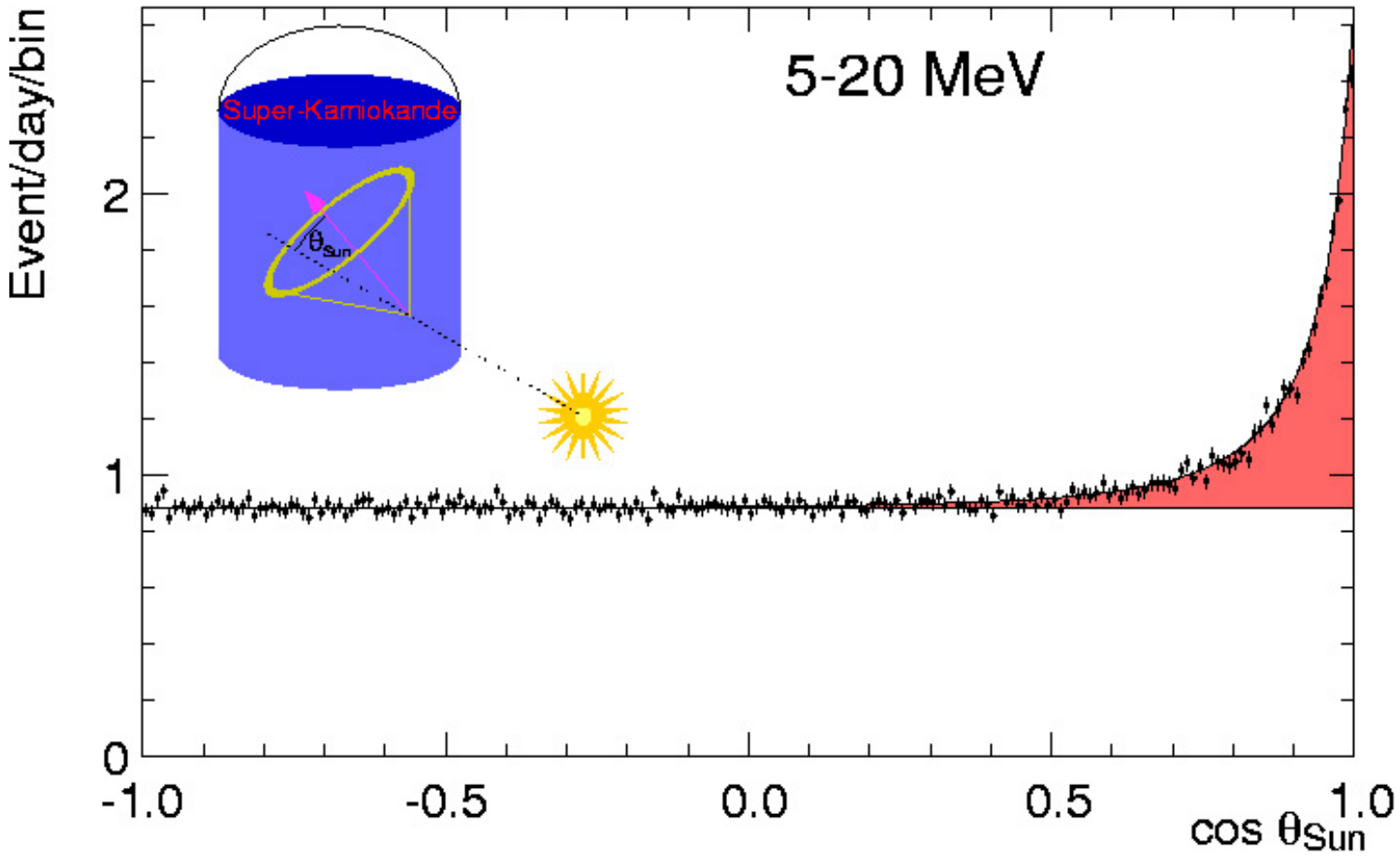

Angular distribution of solar neutrino event candidates in Super-Kamiokande-I.
The angular deviation between the solar and the reconstructed direction of events with total energies ranging between 5 and 20 MeV is shown. From the strong forward peak due to elastic scattering of solar ^8B neutrinos with electrons $22,400 \pm 200_{\text{stat}}$ neutrino interactions were observed in 22,500 metric tons of water during 1496 live days.

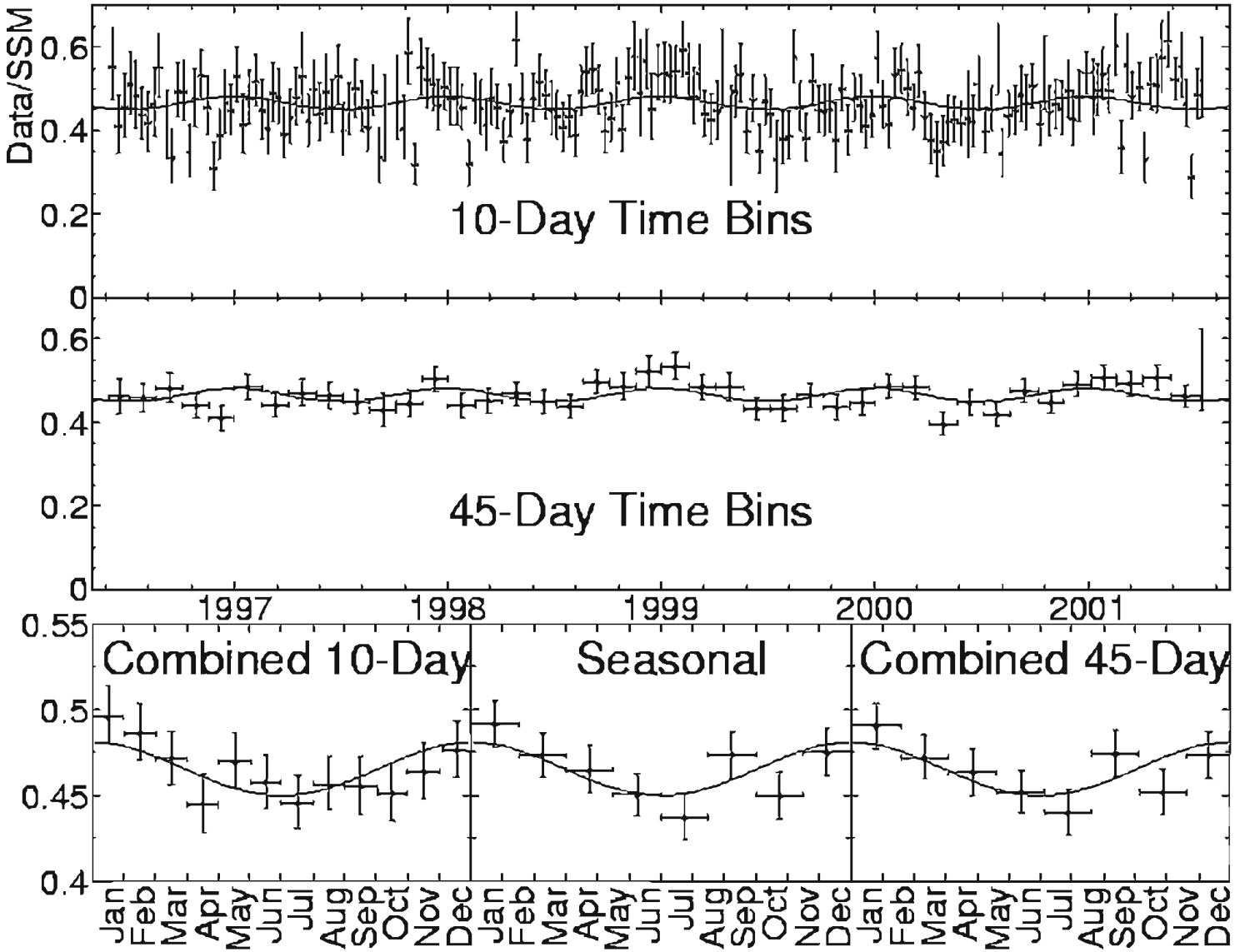
Data/SSM
0.6
0.4
0.2
0
10-Day Time Bins
0.6
0.4
0.2
0
45-Day Time Bins
1997
1998
1999
2000
2001
0.55
0.5
0.45
0.4
Combined 10-Day
Seasonal
Combined 45-Day
Jan
Feb
Mar
Apr
May
Jun
Jul
Aug
Sep
Oct
Nov
Dec

The observed solar neutrino interaction rate is

$$0.465 \pm 0.005^{+0.016}_{-0.015}$$

of the rate expected by the standard solar model (SSM). Assuming only solar ν_e the observed rate corresponds to a ^{8}B flux of

$$\Phi\left(^8\mathrm{B}\right) = (2.35 \pm 0.02_{\mathrm{stat}} \pm 0.08_{\mathrm{syst}}) \times 10^6 \ \mathrm{cm}^{-2}\mathrm{s}^{-1}.$$

All uncertainties given for the time variation data are only statistical and based on an asymmetric Gaussian approximation of the underlying likelihood functions obtained by an unbinned maximum likelihood fit to the $\cos\left(\theta_{\mathrm{Sun}}\right)$ distributions.

The top two panels show the Super-Kamiokande-I rate as a function of time. The topmost panel uses bins of 10 days width, the middle panel displays 45 day bins. The lower left panel combines the 10-day bins into 12 bins to show the yearly cycle assuming asymmetric Gaussians for the probability density functions. The lower right panel shows the yearly variation data in 8 bins obtained from a similar combination of the 45-day data bins. The middle right panel is the yearly variation data in those same 8 bins, but resulting directly from a maximum likelihood fit to the $\cos\left(\theta_{\mathrm{Sun}}\right)$ distribution.

15 D_2O detector SNO

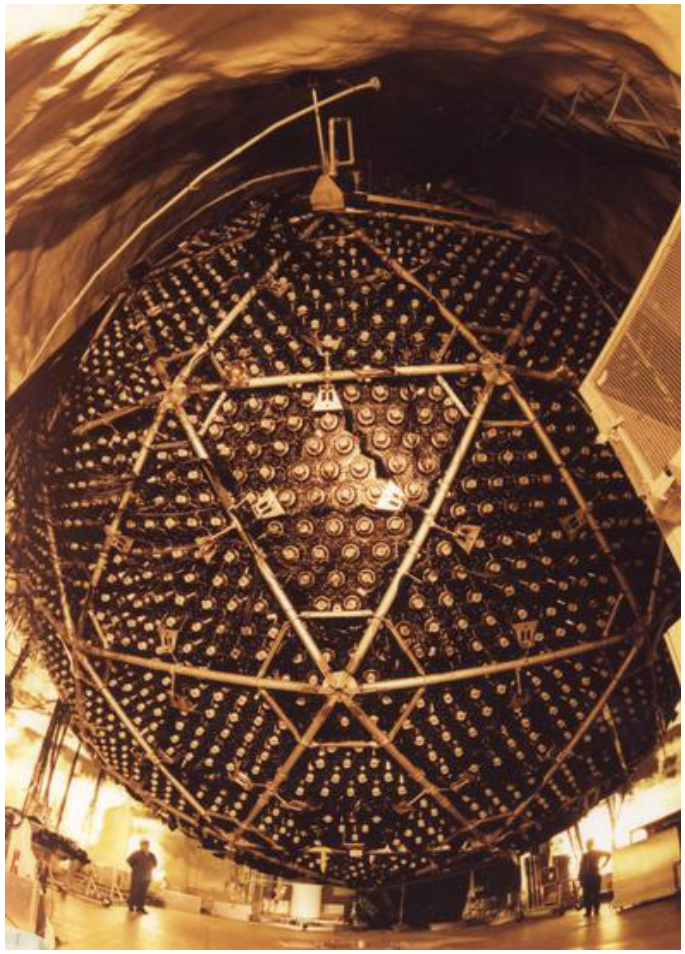

Artist's concept of the SNO detector (left) and a view of the SNO detector after installation of the bottom PMT panels, but before cabling (photo by Ernest Orlando, Lawrence Berkeley National Laboratory).

[From The Sudbury Neutrino Observatory webpage, <http://www.sno.phy.queensu.ca/sno/>.]

Part IV

ATMOSPHERIC NEUTRINOS

16 Why are the atmospheric neutrinos important for astroparticle physics?

The mechanism of muon and neutrino production in the atmosphere is well understood. They come into being from the decay of unstable particles, generated in the collisions of primary and secondary cosmic rays with air nuclei.
However the chain of processes which lead to lepton generation is rather intricate seeing that the primaries and secondaries (both stable and unstable) can repeatedly interact in the atmosphere with absorption, regeneration or overcharging, and dissipation of energy through electromagnetic interactions.

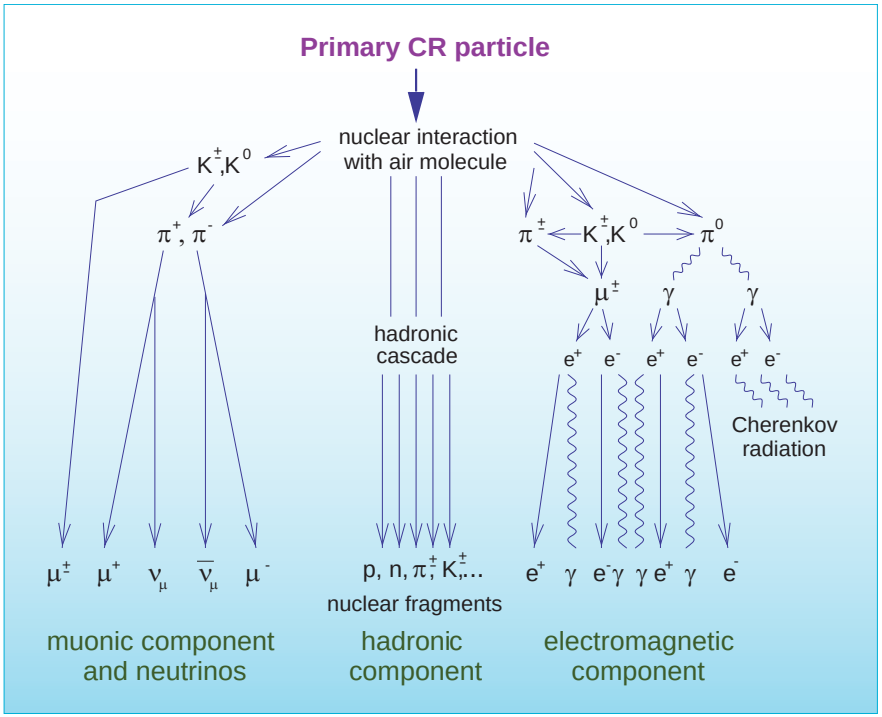

Figure 16: Schematic view of atmospheric cascade initiated by a primary CR particle.

- ⋆ **Geomagnetic effects.** At low energies, the Earth's magnetic field gives rise to the spatial (longitudinal and latitudinal) and angular (zenithal and azimuthal) asymmetries in the lepton fluxes. Complicated structure of the real geomagnetic field, the Earth's penumbra, and re-entrant albedo embarrass the analysis of the geomagnetic effects.
- ⋆ **Solar activity.** Quasi-periodical variations of solar activity modify the low-energy part of the primary cosmic-ray spectrum and therefore affect the muon and neutrino intensities (below some hundreds of MeV), making them time-dependent.
- ⋆ **3D effects.** At very low energies ($E_{\mu,\nu} \lesssim 500$ MeV), the 3-dimensionality of nuclear reactions and decays is important.
- ⋆ **Meteorological effects.** These are essential at all energies of interest.
- ⋆ **Muon polarization and depolarization effects.** Muons whose decay is an important source of neutrinos up to the multi-TeV energy range, change their polarization due to energy loss and multiply scattering, affecting the neutrino spectra.
- ⋆ **Branchy chains.** With increasing energy, life-times of light mesons grow and the production and decay chains become branchy: "anything produce everything".

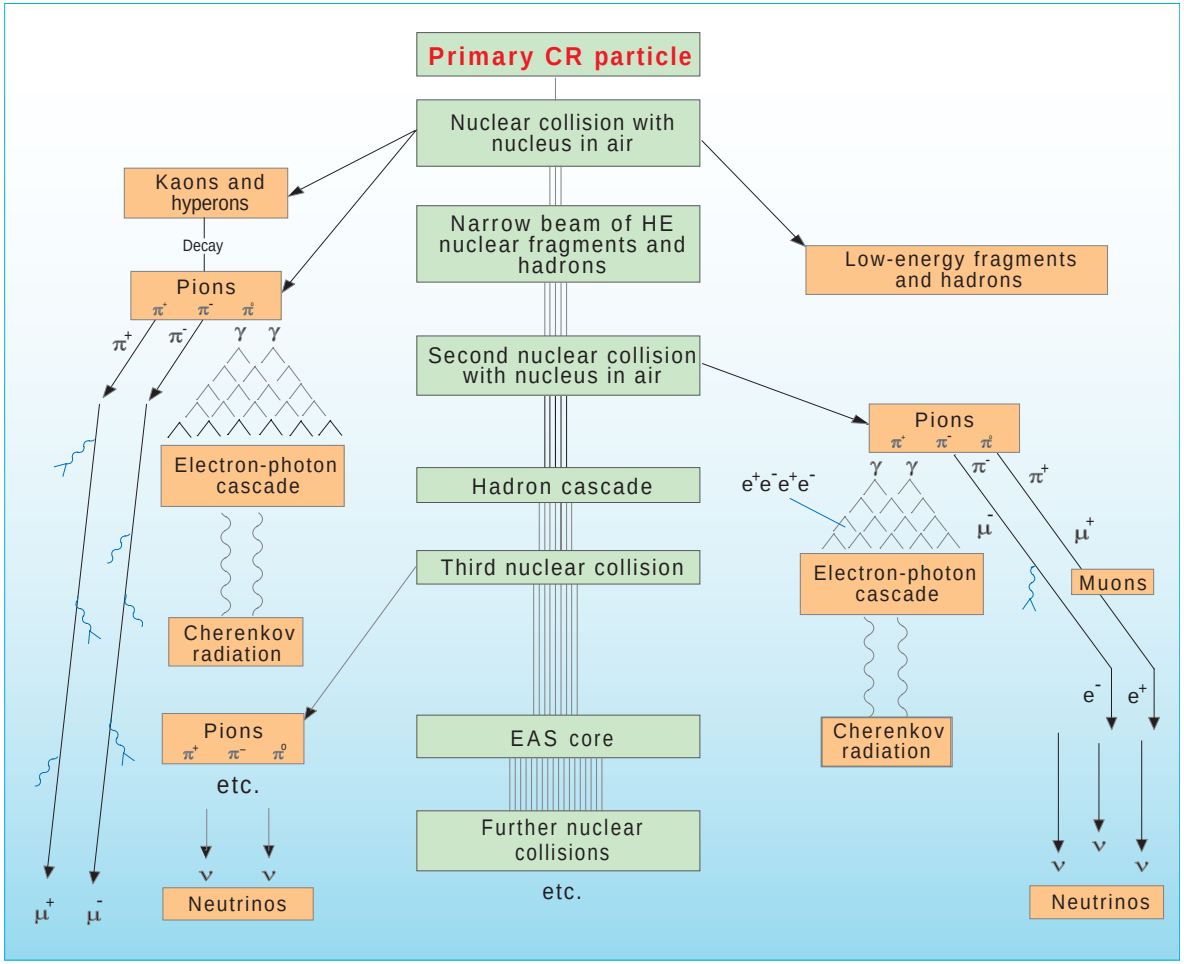

Figure 17: The same as in Fig. 16 but with more details.

Consequently, an accurate calculation of the muon and neutrino fluxes presents a hard multi-factor problem complicated by uncertainties in the primary cosmic-ray spectrum and composition, inclusive and total inelastic cross sections for particle interactions and by pure computational difficulties. But solution of this problem is a prime necessity for the study of many fundamental issues of particle physics, astrophysics, and cosmology.

- **Annoying background.** The AN flux represents an unavoidable background for some key low-energy experiments with underground detectors, e. g.:
  - ⋆ Search for proton decay and $n \longrightarrow \overline{n}$ transitions in nuclei.

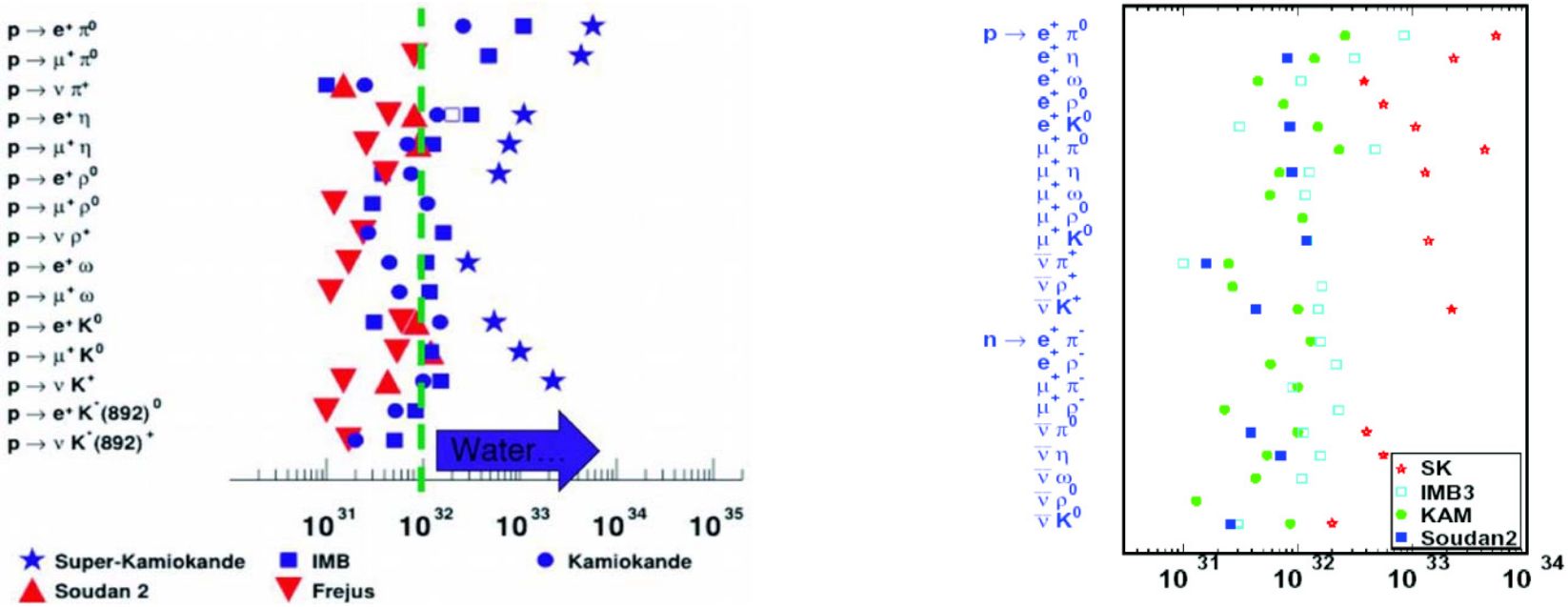

Figure 18: Proton decay limits.

- ⋆ Most of experiments on high-energy neutrino astrophysics with present-day and future large full-size underwater or underice neutrino telescopes.
  Among the astrophysical experiments are
  - detection of neutrinos from the (quasi)diffuse neutrino backgrounds, like pregalactic neutrinos, neutrinos from the bright phase of galaxy evolution, from active galactic nuclei (AGN), and other astrophysical sources,
  - indirect detection of *non-relativistic* dark matter (presumably composed of neutralinos) through neutrinos produced in the annihilation of the dark-matter particles captured in the Earth and the Sun, or
  - direct detection of *relativistic* WIMPs (weakly-interacting massive particles) of astrophysical or cosmological origin.

  These experiments will be an effect of the AN flux of energies from about 1 TeV to some tens of PeV. However, in the absence of a generally recognized and tried model for charm hadroproduction, the current estimates of the ν_μ and (most notably) ν_e backgrounds have inadmissibly wide scatter even at multi-TeV neutrino energies, which shoots up with energy. At $E_\nu \sim 100$ TeV, different estimates of the ν_μ and ν_e spectra vary within a few orders of magnitude.

- **Neutrino oscillations and all that** [the main issue of our lectures]. At the same time, the AN flux is a natural instrument for studying neutrino oscillations, neutrino decay and neutrino interactions with matter at energies beyond the reach of accelerator experiments.

- **HE neutrino interactions.** Measurements of the cross sections for $\nu_\ell N$ and $\overline{\nu}_\ell N$ charged-current interactions at $\sqrt{s} \sim m_W$ ($E_\nu \sim 3.4$ TeV) provide an important test of the Standard Model of electroweak interactions. With modern accelerators, the interactions of neutrinos are studied at energies up to several hundreds of GeV (besides the single very high energy HERA data point extracted from the $ep \to \nu X$ cross section), whereas deep underwater experiments with AN will enable to enlarge the region of neutrino energies up to a few tens of TeV.
- Future "KM3" (cubic-kilometer-size) deep-underwater/ice neutrino telescopes will be able to study the production of the standard vector $q\overline{q}$ resonances (ρ, D_s^* and possibly $\overline{t}b$) and the resonant W^- production ($E_\nu^{\rm res} = m_W^2/(2m_e) \simeq 6.3$ PeV) in $\overline{\nu}_e e^-$ annihilation as well as hypothetical nonstandard interactions of neutrinos like interactions induced by off-diagonal neutral currents or the charged-current processes with production of supersymmetric particles or with an exchange of light leptoquarks and so forth.

  Considerable attention has been focused on a possible nonperturbative behavior in the electroweak sector of the Standard Model, at energies above a threshold $\sqrt{\hat{s}_0} \gg m_W$, responsible for multiple production of gauge and Highs bosons in νN interactions with a sizeable cross section. The AN flux of the appropriate energies (above ~ 10 PeV) proves to be too small. Hopefully, neutrinos from AGN or gamma-ray bursts (GRB) may provide a possibility for studying this phenomenon with future large-scale neutrino telescopes.

In any event, – to correct for the neutrino background and to use the AN flux as the *subject* of investigations or as a *tool* for particle physics, – there is a need to employ accurate, detailed, and reliable calculations for the energy spectra, spatial and angular distributions of AN over a wide range of neutrino energies (from ~ 100 MeV up to the multi-PeV energy range) as well as calculations of the transport of neutrinos through the Earth with taking account for their absorption due to charged currents and regeneration via neutral currents. The latter effects become essential for $E_\nu \gtrsim 1$ TeV.

Admittedly, we are as yet far from that goal, despite of a considerable progress made in the past years.

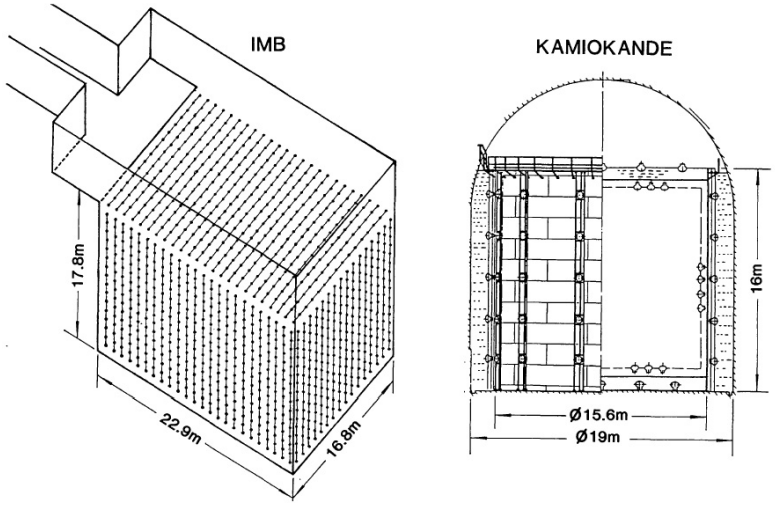

Figure 19: Water Cherenkov detectors.

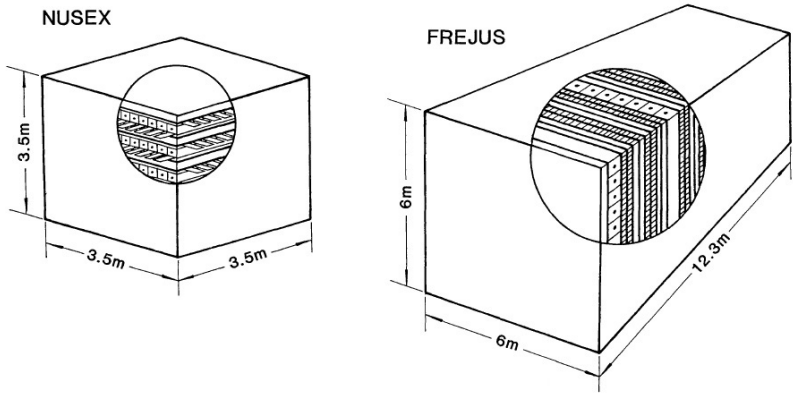

Figure 20: Tracking calorimeter detectors.

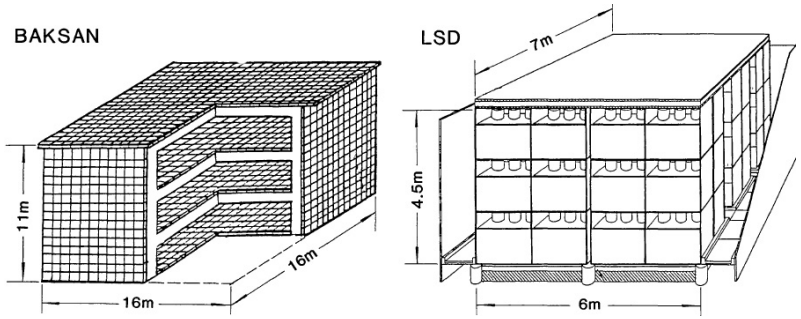

Figure 21: Liquid scintillator detectors.

Figures 19–21[a] show the park of underground detectors (as it was on 1989) capable to catch atmospheric neutrinos. Only the Baksan telescope remains in operation till now (2005).

[a] Borrowed from A. M. Bakich, "Aspects of neutrino astronomy," Space Sci. Rev. **49** (1989) 259–310.

17 Why are the atmospheric muons important for astroparticle physics?

The flux of cosmic-ray muons in the atmosphere, underground, and underwater provides a way of testing the inputs of nuclear cascade models, that is, parameters of the primary cosmic rays (energy spectrum, chemical composition) and particle interactions at high energies. In particular, measurements of the muon energy spectra, angular distributions and the depth-intensity relation (DIR) have much potential for yielding information about the mechanism of charm production in hadron-nucleus collisions at energies beyond the reach of accelerator experiments. This information is a subject of great current interest for particle physics and yet is a prime necessity in high-energy and very high-energy neutrino astronomy.

The present state of the art of predicting the AN flux seems to be more satisfactory at energies below a few TeV. However, the theory meets more rigid requirements on accuracy of the calculations here: for an unambiguous treatment of the current data on the AN induced events in the underground detectors, it would be good to calculate the AN flux with a 10 % accuracy at least, whereas the uncertainties in the required input data (primary spectrum, cross sections for light meson production, etc.) hinder to gain these ends. Because of this, a vital question is a "normalization" (or adjustment) of the calculated model-dependent atmospheric neutrino flux and the muon flux is perhaps the only tool for such a normalization.

Mesotron as the Name of the New Particle

After reading Professor Bohr's address at the British Association last September in which he tentatively suggested the name "yucon" for the newly discovered particle, I wrote to him incidently mentioning the fact than Anderson and Neddermeyer had suggested the name "mesotron" (intermediate particle) as the most appropriate name. I have just received Bohr's reply to this letter in which he says:

"I take pleasure in telling you that every one at a small conference on cosmic-ray problems, including Auger, Blackett, Fermi, Heisenberg, and Rossi, which we have just held in Copenhagen, was in complete agreement with Anderson's proposal of the name 'mesotron' for the penetrating cosmic-ray particles."

ROBERT A. MILLIKAN

California Institute of Technology,
Pasadena, California,
December 7, 1938.

[Phys. Rev. **55** (1939) 105 (a letter to the editor).]

An editorial problem has arisen with regard to the designation of the particle of mass intermediate between the electron and the proton. In the original papers and discussion no less than six different names were used. A vote indicated about equal choice between *meson* and *mesotron* with no considerable support for *mesoton*, *barytron*, *yukon* or *heavy electron*. Except where the authors have indicated a distinct preference to the contrary, we have chosen to use the term *mesotron*.

ARTHUR H. COMPTON

[Rev. Mod. Phys. **11** (1939) 122 (from the foreword to the Proceedings of the Symposium on Cosmic Rays, held at the University of Chicago, June 1939).]

The point is that atmospheric muons and neutrinos are generated in just the same processes. Therefore the accuracy of the neutrino flux calculation can be improved by forcing the poorly known input parameters of the cascade model (including the parameters of the primary CR spectrum and composition) in order to fit the experimental data on the muon energy spectra, angular distributions, charge ratio, and depth-intensity relation.

18 Main sources of atmospheric lepton production

18.1 Conventional ("π, K") leptons

Low-energy leptons ($E_{\mu,\nu} < 10 - 15$ GeV) are produced mainly in the two-particle leptonic decays of charged pions and kaons, $\pi_{\mu 2}$ and $K_{\mu 2}$ (Table 6).

Table 6: Main sources of conventional atmospheric leptons. [The data are from K. Hagiwara *et al.*, Phys. Rev. D **66** (2002) 010001.]

Particle	Exclusive decay mode	Branching ratio
$\mu^{\pm}$	$e^{\pm} + \nu_e(\overline{\nu}_e) + \overline{\nu}_\mu(\nu_\mu)$	$\simeq 100\%$ [a]
$\pi^{\pm}$	$\mu^{\pm} + \nu_\mu(\overline{\nu}_\mu)$	$\simeq 100\%$
$K^{\pm}$	$\mu^{\pm} + \nu_\mu(\overline{\nu}_\mu)$	$(63.43 \pm 0.17)\%$
	$\pi^0 + e^{\pm} + \nu_e(\overline{\nu}_e)$	$(4.87 \pm 0.06)\%$
	$\pi^0 + \mu^{\pm} + \nu_\mu(\overline{\nu}_\mu)$	$(3.27 \pm 0.06)\%$
K_L^0	$\pi^{\pm} + e^{\mp} + \overline{\nu}_e(\nu_e)$	$(38.79 \pm 0.27)\%$ [b,c]
	$\pi^{\pm} + \mu^{\mp} + \overline{\nu}_\mu(\nu_\mu)$	$(27.18 \pm 0.25)\%$ [c]

[a] Including the radiative mode $e^{\pm} + \nu_e(\overline{\nu}_e) + \overline{\nu}_\mu(\nu_\mu) + \gamma$ whose fraction is $(1.4 \pm 0.4)\%$ for $E_\gamma > 10$ MeV. The two modes cannot be clearly separated.

[b] Including most of the radiative mode $\pi^{\pm} + e^{\mp} + \overline{\nu}_e(\nu_e) + \gamma$ with low-momentum γ part.

[c] The value is for the sum of the particle/antiparticle states.

Muon decays is the basic source of ν_e and $\overline{\nu}_e$ in this energy range and the muon polarization is an essential factor affecting the neutrino flavor ratio $(\nu_\mu + \overline{\nu}_\mu) / (\nu_e + \overline{\nu}_e)$ as well as the neutrino to antineutrino ratios, $\nu_e/\overline{\nu}_e$ and $\nu_\mu/\overline{\nu}_\mu$. At higher energies, above 10–15 GeV, the semileptonic decays of charged and neutral longlived kaons (K_{e3} and $K_{\mu 3}$) become important (last four lines in Table 6) and hence the differential cross sections for kaon production in NA, πA and KA interactions are required for the calculations.

Table 7: Most important pionic decays which contribute to the atmospheric lepton production. [The data are from K. Hagiwara *et al.*, Phys. Rev. D **66** (2002) 010001.]

Particle	Exclusive decay mode	Branching ratio
K_S^0	$\pi^+ + \pi^-$	$(68.60 \pm 0.27)\%$
K_L^0	$\pi^+ + \pi^- + \pi^0$	$(12.58 \pm 0.19)\%$
$K^\pm$	$\pi^\pm + \pi^0$	$(21.13 \pm 0.14)\%$
	$\pi^\pm + \pi^\pm + \pi^\mp$	$(5.576 \pm 0.031)\%$
	$\pi^\pm + \pi^0 + \pi^0$	$(1.73 \pm 0.04)\%$
Λ	$p + \pi^-$	$(63.9 \pm 0.5)\%$

With increasing energy, muon decays become ineffective for neutrino production and, since the kaon production cross sections are small compared to the pion production ones, the high-energy AN flux consists mainly of ν_μ and $\overline{\nu}_\mu$. For instance, within the

energy range 1 to 100 TeV, the flavor ratio for the conventional AN flux is a monotonically increasing function of energy varying from about 28 to 34 at $\vartheta = 0^\circ$ and from about 13 to 34 at $\vartheta = 90^\circ$. However, the contribution from decay of charmed particles results in a decrease of the AN flavor ratio (see below).

Contributions from the decay chains $K, \Lambda \to \pi \to \mu \to \nu$ are usually small while not completely negligible. The most important pionic decays which contribute to the atmospheric lepton production are listed in Table 7.

At very high energies there are a few more significant decay modes. These are listed in Table 8.

Table 8: Decays which become significant at very high lepton energies. [The data are from K. Hagiwara *et al.*, Phys. Rev. D **66** (2002) 010001.]

Particle	Exclusive decay mode	Branching ratio
K_S^0	$\pi^\pm + e^\mp + \overline{\nu}_e(\nu_e)$	$(7.2 \pm 1.4) \times 10^{-4}$ [a]
	$\pi^\pm + \mu^\mp + \overline{\nu}_\mu(\nu_\mu)$	–
Λ	$p + e^- + \overline{\nu}_e$	$(8.32 \pm 0.14) \times 10^{-4}$
	$p + \mu^- + \overline{\nu}_\mu$	$(1.57 \pm 0.35) \times 10^{-4}$

[a] The value is for the sum of the particle/antiparticle states.

18.2 Prompt leptons

The dominant contribution to the AN flux at very high energies[a] is due to semileptonic decays of charmed hadrons (mainly $D^{\pm}$, D^{0}, $\overline{D}^{0}$ and Λ_c^{+}). The leptons from this source are called prompt leptons.

There are numerous exclusive decay modes of charmed particles with a lepton pair and one or more hadrons in the final state; the inclusive semileptonic decays of D, D_s, and Λ_c^{+} are shown in Table 9. The dashes indicate the absence of direct data but, owing to the $\mu - e$ universality, one can expect that the branching ratios for electron and muon inclusive modes are close to each other. Branching ratios for pure leptonic modes (with $\ell\nu_\ell$ in final state) are very small except the case of $D_s^{\pm} \to \tau^{\pm} + \nu_\tau(\overline{\nu}_\tau)$. The latter mode is however very important, being the main source of atmospheric tau leptons and tau neutrinos.

Calculations of the prompt lepton fluxes (and even the energy ranges in which these contributions dominate) are very model-dependent. As yet, these fluxes cannot be unambiguously predicted for lack of a generally accepted model for charm production at high energies.

[a] For muons and muon (anti)neutrinos, at $E_{\mu,\nu} > 10 - 100$ TeV for vertical flux and at $E_{\mu,\nu} > 100 - 1000$ TeV for horizontal flux; for electron (anti)neutrinos at energies which are an order of magnitude less (see below).

Table 9: The most important (semi)leptonic decays of charmed hadrons. [The data are from K. Hagiwara *et al.*, Phys. Rev. D **66** (2002) 010001.]

Particle	Decay mode	Branching ratio
$D^{\pm}$	$e^{\pm} + \nu_e(\overline{\nu}_e)$ + hadrons	$(17.2 \pm 1.9)\%$
	$\mu^{\pm} + \nu_\mu(\overline{\nu}_\mu)$ + hadrons	–
D^0	$e^{+} + \nu_e$ + hadrons	$(6.87 \pm 0.28)\%$
	$\mu^{+} + \nu_\mu$ + hadrons	$(6.5 \pm 0.8)\%$
$D_s^{\pm}$	$e^{\pm} + \nu_e(\overline{\nu}_e)$ + hadrons	$(8^{+6}_{-5})\%$
	$\mu^{\pm} + \nu_\mu(\overline{\nu}_\mu)$ + hadrons	–
	$\tau^{\pm} + \nu_\tau(\overline{\nu}_\tau)$ + hadrons	–
	$\tau^{\pm} + \nu_\tau(\overline{\nu}_\tau)$	$(6.4 \pm 1.5)\%$
Λ_c^{+}	$e^{+} + \nu_e$ + hadrons	$(4.5 \pm 1.7)\%$
	$\mu^{+} + \nu_\mu$ + hadrons	–

The salient and almost model-independent features of the prompt neutrino flux are (a) it is practically isotropic within a wide energy range (namely, at $1 \text{ TeV} \lesssim E_\nu \lesssim 3 \times 10^3 \text{ TeV}$, the maximal anisotropy is about 3–4%) and (b) the neutrino to antineutrino ratios and the flavor ratio are close to 1. These features provide a way to discriminate the prompt neutrino contribution through the analysis of the angular distribution and the relationship between "muonless" and "muonfull" neutrino events in a neutrino telescope. Moreover, the anisotropy of the flux of prompt muons for the same energy range is also very small ($\lesssim 20\%$). This fact can be a help in deciding the problem.

19 Atmospheric neutrinos I: Low and intermediate energies

Due to geomagnetic effects, the low-energy AN spectra and angular distributions are quite different for different sites of the globe. Figure 23 displays the predictions of CORT for ten underground neutrino laboratories listed in Table 10. Left panel shows the ν_e, $\overline{\nu}_e$, ν_μ and $\overline{\nu}_\mu$ energy spectra averaged over all zenith and azimuth angles. The ratios of the AN fluxes averaged over the lower and upper semispheres ("up-to-down" ratios) are shown in right panel. As a result of geomagnetic effects, the spectra and up-to-down ratios at energies below a few GeV are quite distinct for five groups of underground labs: 1) SOUDAN + SNO + IMB, 2) HPW, NUSEX + Fréjus, 3) Gran Sasso + Baksan, 4) Kamioka and 5) KGF.

Technical note:

The exact definition of the fluxes of upward- and downward-going neutrinos is given by the following formulas:

$$F_\nu^{\text{down}}(E) = \int_0^1 \langle F_\nu(E,\vartheta)\rangle_\varphi \, d\cos\vartheta, \tag{27a}$$

$$F_\nu^{\text{up}}(E) = \int_{-1}^0 \langle F_\nu(E,\vartheta)\rangle_\varphi \, d\cos\vartheta, \tag{27b}$$

where

$$\langle F_\nu(E,\vartheta)\rangle_\varphi = \frac{1}{2\pi}\int_0^{2\pi} F_\nu\left(E,\vartheta,R_c\left(\Theta,\Phi,\vartheta,\varphi\right)\right)d\varphi, \qquad \text{for} \quad 0 \le \vartheta \le \frac{\pi}{2}, \tag{28a}$$

$$= \frac{1}{2\pi}\int_0^{2\pi} F_\nu\left(E,\vartheta^*,R_c\left(\Theta^*,\Phi^*,\vartheta^*,\varphi^*\right)\right)d\varphi, \quad \text{for} \quad \frac{\pi}{2} \le \vartheta \le \pi, \tag{28b}$$

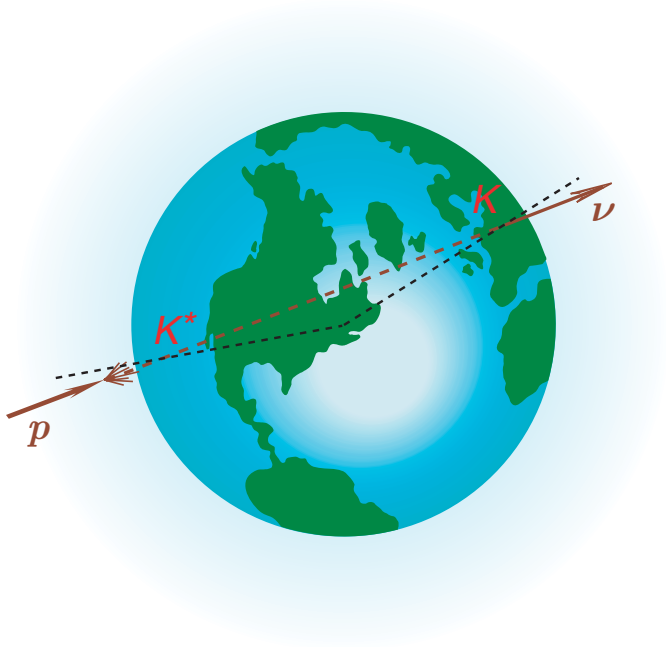

Figure 22: "Neutrinos – antipodes"

$F_\nu\left(E,\vartheta,R_c\right)$ is the neutrino differential energy spectrum on the Earth surface with the oblique geomagnetic cutoff rigidity R_c which is a function of the geomagnetic latitude and longitude, Θ and Φ, and zenith and azimuthal angles, ϑ and φ (all are defined in the frame of the detector).
The starred variables in Eq. (28b) are the corresponding angles defined in the local frame K^* associated with the neutrino entry point.
Clearly, the azimuthal dependence of the neutrino flux is only due to the geomagnetic effects. Therefore, within the framework of the 1D cascade theory, it is a function of three variables E, ϑ and R_c.

It is a useful (and not too trivial) exercise in spherical geometry to prove that

$$\begin{aligned}
\sin\Theta^* &= \sin 2\vartheta \sin\varphi \cos\Theta - \cos\vartheta \sin\Theta, \quad |\Theta^*| < \pi/2, \\
\sin\left(\Phi^* - \Phi\right) &= \sin 2\vartheta \cos\varphi / \cos\Theta^*, \\
\cos\left(\Phi^* - \Phi\right) &= -\left(\sin 2\vartheta \sin\varphi \sin\Theta + \cos 2\vartheta \cos\Theta\right) / \cos\Theta^*, \\
\vartheta^* &= \pi - \vartheta, \\
\sin\varphi^* &= \left(\sin 2\vartheta \sin\Theta + \cos 2\vartheta \sin\varphi \cos\Theta\right) / \cos\Theta^*, \\
\cos\varphi^* &= \cos\varphi \cos\Theta / \cos\Theta^*.
\end{aligned}$$

For near horizontal directions ($|\vartheta - \pi/2| \ll 1$) the above formulas yield

$$\begin{aligned}
\Theta^* &\simeq \Theta + (\pi - 2\vartheta) \sin\Phi, \\
\Phi^* &\simeq \Phi - (\pi - 2\vartheta) \cos\Phi \tan\Theta, \\
\varphi^* &\simeq \varphi + (\pi - 2\vartheta) \cos\Phi \sec\Theta.
\end{aligned}$$

Finally, the 4π averaged flux is

$$\langle F_\nu(E) \rangle_{4\pi} = \int_{-1}^{1} \langle F_\nu(E, \vartheta) \rangle_\varphi \, d\cos\vartheta = \frac{1}{2} \left[F_\nu^{\mathsf{down}}(E) + F_\nu^{\mathsf{up}}(E) \right].$$

Table 10: List of ten past and present underground laboratories. The last column shows the symbols used in Fig. 23.

Lab/Detector	Country	Geographical location		Geomagnetic location		Token
SOUDAN	USA	48.00°N	92.00°W	58.32°	331.78°	• • •
SNO	Canada	46.80°N	82.00°W	57.90°	345.79°	- - - - -
IMB	USA	41.72°N	81.27°W	52.83°	346.30°	.....
HPW	USA	40.60°N	111.00°W	48.71°	311.28°	▲ ▲ ▲
NUSEX	Italy	45.86°N	6.90°E	47.24°	89.09°	▼ ▼ ▼
Fréjus	France	45.14°N	6.69°E	46.59°	88.59°	- · - · - · -
Gran Sasso	Italy	42.45°N	13.57°E	42.64°	94.27°	———
Baksan	Russia	43.30°N	42.70°E	38.06°	121.64°	★ ★ ★
Kamioka	Japan	36.42°N	137.31°E	26.19°	204.48°	□ □ □
KGF	India	3.00°N	78.30°E	3.25°	149.36°	■ ■ ■

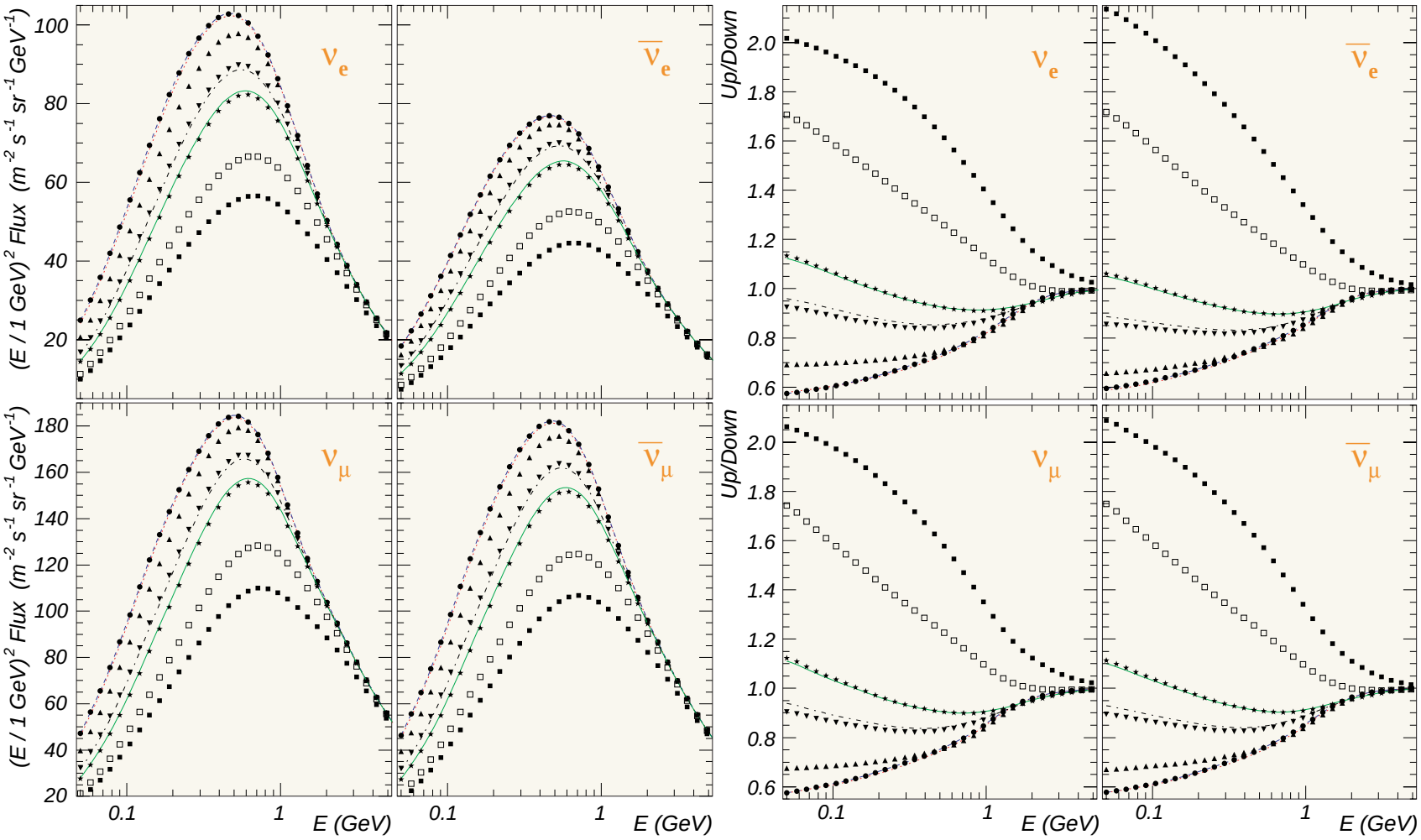

Figure 23: 4π averaged fluxes (left panel) and up-to-down ratios (right panel) of the ν_e, $\overline{\nu}_e$, ν_μ, and $\overline{\nu}_\mu$ fluxes for ten underground laboratories (see Table 10 for the notation).

Figure 24 depicts the zenith-angle distributions of ν_e, $\overline{\nu}_e$, ν_μ and $\overline{\nu}_\mu$ calculated without taking account for geomagnetic effects. Calculations with CORT are done using its "standard" (KM+SS) model for hadronic interactions and also the TARGET-1 model for π/K meson production (including the superposition model for collisions of nuclei) used by Bartol group ["CORT+TARGET"]. The distributions are averaged over azimuth angle and over the eight energy bins indicated near the curves. For comparison, the result of the calculation by Battistoni *et al*. (2000) based on the FLUKA 3D Monte Carlo simulation package is also shown. It allows to "highlight" the 3D effects which are very dependent on neutrino energy and direction of arrival. Note that the primary spectrum model used in the calculation with FLUKA is very close to the recent BESS 98 data, but it is not identical to the parametrization adopted in CORT ("BESS+JACEE fit").

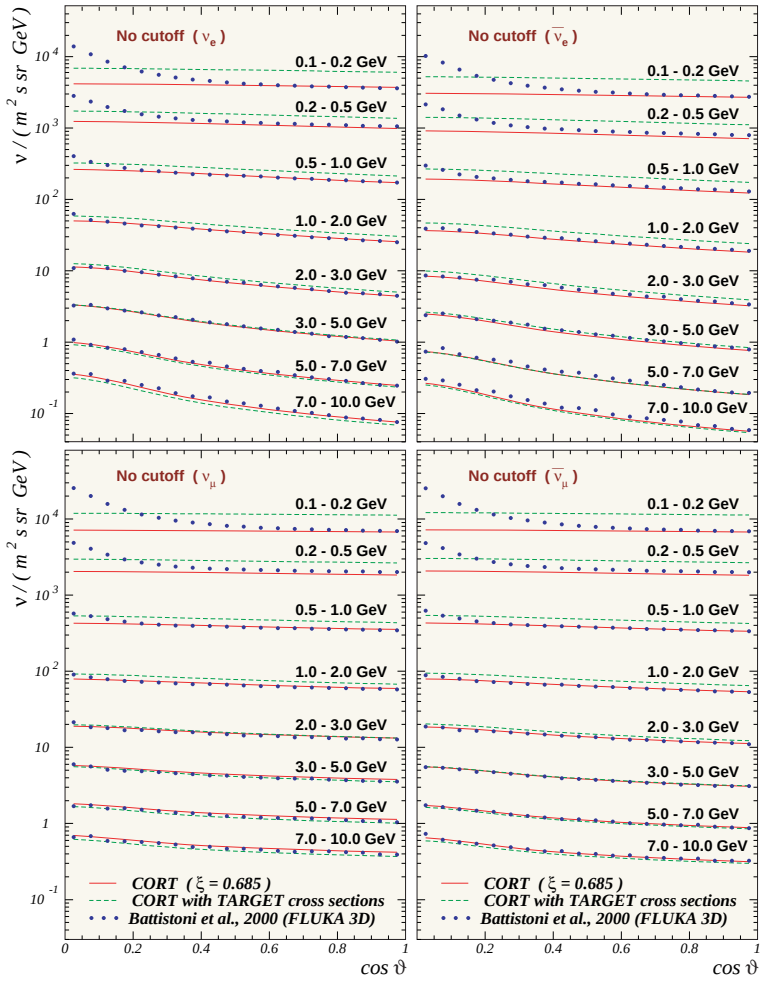

Figure 24: Zenithal distributions of down-going ANs on geomagnetic poles.

Figure 25 shows the same as Fig. 24 but for Kamioka and Gran Sasso.

Figure 26 shows the azimuth-angle averaged zenithal distributions of ν_e, $\overline{\nu}_e$, ν_μ and $\overline{\nu}_\mu$ calculated with FLUKA 3D for several values of neutrino energy and normalized to the same distributions calculated with CORT. The geomagnetic effects are neglected in both calculations.

Figures 24–26 clearly demonstrate that the 3D effects drastically change the angular distributions of low-energy ANs at large zenith angles (near-horizontal directions). However, above $500 - 600$ MeV they become almost negligible and practically disappear at energies above ~ 1 GeV.

Figure 27 shows the ν_e, $\overline{\nu}_e$, ν_μ and $\overline{\nu}_\mu$ energy spectra averaged over both zenith and azimuth angles. The shaded areas are the results obtained with CORT using its standard interaction model. The widths of the areas indicate the uncertainty due to variations of the ξ parameter between 0.517 and 0.710. One sees that this uncertainty is at most 6% and thus it is negligible. The dashed curves correspond to the CORT+TARGET model while the circles show the results of the FLUKA 3D calculation.

Figures 28, 29 and 30 shows some results of early calculations of the AN flux at low and high energies.

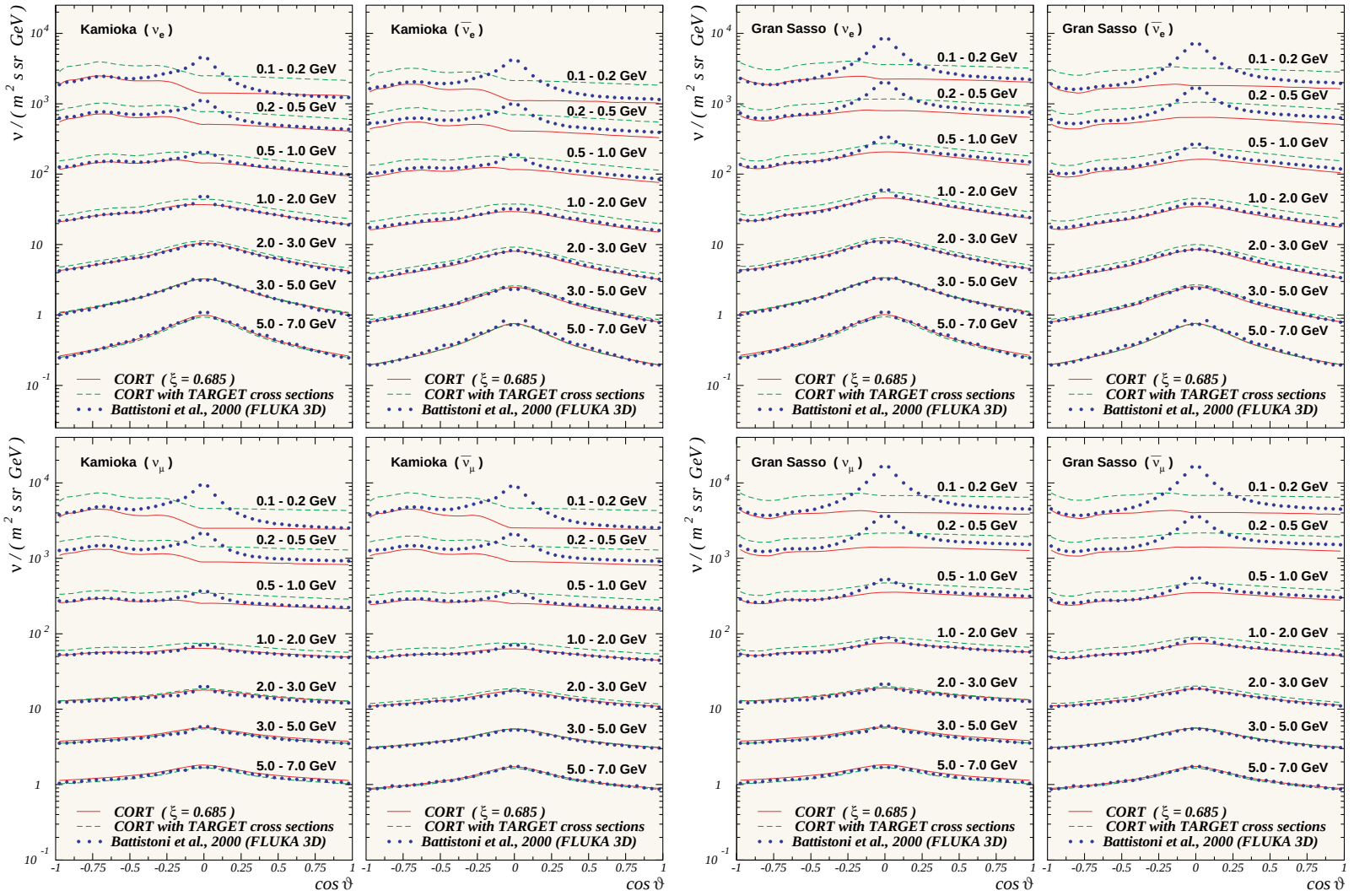

Figure 25: The same as Fig. 24 but for Kamioka and Gran Sasso and for $0 \leq \vartheta \leq 180°$.

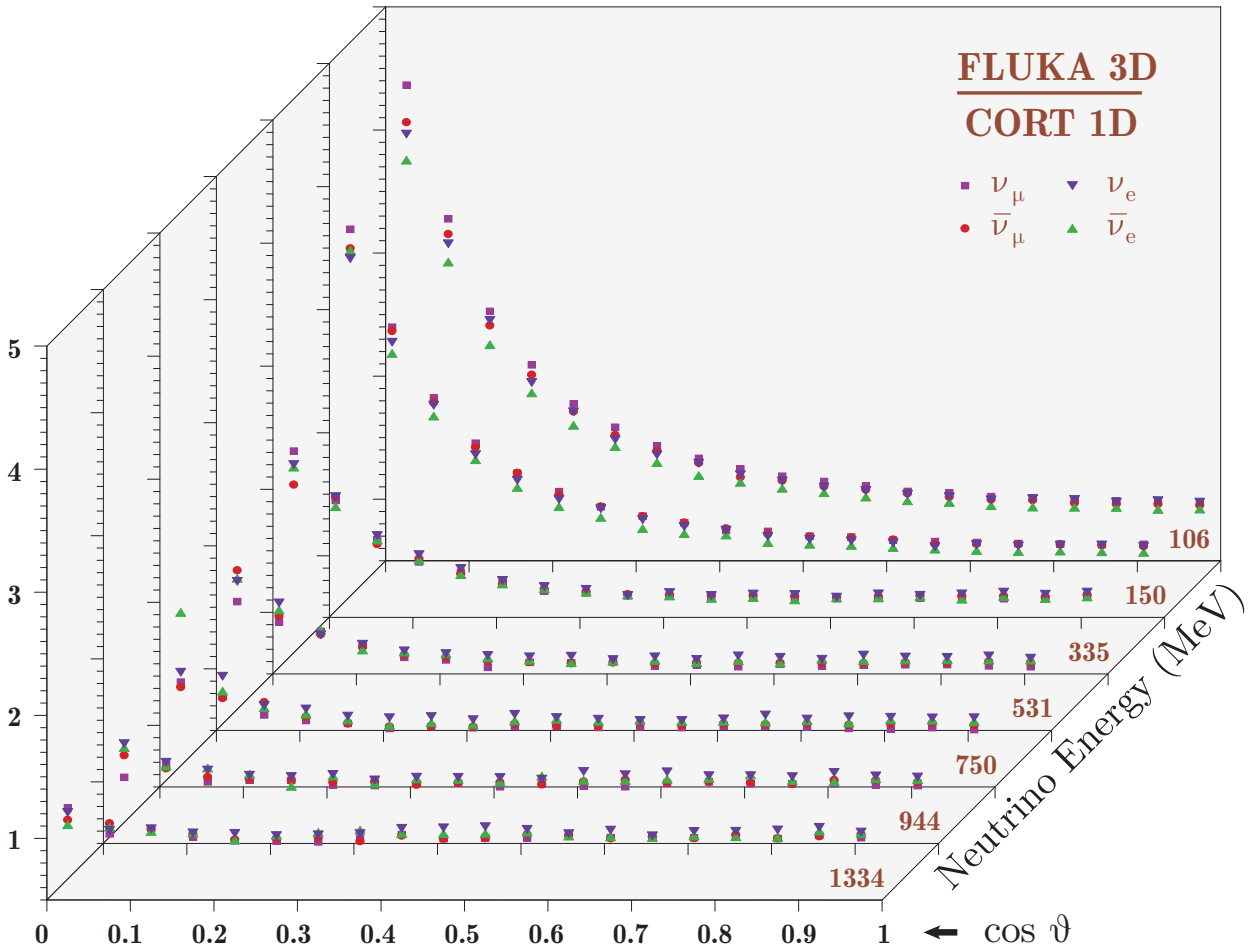

Figure 26: Zenithal distributions of ANs calculated with FLUKA 3D for seven values of neutrino energy and normalized to the same distributions calculated with CORT. The geomagnetic effects are neglected.

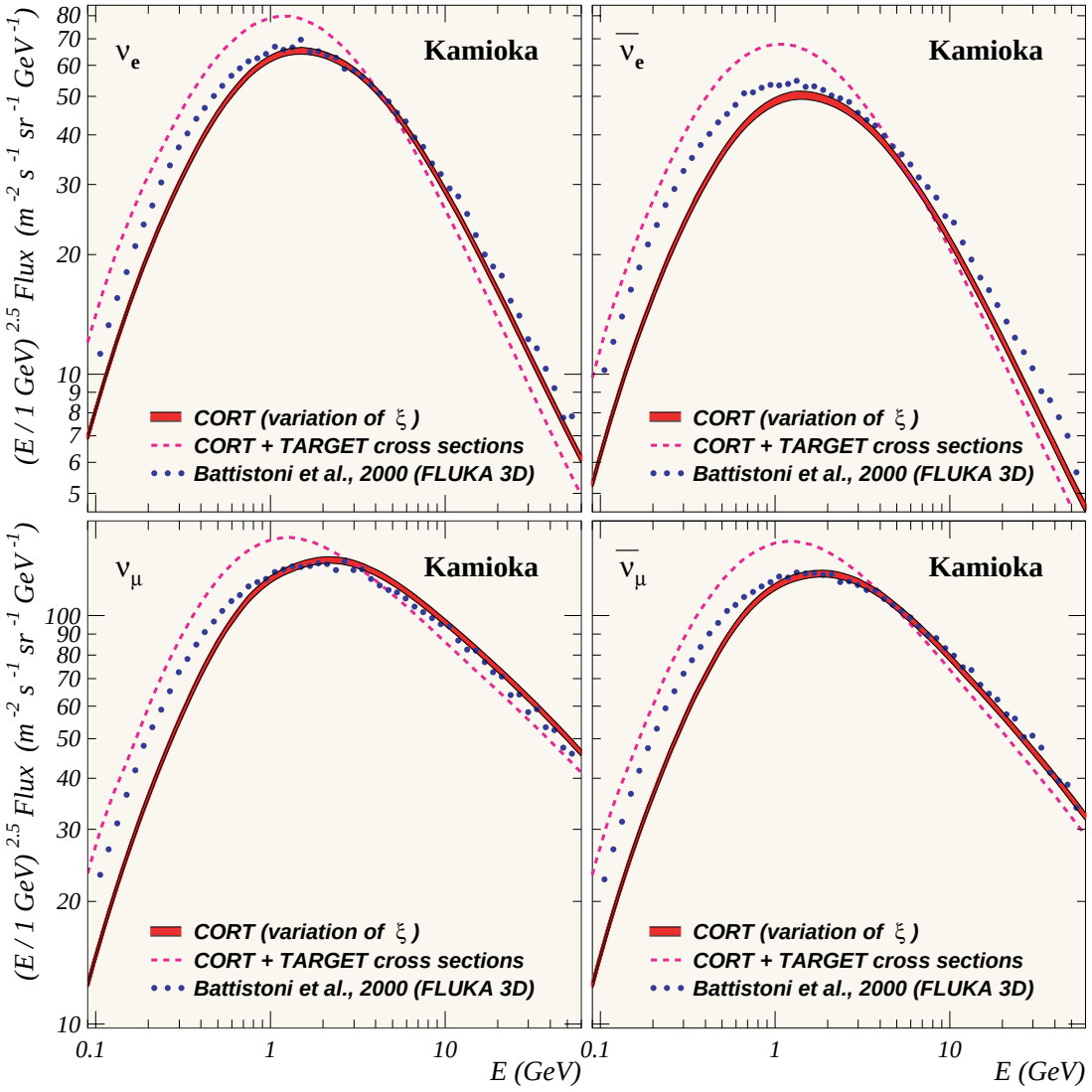

Figure 27: Scaled 4π averaged AN fluxes for Kamioka site.

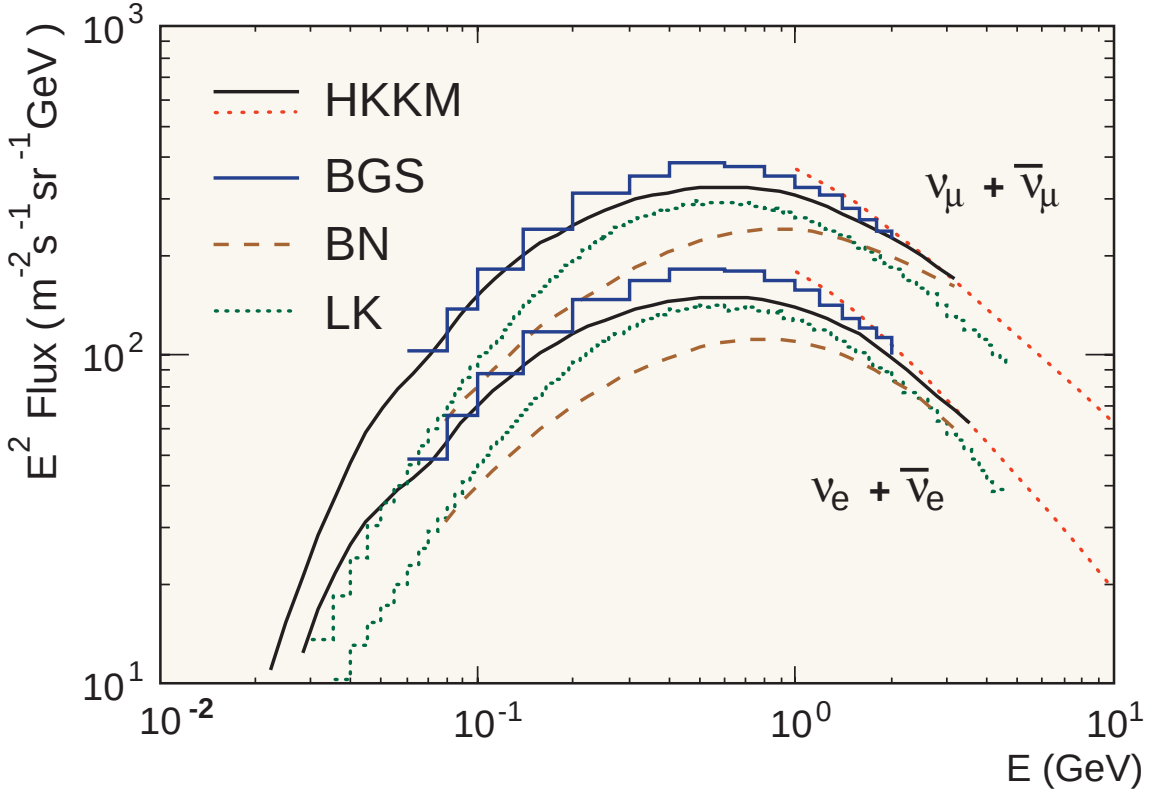

Figure 28: Comparison between early calculations of the low-energy 4π averaged AN fluxes for Kamioka site: M. Honda, T. Kajita, K. Kasahara and S. Midorikawa, Phys. Rev. D **52** (1995) 4985 (HKKM), G. Barr, T. K. Gaisser and T. Stanev, Phys. Rev. D **39** (1989) 3532 (BGS), E. V. Bugaev and V. A. Naumov, Phys. Lett. B **232** (1989) 391 (BN), H. Lee and Y. S. Koh, Nuovo Cim. **105 B** (1990) 883 (LK). The dotted lines represent the results of Honda *et al*. obtained for without geomagnetic cutoff.

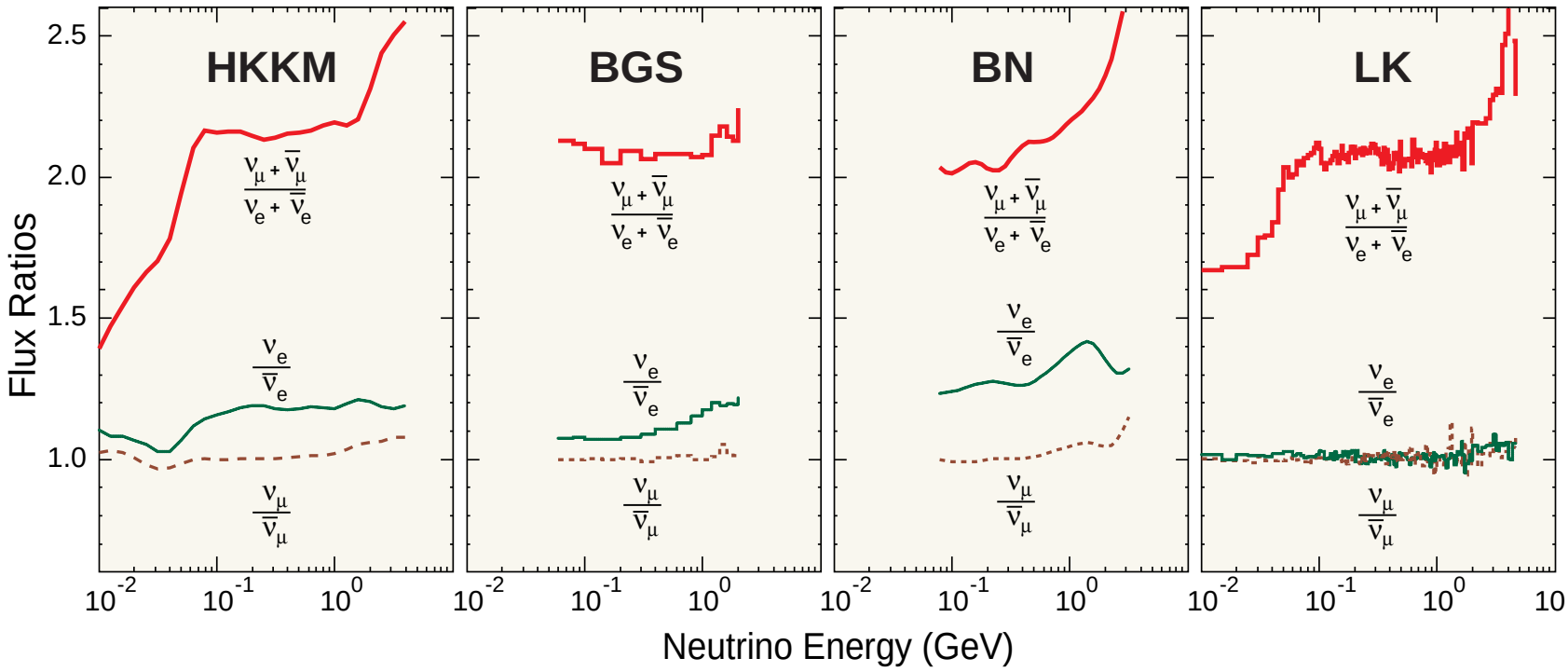

Figure 29: Early calculations of the low-energy 4π averaged AN flux ratios for Kamioka site. Notation is the same as in Fig. 28.

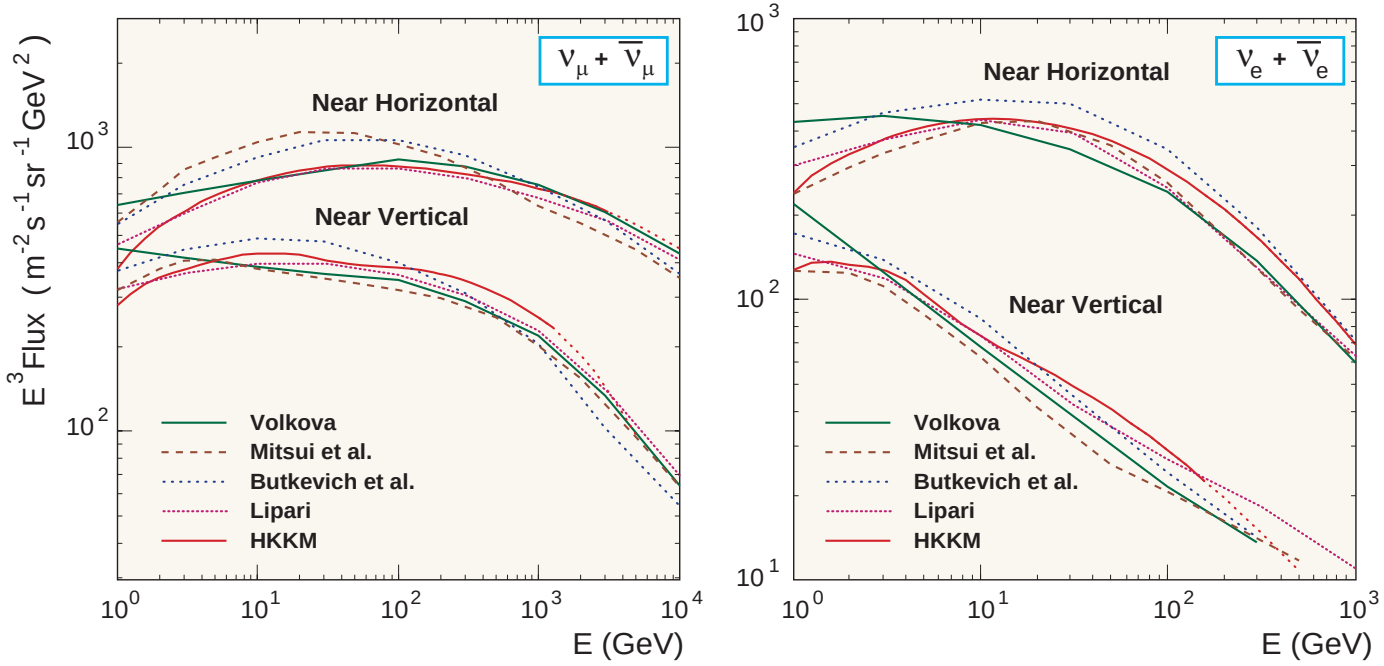

Figure 30: Comparison between early calculations of the AN fluxes above 1 GeV for near horizontal and near vertical directions: M. Honda, T. Kajita, K. Kasahara and S. Midorikawa, Phys. Rev. D **52** (1995) 4985 (HKKM), L. V. Volkova, Yad. Fiz. **31** (1980) 1510 [Sov. J. Nucl. Phys. **50** (1980) 784] (V), K. Mitsui, Y. Minorikawa and H. Komori, Nuovo Cim. **9 C** (1986) 995 (MMK), A. V. Butkevich, L. G. Dedenko and I. M. Zheleznykh, Yad. Fiz. **50** (1989) 142 [Sov. J. Nucl. Phys. **50** (1989) 90] (BDZ), P. Lipari, Astropart. Phys. **1** (1993) 195 (L). The dotted lines represent the results of Honda *et al*. obtained without geomagnetic cutoff.

20 Atmospheric neutrinos II: High energies

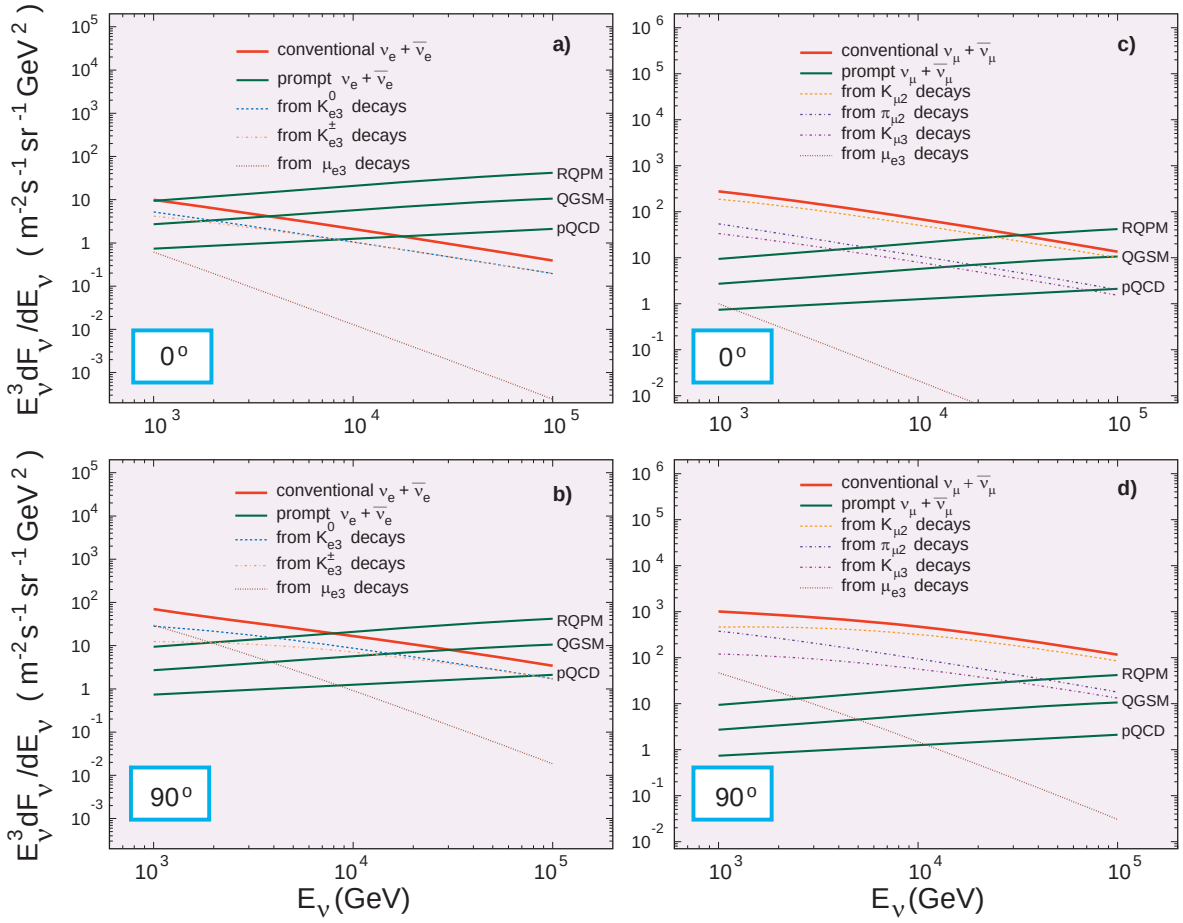

Figure 31: Separate contributions from some mechanisms of neutrino production into the total AN fluxes at $\vartheta = 0^\circ$ and $\vartheta = 90^\circ$ for energies 1 to 100 TeV.

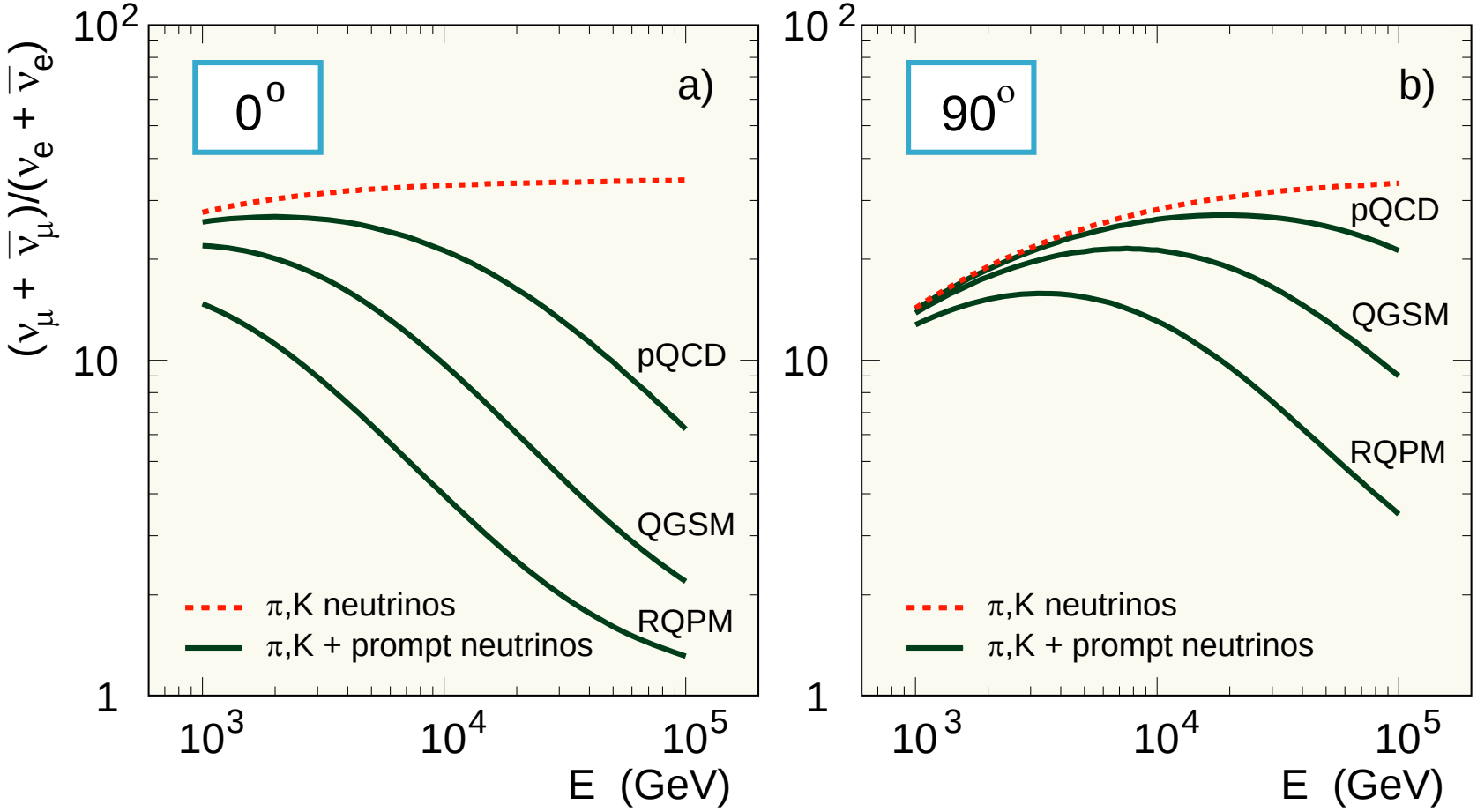

Figure 32: Neutrino flavor ratio vs energy at $\vartheta = 0°$ (a) and $90°$ (b) for the total AN flux calculated without the PN contribution and with taking it into account using the three models for charm production, pQCD, QGSM and RQPM.

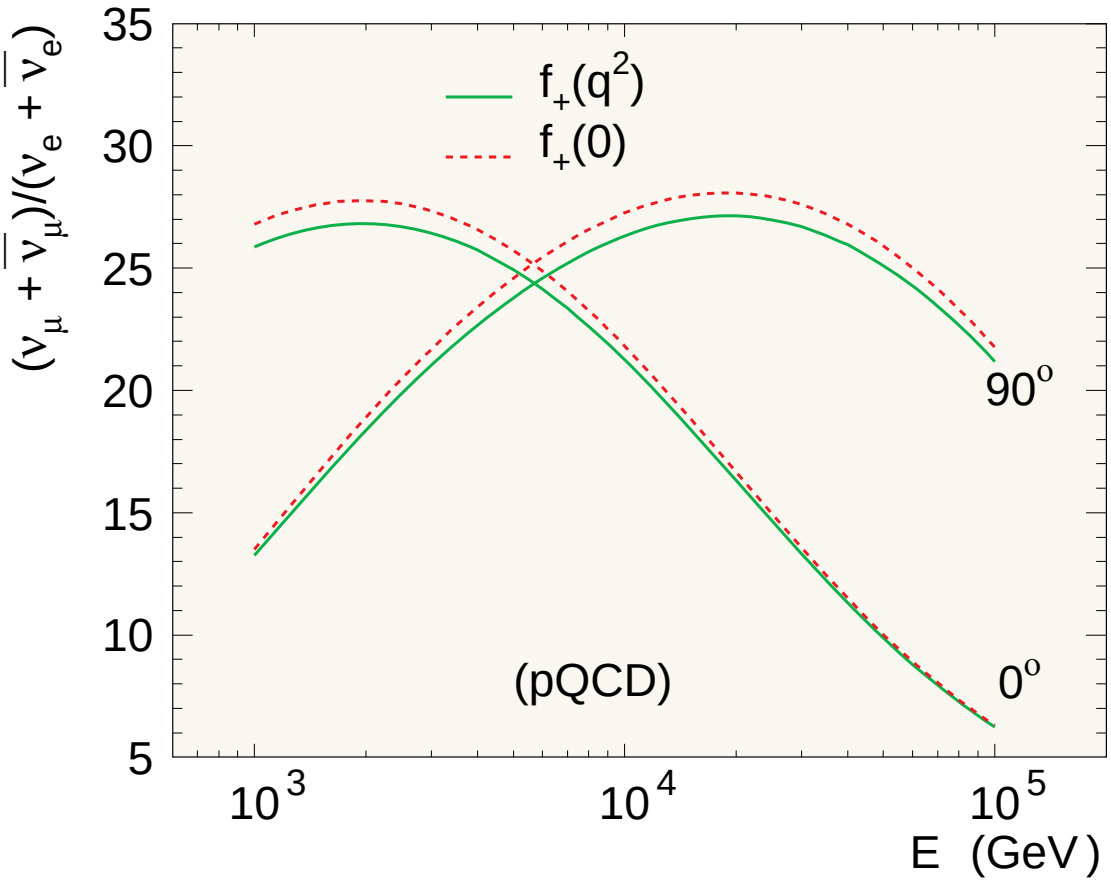

Figure 33: Effect of the q^2-dependent $K_{\ell 3}$ form factors for the neutrino flavor ratio at $\vartheta = 0^\circ$ and 90°. The PN contribution is taking into account using the pQCD model by Thunman *et al.* (1995). The dashed and solid curves are for the constant and q^2-dependent form factors, respectively.

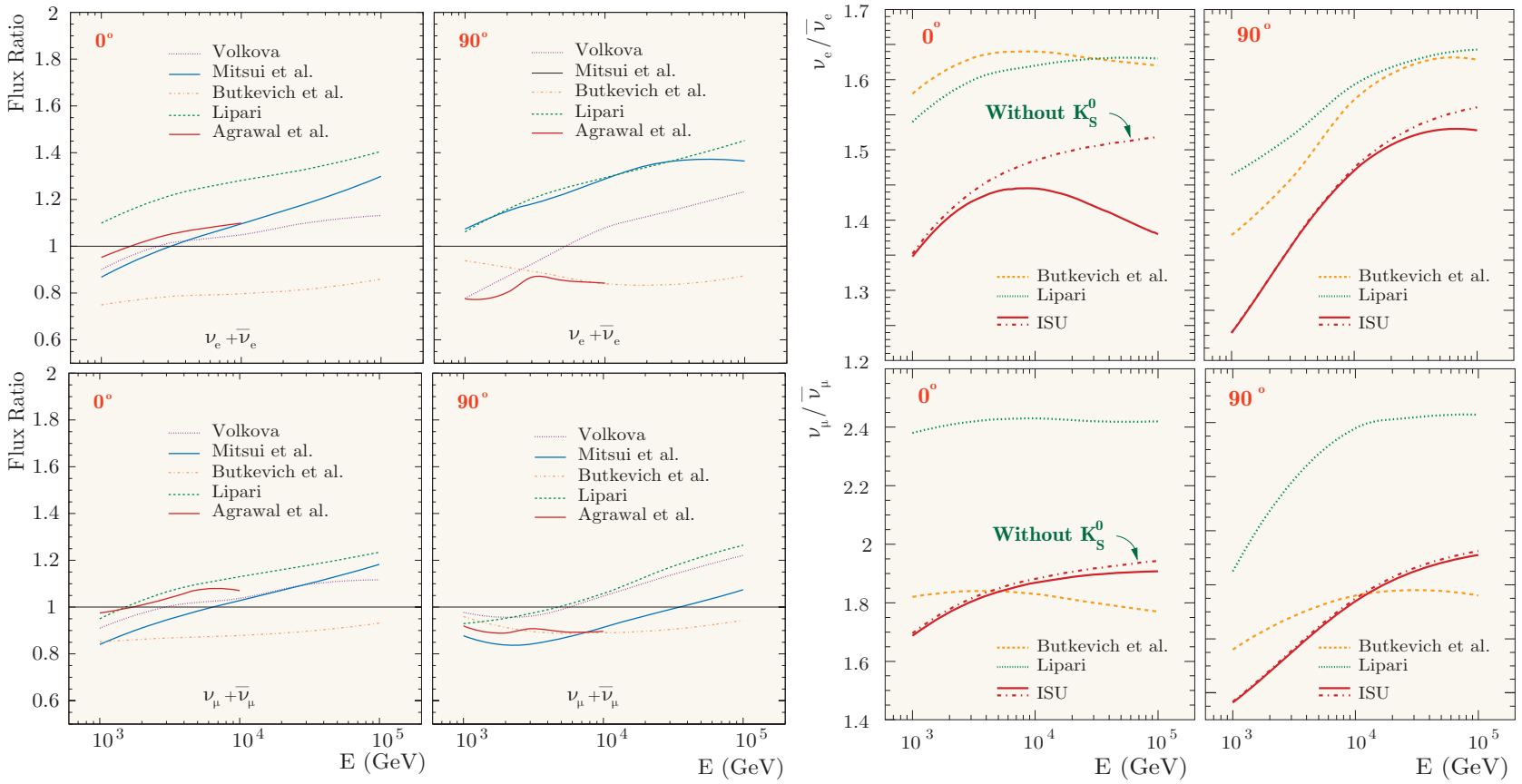

Figure 34: *Four panels on the left:* Conventional $\nu_e + \overline{\nu}_e$ and $\nu_\mu + \overline{\nu}_\mu$ fluxes at $\vartheta = 0°$ and $90°$ calculated by different workers and normalized to the ISU fluxes. *Four panels on the right:* $\nu/\overline{\nu}$ ratios at $\vartheta = 0°$ and $90°$ for the conventional ANs in comparison with the results of different workers. [From V. A. Naumov *et al.*, Nuovo Cim. **111 A** (1998) 129; T. S. Sinegovskaya, Ph. D. Thesis, Irkutsk State University, 2000.]

Figures 35–38 aggregate the differential energy spectra of downward going atmospheric neutrinos calculated within a wide energy range (from 50 MeV to about 20 EeV) for 11 zenith angles. Figures show the "conventional" neutrino contribution (originated from decay of pions, kaons and muons) and the total AN spectra which include the "prompt" neutrino contribution originated from semileptonic decays of charmed hadrons (mainly $D^{\pm}$, D^{0}, $\overline{D}^{0}$ mesons and Λ_c^{+} hyperons).

The prompt neutrino contribution must dominate at very high energies. However the charm hadroproduction cross sections are very model-dependent and cannot be unambiguously predicted for lack of a generally accepted model. As a result the prompt neutrino contribution and even the energies above which the prompt muon and electron neutrinos become dominant are very uncertain as yet

The results are shown in Figs. 35–38 are obtained by using the two phenomenological approaches to the charm production problem: the quark-gluon string model (QGSM) and recombination quark-parton model (RQPM). The prompt muon fluxes predicted by QGSM and RQPM are both consistent with the current deep underground data and may be considered as the safe lower and upper limits for the prompt muon contributions.

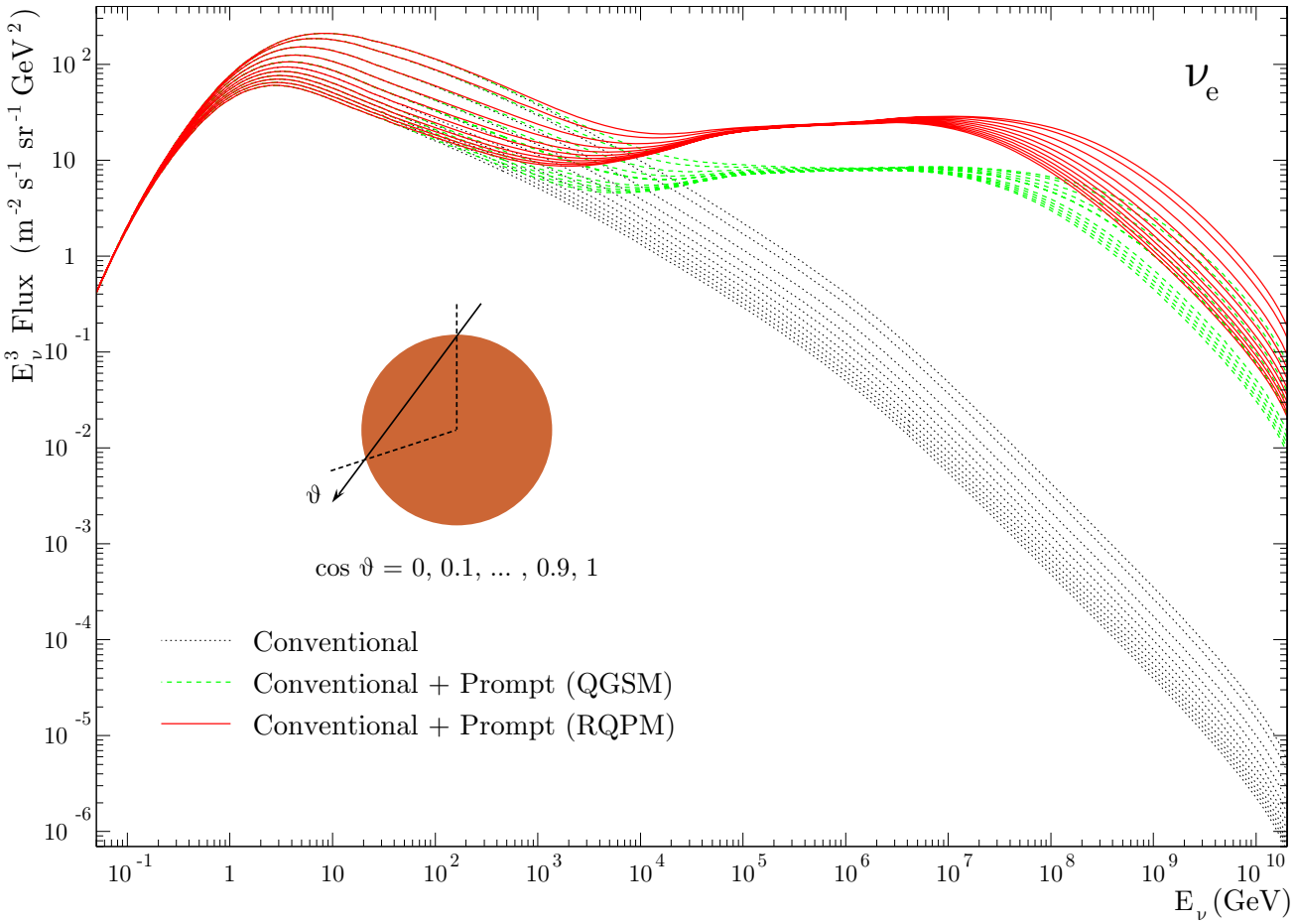

Figure 35: Energy spectra of downward going atmospheric ν_e for 11 zenith angles. Low-energy range is for Kamioka site. At high energies, from smallest to largest fluxes, $\cos\theta$ varies from 0 to 1 with an increment of 0.1 for each group of curves.

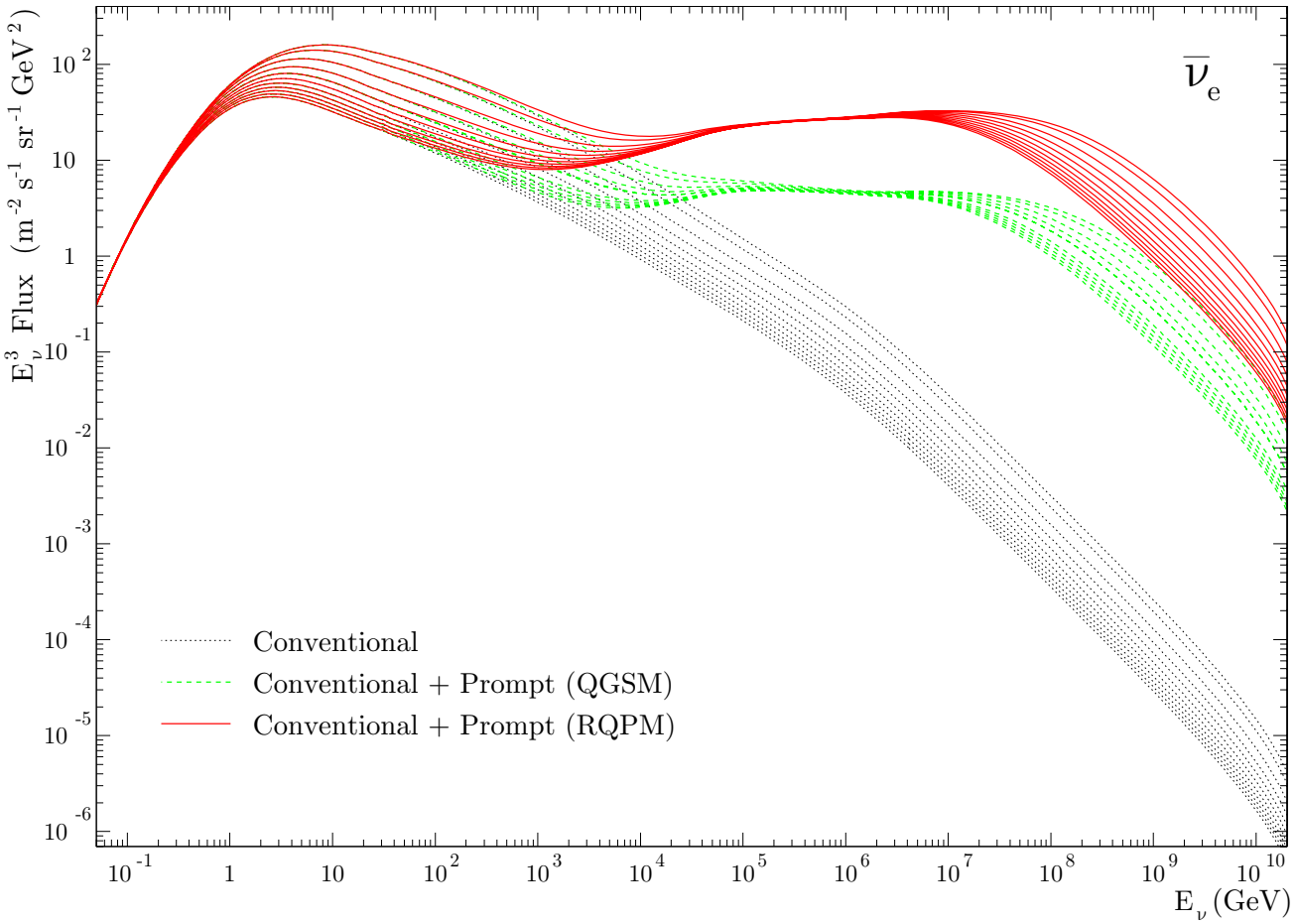

Figure 36: Energy spectra of downward going atmospheric $\overline{\nu}_e$ for 11 zenith angles. Low-energy range is for Kamioka site. At high energies, from smallest to largest fluxes, $\cos\theta$ varies from 0 to 1 with an increment of 0.1 for each group of curves.

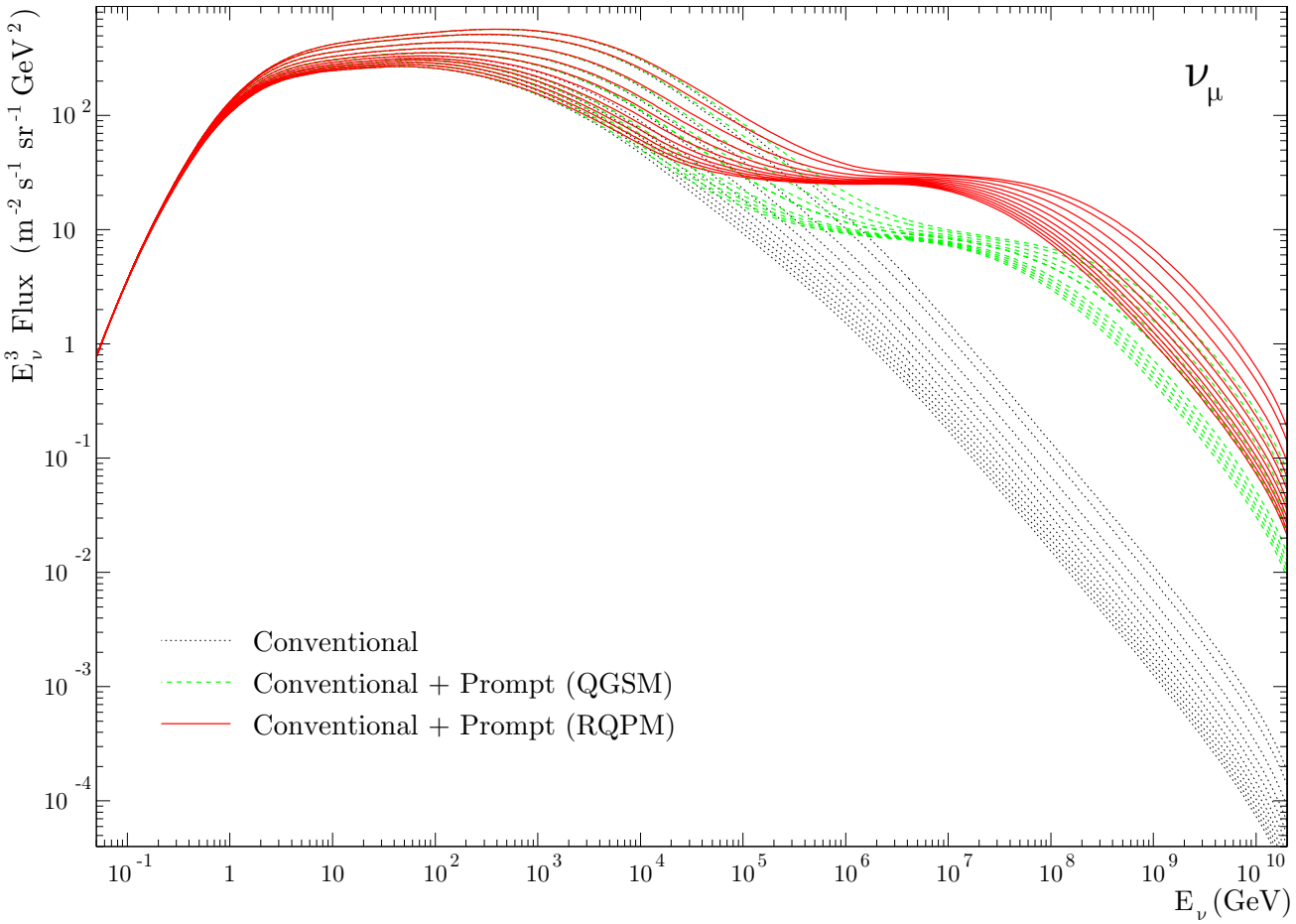

Figure 37: Energy spectra of downward going atmospheric ν_μ for 11 zenith angles. Low-energy range is for Kamioka site. At high energies, from smallest to largest fluxes, $\cos\theta$ varies from 0 to 1 with an increment of 0.1 for each group of curves.

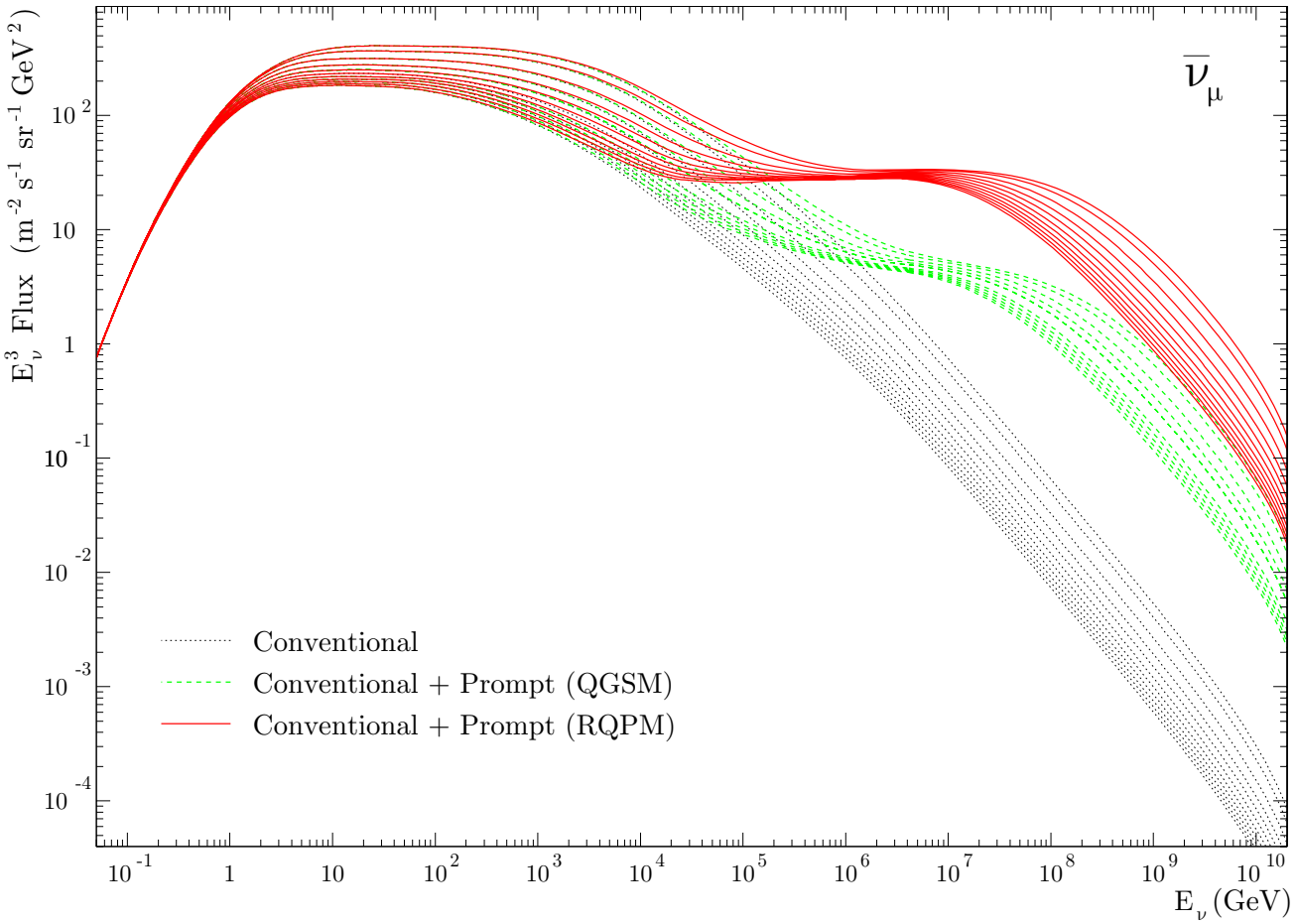

Figure 38: Energy spectra of downward going atmospheric $\overline{\nu}_\mu$ for 11 zenith angles. Low-energy range is for Kamioka site. At high energies, from smallest to largest fluxes, $\cos\theta$ varies from 0 to 1 with an increment of 0.1 for each group of curves.

Part V

ATMOSPHERIC NEUTRINO EXPERIMENTS

21 Data of underground neutrino experiments

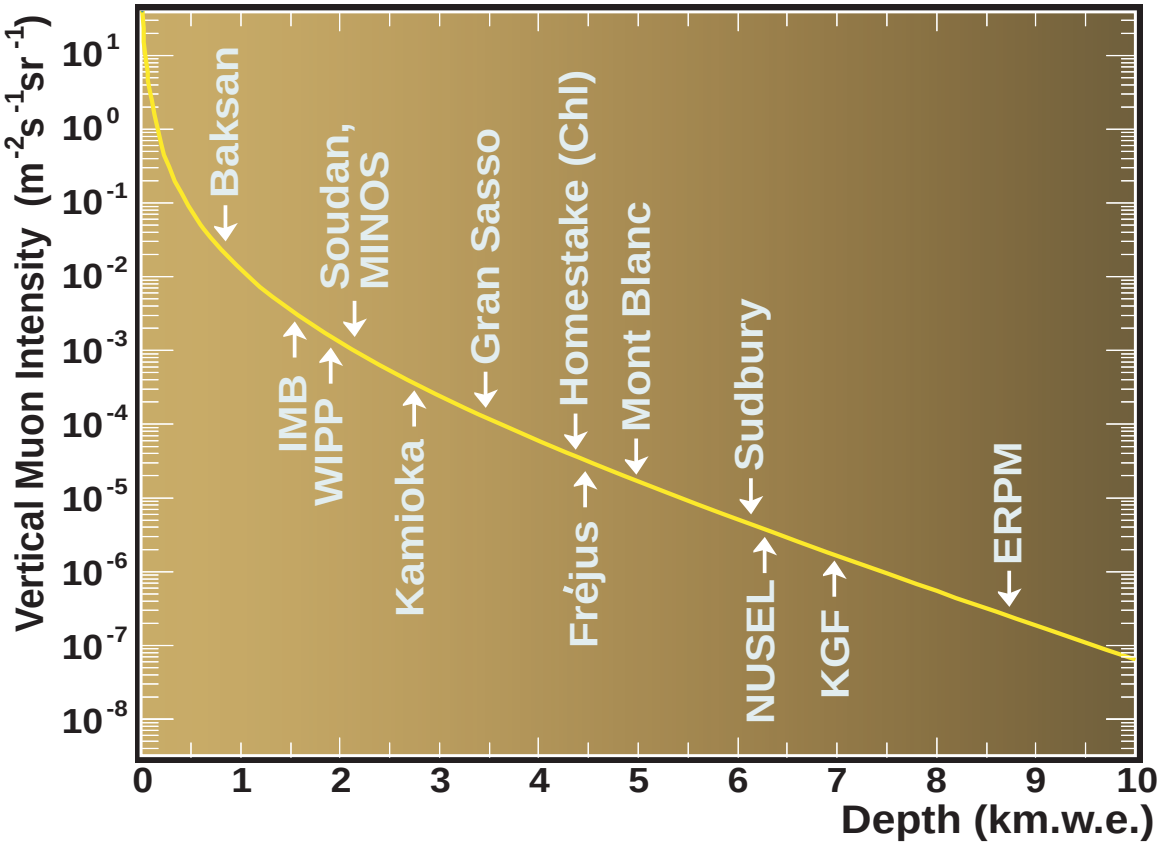

Figure 39: Depths of several underground laboratories. Solid line is the calculated vertical cosmic-ray muon intensity in the standard rock.

Table 11: Summary of atmospheric neutrino experiments that have observed fully contained (FC), partially contained (PC), upward stopping muon (USμ) and upward through-going muon (UTμ) events.[a] [From T. Kajita and Y. Totsuka, Rev. Mod. Phys. **73** (2001) 85.]

Experiment	Status of experiment	Detection technique	Type of events	Fiducial mass (kt)	Total exposure	Number of events
BUST (Baksan)	running from 1978	liquid scintillator	UTμ		10.55 yr	424
NUSEX	finished (1982–1988)	gas counter, iron plate	FC	0.13	0.74 kt · yr	50
Fréjus	finished (1984–1988)	gas counter, iron plate	FC PC	0.70 0.70	2.0 kt · yr 2.0 kt · yr	158 58
Kamiokande	finished (1983–1995)	water Cherenkov	FC PC UTμ	1.04-1.35 1.04	7.7-8.2 kt · yr 6.0 kt · yr 6.7 yr	885 118 372
IMB	finished (1982–1991)	water Cherenkov	FC UTμ USμ	3.30	7.7 kt · yr 3.6 yr 3.6 yr	935 532 85
Soudan 2	running from 1989	gas counter, iron plate	FC	0.77	3.9 kt · yr	371
MACRO	finished (1991–2000)	liquid scintillator + gas counter	ID+US IU UTμ		 5.9 yr[b]	 607
Super-Kamiokande	running from 1996	water Cherenkov	FC PC UTμ USμ	22.5 22.5	61 kt · yr 61 kt · yr 2.94 yr 2.88 yr	7940 563 1187 265

[a] As of 1999. Some data in the last 3 columns have to be updated.

[b] Exposure with the full detector (6 supermodules) is 4.1 yr.

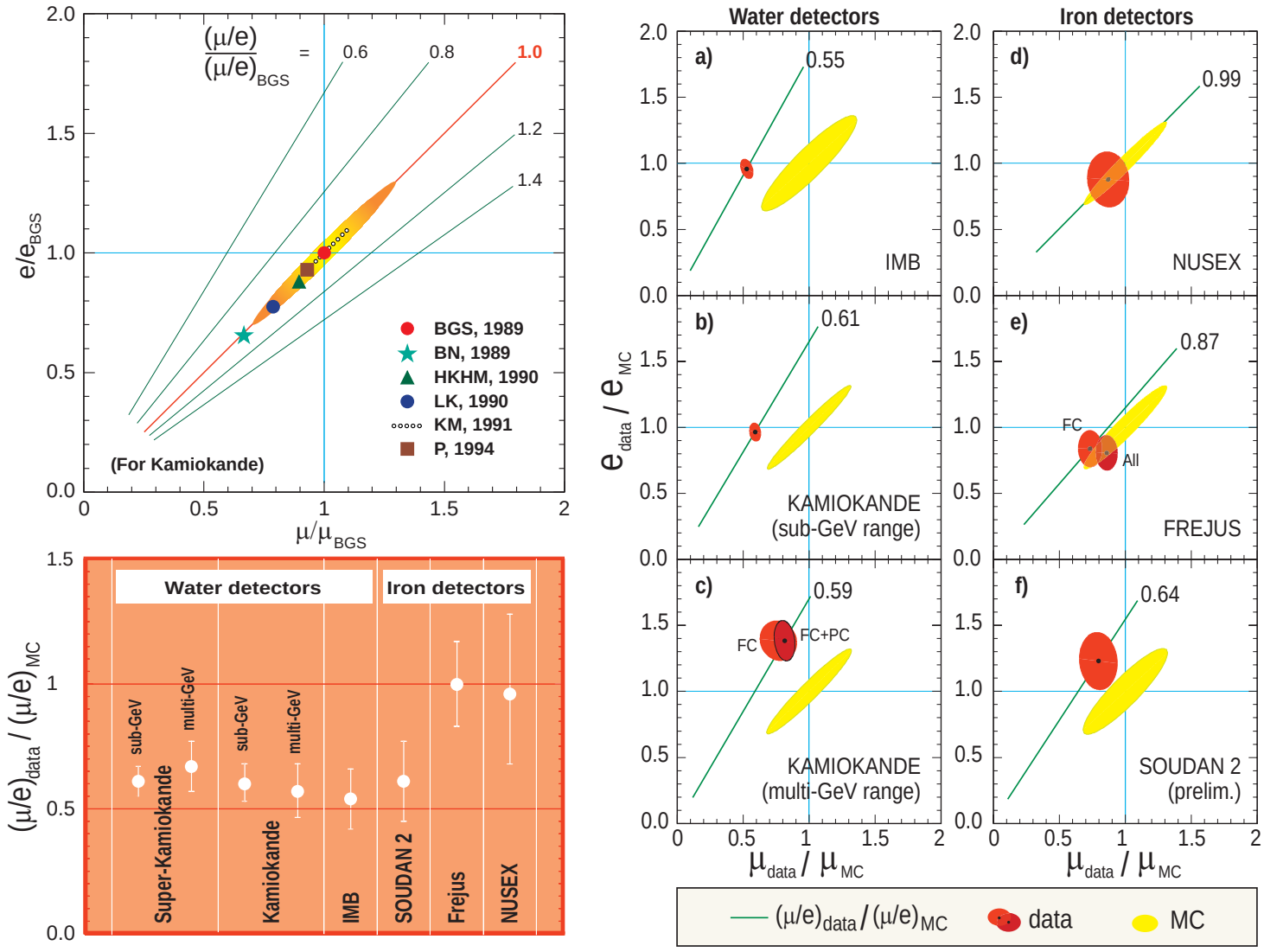

Figure 40: Flavor Ratios.

22 Kamiokande and Super-Kamiokande

Both Kamiokande and Super-Kamiokande are imaging water Cherenkov detectors. They detect Cherenkov light generated by charged particles, in particular, the particles produced by incoming neutrinos in water.

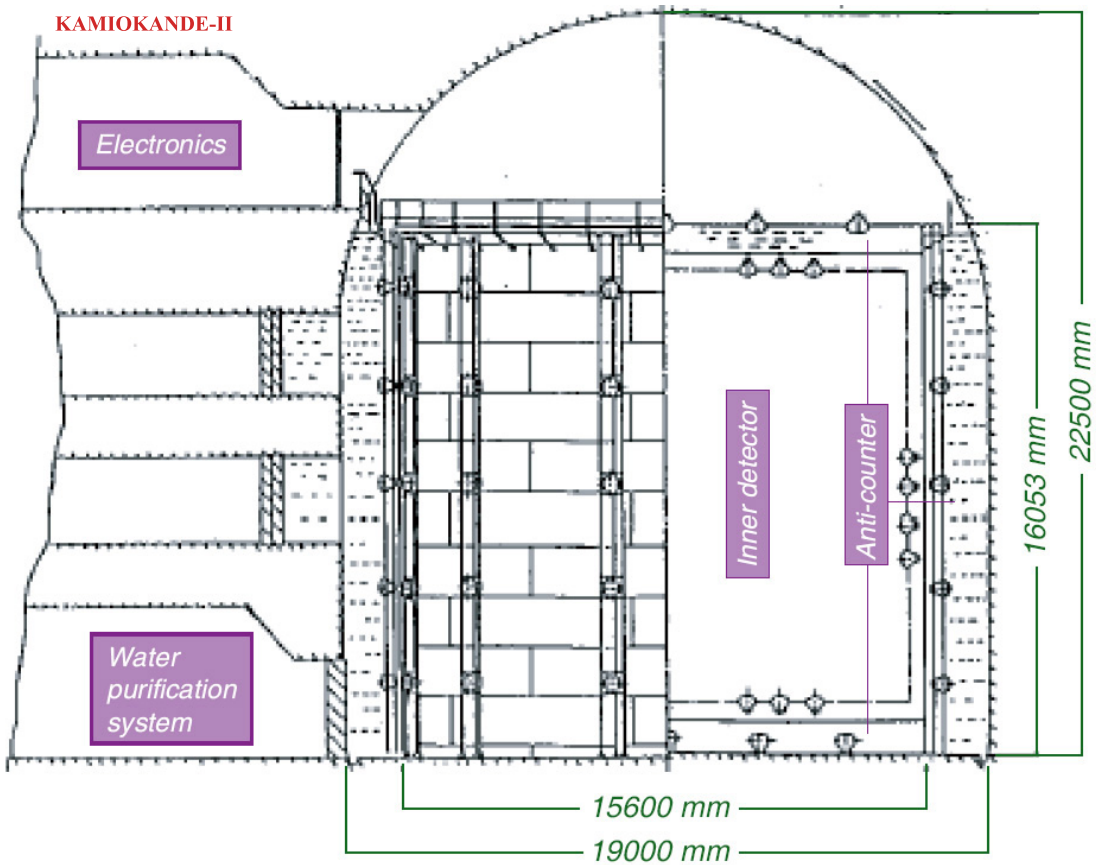

Figure 41: Schematic view of the Kamiokande-II detector. The slantwise hatches mark the surrounding rock. The inner detector contains 3000 tons of water of which 2140 tons are fiducial volume (the area enclosed with dotted-dashed line). It is viewed by 948 20-inch-diameter PMT's mounted on a 1-m grid on the inner surface. The outer (veto) counter surrounds the inner detector and is viewed by 123 PMT's.

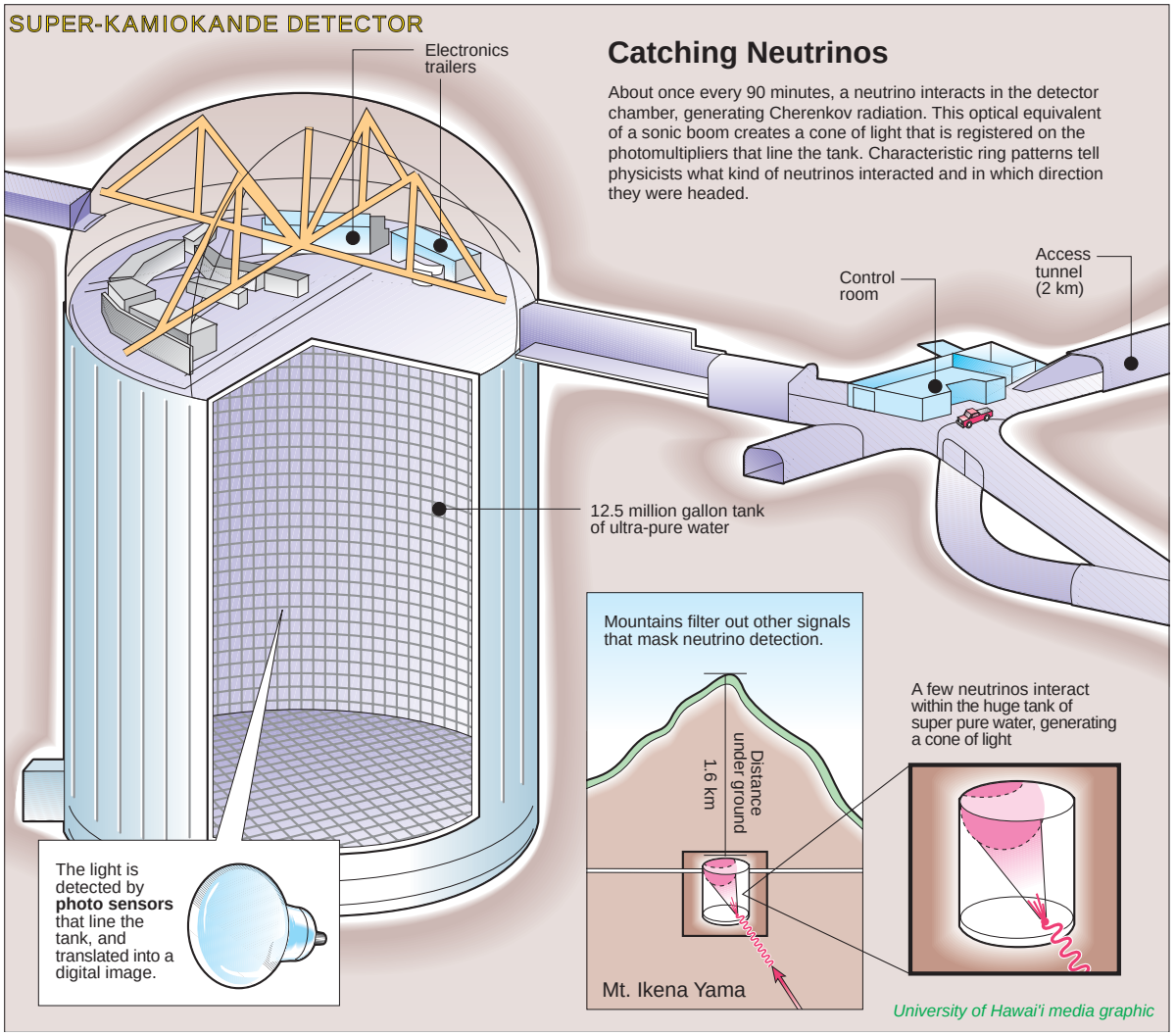

Figure 42: Catching neutrinos with the Super-Kamiokande detector.

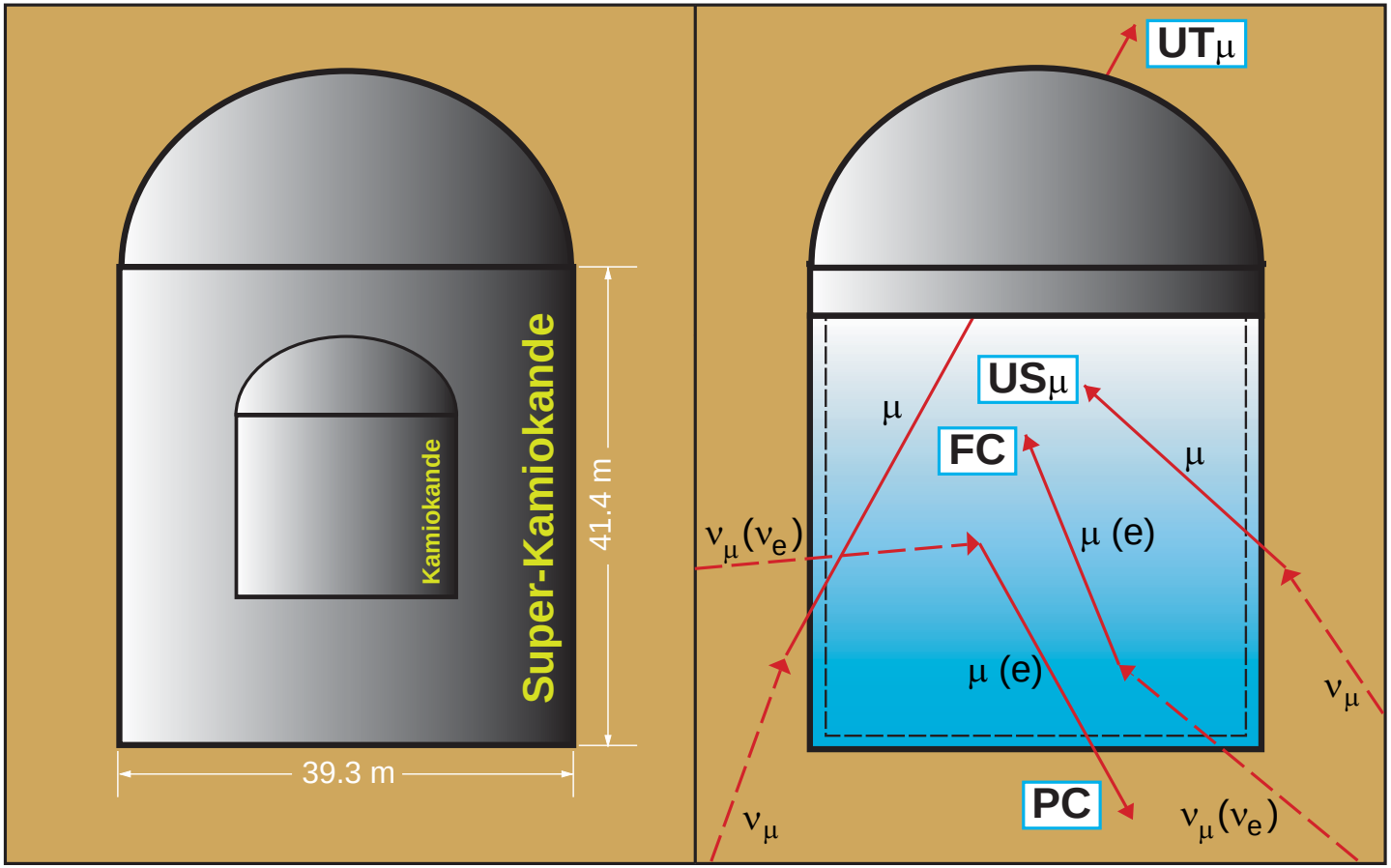

Figure 43: Comparative dimensions of the Kamiokande and Super-Kamiokande (left panel) and neutrino induced event classification (right panel) in these detectors. Abbreviation expansion: FC = Fully Contained, PC = Partially Contained, USμ = Upward-going Stopping Muons, UTμ = Upward Through-going Muons (see also Table 11).

Figures 44–48 in the next few slides are borrowed from Tomasz Barszczak, University of California.[a]

Fig. 44 shows two MC simulated events. In the left panel, a 481 MeV muon neutrino produces a 394 MeV muon which later decays at rest into 52 MeV electron. The ring fit to the muon is outlined. Fuzzy electron ring is seen in yellow-green in lower right corner. This is perspective projection with 110 degrees opening angle, looking from a corner of the Super-Kamiokande detector (not from the event vertex). Color corresponds to time PMT was hit by Cherenkov photon from the ring. Color scale is time from 830 to 1816 ns with 15.9 ns step. The time window was widened from default to clearly show the muon decay electron in different color. In the charge weighted time histogram to the right two peaks are clearly seen, one from the muon, and second one from the delayed electron from the muon decay. Size of PMT corresponds to amount of light seen by the PMT. PMTs are drawn as a flat squares even though in reality they look more like huge flattened golden light bulbs.

In the right panel, a 1063 MeV neutrino strikes free proton at rest and produces 1032 MeV muon. Color scale is time from 987 to 1080 ns with 2.3 ns step. PMTs close to the vertex were hit earlier than PMTs farther away. The same event but in cylindrical projection is shown in Fig. 45. This is a 4π view (full solid angle, 360 degrees around). Un-hit PMTs are hidden but detector grid is shown. The observer is positioned in the event vertex.

[a] See URL <http://www.ps.uci.edu/~tomba/sk/tscan/pictures.html>.

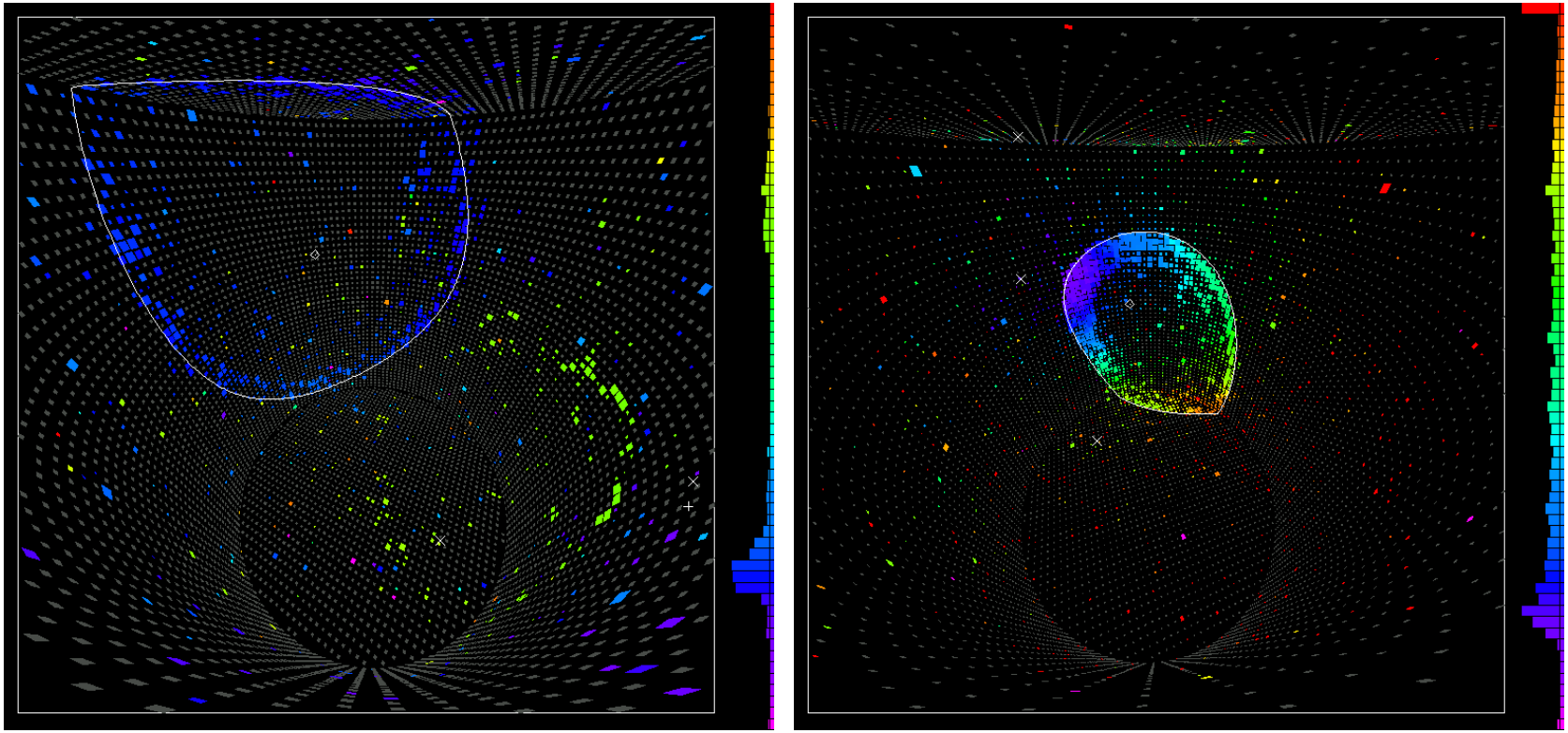

Figure 44: SK MC events. *Left panel*: 481 MeV muon neutrino produces 394 MeV muon which later decays at rest into 52 MeV electron. *Right panel*: 1063 MeV neutrino strikes free proton at rest and produces 1032 MeV muon.

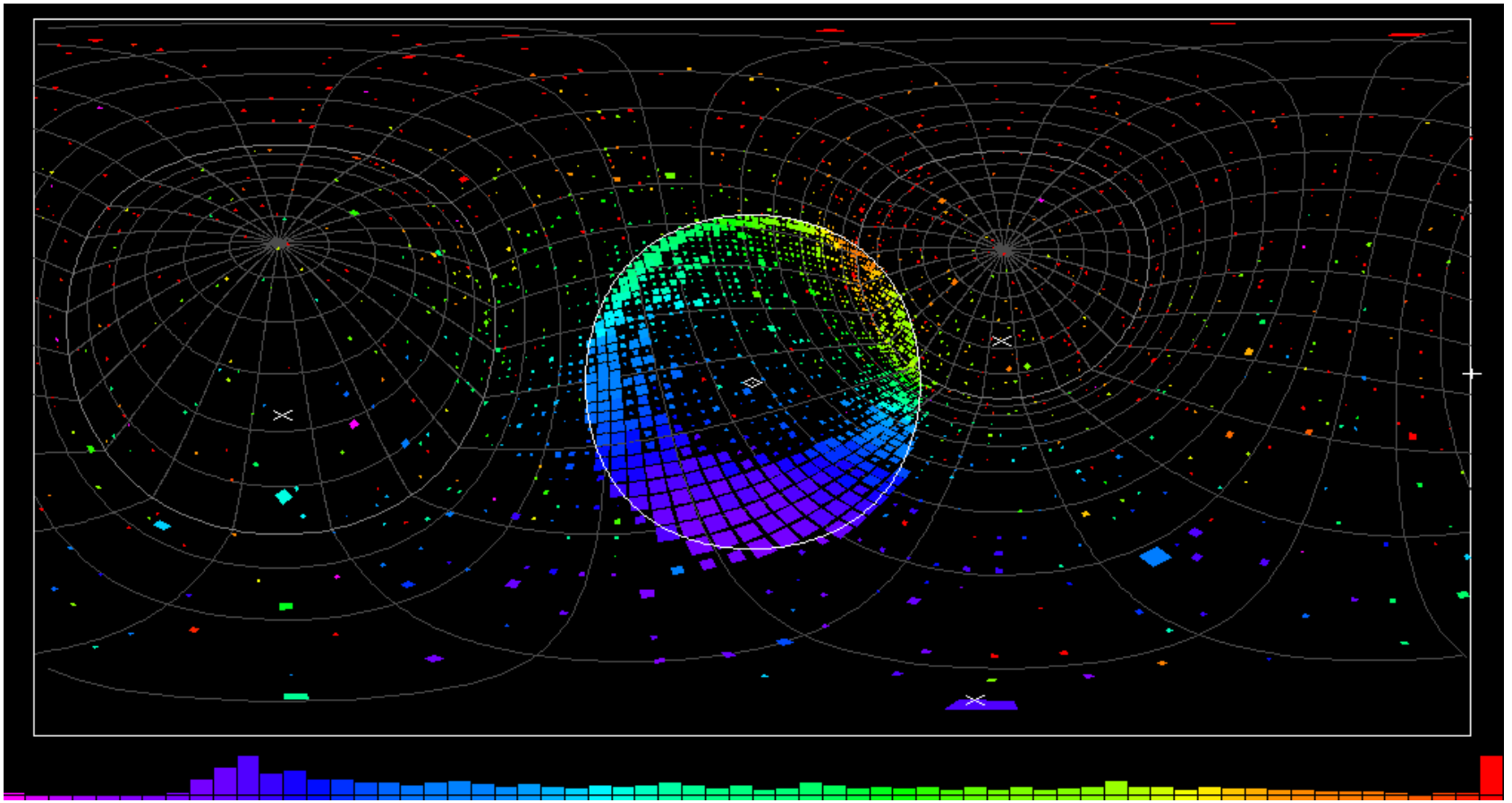

Figure 45: The same event as in the right panel of Fig. 44 but in cylindrical 4π projection. Neutrino strikes free proton at rest and produces 1032 MeV muon. PMTs close to the vertex were hit earlier than PMTs farther away. Un-hit PMTs are hidden but detector grid is shown. The observer is positioned in the event vertex.

Fig. 46 shows a 600 MeV electron (MC). Electron ring is much more fuzzy than muon ring. Electron produces shower of gammas, electrons and positrons. Gammas don't produce Cherenkov light. Electrons and positrons do. In the shower each of them flies at a little bit different angle and each of them makes its own weak Cherenkov ring. All those rings added together produce the observed fuzzy ring. This difference in sharpness of muon and electron rings is used to identify muons and electrons in the Super-Kamiokande. The color time scale spans 87 ns.

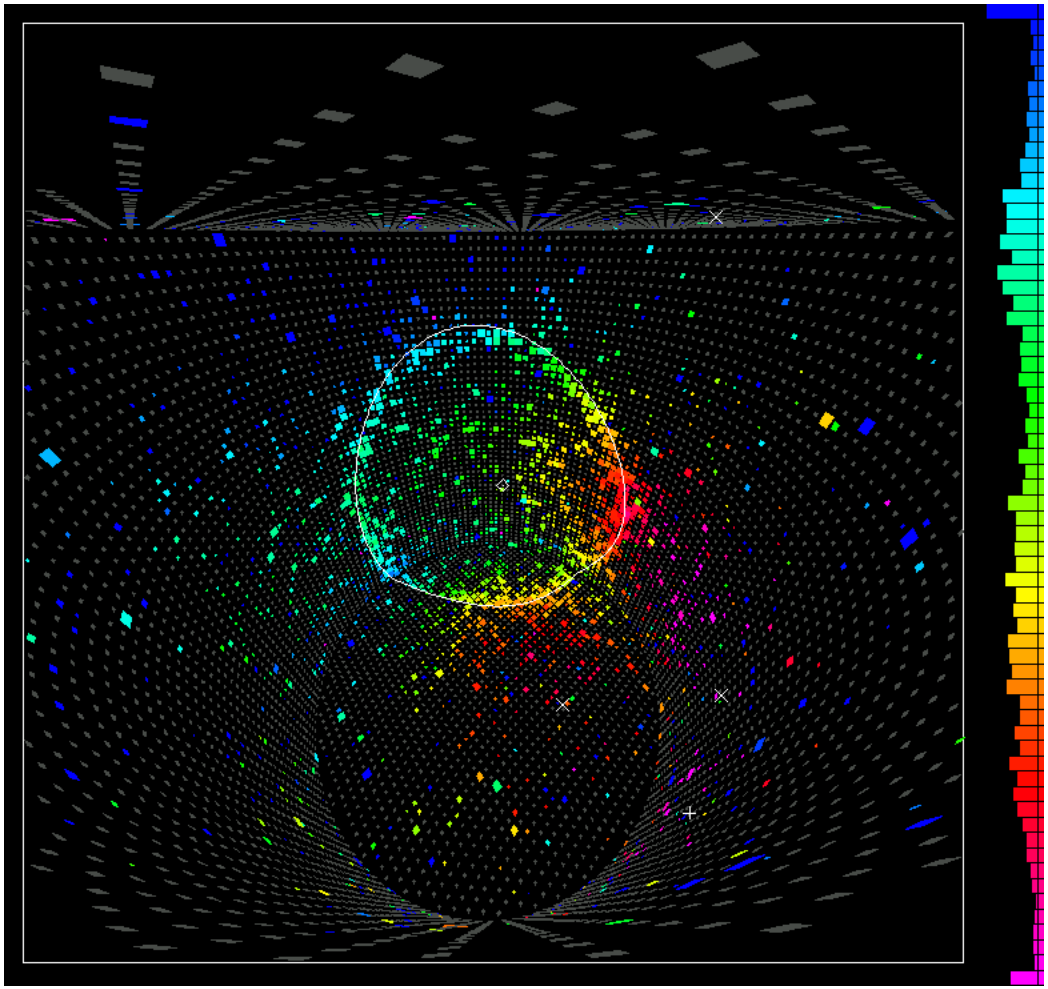

Figure 46: MC simulated 600 MeV electron event in the Super-Kamiokande detector.

Figures 47 and 48 show two real (not Monte Carlo) events recorded in the Super-Kamiokande-I detector.

A real multiple ring event is shown in Fig. 47. This event[a] recorded on 24/09/1997, 12:02:48 was one of the close candidates for proton decay into e^+ and π^0 but it did not pass analysis cuts.

The π^0 would decay immediately into two gammas which make overlapping fuzzy rings. Positron and π^0 would fly in opposite directions.

Time color scale spans 80 ns.

[a] Found by Brett Michael Viren (State University of New York at Stony Brook).

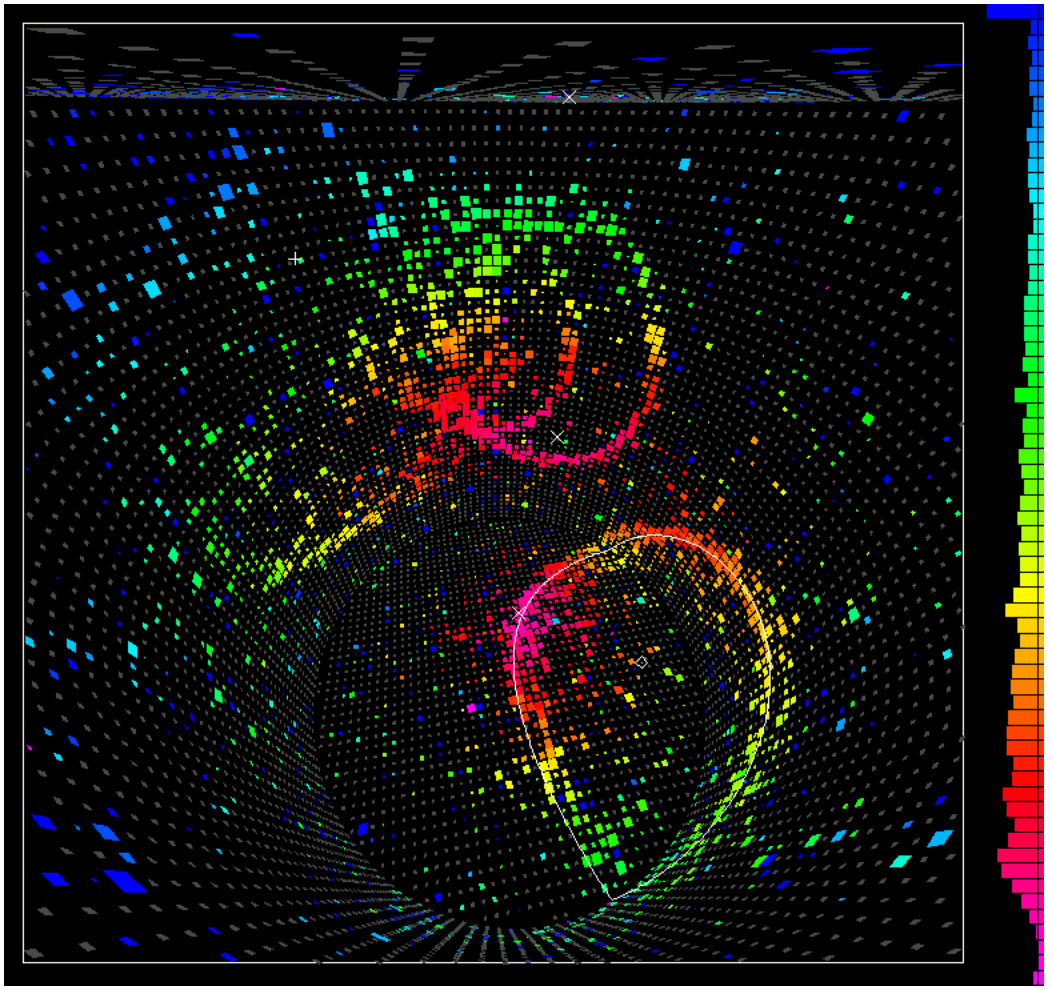

Figure 47: Multiple ring event recorded in the Super-Kamiokande detector on 24/09/1997, 12:02:48.

In Fig. 48, an upward-going through-going muon event recorded on 30/05/1996, 17:12:56 is shown.
The muon entered through the flat circular part of the detector near the bottom of the picture where purple earliest PMT hits can be seen. It exited through the cylindrical side wall in the middle of the picture.
Time color scale spans 262 ns.

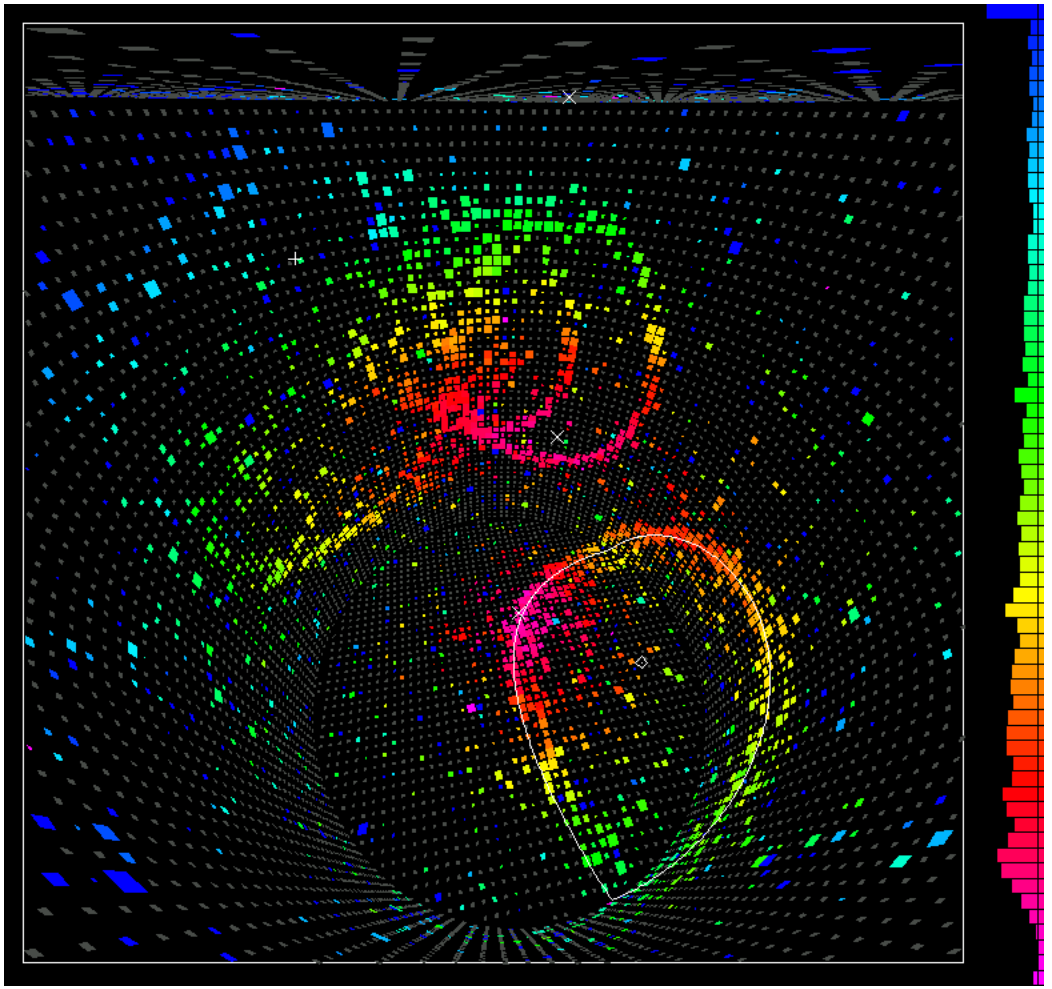

Figure 48: Through-going muon event recorded in the Super-Kamiokande detector on 30/05/1996, 17:12:56.

To determine the identity of the final state particles, a particle identification algorithm was applied which exploited systematic differences in the shape and the opening angle of Cherenkov rings produced by electrons and muons. Cherenkov rings from electromagnetic cascades exhibit a more diffuse light distribution than those from muons (Figs. 49, 50). The opening angle of the Cherenkov cone, which depends on particle's velocity, was also used to separate e's and μ's at low momenta.

The validity of the method was confirmed by a beam test experiment at KEK. The misidentification probabilities for single-ring e-like and μ-like events were estimated to be 0.8% and 0.7% respectively, using simulated CC quasielastic neutrino events.

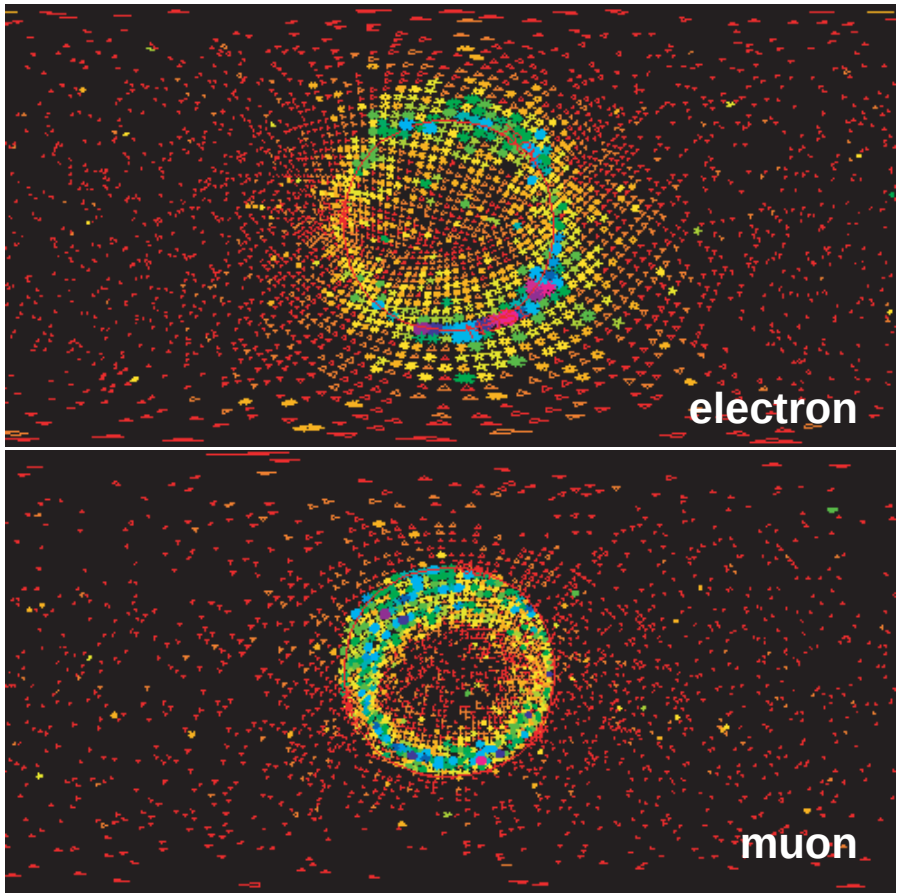

Figure 49: Super-Kamiokande I scan for electron and muon events.

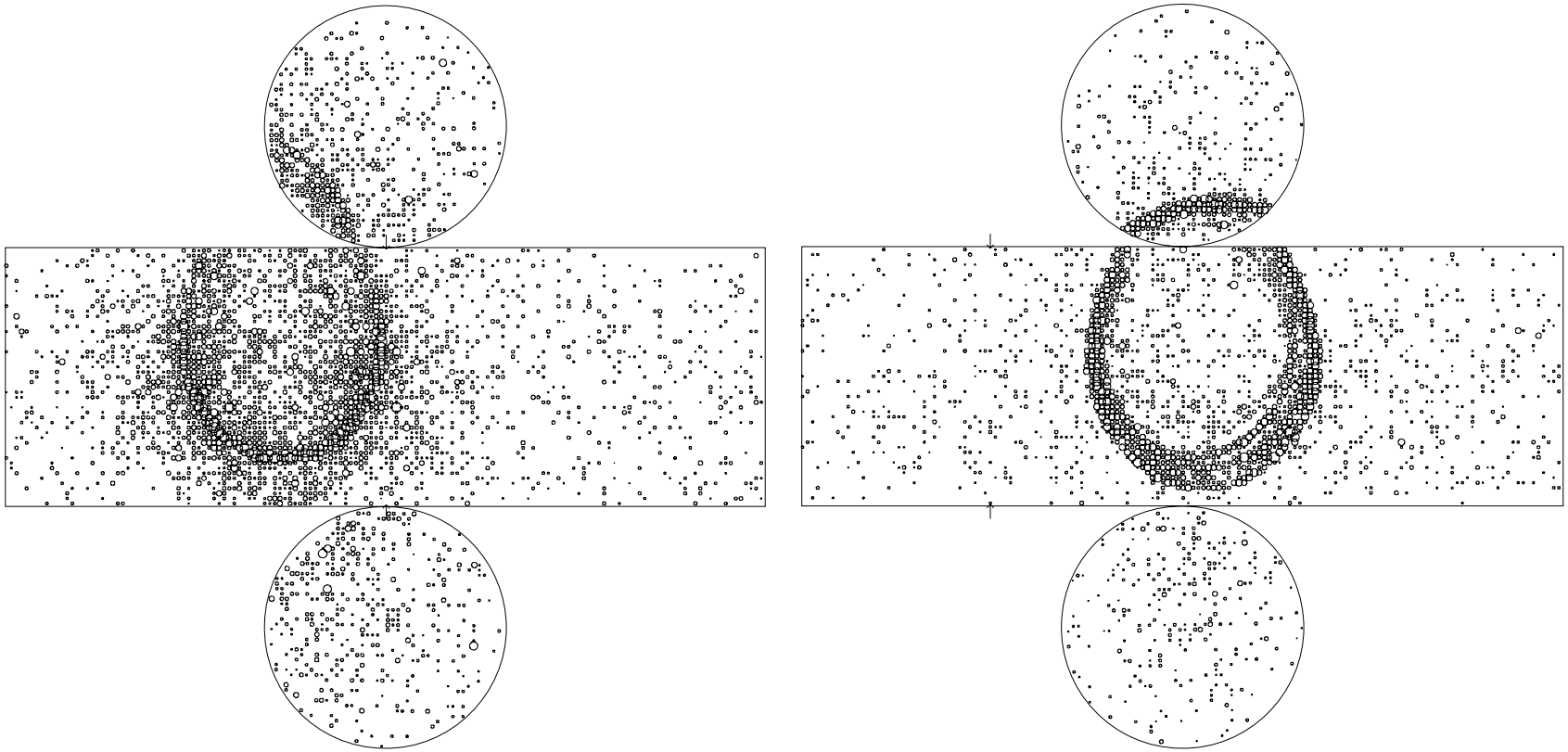

Figure 50: Example event display of a single-ring e-like (left) and μ-like (right) events in Super-Kamiokande I. Cherenkov rings from electromagnetic cascades exhibit a more diffuse light distribution than those from muons.

[From Y. Ashie *et al.* (Super-Kamiokande Collaboration), Phys. Rev. D **71** (2005) 112005 (hep-ex/0501064).]

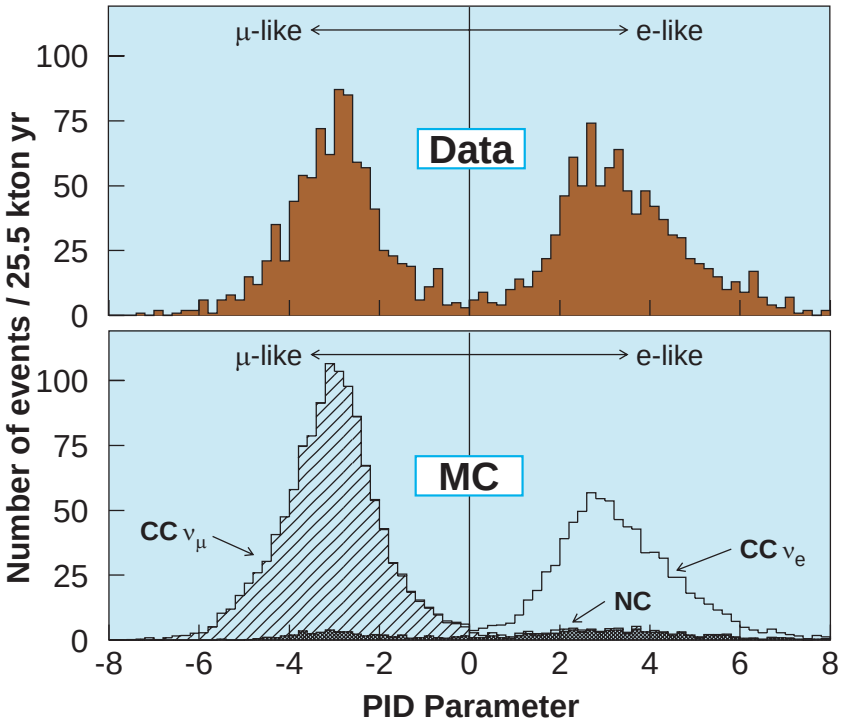

Figure 51: PID parameter in the Super-Kamiokande experiment.

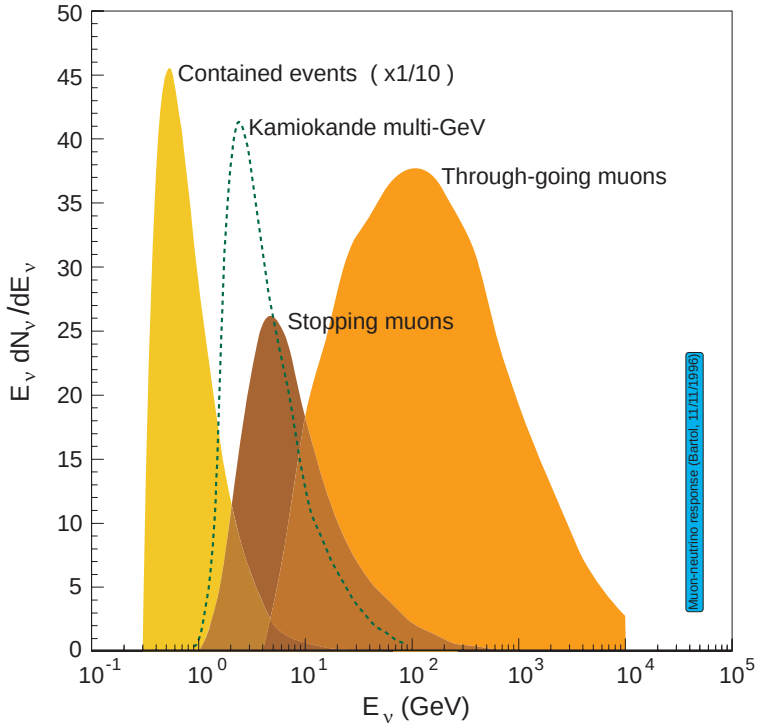

Figure 52: Atmospheric neutrino response for Kamiokande and Super-Kamiokande.

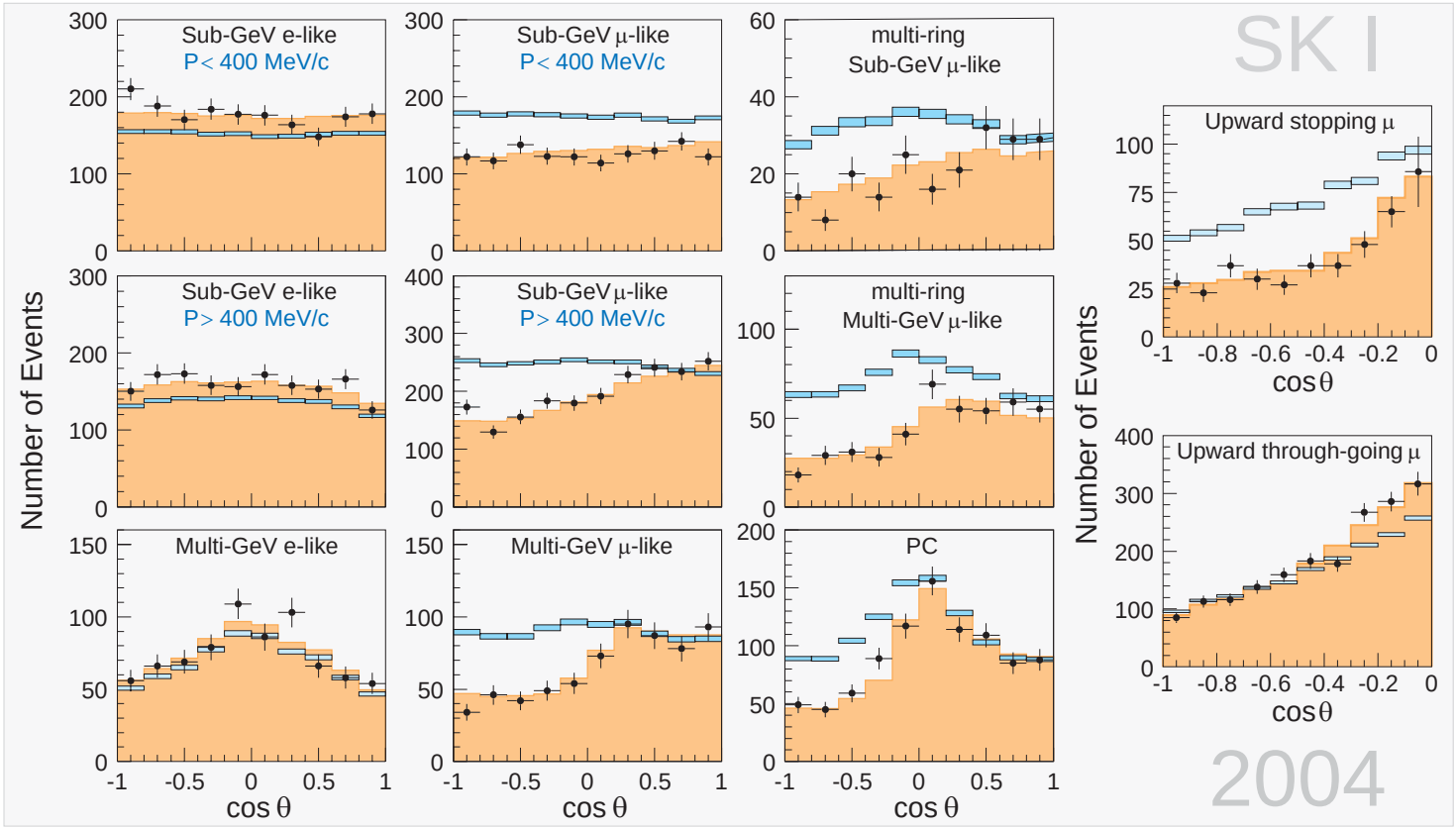

Figure 53: The zenith angle distributions for fully-contained 1-ring, multi-ring, partially-contained and upward events in SK I (1489 day exposure). The points show the data, boxes – the non-oscillated MC events (the height of the boxes shows the statistical error) and the histograms – the best-fit expectations for $\nu_\mu \leftrightarrow \nu_\tau$ oscillations with $\theta = 45^\circ$ and $\Delta m^2 = 0.0021$ eV^2. The height of the boxes shows the statistical error of the MC.

[From Y. Ashie *et al.* (Super-Kamiokande Collaboration), Phys. Rev. D **71** (2005) 112005 (hep-ex/0501064).]

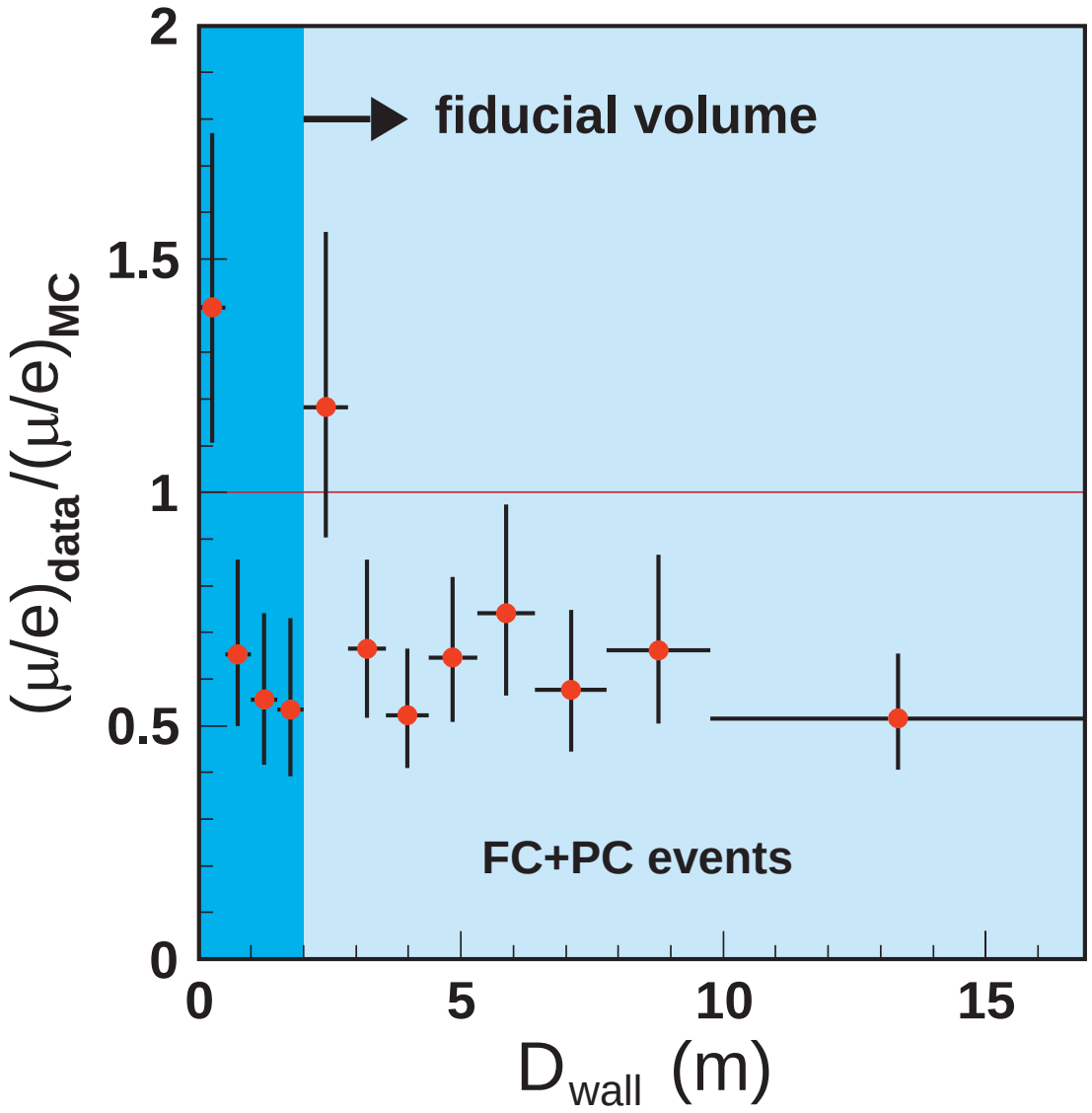

Figure 54: $R_{\mathrm{FC+PC}}$ *vs* $\mathrm{D_{wall}}$, the distance between the event vertex and the nearest inner detector wall, as measured in the Super-Kamiokande experiment for the "multi-GeV" energy range ($E_\nu \gtrsim 1$ GeV). The region $\mathrm{D_{wall}} > 1$ m is the fiducial volume. Error bars show the statistical uncertainties of the data and Monte Carlo.

[From Y. Ashie *et al.* (Super-Kamiokande Collaboration), Phys. Rev. D **71** (2005) 112005 (hep-ex/0501064).]

The allowed neutrino oscillation parameters were estimated by using

- ⋆ FC single-ring sub-GeV below 400 MeV/c,
- ⋆ FC single-ring sub-GeV above 400 MeV/c,
- ⋆ FC single-ring multi-GeV, PC events,
- ⋆ FC multi-ring events and
- ⋆ upward-going muon events separately.

The results are shown in Fig. 55. In this plot, 90 % confidence interval is defined to be $\chi^2 = \chi^2_{\rm min} + 4.61$, where $\chi^2_{\rm min}$ is the minimum χ^2 value including the unphysical parameter region.

The allowed parameter regions suggested by these six sub-samples are consistent.

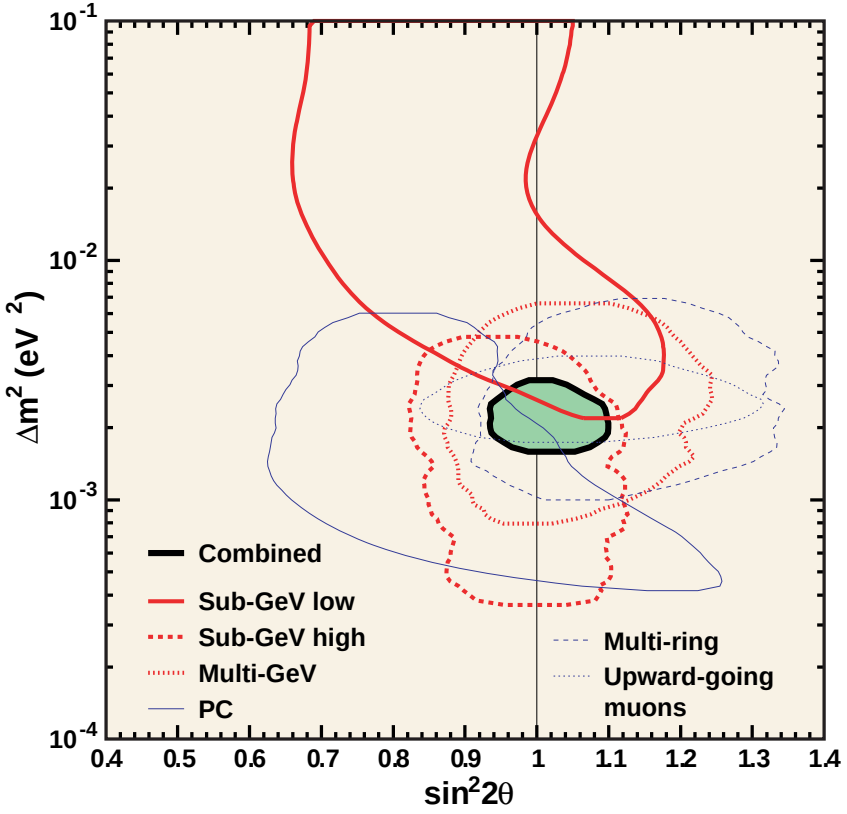

Figure 55: 90 % confidence level allowed oscillation parameter regions for $\nu_\mu \leftrightarrow \nu_\tau$ oscillations from six sub-samples of the SK I. [From Y. Ashie *et al.* (Super-Kamiokande Collaboration), Phys. Rev. D **71** (2005) 112005 (hep-ex/0501064).]

In addition, the same oscillation analyses were repeated using different flux models (but with the same neutrino interaction Monte Carlo program) and different neutrino interaction Monte Carlo program (but with the same flux model).

The 90 % C.L. allowed parameter regions are compared in Fig. 56. Left panel shows the 90% C.L. allowed oscillation parameter regions for $\nu_\mu \leftrightarrow \nu_\tau$ oscillations, based on the NEUT neutrino interaction model, from different flux models Right panel shows the 90% C.L. allowed regions based on NUANCE and NEUT neutrino interaction models for FC+PC events with the flux model of Honda-2004. In this plot, Monte Carlo events from NEUT were used for upward-going muons.

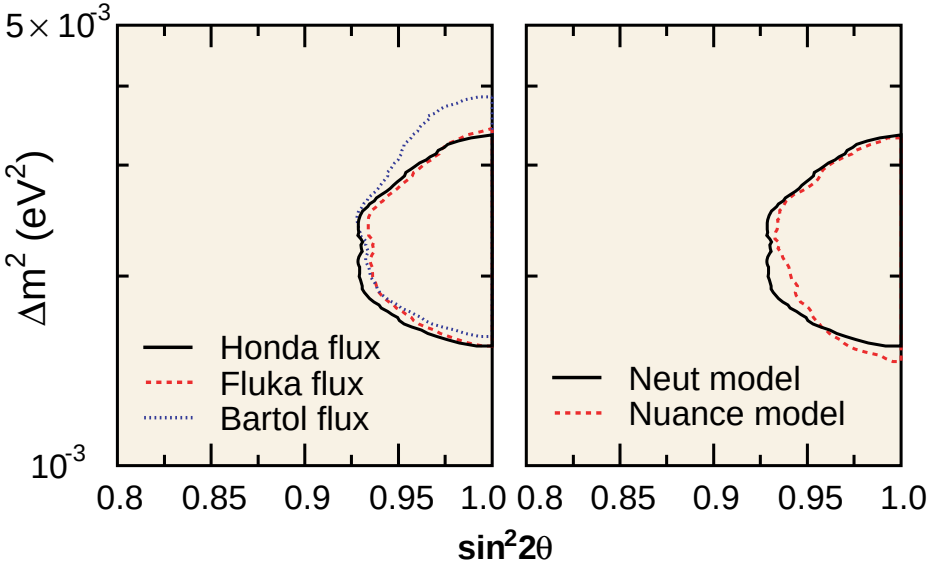

Figure 56: Allowed oscillation parameter regions evaluated with different AN flux models (left and interaction models (right). [From Y. Ashie *et al.* (Super-Kamiokande Collaboration), hep-ex/0501064.]

The allowed regions from these analyses overlap well. However, the allowed region obtained with the Bartol-2004 model allows for slightly higher Δm^2.

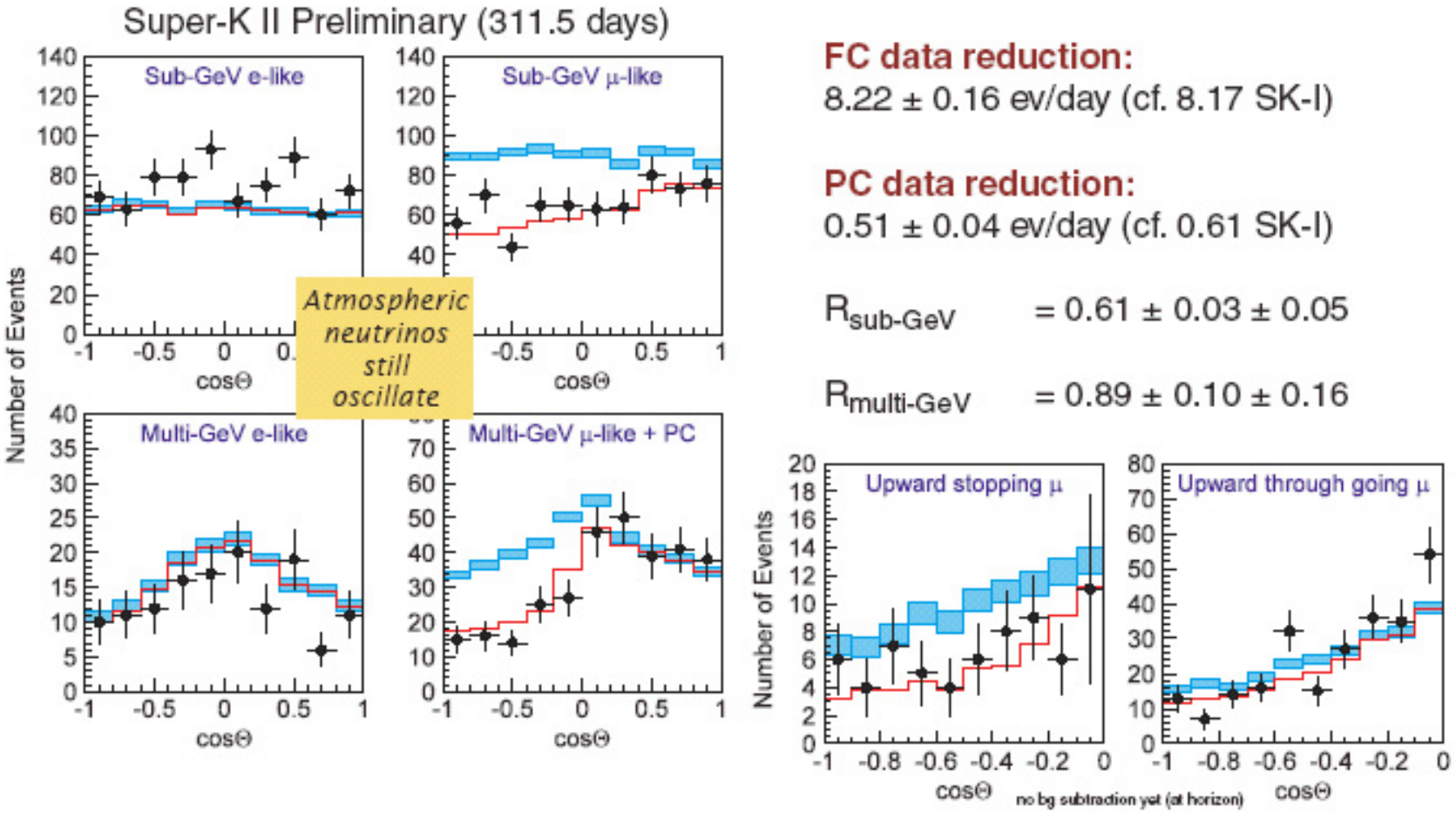

Figure 57: K-II Zenith Angle Distributions (SK-II and SK-I results are consistent).
[From an unpublished report by Ed Kearns on "Neutrino'2004".]

23 MACRO

The MACRO (Monopole, Astrophysics and Cosmic Ray Observatory) is a very large rectangular modular detector ($76.9 \times 12.3 \times 9.9$ m^3) situated in the hall B of the Gran Sasso underground laboratory (see Figs. 58–60).

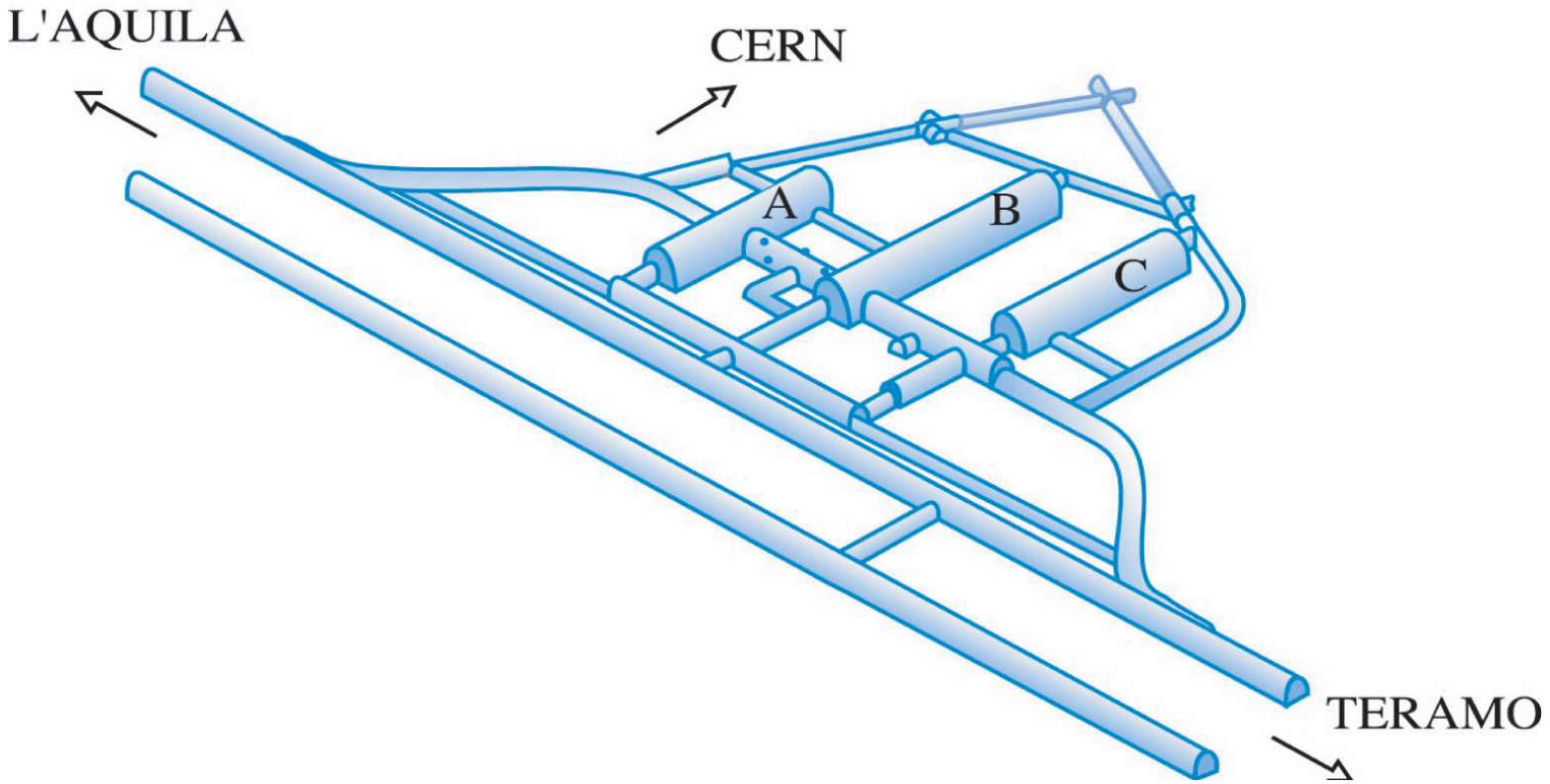

Figure 58: Gran Sasso laboratory underground.

Figure 59: The MACRO detector in the experimental hall B of the Gran Sasso Lab.

The detector consists of six supermodules of $12 \times 12 \times 5$ m^3 each. Each supermodule is made of ten horizontal planes of limited streamer tubes interleaved with passive materials, plus a central horizontal layer of special materials sensible to magnetic monopoles and heavy nuclei.

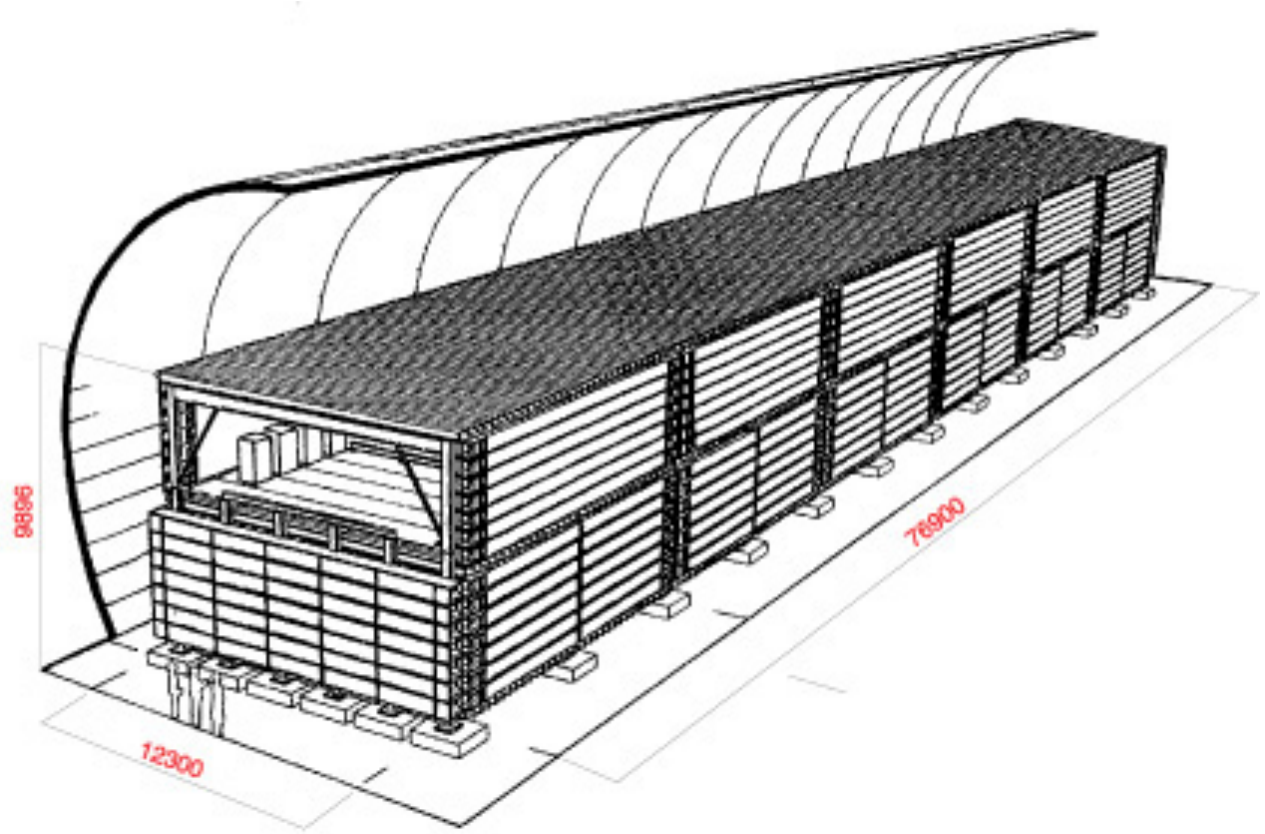

Figure 60: Schematic view of the MACRO detector (dimensions are in mm).

The entire apparatus is surrounded with liquid scintillator counters for fast timing and lateral planes of streamer tubes for tracking. The lower half of the detector is filled with trays of crushed rock absorber alternating with streamer tube planes, while the upper part is open.

The MACRO has a total acceptance for an isotropic flux of downward-going muons of about 5000 m^2 sr. Thanks to its capability in tracking, timing, and particle stopping power determination, it permits the reconstruction of single and multiple muon events and the identification of magnetic monopoles with redundancy in the information.

The main aims of the experiment are

- study of the origin and the composition of high energy cosmic rays;
- detection of magnetic monopoles or, alternatively, the determination of a very stringent limit on their flux;
- detection of neutrinos from stellar collapses;
- study of the atmospheric muon and neutrino physics.

The low energy ν_μ flux can be studied by the detection of neutrino interactions inside the apparatus and by the detection of upward-going muons produced in the rock surrounding it and stopping inside the detector. (Fig. 61, left panel).

Because of the MACRO geometry, muons induced by neutrinos with the interaction vertex inside the apparatus can be tagged with time-of-flight measurement only for upgoing muons. The internal down-going muons (IDμ) with vertex in MACRO and upward going muons stopping inside the detector (USμ) can be identified through topological constraints.

Right panel of Fig. 61 shows the Monte Carlo simulated parent neutrino energy distributions for the three event topologies detected by MACRO. The distributions are normalized to one year of data taking. The internal upgoing muon events (IUμ) are produced by parent neutrinos with energy spectrum almost equal to that of the internal down-going plus upward going stopping μ events.

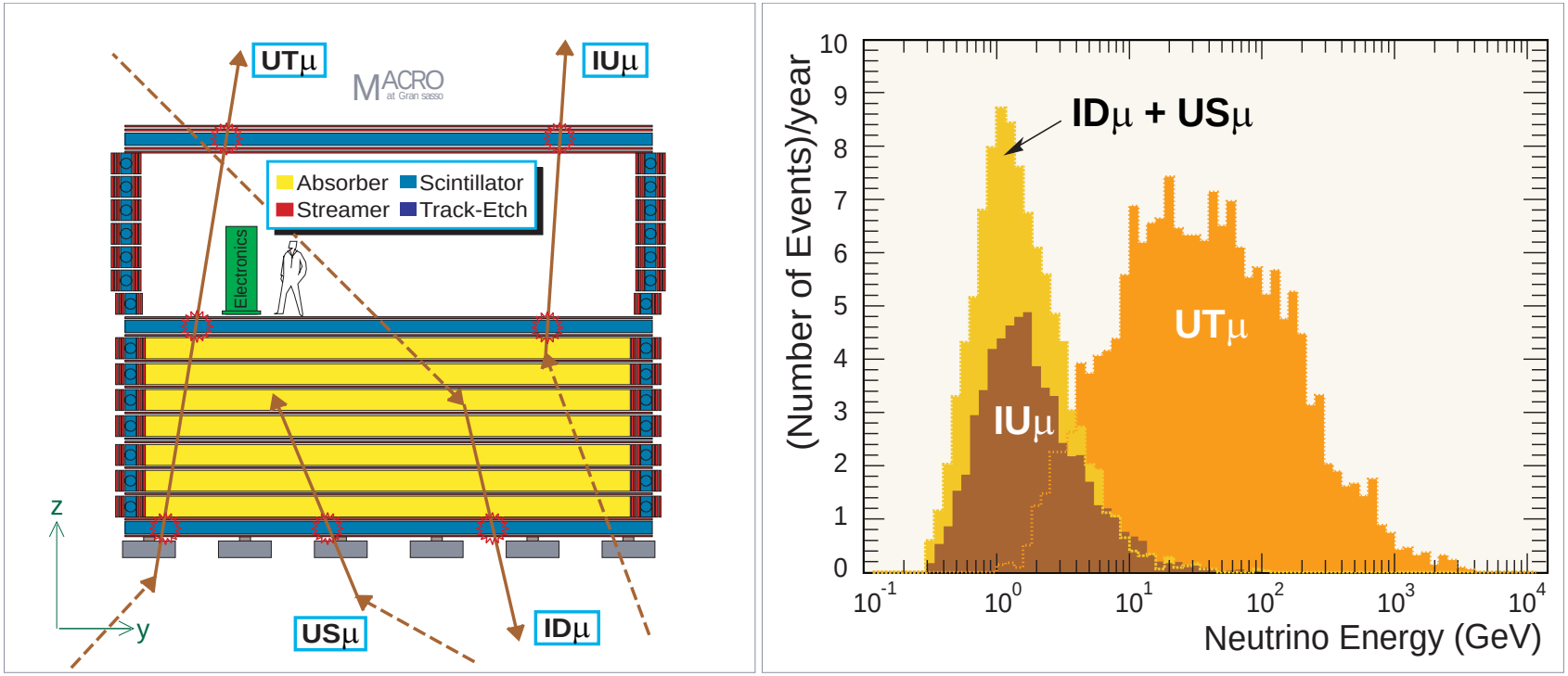

Figure 61: *Left panel*: sketch of different event topologies induced by neutrino interaction in or around MACRO. IUμ = Internal Up-going μ; IDμ = Internal Down-going μ; USμ = Upgoing Stopping μ; UTμ = Upward Through-going μ. The stars represent the scintillator hits. The muon time-of-flight can be measured for the IUμ and UTμ events. *Right panel*: MC simulated distributions of the parent neutrino energy for the three event topologies. The distributions are normalized to one year of data taking. [From M. Ambrosio *et al.* (MACRO Collaboration) Phys. Lett. B **478** (2000) 5 (hep-ex/0001044).]

Figures 62 and 63 show a few-year's old AN results of the MACRO experiment.

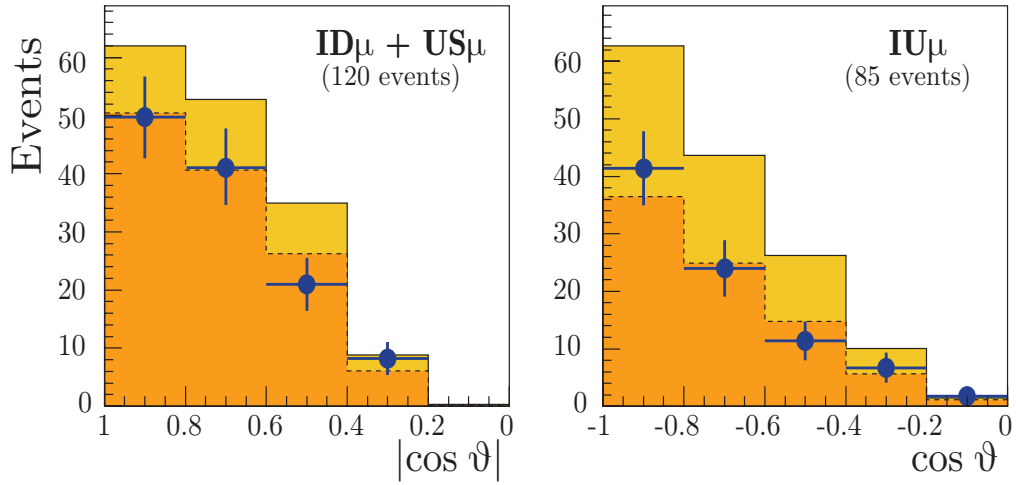

Figure 62: Angular distributions of IDμ+USμ and IUμ events in MACRO. MC histograms are for nonoscillating (higher) and oscillating ANs.

Figures 64 and 65 in next slides [borrowed from M. Ambrosio *et al.* (MACRO Collaboration), Eur. Phys. J. C **36** (2004) 323–339 and G. Giacomelli and A. Margiotta (for the MACRO Collaboration), Yad. Fiz. **67** (2004) 1165–1171 [Phys. Atom. Nucl. **67** (2004) 1139–1146] (hep-ex/0407023)] show the most recent data.

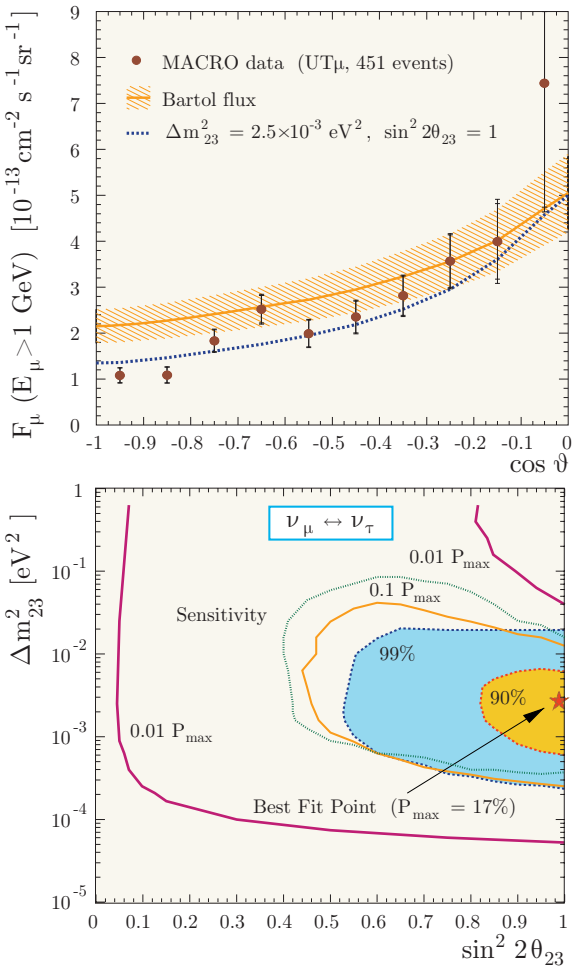

Figure 63: Some old results from the MACRO experiment.

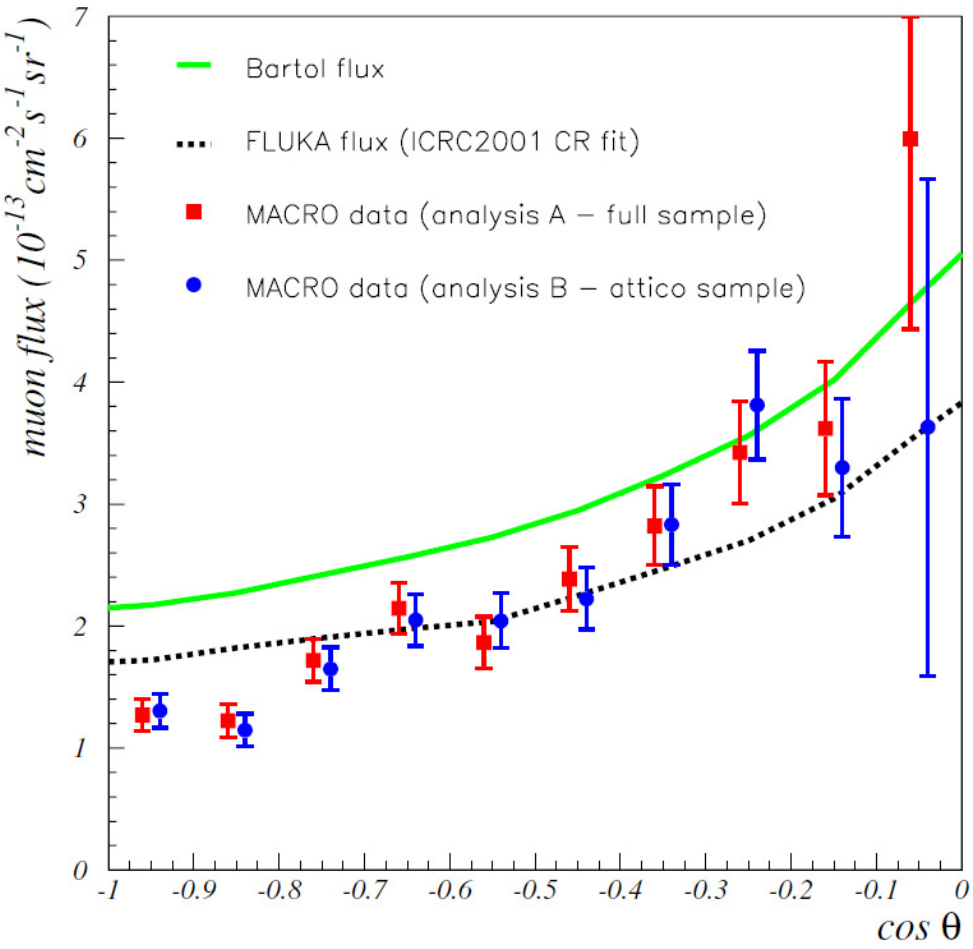

Figure 64: Comparison of with A and B analyses of upward through-going muons in MACRO with calculations.

Figure 64 shows a comparison of the UT muon fluxes measured with MACRO by means of the different analysis procedures, A (full sample, 902 events) and B (*attico* [from an upper part of the detector] sample, 870 events). The experimental points are slightly shifted horizontally to distinguish the two analyses. Statistical and systematic errors are displayed. The nonoscillated Bartol and FLUKA fluxes, assuming $E_\mu > 1$ GeV, are shown (the theoretical error is not displayed). The fit to the new CR measurements is used for the FLUKA flux.

[Borrowed from M. Ambrosio *et al.* (MACRO Collaboration), "Measurements of atmospheric muon neutrino oscillations, global analysis of the data collected with MACRO detector," Eur. Phys. J. C **36** (2004) 323–339.]

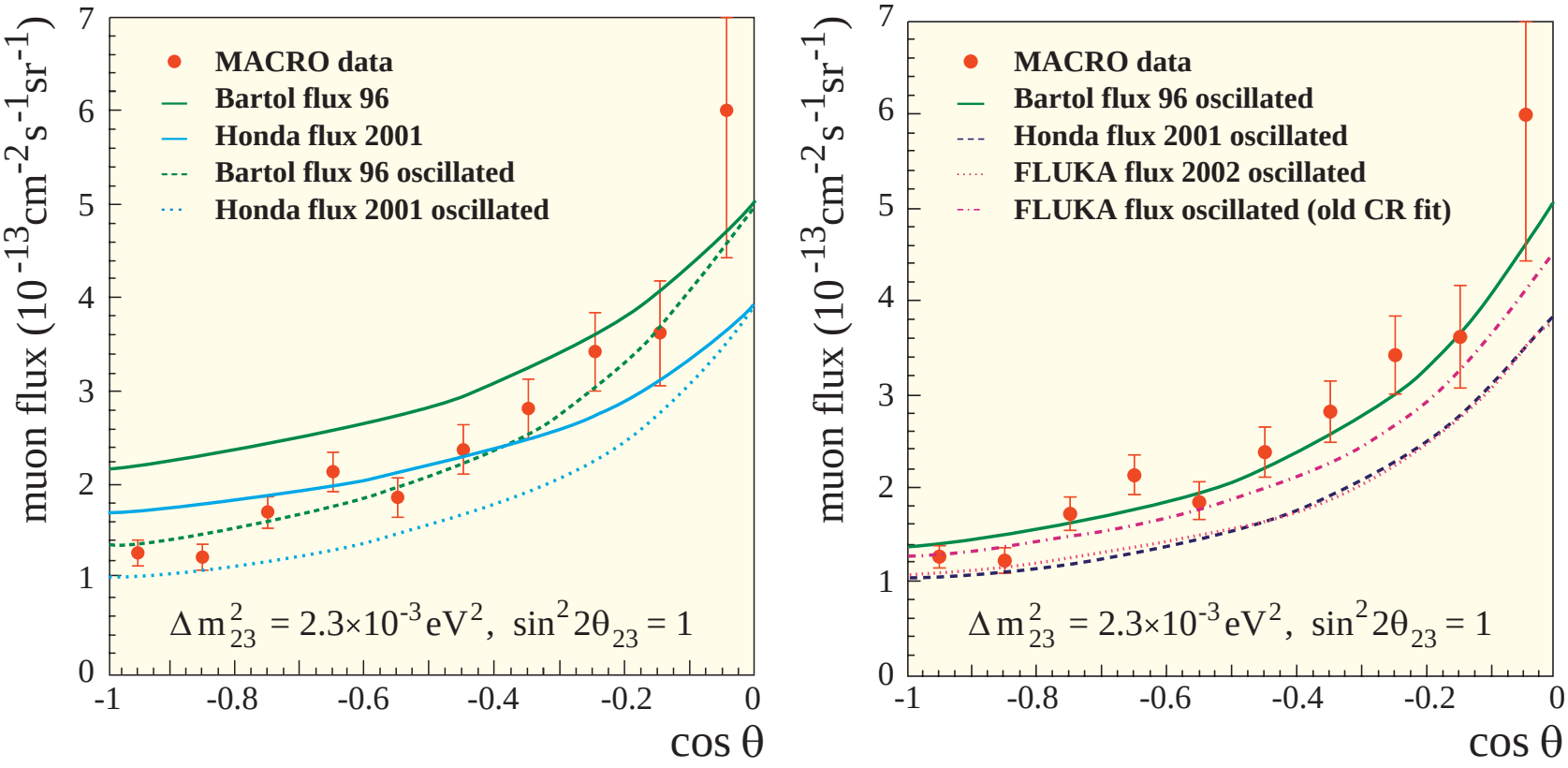

Figure 65: Comparison of the measured angular distribution for upward through-going muons in MACRO with nonoscillated and oscillated (assuming maximal $\nu_\mu - \nu_\tau$ mixing and $\Delta m^2 = 2.3 \times 10^{-3}$ eV^2) AN flux obtained from different MCs. [From G. Giacomelli and A. Margiotta (for the MACRO Collaboration), Yad. Fiz. **67** (2004) 1165–1171 [Phys. Atom. Nucl. **67** (2004) 1139–1146] (hep-ex/0407023); see also M. Ambrosio *et al.* (MACRO Collaboration), Eur. Phys. J. C **36** (2004) 323–339.]

24 SOUDAN 2

The Soudan 2 detector is located in an underground laboratory in the Tower-Soudan Iron Mine 1/2 mile (2,090 m.w.e.) beneath Soudan, Northern Minnesota, USA.

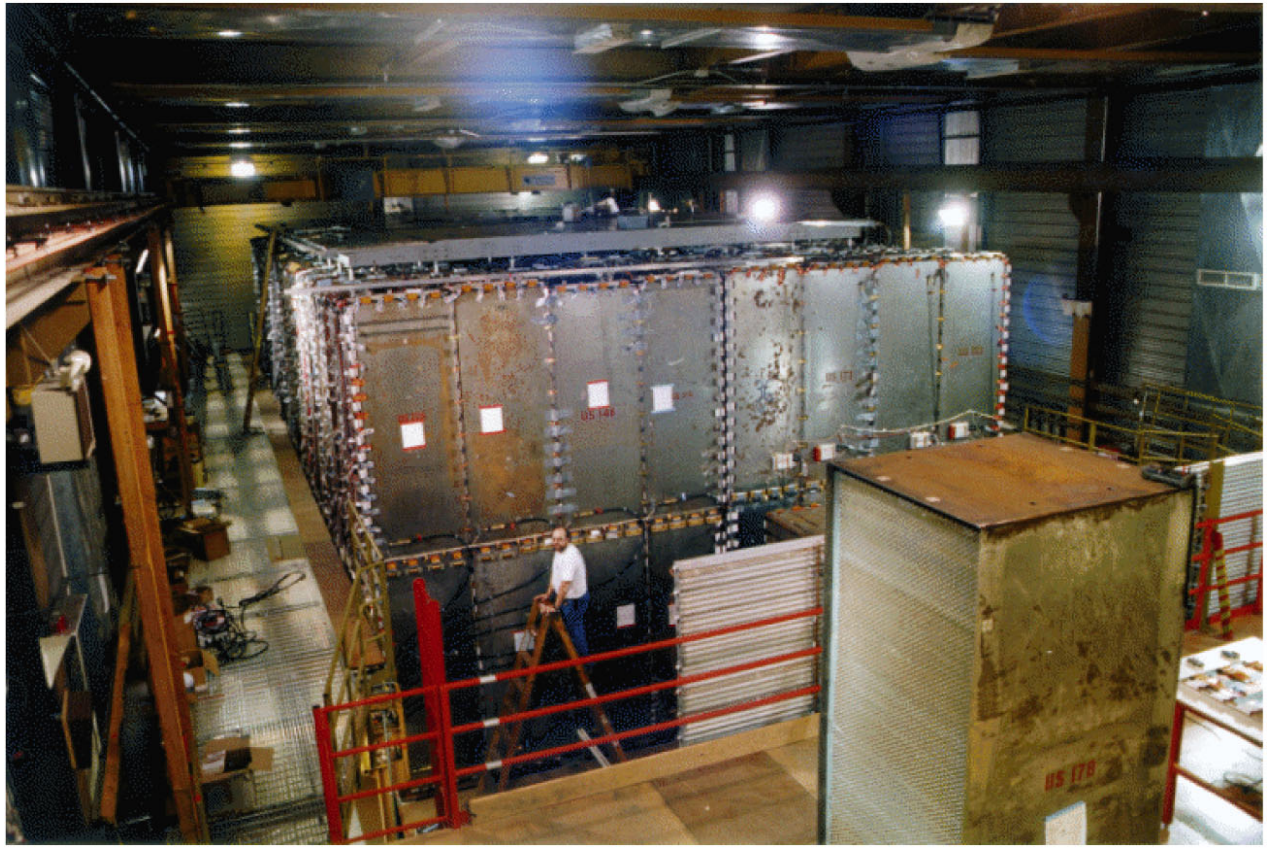

Figure 66: The SOUDAN 2 iron calorimeter modules in the experimental hall.

The detector is a 960 ton gas ionization, time projection calorimeter surrounded by an active shield of proportional tubes (Fig. 67). The calorimeter is comprised of 224 independent modules, each $1 \times 1.1 \times 2.7$ m^3 (shown in the right of Fig. 67).

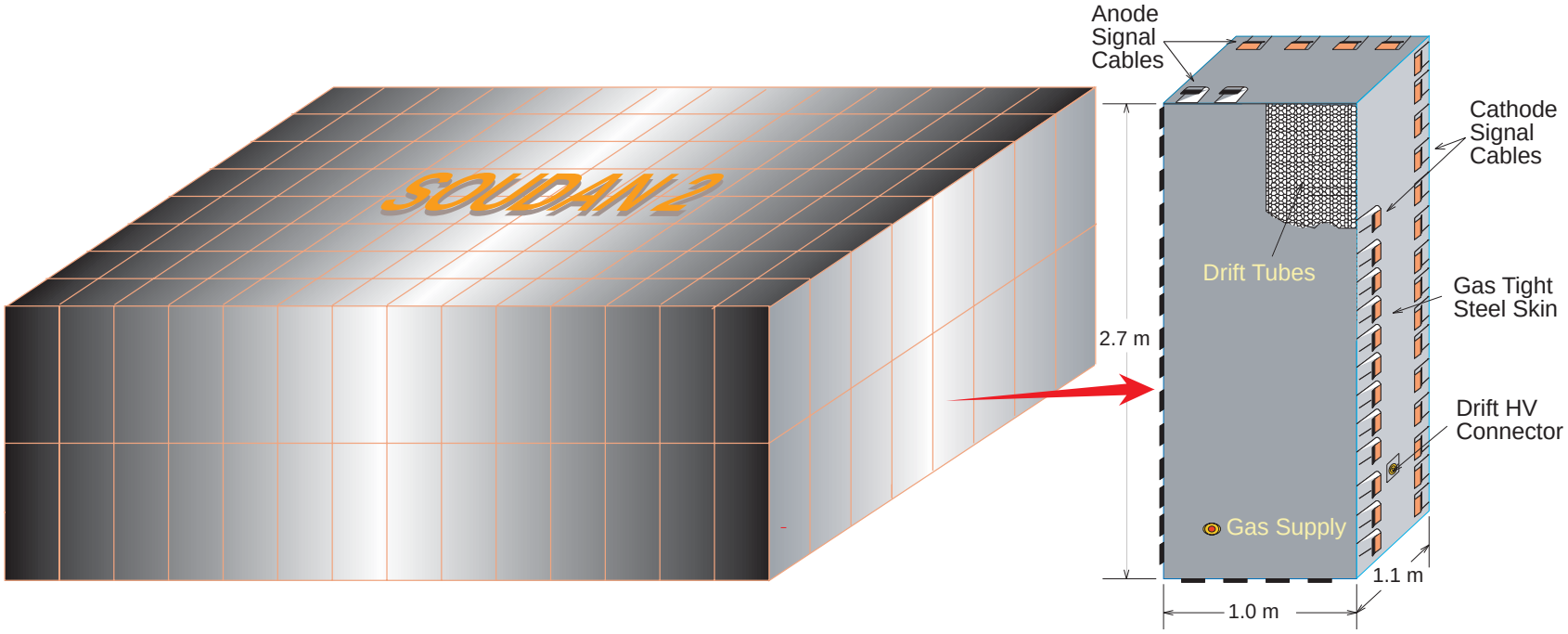

Figure 67: Schematic view of the SOUDAN 2 detector and its module (zoomed).

The modules, each of which weighs about 5 tons are constructed inside gas-tight, steel boxes. The boxes are filled with a mixture of 85% argon, 15% carbon dioxide gas. Most of the mass in each module is located in 240 corrugated steel plates, which are layered

horizontally giving the inside of each module the appearance of a large honeycomb. Each module contains a tightly packed honeycomb array of 15,120 drift tubes set in a steel absorbing medium giving an average density of 1.6 gm/cc. The drift tube array provides 3-dimensional hit reconstruction, with an r.m.s. accuracy of 1.12 cm in the drift direction and 3.5 mm in the orthogonal plane, together with the power stopping sampling.[a] The modules are close packed in an array 2 high by 8 across by 14 deep to form a detector 5.4 m high, 8 m across and 15 m long.

The primary physics goals of the experiment:

- search for nucleon decay;
- study atmospheric neutrino physics, in particular to look for evidence of neutrino oscillations;
- search for magnetic monopoles;
- search for neutrinos from Active Galactic Nuclei;
- search for astrophysical point sources of cosmic rays;
- study the chemical composition of primary cosmic rays.

The target exposure for the experiment of 5 Kton-years has been achieved. Beyond this there is a possibility of incorporating the detector into the MINOS experiment which is designed to search for and measure neutrino oscillations and neutrino mass using a

[a] For a detailed description of the calorimeter see W. W. M. Allison *et al.*, Nucl. Instrum. Meth. A **376** (1996) 36; W. W. M. Allison *et al.*, Nucl. Instrum. Meth. A **381** (1996) 385.

controlled, accelerator produced neutrino beam. The neutrino beam will be generated in the Fermilab neutrino beam line (near Chicago) and passed through the Earth to the Soudan Mine 730 km away where the new MINOS experiment will be located. A search for neutrino oscillations over this long baseline will cover the same region of oscillation parameters as the atmospheric neutrino anomaly reported by the Super-Kamiokande, MACRO and Soudan 2 experiments.

There are two energy detectors located on the Earth's surface near the entrance to the Soudan mine and operated in coincidence with the deep underground calorimeter to provide air shower information.

One is a flat array of detectors called proportional tubes located in a house trailer parked about 100 m east of the mine shaft. This array, 15 m long by 4 m wide, measures the amount of energy left in the Earth's atmosphere by a cosmic ray, while the Soudan 2 detector measures characteristics of the muons associated with the same cosmic ray. The correlation between surface and underground data yields information about the properties of the original cosmic ray, as it entered the atmosphere.

A second kind of energy detector, located near the proportional tube array, is called an atmospheric Cherenkov detector. It also measures cosmic ray energy deposition in the atmosphere, but by a different technique. The Cherenkov detector is sensitive to very faint light produced in the atmosphere as the cosmic ray propagates downward. This light is so faint that the atmospheric Cherenkov detector is usable only on clear nights when the moon is not visible. It also operates in conjunction with the Soudan 2 detector.

Figures 68 and 69 show a 10 year's old (but still interesting) AN results of the SOUDAN 2 experiment.

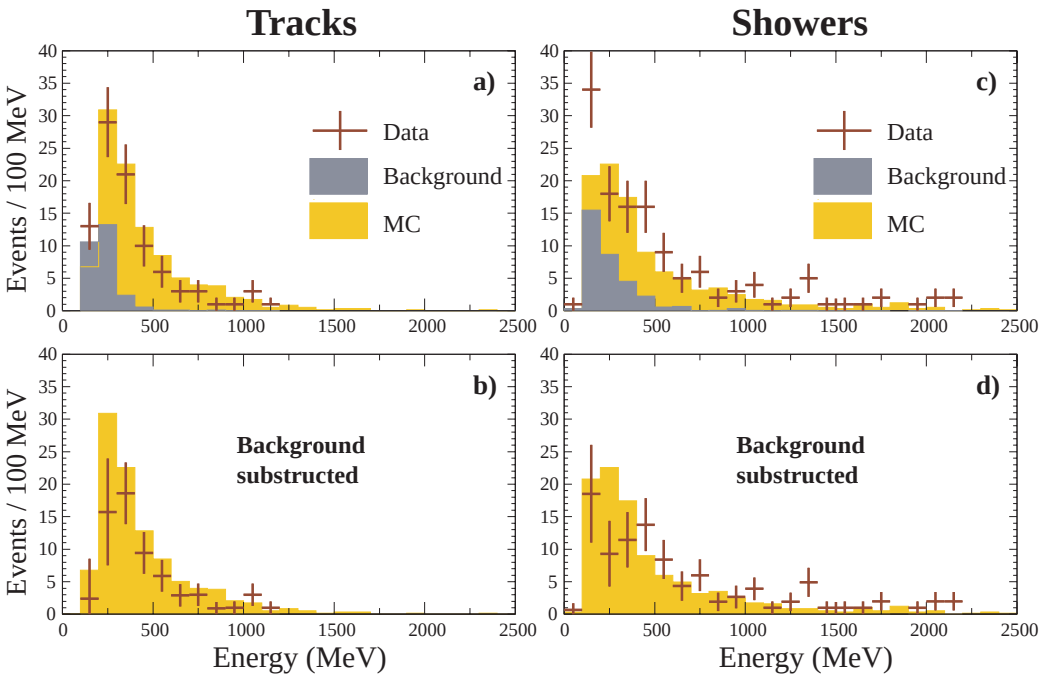

Figure 68: Energy distributions of SOUDAN 2 events.

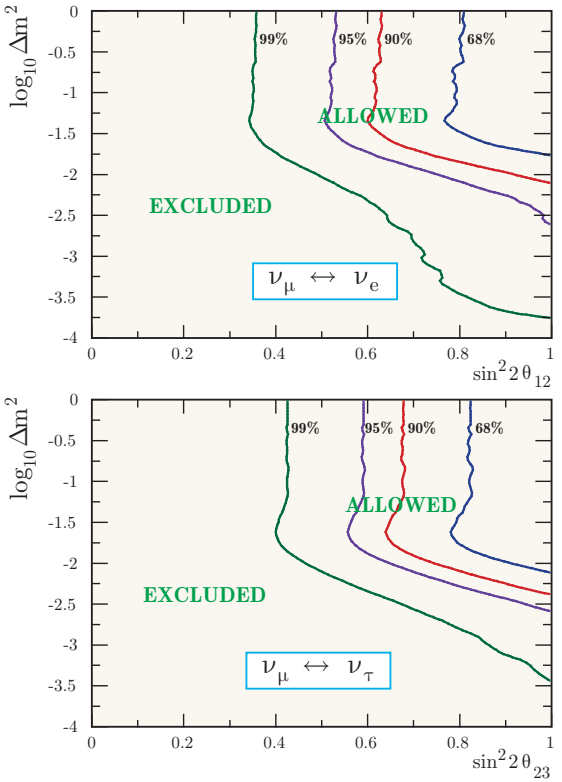

Figure 69: Allowed and excluded regions of $\sin^2 2\theta_{ij}$ and Δm^2 obtained from the old SOUDAN 2 data for two scenarios of neutrino mixing.

Figures 70–72 below [borrowed from M. C. Sanchez *et al.* (Soudan 2 Collab.), Phys. Rev. D **68** (2003) 113004 (hep-ex/0307069) and P. J. Litchfield (for the Soudan 2 Collab.), Nucl. Phys. B (Proc. Suppl.) **138** (2005) 402-404.] show the most recent data.

Figure 70 shows the zenith-angle and azimuth-angle distributions for high resolution (HiRes) events in SOUDAN 2 collected during the 7.36 kiloton-year (5.90 fiducial kiloton-year) exposure of the detector. The points with error bars are the data. The dashed histograms are the sum of the predicted nonoscillated neutrino distribution (with the Bartol 96 AN flux) plus the fitted rock contribution. The solid histograms are the prediction of the best-fit parameters of this analysis. The dotted histograms are the contribution of the rock background. Note the depletion of μ-flavor events at all but the highest value of $\cos\theta$.

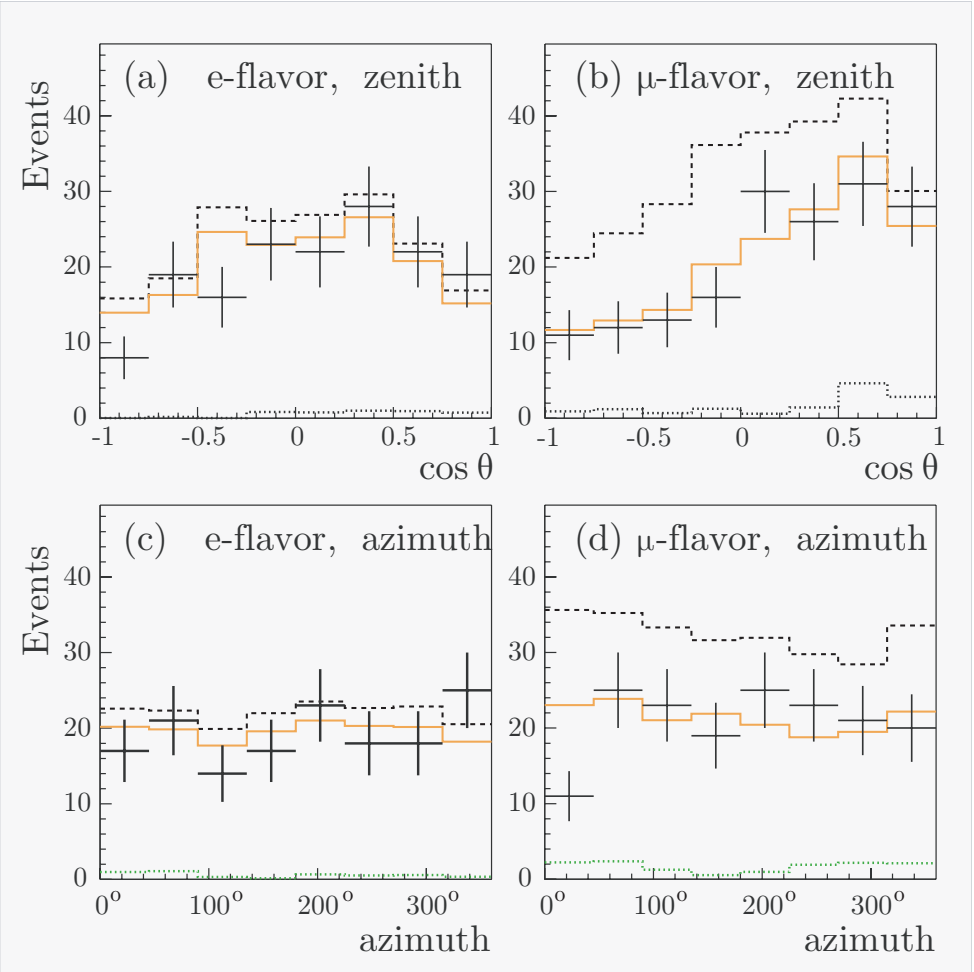

Figure 70: Angular distributions for high resolution events in SOUDAN 2.

Figure 71 shows the HiRes $\log_{10}(L/E)$ distribution e-flavor (top) and μ-flavor (bottom) events in SOUDAN 2. The points with error bars are the data. The dashed histograms are the prediction of the nonoscillated Monte Carlo plus the fitted qs-rock contribution. The solid histograms are the same but with the Monte Carlo (with the Bartol 96 AN flux) weighted by the best fit oscillation parameters from the analysis. The dotted histograms are the contribution of the rock background. A depletion of μ-flavor events above values of $\log_{10}(L/E)$ of approximately 1.5 can be seen. Below this value there is little, if any, loss of events. This implies an upper limit on the value of Δm^2 of about 0.025 eV^2.

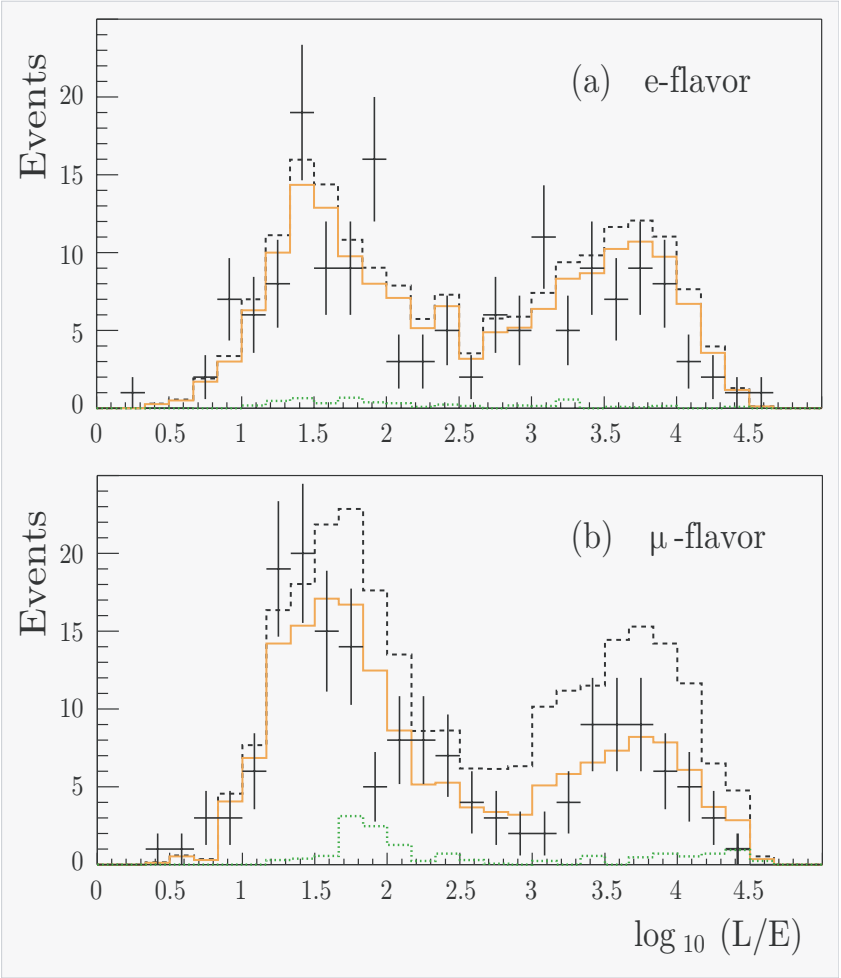

Figure 71: The HiRes $\log_{10}(L/E)$ distribution for e- and μ-flavor events in SOUDAN 2.

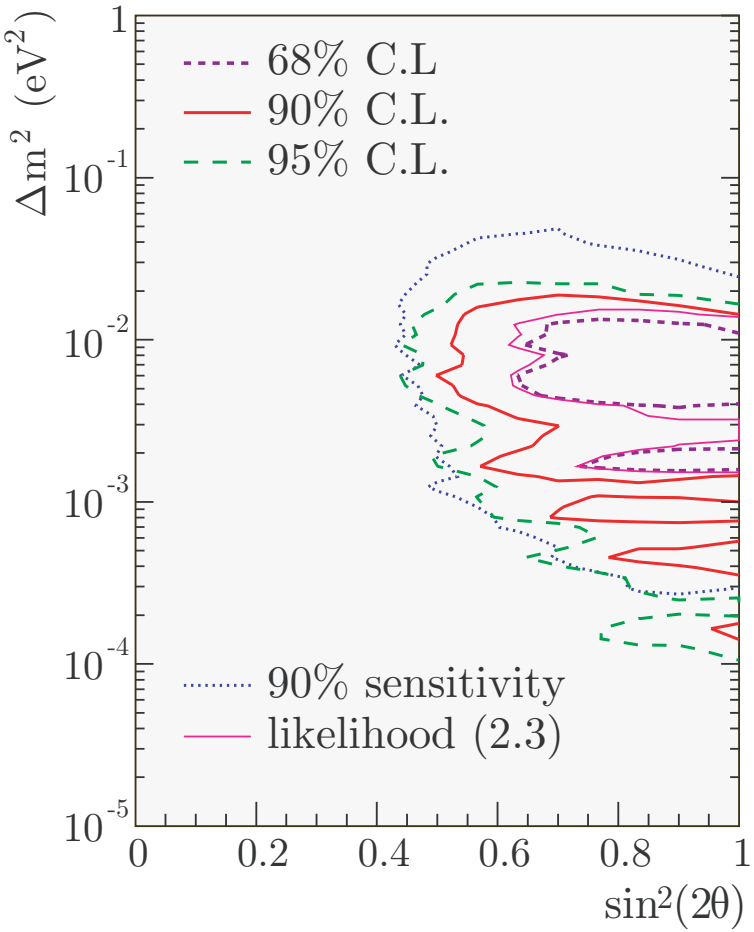

Figure 72: Confidence level contours from the Feldman-Cousins analysis of the SOUDAN 2 events.

Figure 72 shows the confidence level contours from the Feldman-Cousins analysis of the SOUDAN 2 events: 68% (short dashed line), 90% (thick solid line) and 95% (long dashed line). The dotted line is the 90% sensitivity for the best-fit $(\sin^2 2\theta, \Delta m^2)$ point. The thin solid line is the contour defined by a data likelihood rise, $\Delta\mathcal{L}$, of 2.3 (Fig. 73).

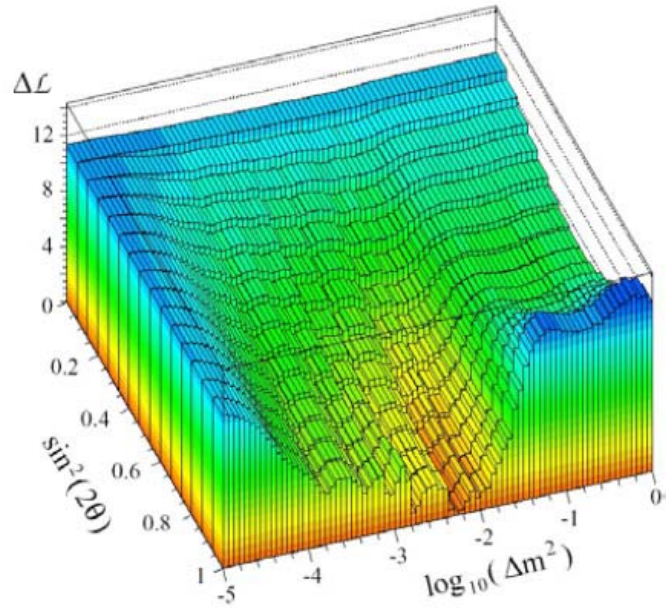

Figure 73: The data likelihood difference.

25 NUSEX

References:

1. G. Battistoni *et al.*, "Fully contained events in the Mont Blanc nucleon decay detector", Phys. Lett. B **118** (1982) 461–465.
2. G. Battistoni *et al.*, "Nucleon stability, magnetic monopoles and atmospheric neutrinos in the Mont Blanc experiment", Phys. Lett. B **133** (1983) 454–460.
3. G. Battistoni *et al.*, "An experimental study of the neutrino background in underground experiments on nucleon decay", Nucl. Instrum. Meth. **219** (1984) 300–310.
4. G. Battistoni *et al.*, "The NUSEX detector," Nucl. Instrum. Meth. A **245** (1986) 277–290.
5. M. Aglietta *et al.* (NUSEX Collaboration), "Experimental study of atmospheric neutrino flux in the NUSEX experiment", Europhys. Lett. **8** (1989) 611–614.
6. M. Aglietta *et al.* (NUSEX Collaboration), "Experimental study of upward stopping muons in NUSEX", Europhys. Lett. **15** (1991) 559–564.

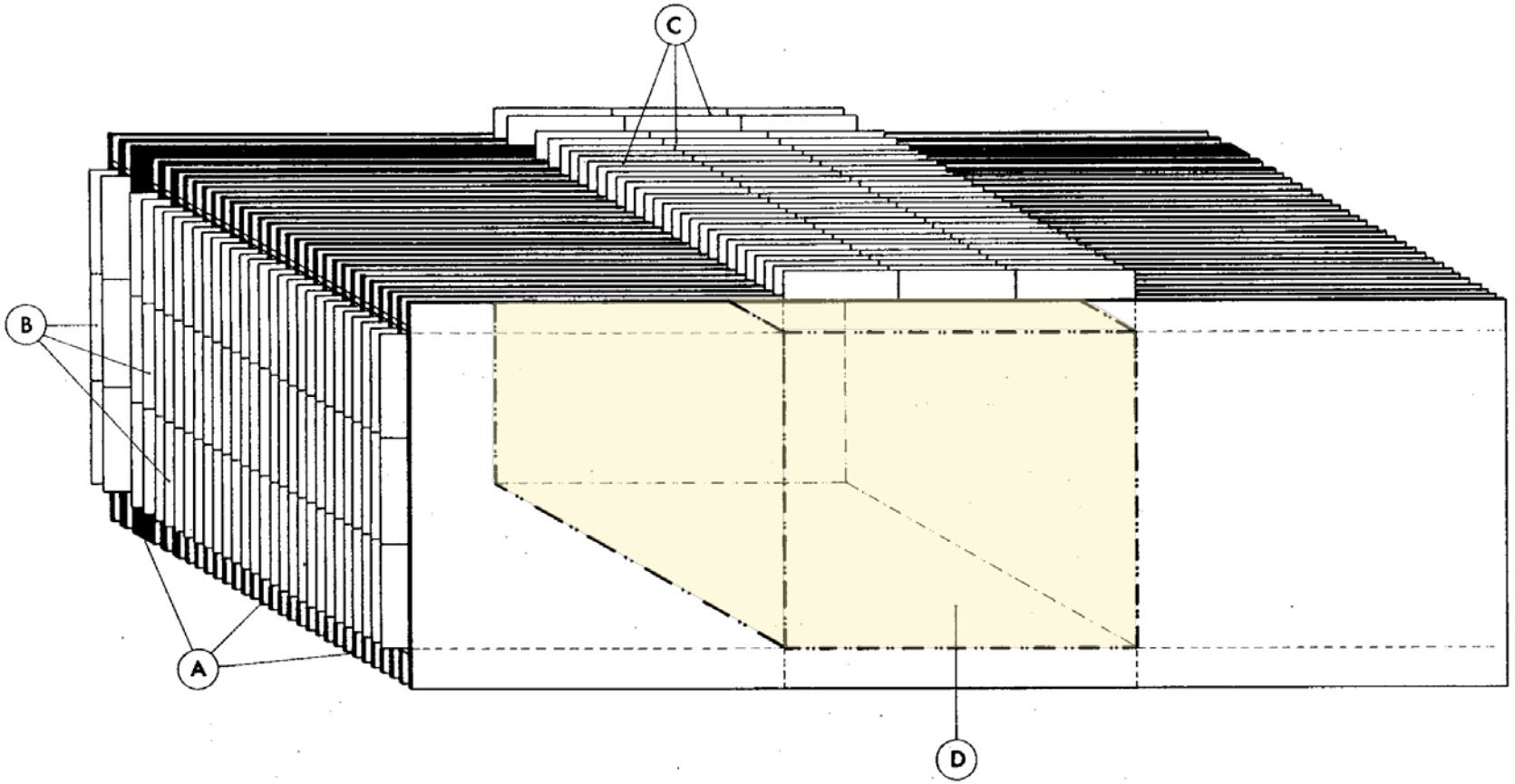

Figure 74: A scketch of the detector used in the NUSEX experiment: (A) the vertical iron plates; (B) the detector tubes plus the x-strips; (C) the y-strips; (D) the fuducial volume. [From G. Battistoni *et al.*, Nucl. Instrum. Meth. **219** (1984) 300–310.]

26 Fréjus

References:

1. P. Bareyre *et al.* (AACHEN – ORSAY – PALAISEAU – SACLAY – WUPPERTAL Collaboration), "Status of the Fréjus experiment and preliminary results on contained events", Nuovo Cim. **9 C** (1986) 159–166.
2. C. Berger *et al.* (Fréjus Collaboration), "The Fréjus nucleon decay detector", Nucl. Instrum. Meth. A **262** (1987) 463–495.
3. C. Berger *et al.* (Fréjus Collaboration), "Study of atmospheric neutrino interactions with the Fréjus detector", Phys. Lett. B **227** (1989) 489–494.
4. C. Berger *et al.* (Fréjus Collaboration), "A study of atmospheric neutrino oscillations in the Fréjus experiment", Phys. Lett. B **245** (1990) 305–310.
5. C. Berger *et al.* (Fréjus Collaboration), "Experimental determination of neutrino background expected in the Frejus nucleon decay detector", Nucl. Instrum. Meth. A **302** (1991) 406–414.
6. K. Daum *et al.* (Fréjus Collaboration), "Determination of the atmospheric neutrino spectra with the Fréjus detector", Z. Phys. C **66** (1995) 417–428.
7. W. Rhode *et al.* (Fréjus Collaboration), "Limits on the flux of very high-energetic neutrinos with the Fréjus detector", Astropart. Phys. **4** (1996) 217–225.

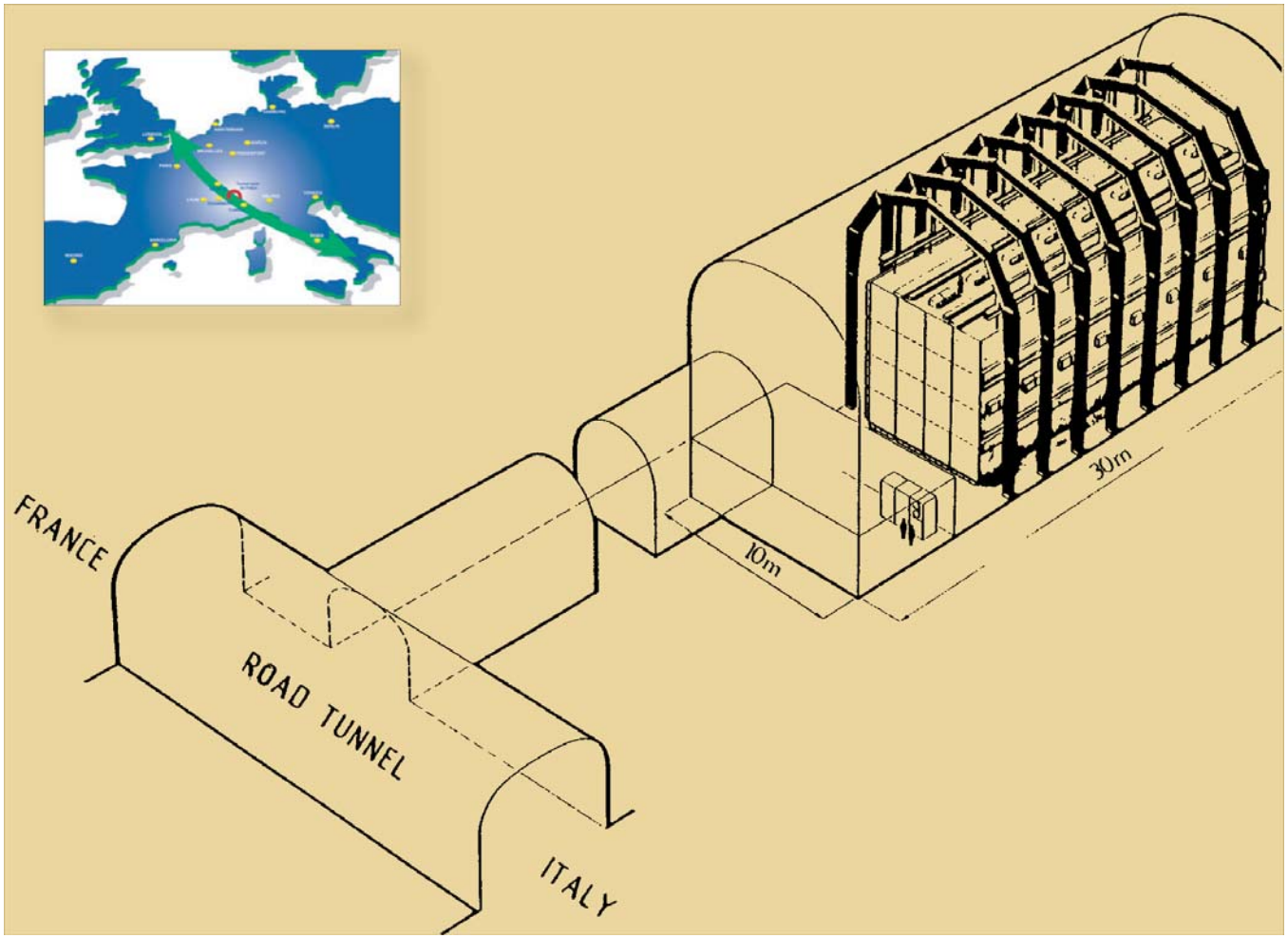

Figure 75: Schematic view of the Fréjus underground Laboratory. [From C. Berger *et al.* (Fréjus Collaboration), Nucl. Instrum. Meth. A **262** (1987) 463–495.]

27 BUST

The Baksan Underground Scintillation Telescope (BUST) located at the Baksan Neutrino Observatory of the Institute for Nuclear Research, RAS consists of 4 horizontal layers of thick ($0.30 \times 200 \times 200$ m^3) liquid scintillator separated by concrete absorber (8 radiation lengths each). It has also 4 vertical scintillator planes surrounding the horizontal ones.

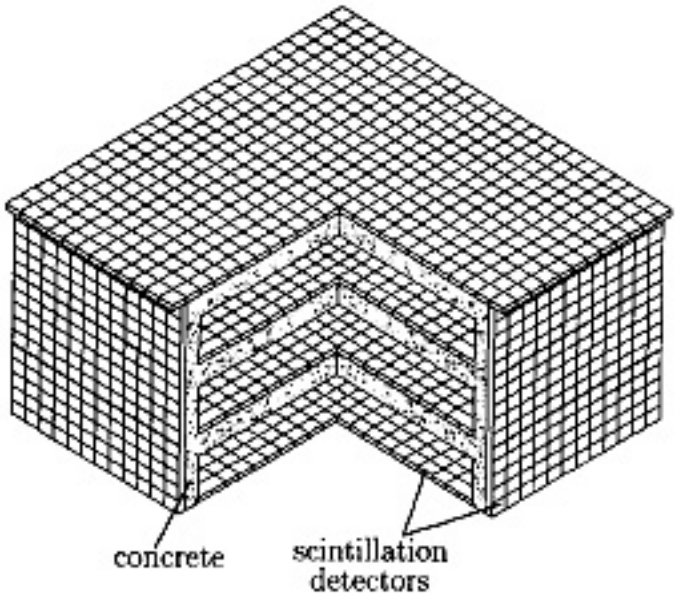

Figure 76: Schematic sectional view of the BUST (*left panel*) and of one of its horizontal scintillator planes (*right panel*).

The full detector dimensions are $16.7 \times 16.7 \times 11.2$ m^3 and the full volume is about 3000 m^3. Each of three lower horizontal scintillator layers consists of 400 tanks of $70 \times 70 \times 30$ cm^3 size, viewed by 6 inch PMTs (FEU-49). The top layer consists of 576 detectors. It is located at a depth of about 850 hg/cm^2 below Andyrchi mountain.

There are also ground installations which can operate in coincidence with the BUST: ANDYRCHI for detecting extensive atmospheric showers (it is located over the BUST and covers an area of about 5×10^4m^2) and a set of ground facilities KOVYOR comprising Large Muon Detector, Scintillation Telescope and Neutron Monitor for studying the hard component of cosmic rays and EAS.

28 Upward through-going muons

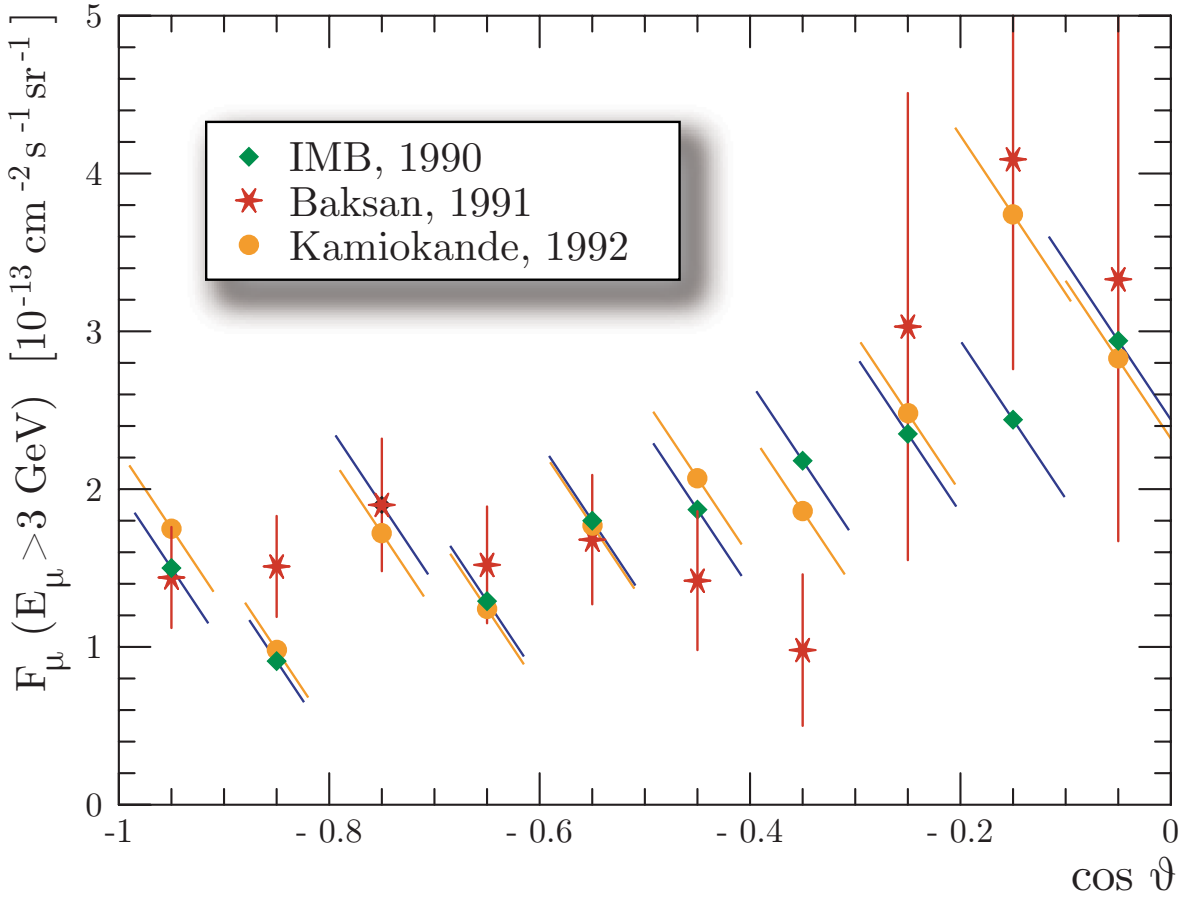

Figure 77: Zenith-angle distributions of upward through-going muons measured in earlier underground experiments and converted to a single energy threshold of 3 GeV.

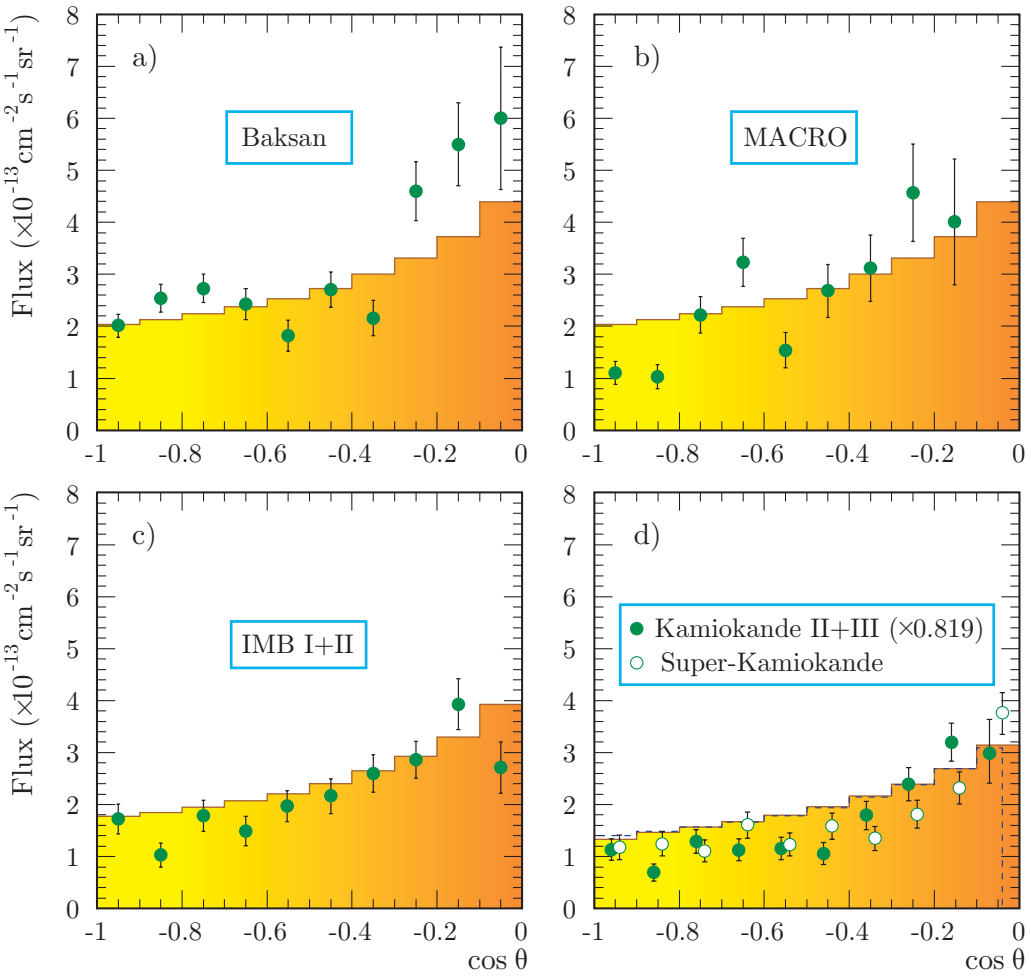

Figure 78: Zenith-angle distributions of upward through-going muons observed in 5 experiments.

Figure 78 shows the zenith-angle distributions of upward through-going muons measured in Baksan, MACRO, IMB I+II, Kamiokande II+III and Super-Kamiokande I. The scale of Kamiokande is normalized to that of Super-Kamiokande. The histograms are calculated with GRV94 PDF set for Kamiokande (dashed) and Super-Kamiokande (solid) and with MSR(G) PDF set for the other experiments. The Bartol-96 muon flux and muon energy loss according to Lohmann *et al.* ("CERN Yellow Report") are used in the calculations.

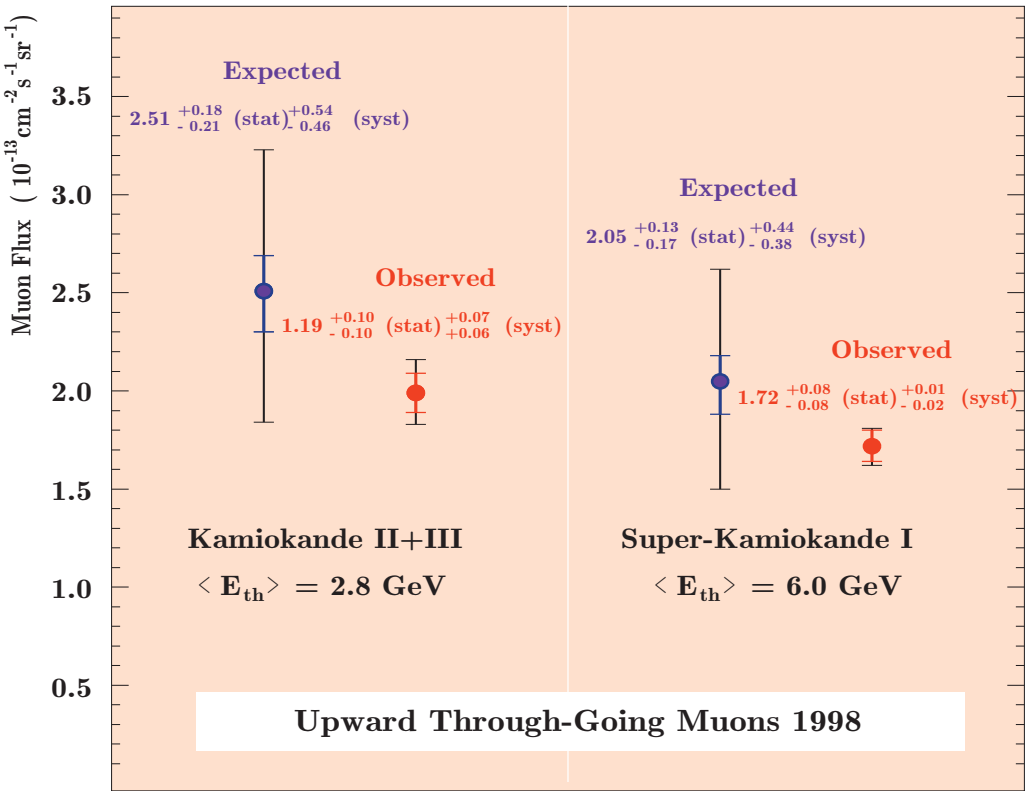

Figure 79: Expected and observed total fluxes of upward through-going muons for Kamiokande II+III and Super-Kamiokande I. [From S. Hatakeyama, "Search for muon neutrino oscillations in Kamiokande and Super-Kamiokande," Ph.D. thesis (1998).]

Figure 79 shows the expected and observed total fluxes of upward through-going muons for Kamiokande II+III and Super-Kamiokande I (the data collected before 1998). Inside error bars of the expected flux are the differences in the models and the outside ones are the same plus 20% uncertainty of each model (which comes from the uncertainty in the atmospheric muon neutrino fluxes. The inside errors of the observed fluxes are combined statistical and systematic errors.

In fact the "theoretical" uncertainty may be much larger than 20% (see Table 12).

Table 12: Theoretical uncertainties in the absolute flux of upgoing muons.

Primary CR energy spectrum	$\sim 20\%$
Primary CR charge/isotopic composition (n/p ratio)	to 3%
Cross sections of pion production in NA interactions and pion regeneration (π^+/π^- ratio)	to 5%
Cross sections of CC induced $\nu_\mu N$ and $\overline{\nu}_\mu N$ interactions	$\sim 10\%$
Cross sections of NC induced $\nu_\mu N$ and $\overline{\nu}_\mu N$ interactions (responsible for neutrino regeneration in the Earth)	$\sim 1\%$
Nuclear effects in ν_μ ($\overline{\nu}_\mu$) interactions with matter	to 2%
Composition and inhomogeneity of the detector surrounding (affect the muon energy loss)	to 2%
Muon range struggling in the surrounding rock	to 1%
Other uncertainties and methodical simplifications	a few %
Prompt neutrino contribution	?
Omitted backgrounds	?

Total uncertainty may be as large as 25–35%

Part VI

NEUTRINO TELESCOPES

29 Detectors for high-energy neutrino astronomy

In 1960, Markov[a] and Reines[b] independently suggested to catch high-energy cosmic neutrinos via their charged current interactions using the ocean as a detector medium by observing the Cherenkov light of the produced muons and, simultaneously, as a screen for the cosmic-ray and solar light backgrounds.[c] Up-going muons can be identified in a background of down-going, cosmic ray muons which are more than 10^5 times more frequent for a depth of about 12 km. The Earth is therefore also serves as a part of the detector, being the natural filter and "discriminator". This makes neutrino detection possible over the hemisphere of sky faced by the bottom of the detector.

It was thought that the ocean is a rather inexpensive target, the detector can be build modular and enlarged when necessary. The detector can take the advantage of the rising cross section for neutrino-nucleon interactions with energy. As the range of the

[a] M. A. Markov, in Proc. of 1960 Annual International Conf. on High Energy Physics at Rochester, edited by E. C. G. Sudarshan, J. H. Tinlot and A. C. Melissinos (University of Rochester, NY, 1960), p. 578. See also M. A. Markov and I. M. Zheleznykh, Nucl. Phys. **27** (1961) 385–394.

[b] F. Reines, Ann. Rev. Nucl. Sci. **10** (1960) 1. Greisen, in the same journal volume [K. Greisen, Ann. Rev. Nucl. Sci. **10** (1960) 63] also mentioned the idea of neutrino astronomy as a "fanciful proposal".

[c] Probably the idea of Reines was a natural consequence of the following note by F. Reines, C. L. Cowan and H. W. Krusenot, "Conservation of the number of nucleons," Phys. Rev. **109** (1958) 609–610 concerning experimental search for nucleon decay:

> *Higher sensitivity could be obtained both by using larger counters and by going deep underground or in the ocean to eliminate cosmic rays.*

final state muon increases with energy, the effective detector volume is growing as well with energy. Furthermore, it is expected that the energy spectra from many point astrophysical sources fail off less step that from atmospheric neutrinos.

Thus the deep underwater detectors can be used as telescopes for high-energy neutrino astronomy.

The optical requirements on the detector medium are severe. A large absorption length is needed because it determines the required spacing of the optical sensors and, to a significant extent, the cost of the detector. A long scattering length is needed to preserve the geometry of the Cerenkov pattern. Nature has been kind and offered ice and water as the natural Cerenkov media. Their optical properties are, in fact, complementary. Water and ice have comparable attenuation lengths, with the roles of scattering and absorption reversed. Optics seems, at present, to drive the evolution of ice and water detectors in predictable directions: towards very large telescope area in ice exploiting the long absorption length, and towards lower threshold and good muon track reconstruction in water exploiting the long scattering length.

Figure 80[d] shows a map of present-day underwater/ice Cherenkov neutrino telescope projects (see also Table 13 for a summary of their status).

[d] By Francis Halzen <http://icecube.wisc.edu/~halzen/>.

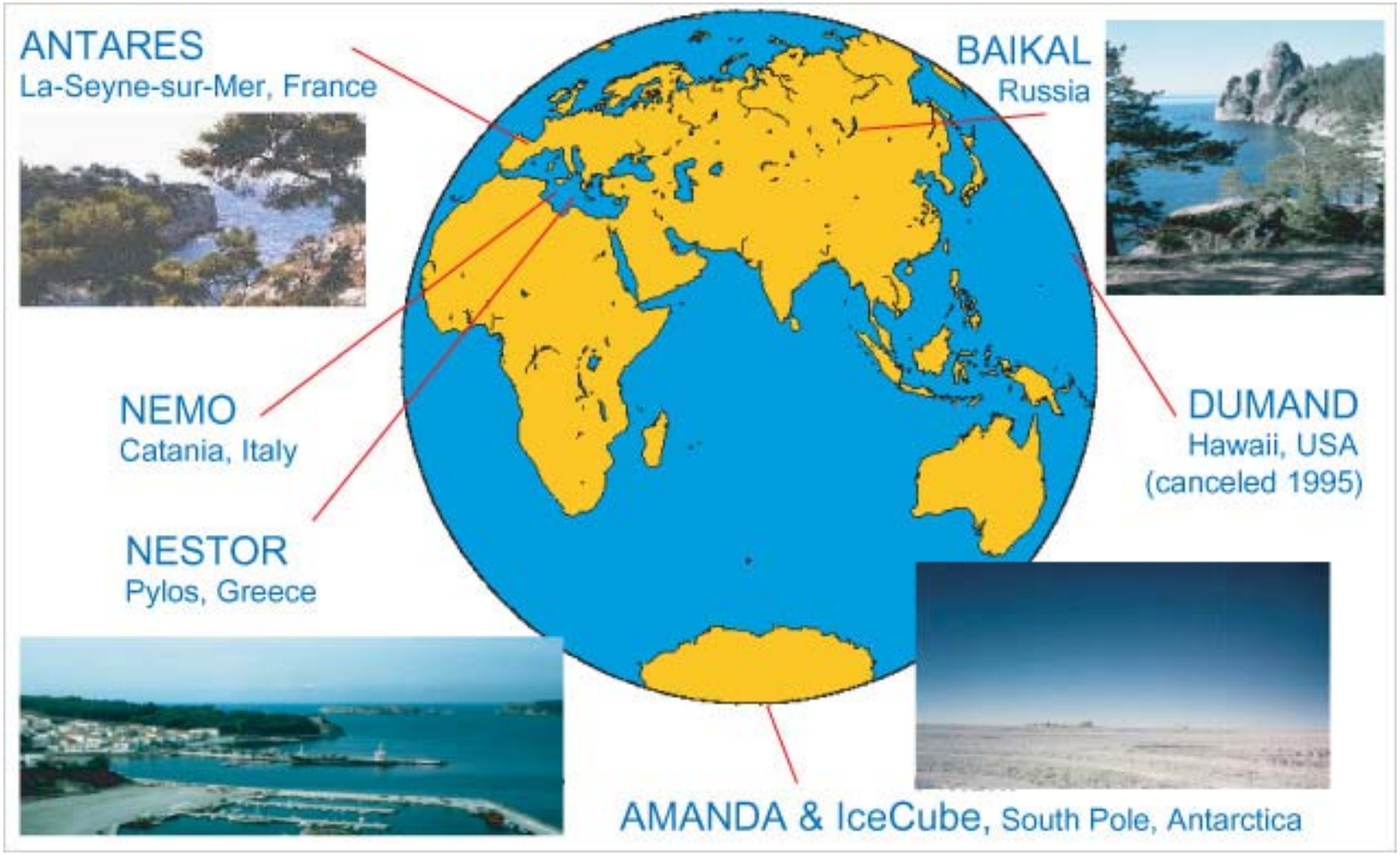

Figure 80: A map of underwater/ice Cherenkov neutrino telescope projects [by Francis Halzen <http://icecube.wisc.edu/~halzen/>].

Table 13: Past, present and future underwater/ice neutrino telescopes.

Lab/Location/Stage	Year(s)	Sensitive area* (10^3 m^2)	Status (fall, 2003)
DUMAND I, II *Pacific near Hawaii Big Island; at a depth of ~4.5 km*	Historically first underwater project. Closed down...**		
BAIKAL NT *Lake Baikal, East Siberia; at a depth of about 1.1. km*			
NT-36	1993-95	0.15-0.20	Stepwise deployment & going into operation
NT-72	1995-96	0.4-3.0	
NT-96	1996-97	0.8-6.0	
NT-144	1997-98	1.0-8.0	
NT-200	1998	2.0-10.0	Operates
AMANDA *South Pole; at a depth of 0.8 to 2 km*			
AMANDA A	1994	Small	Stepwise deployment & going into operation
AMANDA A	1996	1.0	
AMANDA B4	1998	5-6	
AMANDA II	2000	30-50	Operates
AMANDA KM3 or IceCube	2005	1000	Under construction
NESTOR *Ionian Sea near Pylos, Peloponnesos, Greece; at a depth of about 3.8 km*	2004 ?	1st phase: 20 KM^3 in prospect	Under construction & test
ANTARES *Mediterranean near Toulon, France; at a depth from 2.4 to 2.7 km (the most appropriate site is identified)*	2004 ?	to 100-200 KM^3 in prospect	R & D
NEMO *Capo Passero (Sicily), Italy; at a depth of about 3.4 km*	?	to 3500 KM^3 in prospect	R & D

Notes to Table 13:

*) The sensitive (effective) area is an increasing function of muon energy. For example, the estimated effective area of the Baikal NT-200 is about 2300 m^2 and 8500 m^2 for 1-TeV and 100-TeV muons, respectively.

**) Some 1-string prototypes of the DUMAND array were deployed and several useful results were obtained.

30 Again Cherenkov...

The underwater/ice neutrino telescopes collect Cherenkov light from high-energy muons, electromagnetic and hadronic showers generated by neutrinos in the detector medium. This light can be recorded at distances up to about 100 m depending upon the light absorption of water or ice. Light pulses from lasers, widely used in these arrays for calibration, can be recorded over even larger distances. At such distances, the difference between phase and group velocities of light in water or ice is essential.[a]

Let us discuss this difference in short.

A few facts from school physics

First of all we consider the simplest monochromatic sine wave

$$A(\mathbf{r}, t) = A_0 \cos(\mathbf{kr} - \omega t).$$

The speed at which the shape of this wave is moving is given by the condition (see Fig. 81)

$$\mathbf{k}\Delta\mathbf{r} - \omega\Delta t = 0, \quad \Delta t \to 0.$$

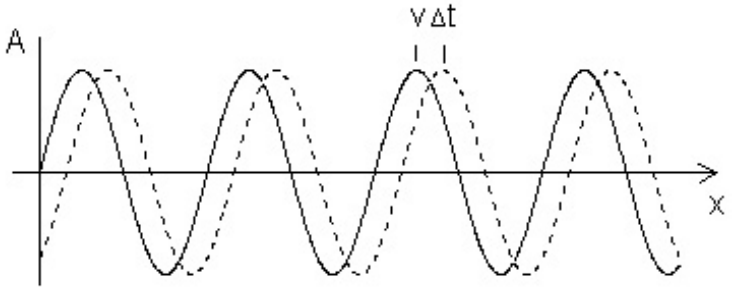

Figure 81: A sine wave.

[a] L. A. Kuzmichev, "On the velocity of light signals in deep underwater neutrino experiments," Nucl. Instrum. Meth. A **482** (2002) 304–306 (hep-ex/0005036). Baikal NT experience shows that v_g rather than v_p must be used for time-calibration of the detector modules with an outside laser.

Consequently the speed

$$\mathbf{v}_p = \dot{\mathbf{r}} = \lim_{\Delta t \to 0} \frac{\Delta \mathbf{r}}{\Delta t} = \nabla_{\mathbf{k}} \omega$$

is called the phase velocity of the wave.

Let us now consider a signal consisting of two superimposed sine waves with slightly different frequencies and wavelengths, i.e., a signal with the amplitude function

$$A(\mathbf{r}, t) = A_0 \cos\left[(\mathbf{k} - \mathbf{K})\,\mathbf{r} - (\omega - \Omega)t\right] + A_0 \cos\left[(\mathbf{k} + \mathbf{K})\,\mathbf{r} - (\omega + \Omega)t\right]$$

Using a well-known trigonometric identity we can express the overall signal as

$$A(\mathbf{r}, t) = B(\mathbf{r}, t) \cos(\mathbf{kr} - \omega t),$$

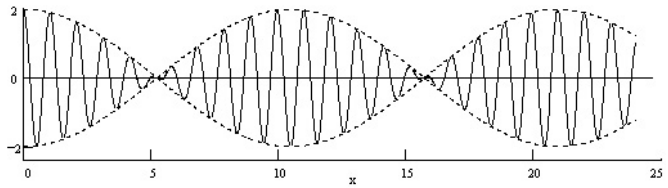

Figure 82: A modulated wave.

where

$$B(\mathbf{r}, t) = 2A_0 \cos\left(\mathbf{Kr} - \Omega t\right).$$

This can be somewhat loosely interpreted as a simple sinusoidal wave with the angular velocity ω, the wave vector $\mathbf{k}$ and the modulated amplitude $B(\mathbf{r}, t)$ (see Fig. 82).

In other words, the amplitude of the wave is itself a wave and the phase velocity of this modulation wave is $\mathbf{v}_g = \nabla_{\mathbf{K}} \Omega$. The propagation of information or energy in a wave always occurs as a change in the wave.

An obvious example is changing the wave from being absent to being present, which propagates at the speed of the leading edge of a wave train. More generally, some modulation of the frequency and/or amplitude of a wave is required in order to convey information, and it is this modulation that represents the signal content.

Hence the actual speed of content in the situation described above is $\mathbf{v}_g$. This is the phase velocity of the amplitude wave, but since each amplitude wave contains a group of internal waves, $\mathbf{v}_g$ is called the group velocity.

Ergo, we have to use v_g.

In the generic case the group velocity of an electromagnetic wave in a matter with the dispersion relation $\omega = \omega(\mathbf{k})$ is defined by

$$\mathbf{v}_g = \nabla_{\mathbf{k}}\omega(\mathbf{k}).$$

In a transparent optical medium the refractive index $n = n(k)$ is defined as the ratio c/v_p. Now, since $v_p = \omega/k$, we have $\omega = ck/n$. Therefore

$$v_g = \frac{\partial\omega}{\partial k} = \frac{c}{n} - \frac{ck}{n^2}\frac{dn}{dk} = v_p\left(1 - \frac{k}{n}\frac{dn}{dk}\right).$$

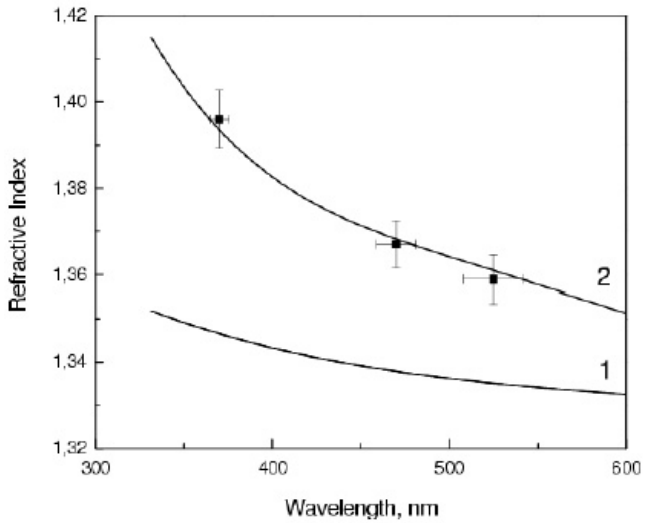

Figure 83: Wavelength dependencies of n (curve 1) and $n_g = n - \lambda\partial n/\partial\lambda$ (data points and curve 2) for distilled Baikal water. [From B. K. Lubsandorzhiev *et al.*, Nucl. Instrum. Meth. A **502** (2003) 168–171 (astro-ph/0211079).]

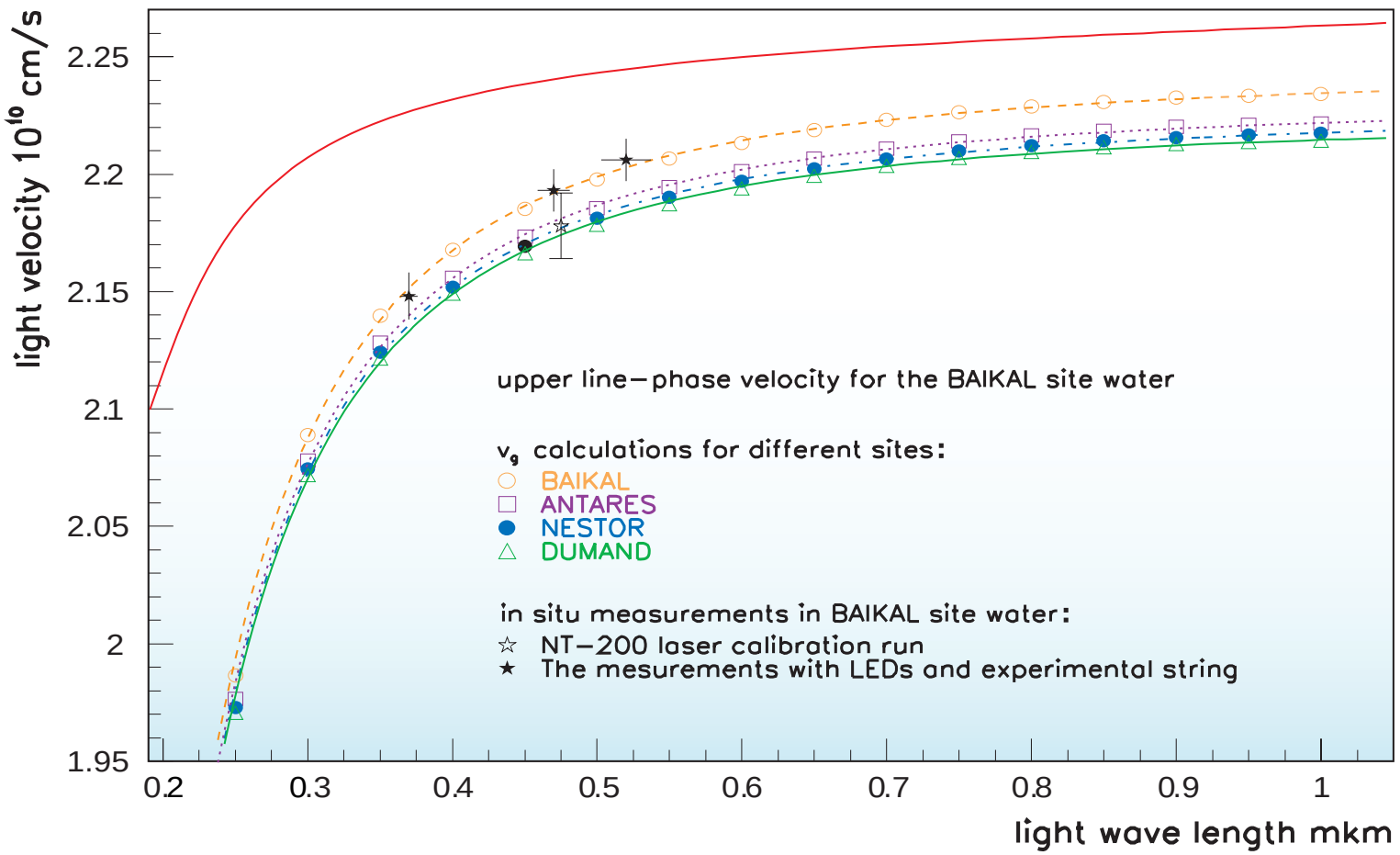

Figure 84: Light velocity vs light wavelength for several underwater neutrino telescope projects. The stars correspond to the experimental results. Other points and lines are calculated data. [From I. A. Danilchenko, "The dispersion formula and the light group velocity in a water," physics/0306020, submitted to Nucl. Instrum. Meth. A).]

31 DUMAND

The DUMAND (Deep Underwater Muon and Neutrino Detector) proposal aimed for a $250 \times 250 \times 500$ m^3 array of 756 detector modules to be located at a depth of about 4.5–4.8 km in the Pacific Ocean ~ 30 km due west from the Kona Coast of the Island of Hawaii.

The expanded schematic diagram in Fig. 85 shows the underwater location of the detector, the full array of 36 strings with optical sensors and a single PMT module.

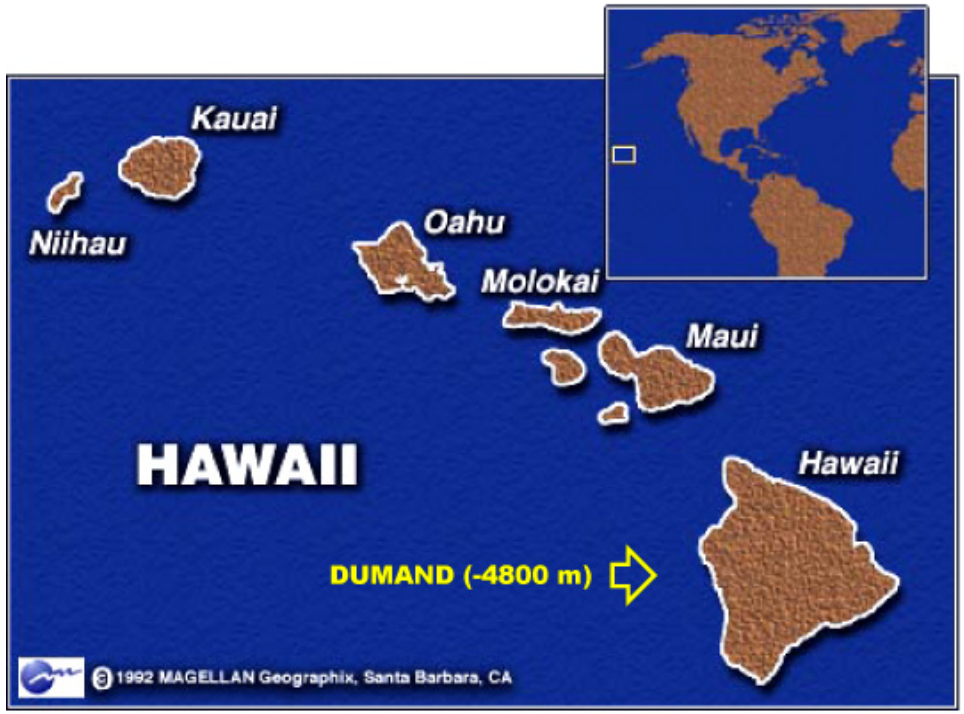

The enclosed target mass of the detector was planned to be of about 30 Mtons and its effective area of about 10^5 m^2. The angular resolution was estimated at 15 to 45 mrads, depending on the muon energy.

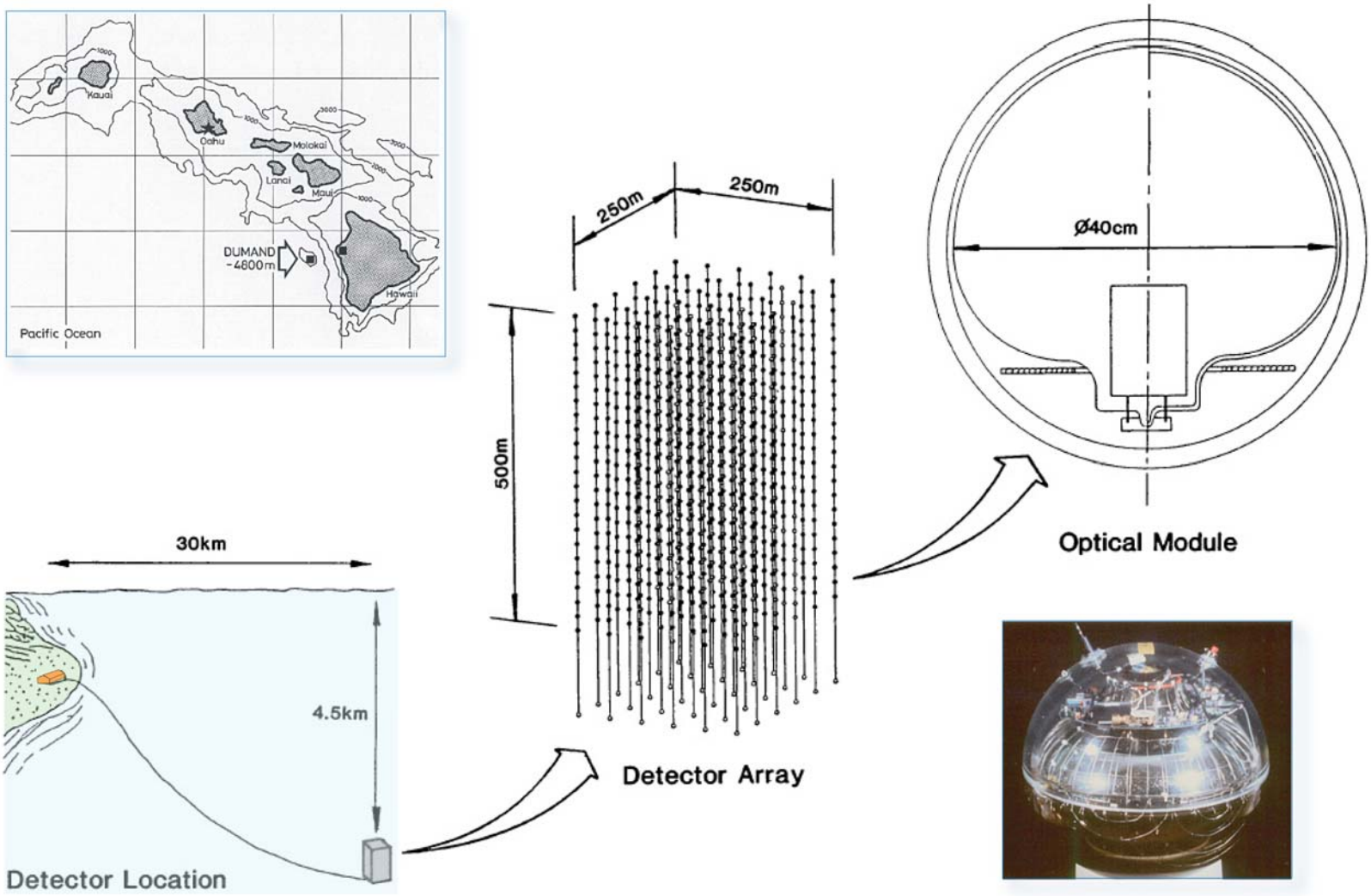

Figure 85: Proposed configuration of the DUMAND detector.

In the middle of 90s, the DUMAND Collaboration intended to deploy a prototype 9-string array (Fig. 86) in two phases: first 3 strings (the triad) as a demonstration, and the remaining 6 strings (complete octagon, plus center string) after about 1 year of testing and operation. The effective detection area of the full 9-string array was estimated as $\sim 2 \times 10^4$ m^2.

The Island of Hawaii was selected for the deployment due to exceptional water clarity, proximity of an abyssal plain (4.8 km) with appropriate seabed characteristics to a suitable shore site (30 km away), pre-existing laboratory infrastructure at the shore site (due to an ocean thermal energy research project).

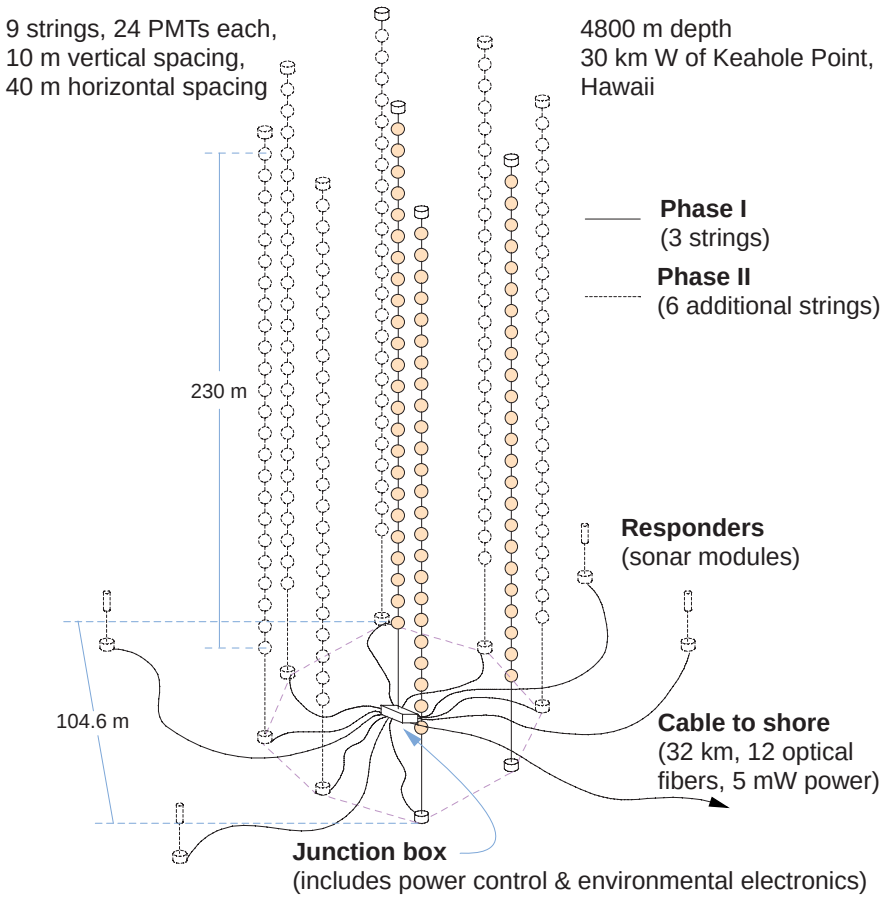

Figure 86: A sketch of the DUMAND-II underwater neutrino detector. [From R. J. Wilkes, astro-ph/9412019.]

32 Baikal neutrino telescope

The Lake Baikal neutrino experiment exploits the deep water of the great Siberian lake as a detection medium for high-energy neutrinos via muons and electrons generated in neutrino interactions.

Figure 87: *Left panel:* space image of wintry Baikal. *Right panel:* ice campus of the collaboration with Khamar-Daban mountain at skyline (March, 1987). [From http://nt200.da.ru/.]

The neutrino telescope NT-200, put into operation at April, 1998, is located in the

southern part of the lake (51.50° N, 104.20° E) at a distance of 3.6 km from the nearest shore and at a depth of about 1.1 km. The distance to the opposite shore is more than 30 km. This asymmetry allows to study the asymmetry in the azimuth distribution of muons arriving at large zenith angles.

The absorption length of water at the site is about 20 m for wavelengths between 470 and 500 nm, and seasonal variations are less than 20%. Light scattering is subjected strongly to seasonal variations and to variations from year to year.

Figure 88[a] shows the layout of the Baikal NT-200 and the preceding array NT-96 (on the right) which took data between April 1996 and March 1997.[b] The NT-200 consists of 192 optical modules (OMs) at 8 strings arranged at an umbrella-like frame. Pairs of OMs are switched in coincidence with a 15 ns time window and define a channel. The array is time-calibrated by two nitrogen lasers. Of these, one (fiber laser) is mounted just above the array. Its light is guided via optical fibers to each OM pair. The other (water laser) is arranged 20 m below the array. Its light propagates directly through water. The expansion on the left of the figure shows two pairs of optical modules ("svjaska") with the electronics module, which houses parts of the readout and control electronics. Three underwater electrical cables connect the detector with the shore station.

[a] Description of the telescope and figures 88 and 90 are borrowed from Ch. Spiering *et al.* (Baikal Collaboration), Prog. Part. Nucl. Phys. **40** (1998) 391 [astro-ph/9801044]; V. A. Balkanov *et al.* (Baikal Collaboration), Yad. Fiz. **63** (2000) 1027 [Phys. Atom. Nucl. **63** (2000) 951] (astro-ph/0001151).

[b] Various stages of the stepwise increasing detector are NT-36 (1993–1995), NT-72 (1995–1996), NT-96 (1996–1997) and NT-144 (1997–1998).

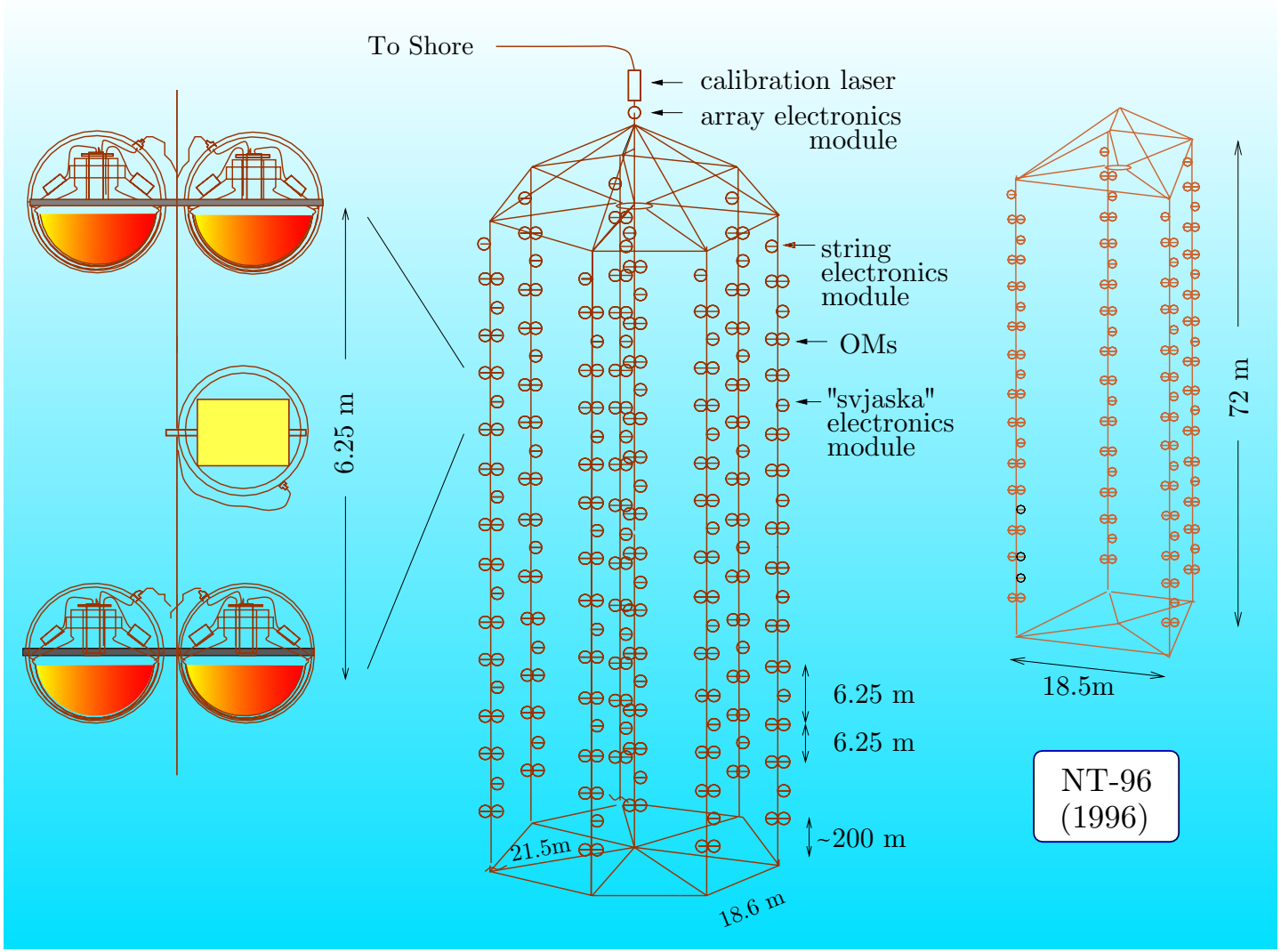

Figure 88: NT-200 and NT-96 schematic view (see text for description and references).

Overall view of the NT-200 telescope is shown in Fig. 89. Here, 1, 2 and 3 are cables to shore; 4, 5 and 6 are the string stations for shore cables; 7 is the string with the telescope; 8 is the hydrometric string; 9–14 are the ultrasonic emitters.
The insert at the left bottom of the figure shows two pairs of optical modules (OM) together with the electronic module controlling the OMs. Shown are two pairs of OMs directed face to face.

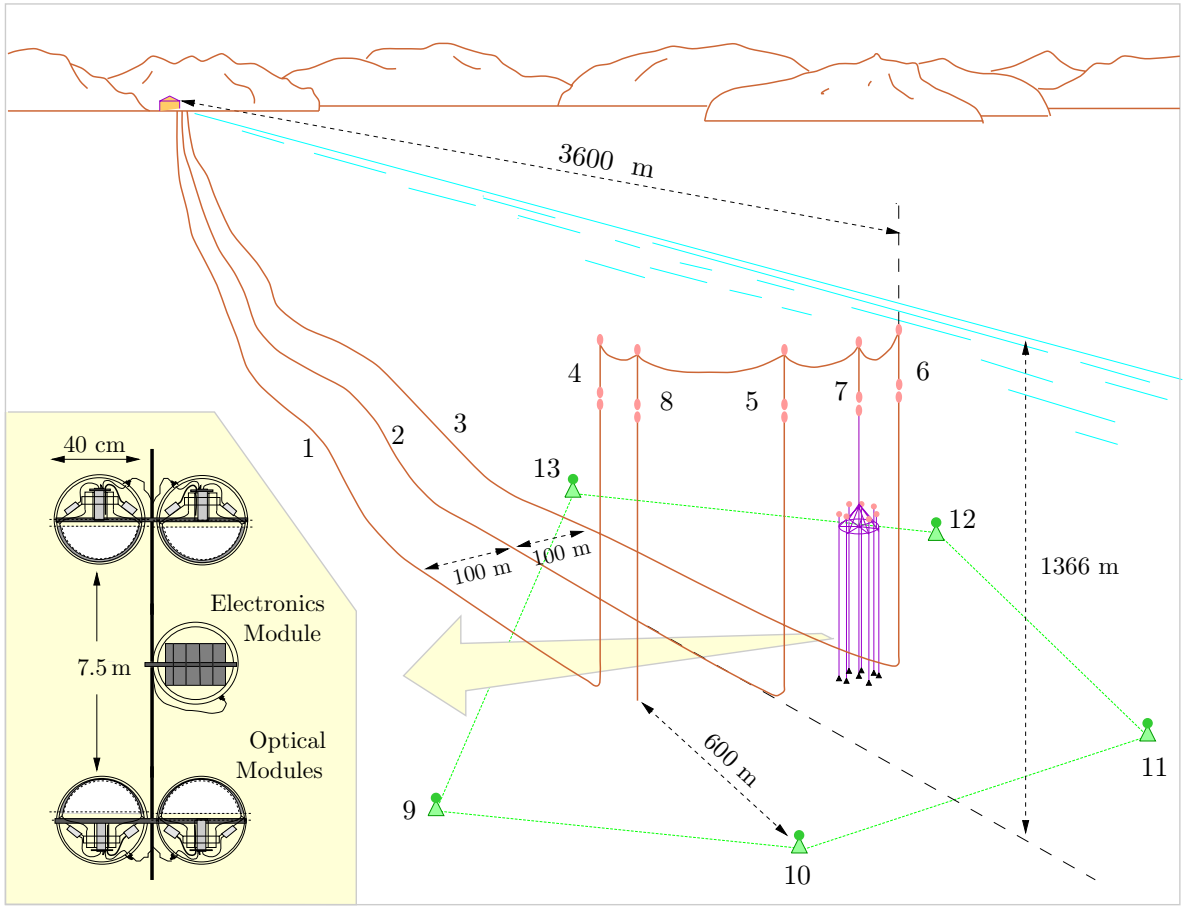

Figure 89: Overall view of the NT-200 complex in Lake Baikal. [From V. A. Balkanov *et al.*, "In-situ measurements of optical parameters in Lake Baikal with the help of a neutrino telescope," Appl. Opt. **33** (1999) 6818–6825 (astro-ph/9903342).]

Fig. 90 displays three neutrino candidates separated during 18 days of the NT-96 exposition (the time period between April 16 and May 17, 1996).

(a) A "gold plated" 19-hit neutrino event. Hit channels are in color. The thick line gives the reconstructed muon path, thin lines pointing to the channels mark the path of the Cherenkov photons as given by the fit to the measured times. The areas of the ellipses are proportional to the measured amplitudes. The fake probability of this event was estimated to be smaller than 1%.

(b) An unambiguous 14-hit neutrino candidate.

(c) An ambiguous event reconstructed as a neutrino event (dashed line) but with a second solution above the horizon (solid line). This event is assigned to the sample of downward going muons.

The data set collected with NT-200 during 268 live days (till 1999) yields 84 upward going muons. The MC simulation of upward muon tracks due to atmospheric neutrinos gives 80.5 events. The skyplot of the upward muons is shown in Fig. 91. Fig. 92 shows a comparison between the measured and simulation angular distributions.

Fig. 96 shows NT-200+ – an upgrade of the NT-200 by three sparsely instrumented distant outer strings which will increase the fiducial volume for high-energy cascades to a few dozen Mtons. Correspondingly, the NT-200+ sensitivity will be 4 times better than that of NT-200, with a moderate 20% increase of optical modules only. A prototype string of 140 m length with 12 optical modules was deployed in March 2003, and electronics, data acquisition and calibration systems for NT-200+ have been tested.

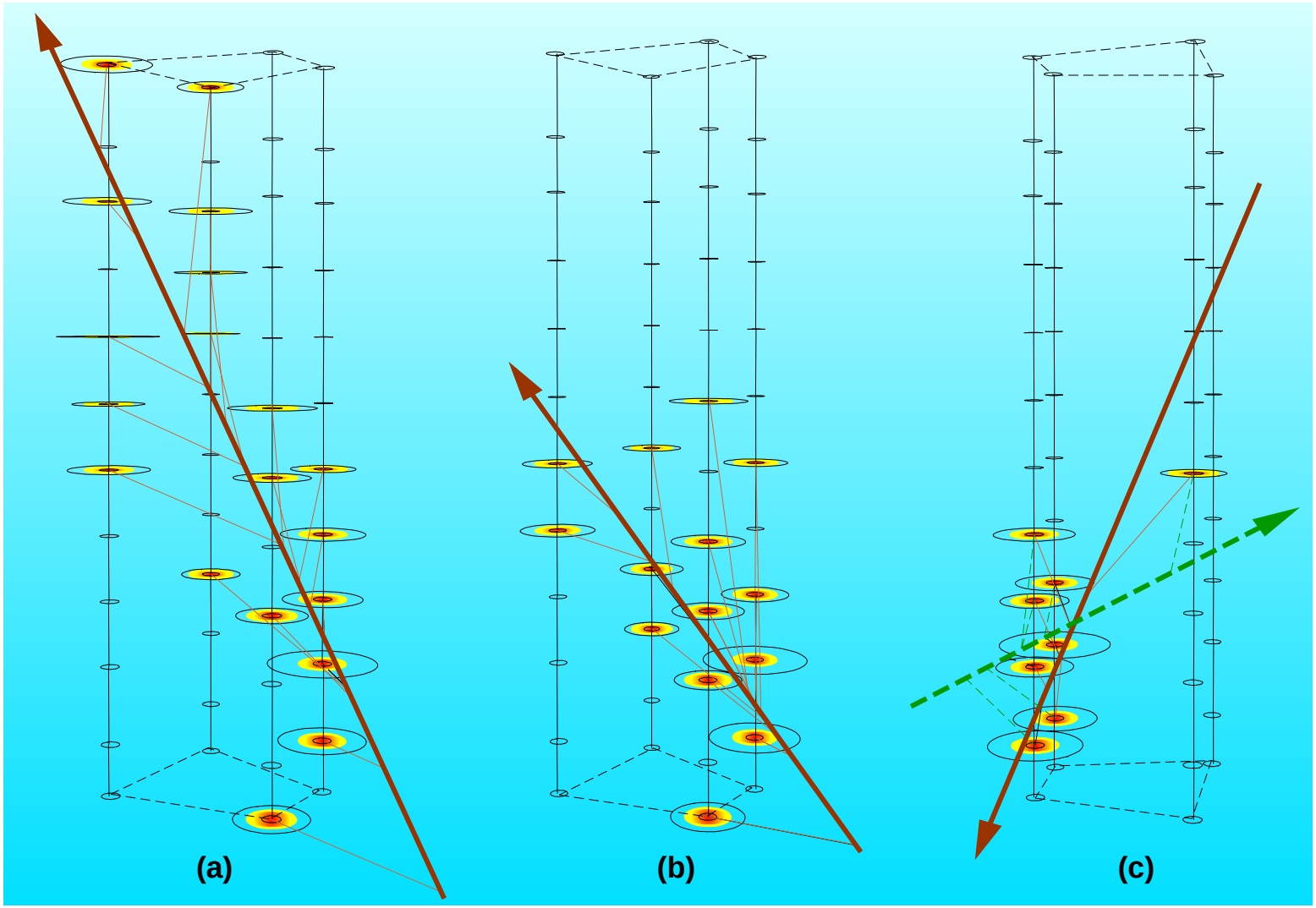

Figure 90: Three neutrino candidates recorded in NT-96 (see text for details).

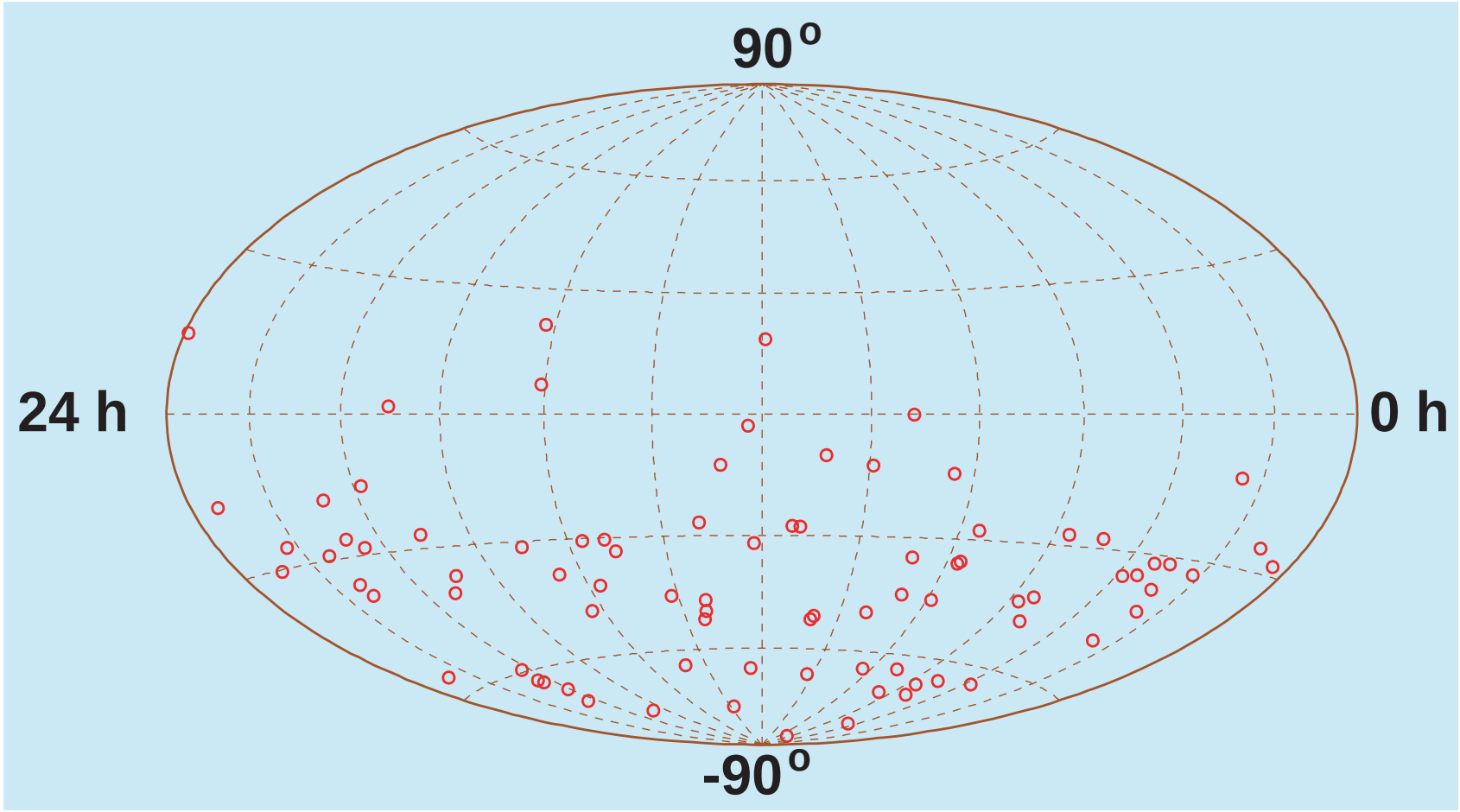

Figure 91: Skyplot (in equatorial coordinates) of 84 upward-going muon events recorded in the Baikal NT-200 experiment. [From R. Wischnewski (for the Baikal Collaboration), contribution to the 28th ICRC, Tsukuda, Japan, July 31 – August 7, 2003 (astro-ph/0305302).]

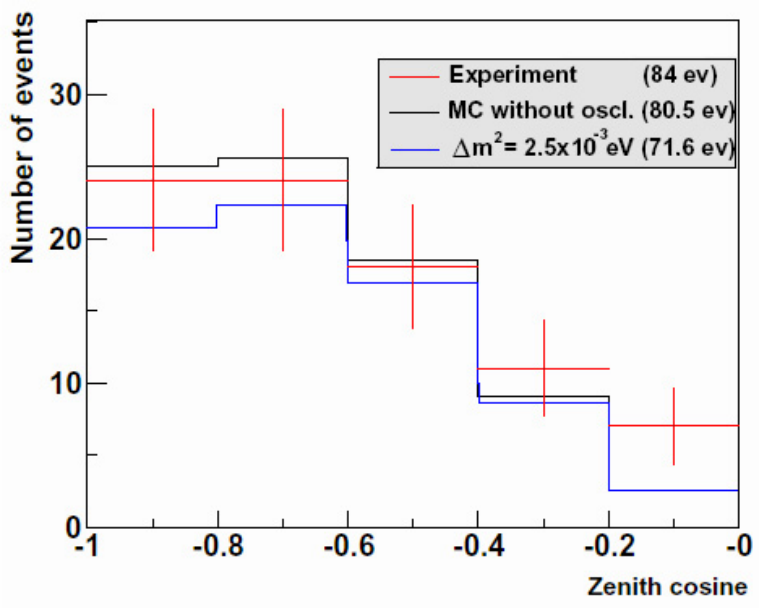

Figure 92: Zenith angle distribution of 84 upward-going reconstructed events in the Baikal NT-200 experiment and MC simulated distribution of upward muon tracks due to atmospheric neutrinos. $E_{\text{th}} = 15 - 20$ GeV in this experiment.

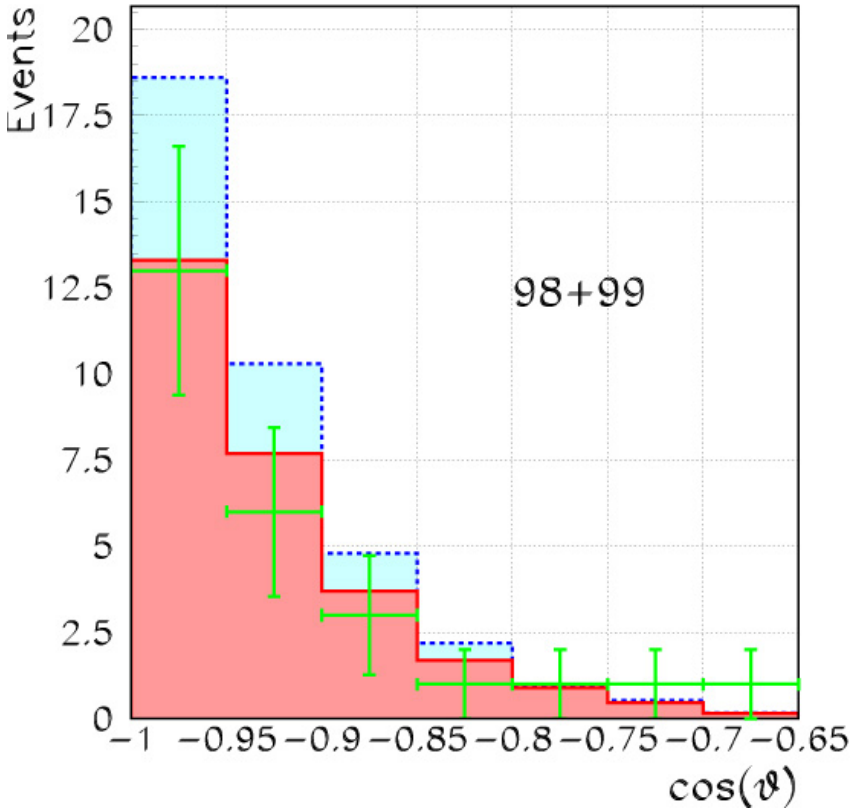

Figure 93: The same as in Fig. 92 but for selected neutrino candidates. $E_{\text{th}} = 10$ GeV.

[From V. Aynutdinov *et al.*, "The BAIKAL neutrino project: Status, results and perspectives," Nucl. Phys. B (Proc. Suppl.) **143** (2005) 335–342.]

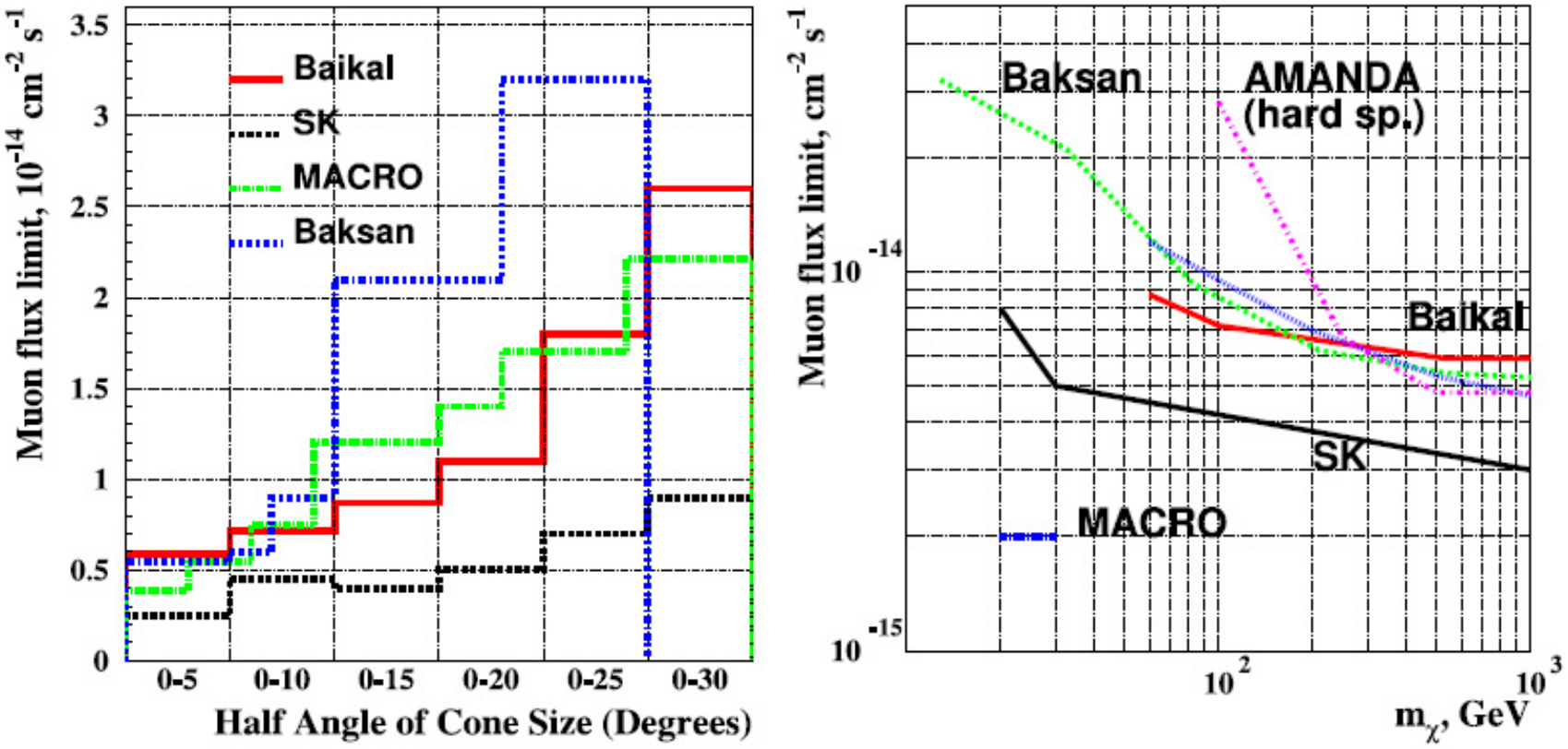

Figure 94: Limits on the excess muon flux from the center of the Earth vs half-cone of the search angle (left panel) and as a function of WIMP mass (right panel).

[From V. Aynutdinov *et al.*, "The BAIKAL neutrino project: Status, results and perspectives," Nucl. Phys. B (Proc. Suppl.) **143** (2005) 335–342.]

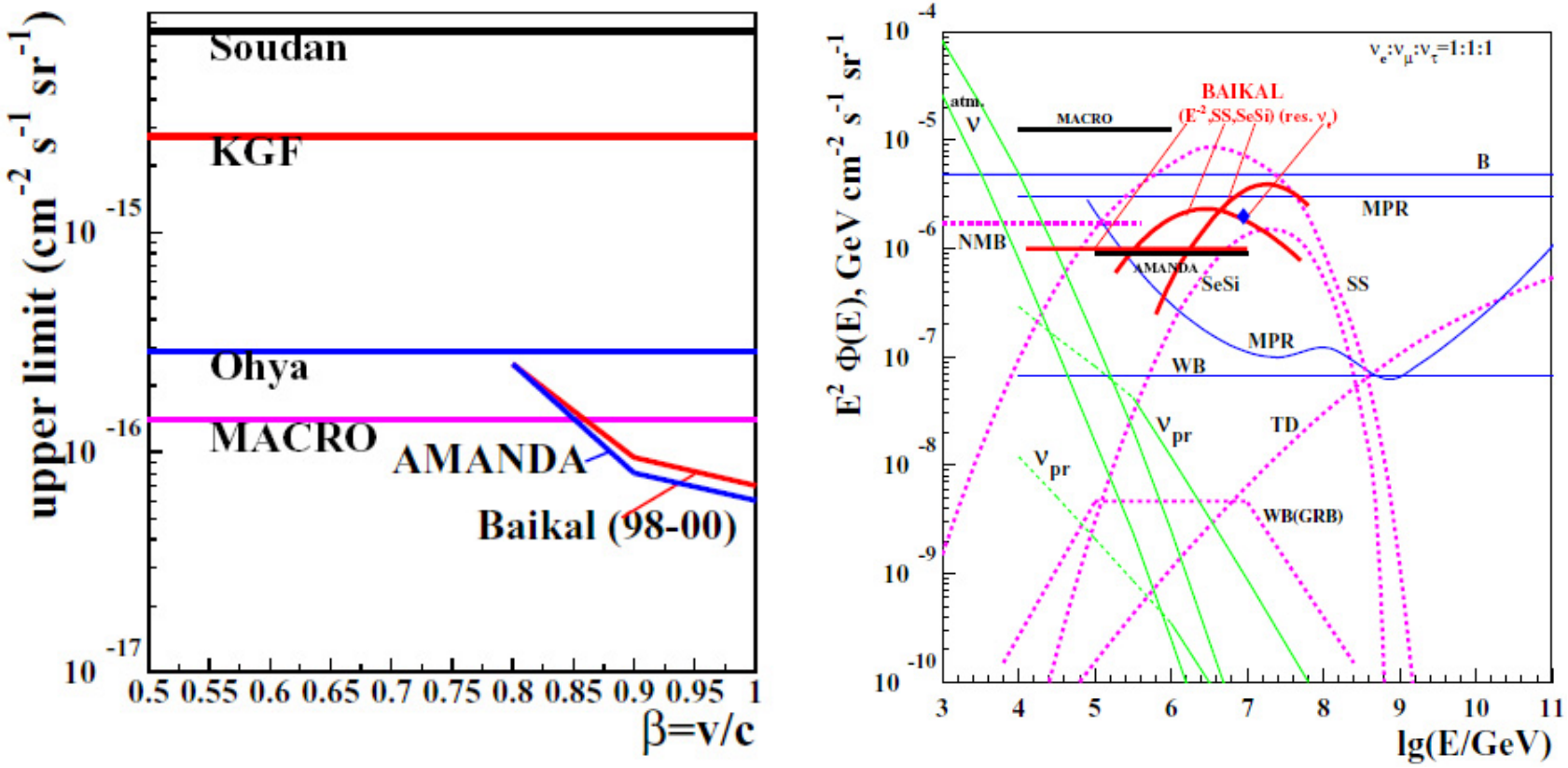

Figure 95: Upper limits on the flux of fast monopoles (left panel) and neutrino fluxes (right panel) obtained in different experiments. The neutrino fluxes expected from some astrophysical sources are also shown in the right panel.

[From V. Aynutdinov *et al.*, "The BAIKAL neutrino project: Status, results and perspectives," Nucl. Phys. B (Proc. Suppl.) **143** (2005) 335–342.]

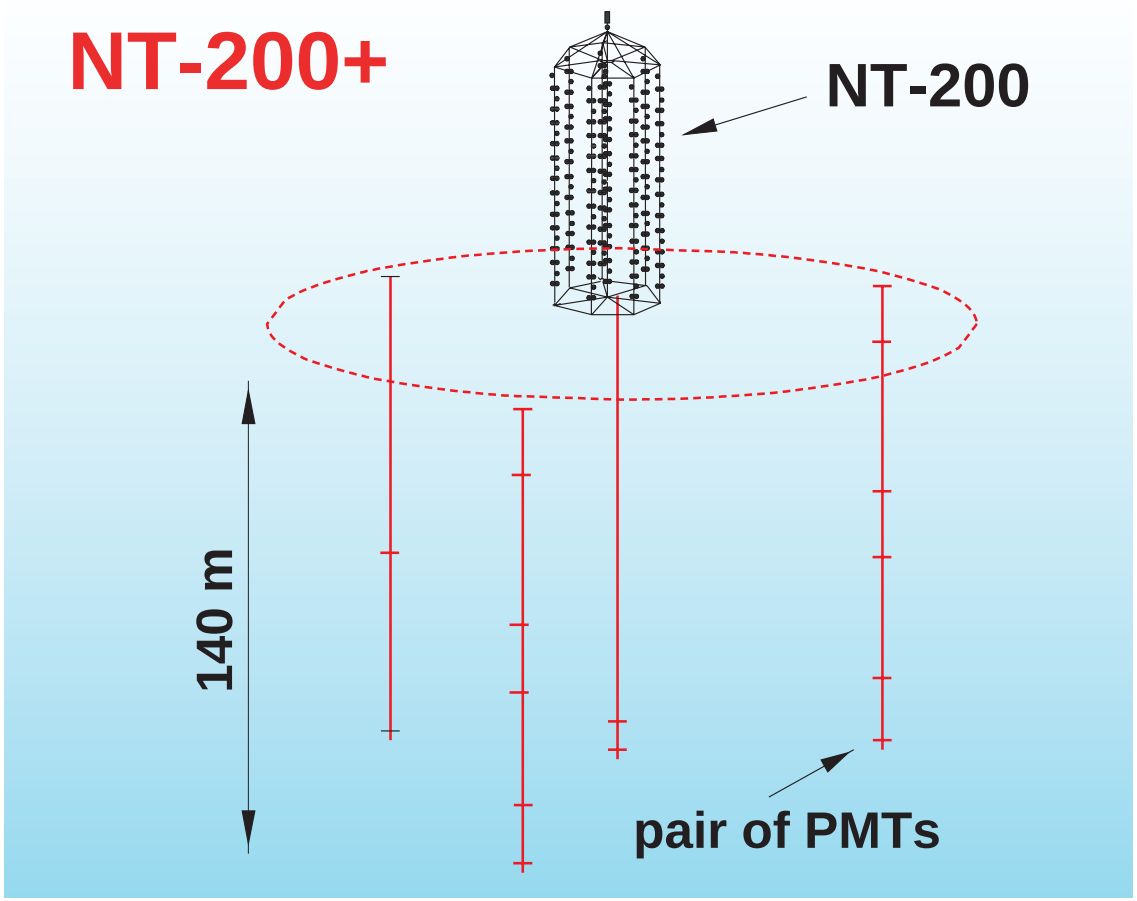

Figure 96: Future NT-200+ configuration. Three additional outer plus one possible central strings will allow a much better vertex identification and hence a significantly more precise measurement of cascade energy in a volume around the NT-200.

[From R. Wischnewski, 2003 (see caption to Fig. 91).]

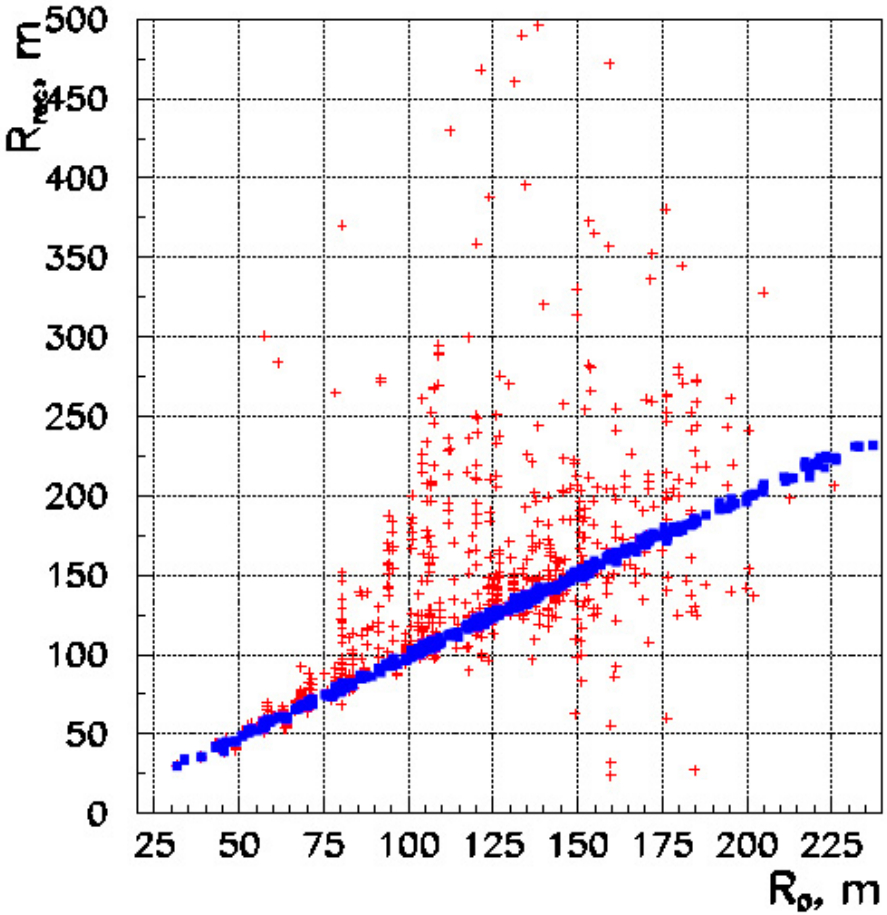

Figure 97: Reconstructed vs simulated coordinates of cascades in NT-200+ (rectangles) and NT-200 (crosses).

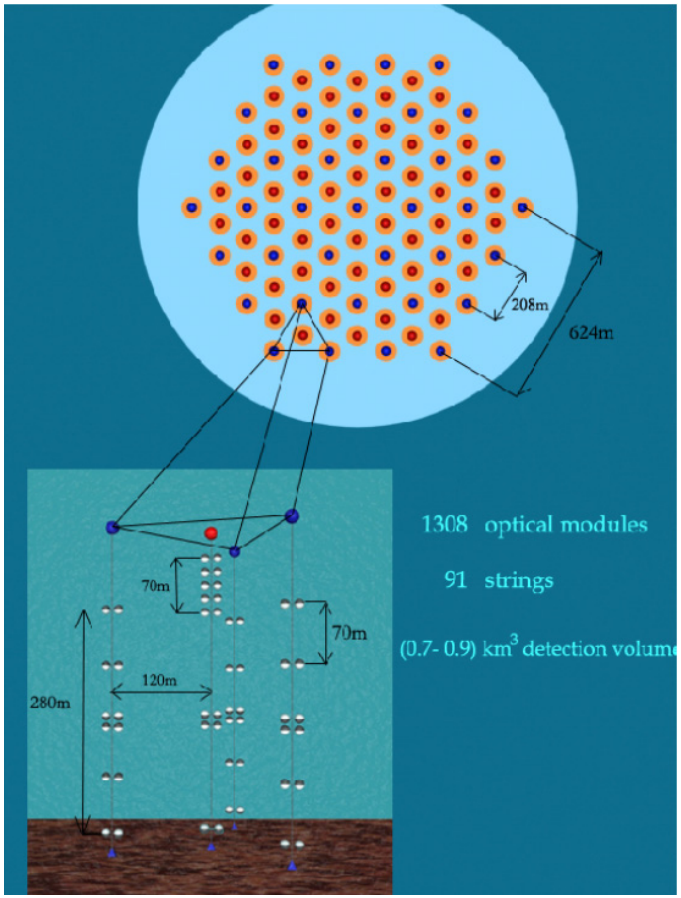

Figure 98: Top view of a Gigaton Volume Detector in Lake Baikal with sketch of one of its sub-arrays.

33 AMANDA

The AMANDA (Antarctic Muon And Neutrino Detector Array) detector is located at the South Pole station, Antarctica. Figures 99 and 100 show the South Pole Station.

Figure 99: Construction of the South Pole Station as of February, 2002.
[From http://www.amanda.uci.edu/.]

The detector uses the 2.8 km thick ice sheet at the South Pole as a neutrino target, Cherenkov medium and cosmic ray flux attenuator. The detector consists of vertical

strings of optical modules (OMs) – photomultiplier tubes sealed in glass pressure vessels – frozen into the ice at depths of 1500–2000 m below the surface.

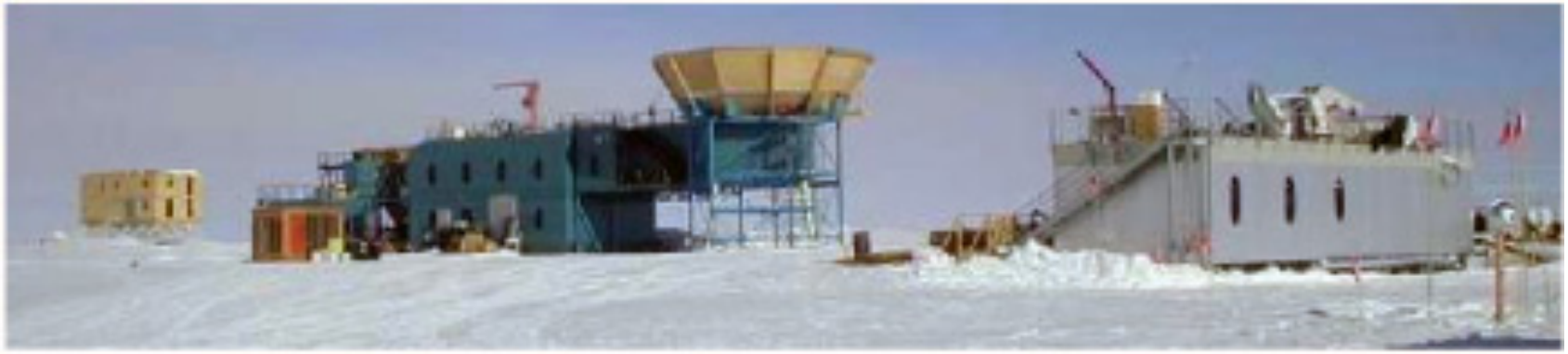

Figure 100: The South Pole Station. The AMANDA-II telescope electronics are located on the 2nd floor of MAPO, the blue building shown in this picture.
[From http://www.amanda.uci.edu/.]

Fine photos of the Amundsen-Scott South Pole Station are given in Figs. 101 and 102.[a]

[a] Borrowed from the Francis Halzen's homepage <http://icecube.wisc.edu/~halzen/>.

Figure 101: Amundsen-Scott South Pole Station.

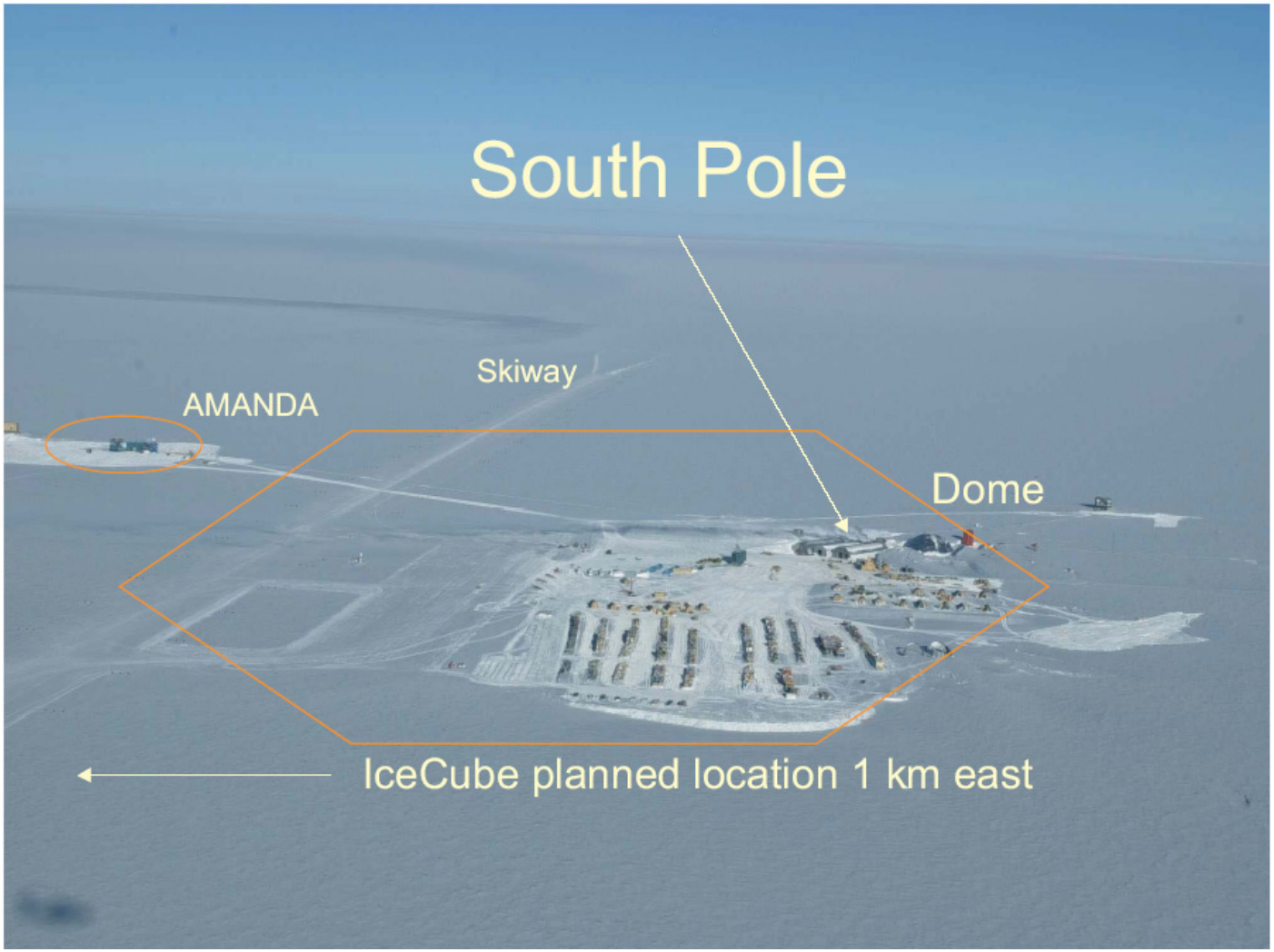

Figure 102: One another vie of the South Pole Station.

Figure 103 shows the current configuration of the AMANDA detector. The shallow array, AMANDA-A, was deployed at depths of 800 to 1000 m in 1993–1994 in an exploratory phase of the project. Studies of the optical properties of the ice carried out with AMANDA-A showed a high concentration of air bubbles at these depths, leading to strong scattering of light and making accurate track reconstruction impossible. Therefore, a deeper array of 10 strings with 302 OMs was deployed in the austral summers of 1995–1996 and 1996–1997 at depths of 1500–2000 m. This detector is referred to as AMANDA-B10. It was augmented by 3 additional strings in 1997–1998 and 6 in 1999–2000, forming the AMANDA-II array. This detector has been calibrated and in operation since January 2000.

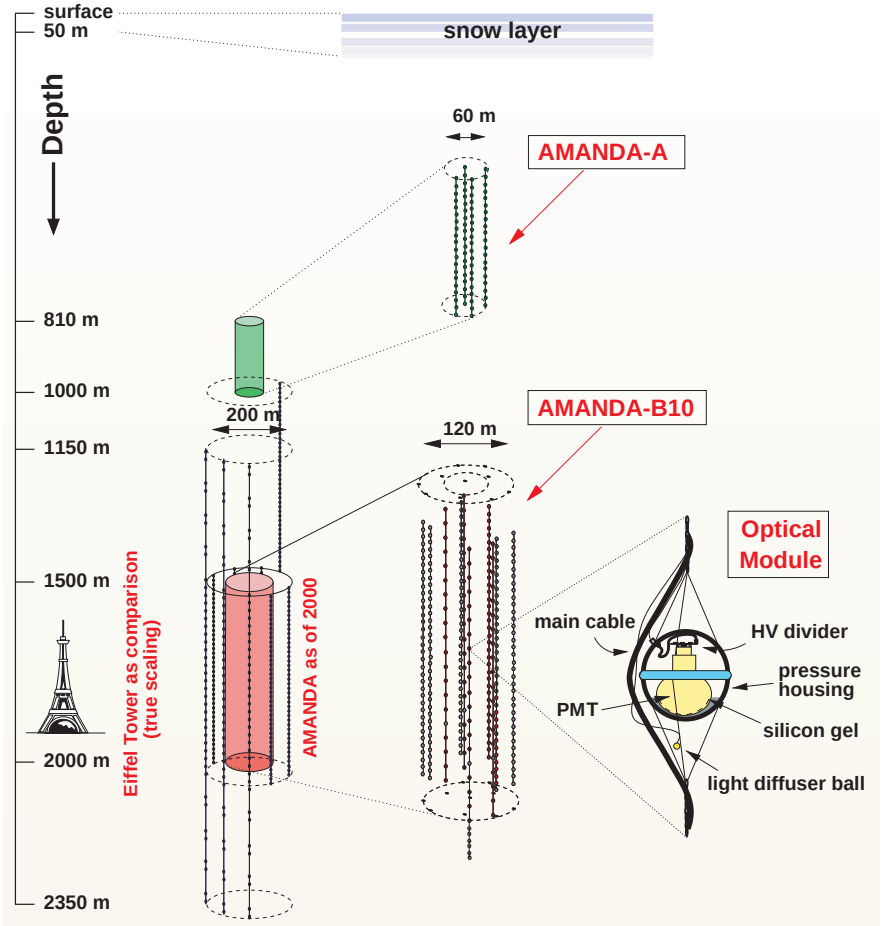

Figure 103: Schematic view of the AMANDA-II array at the South Pole. [From J. Ahrens *et al.*, Phys. Rev. D **66** (2002) 012005 [astro-ph/0205109].]

Figure 104 is an artistic view of a neutrino induced event in the AMANDA detector while Fig. 105 displays three real neutrino candidates. Let us describe these in some details.

(a) Event display of an upgoing muon event. The gray scale indicates the flow of time, with early hits at the bottom and the latest hits at the top of the array. The arrival times match the speed of light. The sizes of the ellipses correspond to the measured amplitudes.

(b) The upgoing muon event has a smooth distribution of hits along the extended uniform track. The track-like hit topology of this event can be used to distinguish it from background events.

(c) A background event with a poor smoothness value and a large deviation from a straight line.

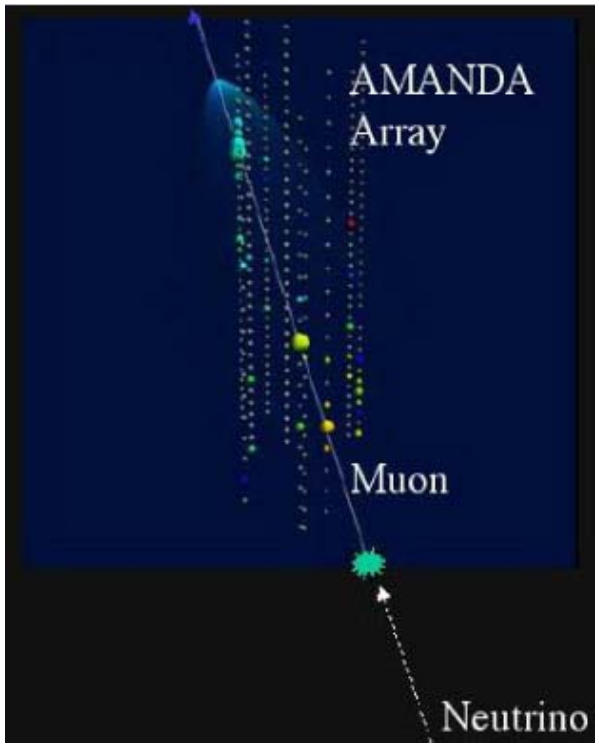

Figure 104: Artistic view of a ν induced event in the AMANDA detector.

Two more neutrino candidates (both were recorded on May 11, 2000) are shown in Fig. 106 borrowed from URL `<http://amanda.physics.wisc.edu/>`.[a]

[a] In this site, there a lot of nice animated images relevant to the subject.

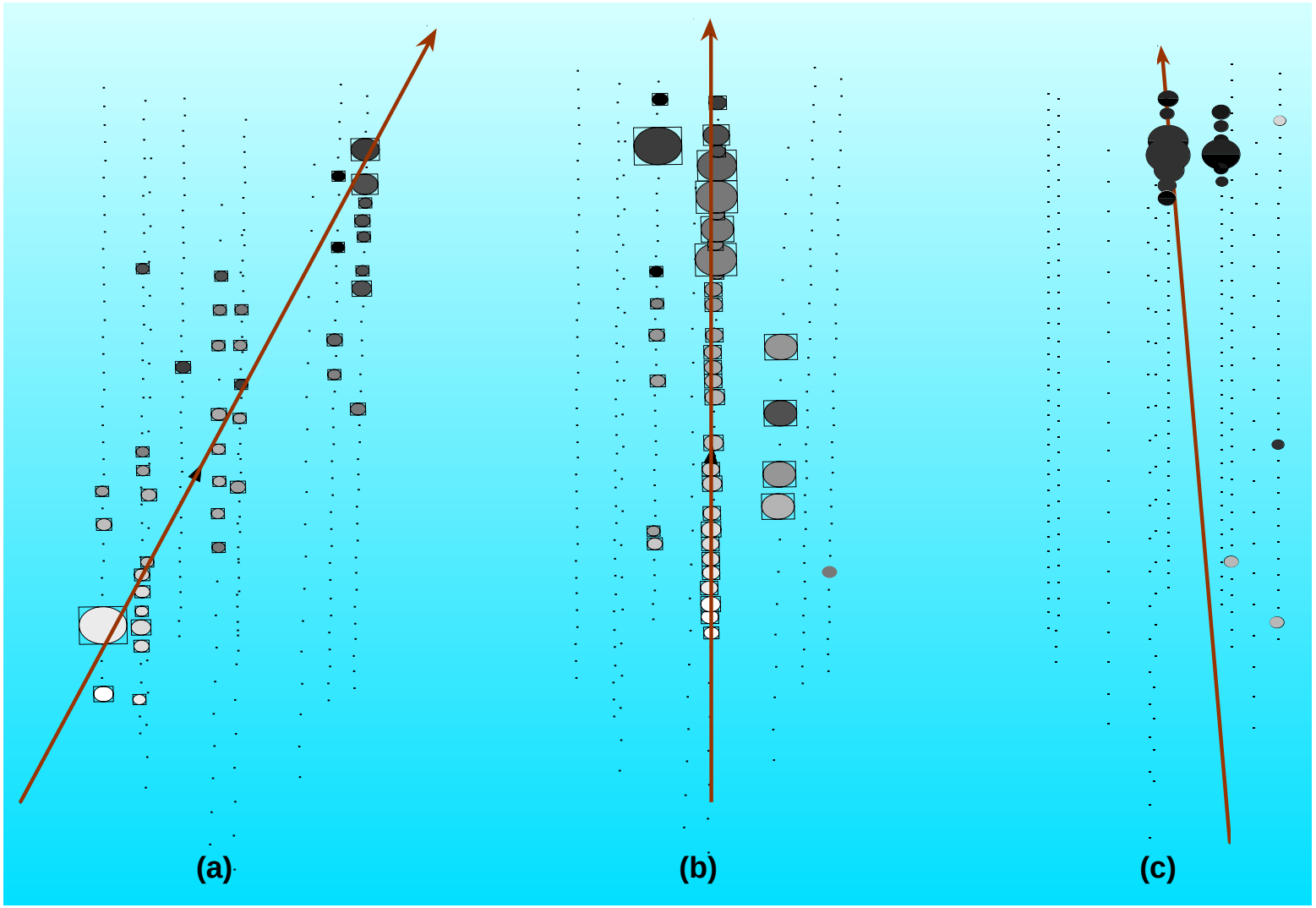

Figure 105: Three neutrino candidates recorded in AMANDA-B10 (see text).

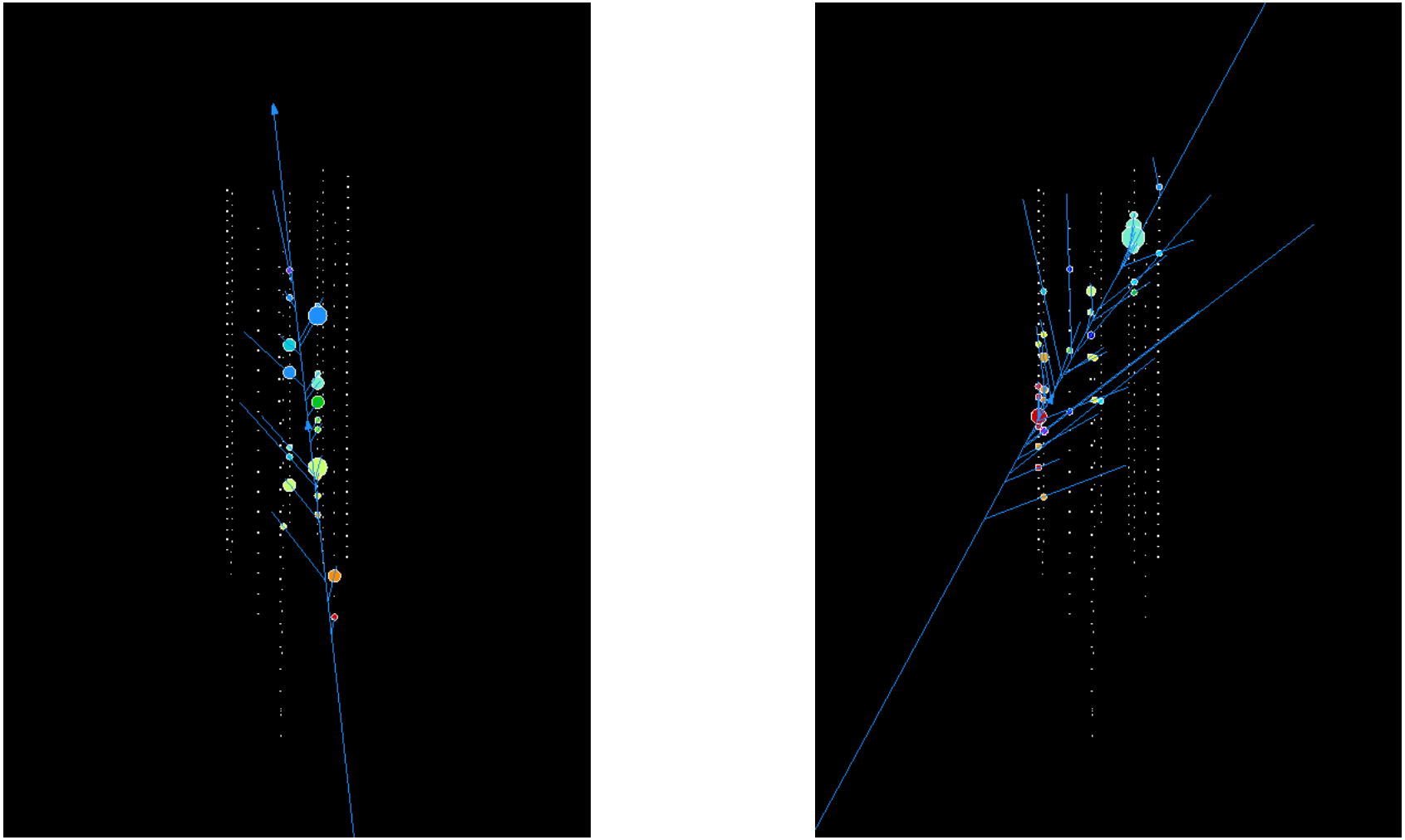

Figure 106: Two more neutrino candidates in AMANDA, #910225 and #10604848 (both were recorded on May 11, 2000). [From <http://amanda.physics.wisc.edu/>.]

Figure 107 shows the skyplot (equatorial coordinates) of all the candidate neutrino events found in AMANDA-B10.The distribution of the events on the skyplot is consistent with a random distribution. The combined skyplot of the AMANDA-B10 and Baikal NT-200 candidate neutrino events is shown in Fig. 108.

The angular distribution for the 204 events is shown in Fig. 109 and compared to that for the simulation of atmospheric neutrinos.[a] In the figure the Monte Carlo events are normalized to the number of observed events to facilitate comparison of the shapes of the distributions. The agreement in absolute number is consistent with the systematic uncertainties in the absolute sensitivity and the flux of high-energy atmospheric neutrinos. The shape of the distribution of data is statistically consistent with the prediction from atmospheric neutrinos.

Preliminary results on the neutrino energy spectra are shown in Fig. 110. For the first time, the spectrum was measured up to 100 TeV. It is compared to the high-energy data from the Fréjus experiment[b] and with the horizontal and vertical AN flux parametrizations according to Volkova.[c] The error bars give the statistical error from the unfolding procedure plus an overall systematic uncertainty. The reconstructed data are in agreement with current calculations of the AN flux and shows an overlap with the Fréjus results.

---

[a] For more recent data see E. Andres *et al.*, Nature **423** (2001) 415.

[b] K. Daum *et al.* (Fréjus Collaboration), Z. Phys. C **66** (1995) 417;
W. Rhode *et al.* (Fréjus Collaboration), Astropart. Phys. **4** (1996) 217.

[c] L. V. Volkova, Yad. Fiz. **31** (1980) 1510 [Sov. J. Nucl. Phys. **31** (1980) 784].

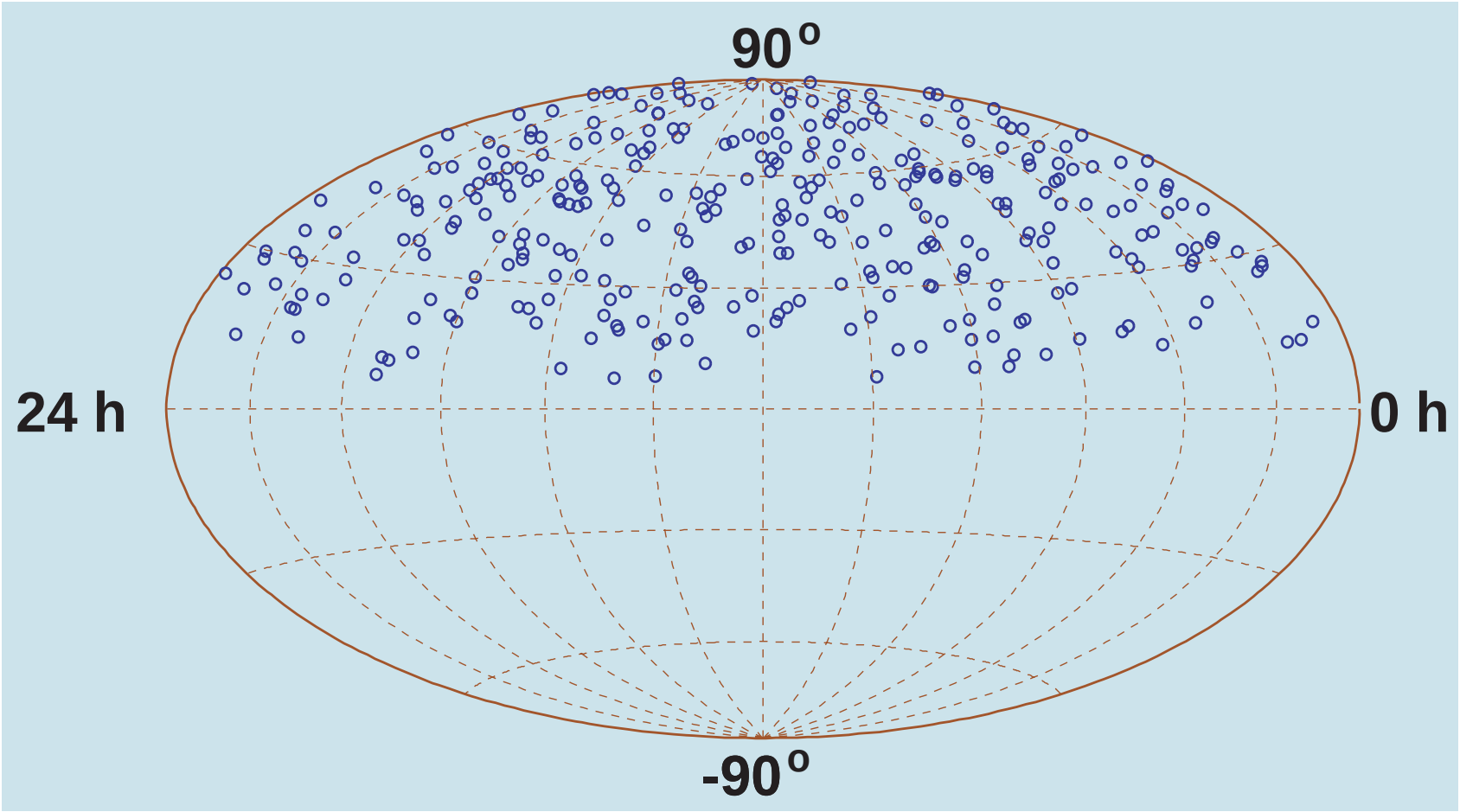

Figure 107: Skyplot of upward-going events as seen with AMANDA-B10 in 1997 in equatorial coordinates. The background of non-neutrino events is estimated to be less than 10%. [From J. Ahrens *et al.* (2002); see caption to Fig. 103.]

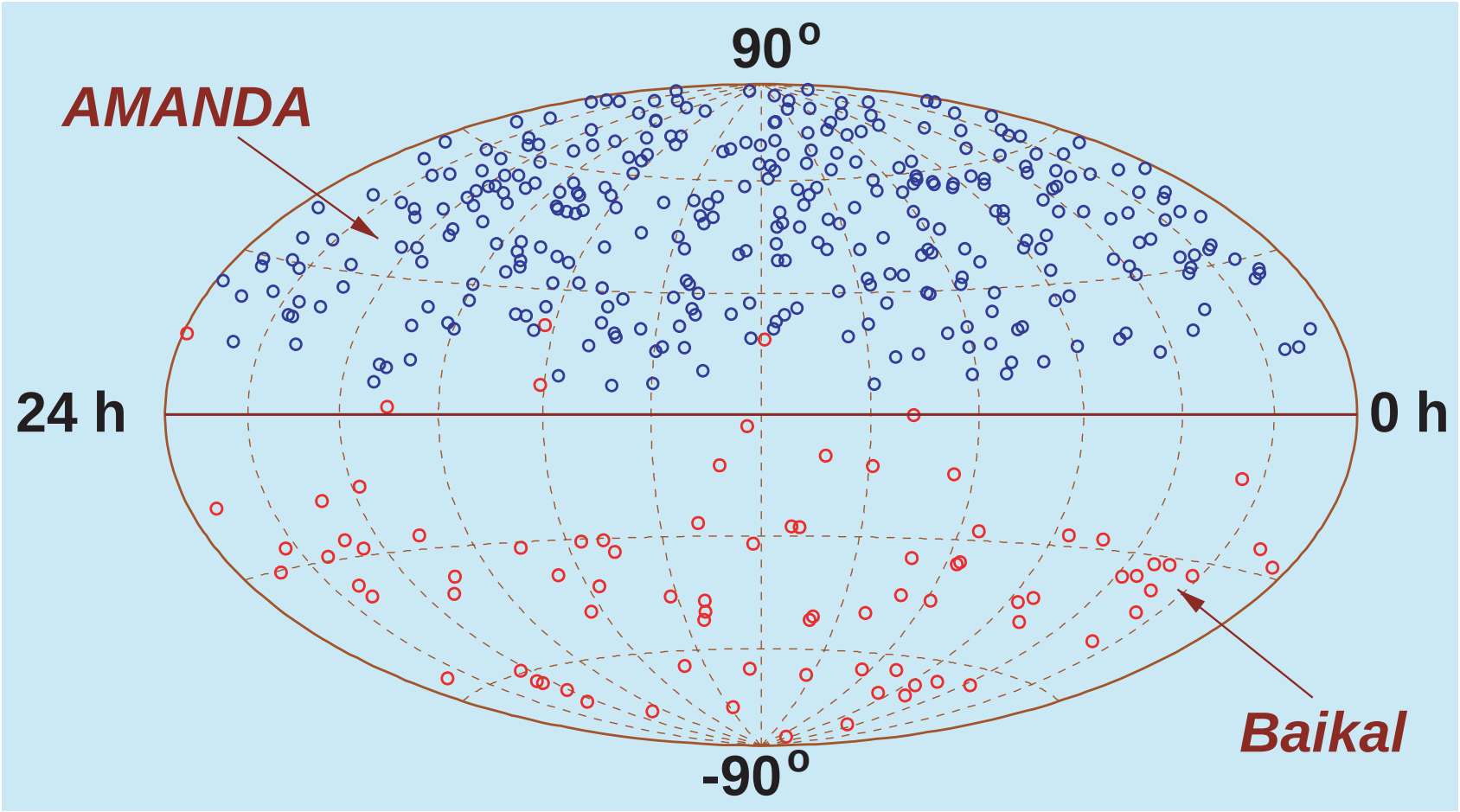

Figure 108: Merged skyplot of upward-going events recorded in both Baikal NT-200 and AMANDA-B10 experiments. The data are the same as in Figs. 91 and 107.

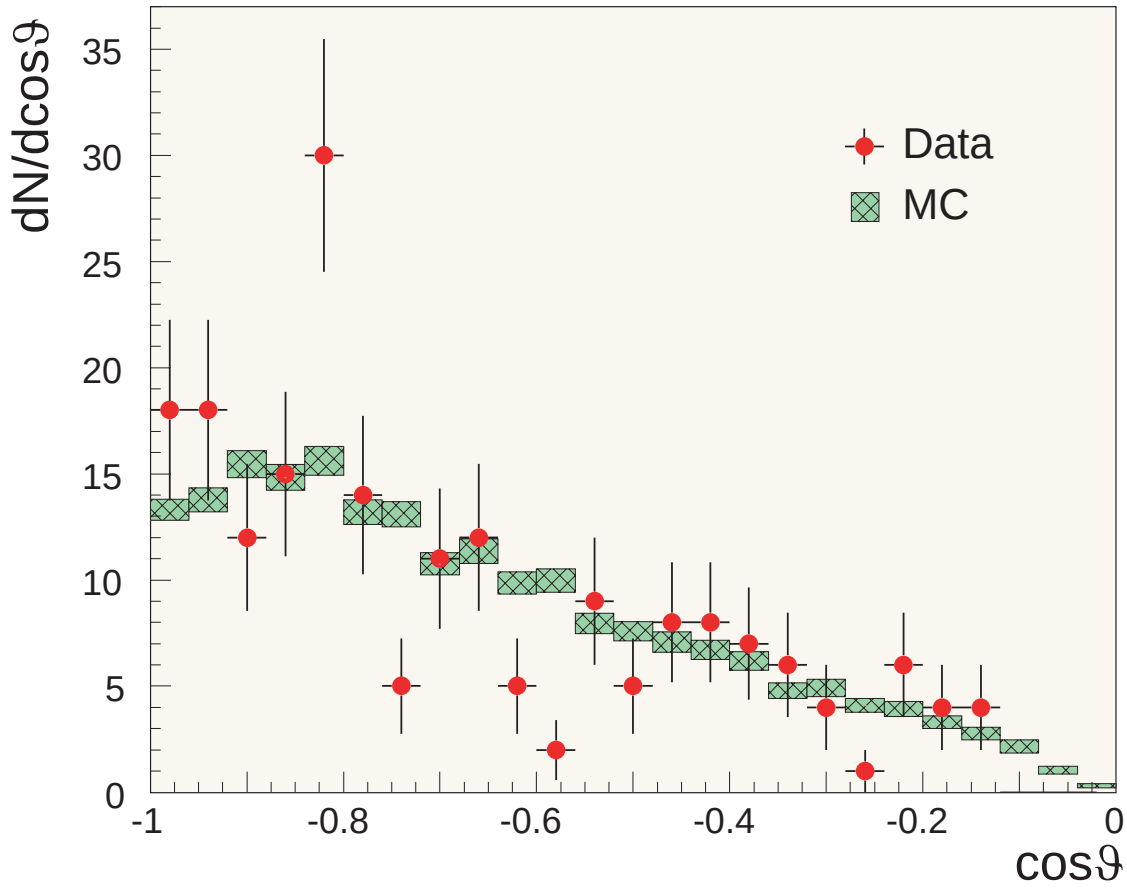

Figure 109: Zenith angle distribution of 204 upward-going reconstructed events in the AMANDA-B10 experiment and MC simulated distribution of upward muon tracks due to atmospheric neutrinos. The size of the hatched boxes indicates the statistical precision of the atmospheric neutrino simulation. The Monte Carlo prediction is normalized to the data. [From J. Ahrens *et al.* (2002); see caption to Fig. 103.]

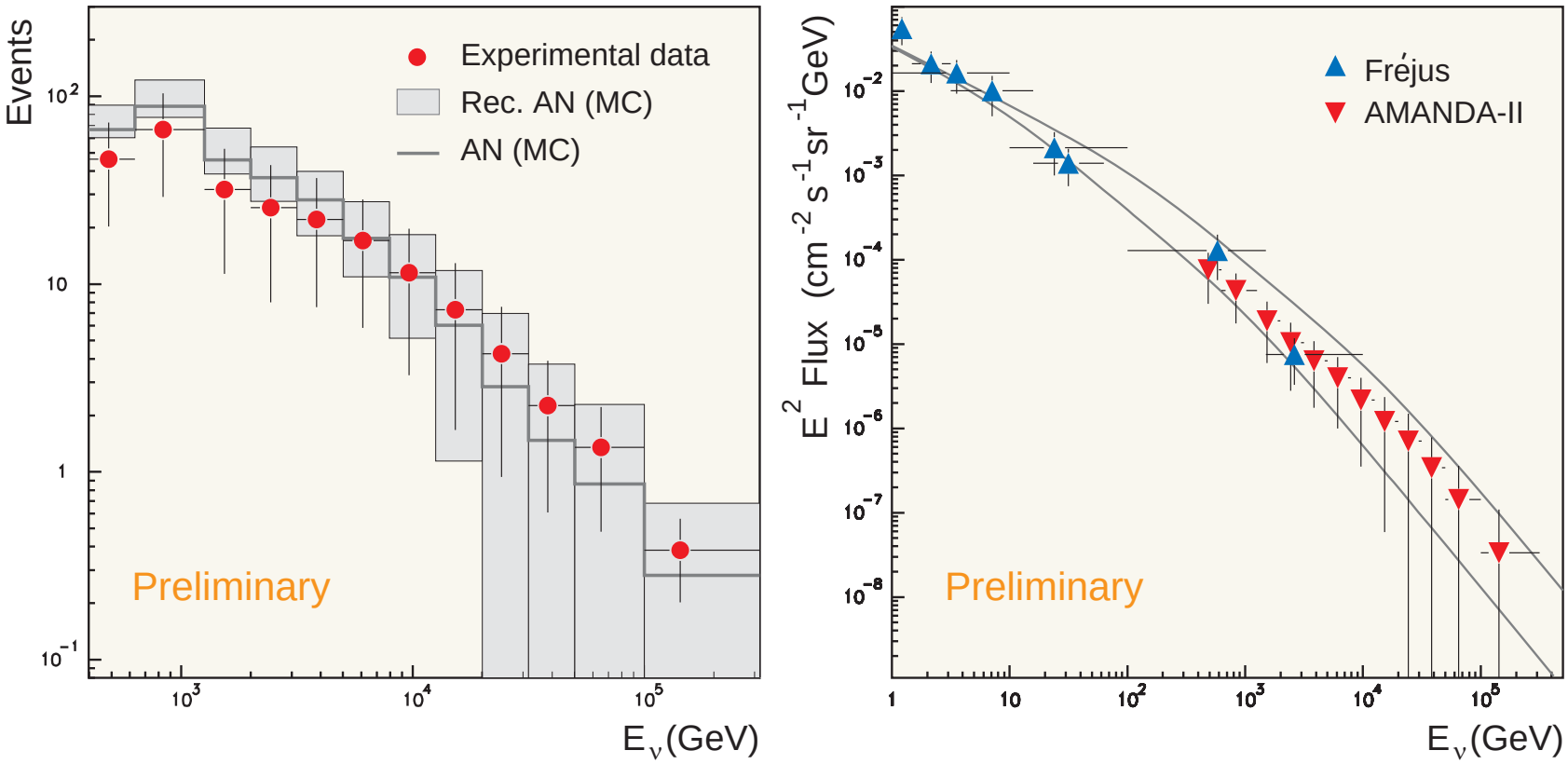

Figure 110: Reconstructed neutrino spectra in AMANDA-II. *Left panel:* on filter level (solid: energy distribution of atmospheric neutrino expectation, boxes: unfolded energy distribution of AN (MC), points: reconstructed data). *Right panel:* reconstructed fluxes compared to Fréjus data. [From H. Geenen (for the AMANDA Collaboration), contribution to the 28th ICRC, Tsukuda, Japan, July 31 – August 7, 2003 (see the AMANDA Berkeley Group homepage <http://area51.berkeley.edu/>).]

34 KM3 projects (IceCube, NEMO, NESTOR,...)

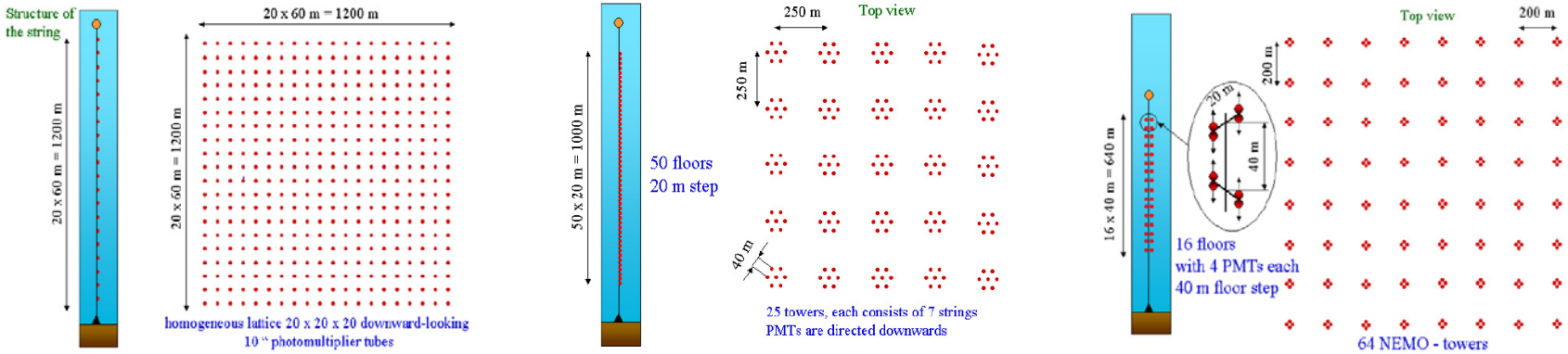

Figure 111: Future KM3 neutrino telescope geometries. *Left panel:* schematic view of a homogeneous detector with 8000 PMTs (not quite optimal to be built); *middle panel:* the layout of a NESTOR-like detector with 8750 PMTs; *right panel:* the layout of a NEMO-like detector with 4096 PMTs. These three designs have very different degrees of homogeneity. One more difference may be due to various numbers of downward-looking and upward-looking PMTs (down-down, up-down, etc.).

[From D. Zaborov, "Comparison of different KM3 designs using Antares tools," in Proc. of the Workshop on Technical Aspects of a Very Large Volume Neutrino Telescope in the Mediterranean Sea "'VLVνT', Amsterdam, October 5-8, 2003, ed. by E. de Wolf (NIKHEF, Amsterdam, The Netherlands), pp. 104–108.]

Part VII

FUTURE UNDERGROUND

35 List of relevant experimental projects

- Experiments at **LNGS** [+ **CERN** ν beam(s)]:
  - ⋆ 0.2 kton iron/emulsion detector **OPERA** (**O**scillation **P**roject with **E**mulsion–t**R**acking **A**pparatus),
  - ⋆ **ICAN^{O}E** $=$ 5 kton solid target **ICARUS** (**I**maging **C**osmic **A**nd **R**are **U**nderground **S**ignals) $+$ 8 kton solid target **N^{O}E** (**N**eutrino **O**scillation **E**xperiment),
  - ⋆ 34 kton magnetized tracking calorimeter **MONOLITH** (**M**assive **O**bservatory for **N**eutrino **O**scillations or **LI**mits on **TH**eir existence);
- experiments with **NuMI** (**N**eutrinos at the **M**ain **I**njector) beam line facility at **FNAL**:
  - ⋆ **MINOS** (**M**ain **I**njector **N**eutrino **O**scillation **S**earch) with two magnetized iron detectors [near (~ 1 kton) $+$ far (5.4 kton)], **atmospheric ν analysis underway (!)**,
  - ⋆ **MINERνA** (**M**ain **IN**njector **E**xpe**R**iment: **ν-A**),
  - ⋆ **NOνA** (**N**uMI **O**ff-Axis ν_e **A**ppearance experiment);
- 650 kton underground water Cherenkov detector **UNO** (**U**ltra underground **N**ucleon detector and neutrino **O**bservatory);
- Multi-megaton water Cherenkov detector **TITAND** (**T**otally **I**mmersible **T**ank **A**ssaying **N**ucleon **D**ecay) [former name **TITANIC**];
- and many others [**(Mini)BooNE**, **FLARE** and **MiniLANNDD** at **FNAL**, **LANNDD** at **WIPP**, **3M** at **NUSEL**, **Super-ICARUS** and **Aqua-RICH** at **LNGS**, **T2K** at **J-PARC**, **Hyper-Kamiokande**, **MEMPHYS** at **Fréjus**, **INO**, **SCIPIO**,...

36 Project MEMPHYS as an example

The MEMPHYS (MEgaton Mass PHYSics) is a project for a Megaton scale water Cherenkov detector in a large international underground laboratory in the Fréjus tunnel.[a]

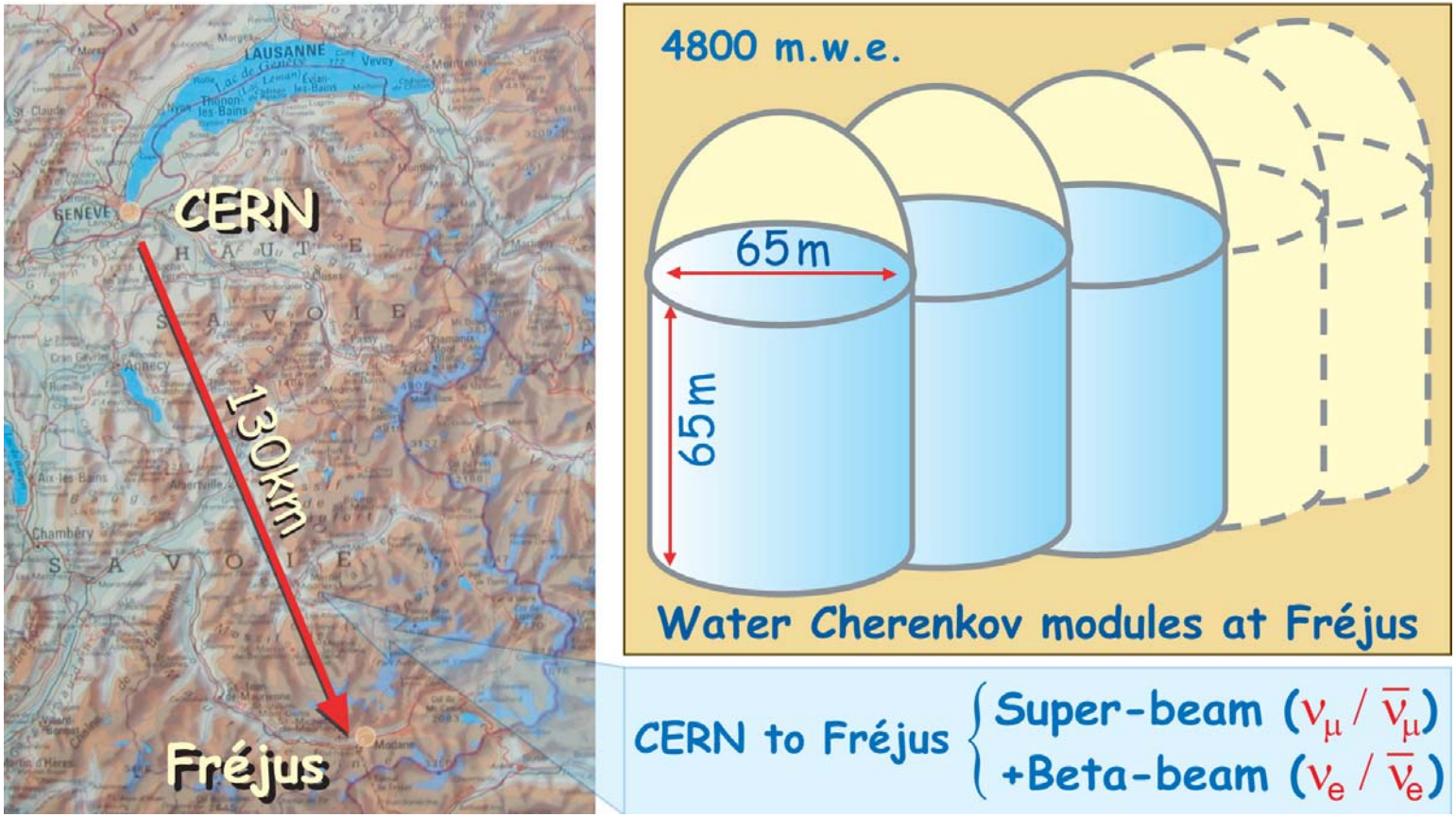

[a] For more details see J. E. Campagne, M. Maltoni, M. Mezzetto, and T. Schwetz, "Physics potential of the CERN-MEMPHYS neutrino oscillation project," hep-ph/0603172 and references therein.

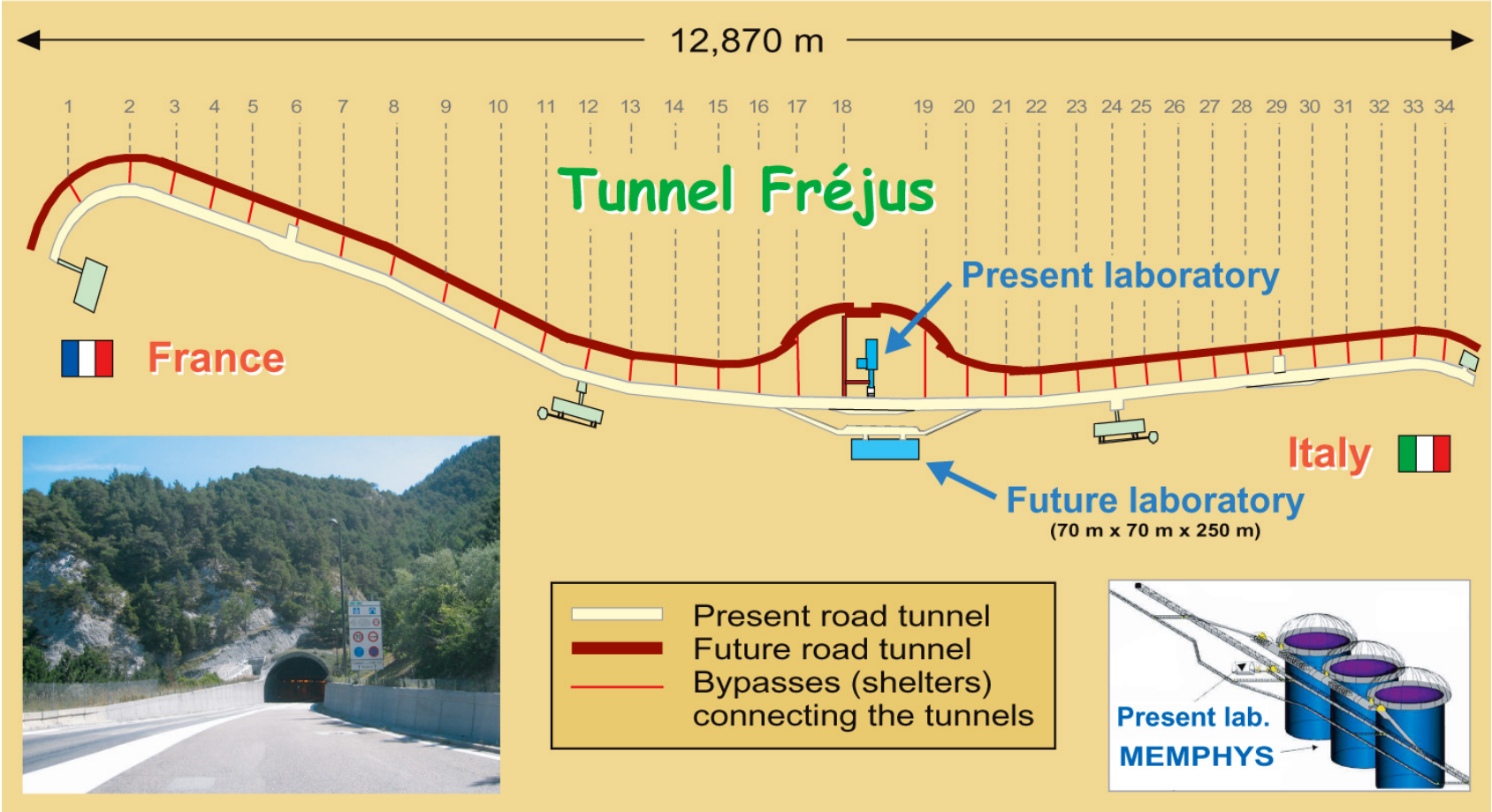

A preliminary investigation shows the feasibility to excavate in the middle of the Fréjus tunnel at a depth of 4800 m.w.e. up to five shafts of about $250,000$ m^3 each to place 3 to 4 water Cherenkov modules and a liquid argon detector (of about 100 kt total mass).

Main results of the preliminary study are

1. the best site (rock quality) is found in the middle of the mountain, at a depth of 4800 m.w.e.;
2. of the two considered shapes : "tunnel" and "shaft", the "shaft (= well) shape" is strongly preferred;
3. Cylindrical shafts are feasible up to a diameter $\oslash = 65$ m and a full height $h = 80$ m (volume $\approx 250,000$ m^3);
4. with "egg shape" or an "intermediate shape" the volume of the shafts could be still increased (to $\oslash = 70$ m);
5. the estimated cost is $\sim 80 \times 10^6$ Euros $\times$ Number of shafts.

Detector basic unit:

a cylinder (*a la* SK) 65 m diameter and 65 m height $\Rightarrow 215$ kt of water ($\sim 4 \times$ SK) taking out 4 m from outside for veto and fiducial cut $\Rightarrow 146$ kt fiducial target.

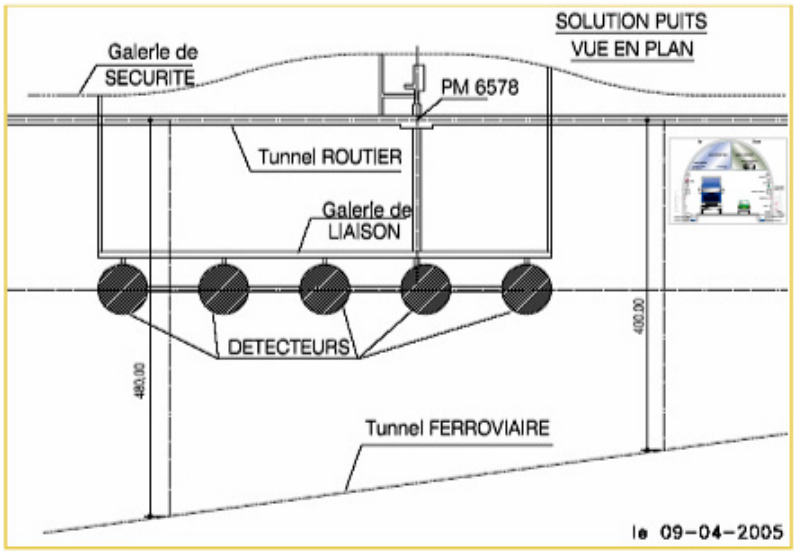

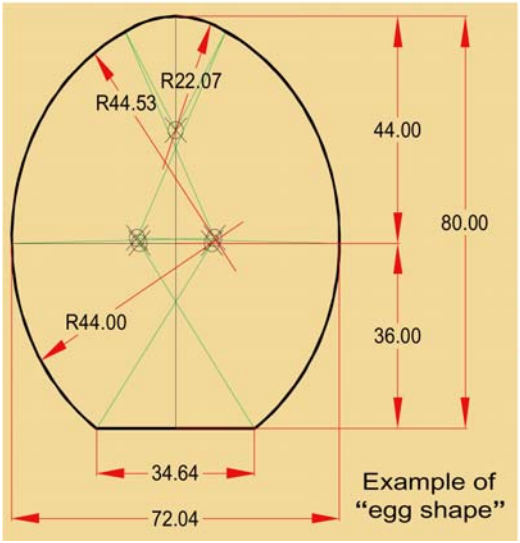

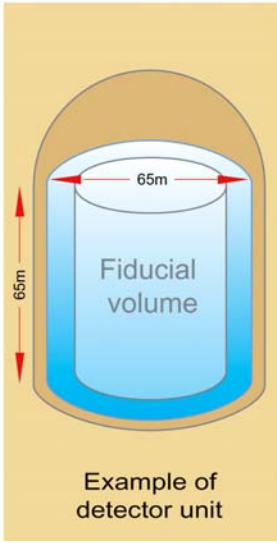

Mechanics and photoelectonics is under R&D to minimize the cost to quality ratio.

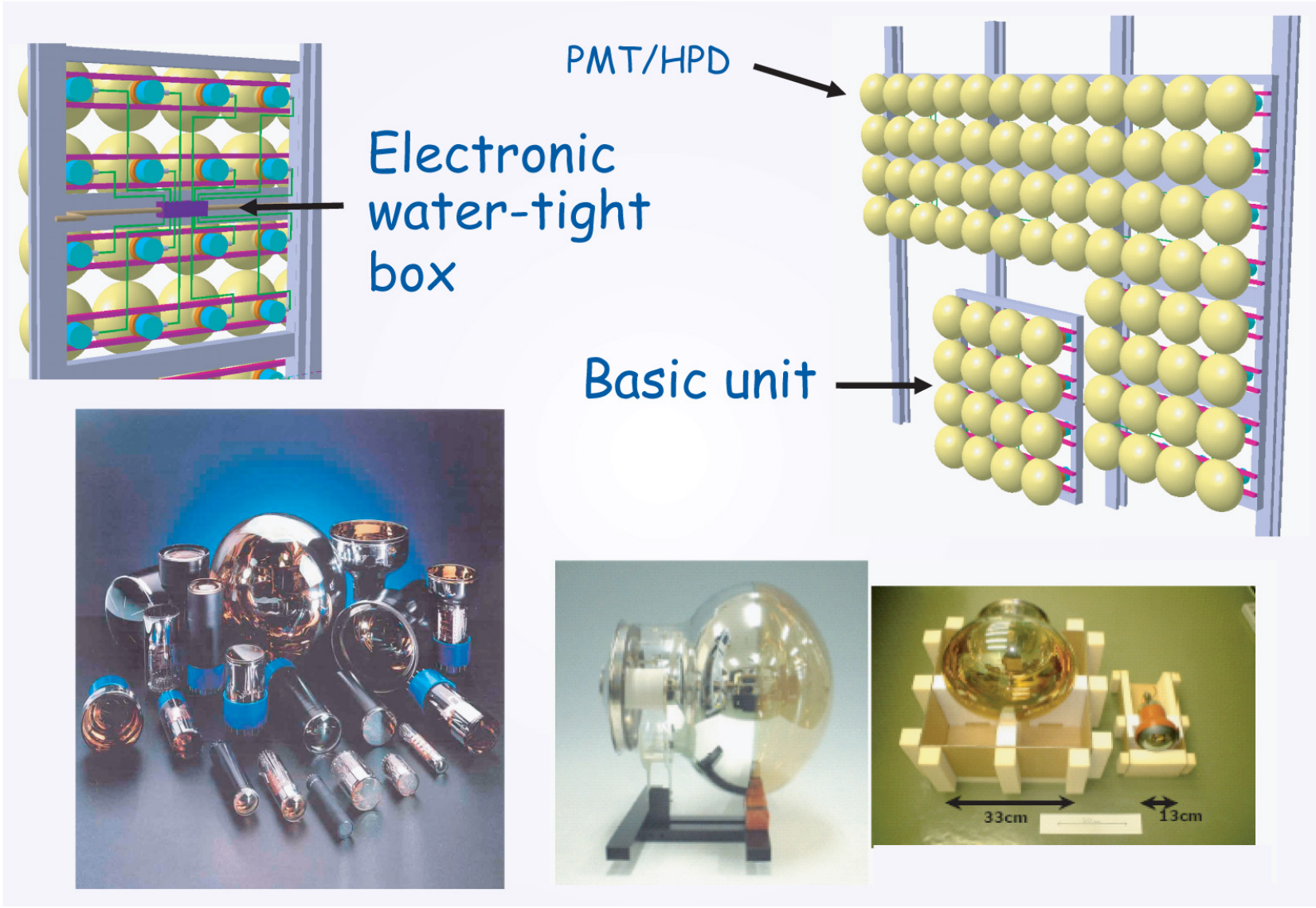

Physics goals and potential

- ⋆ proton decay (for 5 Megaton $\times$ years):
  - $\tau\left(p \to e^+ p^0\right) \approx 10^{35}$ years,
  - $\tau\left(p \to nKp^+\right) \approx 2 \times 10^{34}$ years,
  - complementarity with liquid argon detector.
- ⋆ Neutrino bursts from supernovae explosion (collapse studies and explosion alerts):
  - $\sim 200,000$ events from a SN at 10 kpc,
  - ~ 30 events from Andromeda,
  - ~ 2 events at 3 Mpc.
- ⋆ Relic Neutrinos from past supernovae explosions (for 5 Megaton $\times$ years):
  - ~ 100 events with pure water,
  - $2000/4000$ events with gadolinium loaded water.
- ⋆ Solar and atmospheric neutrinos.
- ⋆ Neutrino SPL super-beam (SB) and beta-beam (βB) from CERN.